Dynamics, formation and segregation of the cytoplasmic chemoreceptor cluster in *Rhodobacter sphaeroides*

CHRISTOPHER WILLIAM JONES

St. Peter's College
University of Oxford
Trinity Term 2013

A THESIS SUBMITTED FOR THE DEGREE OF
DOCTOR OF PHILOSOPHY

Abstract

DYNAMICS, FORMATION AND SEGREGATION OF THE CYTOPLASMIC CHEMORECEPTOR CLUSTER IN *Rhodobacter sphaeroides*

Christopher William Jones

St. Peter's College, University of Oxford

Submitted for the degree of Doctor of Philosophy, Trinity Term 2013

The internal organisation of bacteria is far more complex than originally thought. Many components of the cell have specific localisation patterns. Proteins are localised to many different regions of the cell by numerous mechanisms, and often their function depends on correct localisation.

Bacterial and plasmid DNA are also highly organised and actively positioned. These tightly regulated positioning patterns ensure stable maintenance of genetic material. Members of the ParA/MinD family of ATPases are responsible for the segregation of a large number of bacterial chromosomes and plasmids. Recently members of this family have been shown to position and segregate protein complexes. One such complex is the cytoplasmic chemosensory cluster of *Rhodobacter sphaeroides*. This large complexes are segregated from a single cluster positioned at the mid-cell to two clusters at $^1/_4$, $^3/_4$ positions by the ParA homologue PpfA using the nucleoid as a scaffold. This ensures that each daughter cell inherits a cluster.

This study sought to investigate this cytoplasmic chemosensory cluster, and its positioning and segregation by PpfA through the cell cycle.

The use of fluorescence recovery after photobleaching revealed that like membrane bound chemoreceptor arrays the cytoplasmic cluster of *R. sphaeroides* is a highly stable complex. The difference seen between the cytoplasmic cluster and the data reported for the membrane bound cluster of *Escherichia coli* is probably due to the lack of membrane helping hold the array together.

Investigation of the role of PpfA in segregation of the cytoplasmic cluster, using fluorescence imaging and single molecule tracking with a range of mutants through the cell cycle, suggest that it uses a mechanism unlike any reported for ParA homologues. Single molecule tracking of PpfA molecules shows that the chemoreceptor TlpT stabilises PpfA molecules resulting in slower diffusion of PpfA molecules at the cluster. The use of a Δ*ppfA* mutant shows that PpfA restrains the movement of the cluster, together these results suggest a model in which TlpT stabilises PpfA's interaction with the nucleoid and PpfA positions the cluster.

Declaration

The work in this thesis was undertaken in the Department of Biochemistry at the University of Oxford. Work was performed between October 2009 and October 2013 under the supervision of Prof. J.P. Armitage. All the work in this thesis is my own unless stated and has not been submitted for a degree at this or any other university.

Acknowledgements

I would like to thank Prof. Judy Armitage for her support and supervision over the course of my DPhil, and for providing me with the opportunities and freedom to explore interesting and exciting research.

Though my time in the lab a number of people have been of great help and support. I would especially like to thank Steven Porter, George Wadhams, David Wilkinson, Mark Roberts, Nick Delalez, and Nelly Dubarry. I would also like to thank all members of the lab both past and present.

Thank you to Dr. Achillefs Kapanidis for allowing me to use his microscope to do the single molecule microscopy work, and to Federico Garza de Leon for all his help in using the microscope and analysing the data.

I would like to thank all the friends I have made during my time in Oxford, both from the Department and from College, for making time outside the lab so much fun.

Contents

List of Figures

List of Tables

Abbreviations

1D	One dimensional
2D	Two dimensional
3D	Three dimensional
ATP	Adenosine triphosphate
bp	Base pair
BSA	Bovine serum albumin
CCD	Charge-coupled device
CFP	Cyan fluorescent protein
CCW	Counter-clockwise
CW	Clockwise
DAPI	4′,6-diamidino-2-phenylindole
D_{app}	Apparent diffusion coefficient
DIC	Differential interference contrast
DNA	Deoxyribonucleic acid
dNTP	deoxynucleoside-5′-triphosphate
EM	Electron microscopy
FRAP	Fluorescence recover after photobleaching
GFP	Green fluorescent protein
GUI	Graphical user inferface
IPTG	Isopropyl β-D-thiogalactoside
Kan	Kanamycin

kb	Kilo base
kDa	Kilo Dalton
MSD	Mean squared displacement
MCP	Methyl accepting protein
Nal	Nalidixic acid
OD_{600nm}	Optical density at 600nm
OD_{700nm}	Optical density at 700nm
ori	Origin of replication
PALM	Photoactivatable localisation microscopy
PAmCherry	Photo activatable mCherry
PCR	Polymerase chain reaction
PMF	Proton motive force
PSF	Point spread function
px	Pixel
ter	Terminus of replication
Tlp	Transducer like protein
$t_{1/2}$	Half-time
WT	Wild-type
YFP	Yellow fluorescent protein

Chapter 1

Introduction

1.1 Bacterial Motility and Taxis

In the laboratory bacteria are often grown shaking in rich media, and thus literally bathed in food, however in their natural environments bacteria can experience large changes in conditions. In order to ensure optimum growth across these changing environments they must be able to adapt to these changes in multiple ways, using changes in gene expression or behaviour.

A clear example of adaptive behaviour in varying environments is the ability to move in response to changing conditions; moving towards favourable conditions and away from unfavourable ones, a process known as taxis. Bacterial species have demonstrated taxis in response to a wide range of stimuli. Examples of such stimuli include magnetic fields (magnetotaxis) [103], oxygen (aerotaxis) [154], light (phototaxis) [159], temperature (thermotaxis) [63], molecules (chemotaxis) [4], and internal energetic state of the cell (energy taxis) [1].

In order to move towards or away from such stimuli bacteria have evolved a number of distinct approaches to motility (reviewed in [89]). These include various strategies for both moving across solid surfaces and for swimming through

liquid media.

Flavobacterium johnsoniae moves by rapidly gliding over surfaces. This is mediated by the surface attachment and flow of proteins in the outer membrane of the bacteria resulting in translocation of the cell body [121].

Myxococcus xanthus uses two mechanisms for surface motility, both distinct from each other and that of *F. johnsoniae*. The first, termed A-motility involves focal adhesion complexes attaching to the surface and propel the cell body forward [113]. The second, S-motility, depends on the extension, surface attachment and retraction of type IV pili [29]. Surface movement can also be mediated by the coordinated rotation of semi-rigid helical filaments projecting from the cell, flagella [91].

However by far the most prevalent use of flagella in bacterial motility is in swimming through aqueous environments [4]. Swimming bacteria using flagella based motility show a variety of swimming patterns, these variations are discussed in 1.2.

Motility and taxis provide clear advantages to cells over non-motile and non-tactic cells. These advantages extend beyond simply searching for the conditions which are beneficial for growth in isolation. Many bacterial species have life cycles which involve interaction with other organisms, and motility and chemotaxis play important roles in enabling the initiation of these favourable interactions. Disruption of the chemotaxis signalling pathway of *Helicobacter pylori* (which infects the gastrointestinal track resulting in ulcers) results in reduced pathogenicity [153]. Multiple symbiotic relationships require both motility and chemotaxis. The ability of *Azospirillum brasilense* to colonise wheat roots is dependent on both its mobility and chemotactic performance [192]; non-motile *Vibrio fisheri* mutants are unable to colonise the light organ of their symbiotic squid host [65].

As well as using motility and chemotaxis to interact with host species, for either

pathogenesis or symbiosis, bacteria also use them to interact with surfaces, individuals of the same species, and other bacterial species through the formation of biofilms, this has been shown in a number of species, including *Vibrio cholerae* [117], *Agrobacterium tumefaciens* [112], and *Rhodobacter sphaeroides* [207].

Whilst motility and taxis result in competitive advantages in all the above examples, these advantages do not come cheaply. Motility is an energetically expensive activity (especially the production of large protein assemblies which generate it), so much so that when placed in an environment in which motility no longer conveys an advantage, such as shaking liquid media all *Salmonella typhimurium* cells become non-flagellate (and thus non-motile) via spontaneous mutations within 10 days [110]. These non-flagellate cells displayed a $\sim$2% advantage in growth rate over WT cells when grown in shaking liquid media.

This large energetic cost highlights the importance of motility and taxis to many bacterial species in their native environment. Given this importance it follows that increased understanding of bacterial motility and taxis can provide the basis for development of treatments against pathogenic bacteria as well as positive applications of bacteria in industrial and agricultural settings.

1.2 Flagella-Mediated Taxis

Flagellate bacteria all use a rotary filament to produce cellular locomotion but they can have different patterns and numbers of flagella.

Monotrichous bacteria possess a single flagellum, examples include *Caulobacter cresentus* [3] and *R. sphaeroides* [134]. These two species position their flagellum differently, with polar positioning in *C. crescentus* and sub-polar in *R. sphaeroides* , indicating the variety seen even within single flagellar bacteria.

Peritrichous bacteria possess multiple flagella. *S. typhimurium* and *E. coli* are both examples of peritrichous bacteria, these species produce between 4 and 8 flagella from the sides of the cell which come together to form a bundle at the rear of the swimming cell [4]. Other bacterial species also produce multiple flagella but position them with greater specificity, for example *V. fisheri* produces and positions multiple flagella at one of the cell poles [210], such bacteria are termed lophotrichous.

Some bacteria can regulate flagella number depending on the form of motility required. *Proteus mirabilis* typically has 4 - 10 flagella, however when swarming on solid surfaces it increases the number of flagella by up to five fold [188]. As well as regulating the number of flagella some bacterial genomes encode multiple flagellar systems. *Vibrio parahaemolyticus* swims using a single polar flagellum, however when moving on surfaces it expresses a second set of flagellar genes to produce multiple lateral flagella [96].

An interesting variation on the use of flagella for locomotion is that of the spirochaetes. Spirochaetes, such as *Treponema pallidum*, possess flagella which do not penetrate the outer membrane, and instead exist within the periplasmic space [32]. The rotation of the flagella results in rotation of the spiral shaped flexible cell body causing cellular movement through viscous environments.

However the ability of bacteria to use flagella to propel themselves is not sufficient to generate the directional movement required for tactic behaviour. Directional movement is achieved through the combination of 'runs', where flagella are used to generate propulsion, and 'tumbles', where forward motion ceases and the cell body reorientates. If there is no control over the frequency of tumbling events then the bacterial motion results in a 'random walk' and no net directionality in movement, see fig. 1.1 A. However if there is control over the tumbling frequency then in response to chemical stimuli chemotaxis can occur. This hap-

pens by increasing the tumbling frequency in response to worsening conditions, and decreasing the frequency in response to improving conditions, thus when moving in unfavourable directions the cell changes direction more often. This results in a 'biased random walk' towards favourable conditions, see fig. 1.1 B.

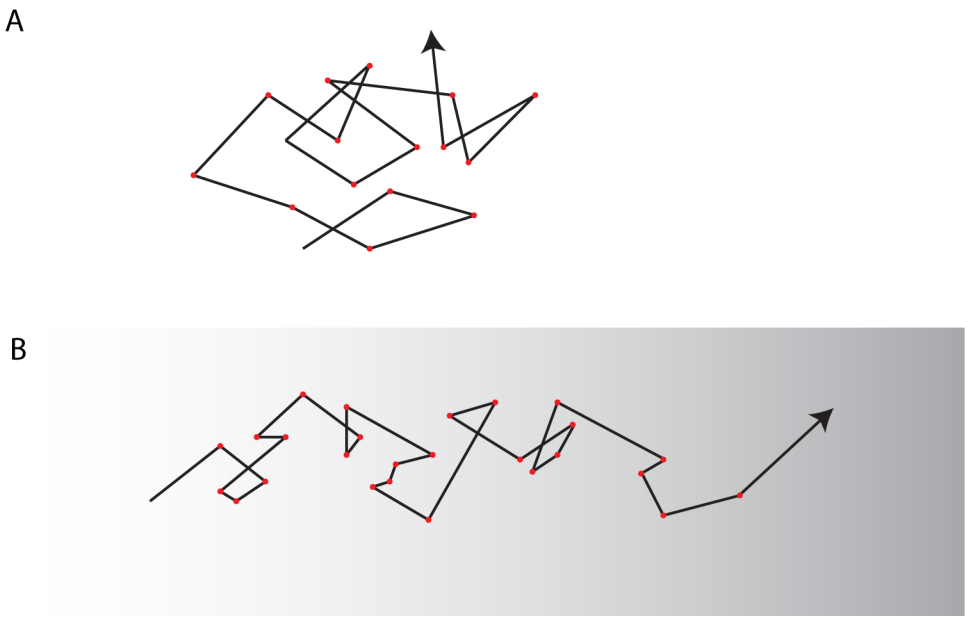

Figure 1.1: Directional movement by biased random walk. **A:** In the absence of a chemical gradient bacteria move by random walk with no net directionality to their movement. **B:** When a chemical gradient is present, represented as the gradient from light (unfavourable) to dark (favourable), bacteria use a biased random walk to produce net directional movement up the gradient. Black lines represent runs, and red dots tumbles.

The core mechanism by which flagellate bacteria achieve these tumbling events is similar across species but shows variation in complexity. The best studied model organism for flagellar motility and chemotaxis is *E. coli* . When swimming (i.e. a run) its flagella rotate in a counter-clockwise (CCW) direction resulting in rotation of the flagellar bundle and locomotion. Tumbling is caused by one or more flagella switching rotational direction to clockwise (CW), resulting in the bundle breaking apart. Due to the small size of bacteria they have a very small Reynolds number, meaning that they possess very little inertia, thus upon cessation of propulsion the cells stop immediately. With multiple flagella now pointing in

various directions and rotating in different directions the cell randomly reorientates as a result of Brownian motion. Once all the flagella return to CCW rotation the flagellar bundle can reform and the cell will swim off in a new random direction [14].

Clearly however this paradigm cannot be extended to monotrichous bacterium. The monotrichous bacteria *R. sphaeroides* achieves tumbling events by stopping rotation of the flagellum rather than the switching of direction of rotation, whilst stopped the cell reorientates through Brownian motion [134].

1.3 Chemotaxis

As discussed above tactic behaviour is dependent on the ability to modulate tumbling frequency in response to stimuli. For chemotaxis this requires a link between environmental conditions and the flagellar motor output. This link is a two component signalling pathway consisting of a histidine-aspartate phosphorelay (HAP). The two components of HAP systems are a dimeric histidine protein kinase (HPK) and a response regulator (RR). HAP signalling pathways are common in bacteria, as well as being found in a small number of eukaryotic organisms [197]. The signal is transduced by senosry domain of the HPK sensing a stimulus and trans-autophosphorylating a specific histidine residue on the other monomer. This phosphoryl group is then transferred to a specific aspartate residue on the receiver domain of the response regulator. The phosphorylated response regulator then goes on to elicit downstream effects, often gene transcription regulation (two component signalling in bacteria is reviewed [21]).

Bacteria use modified HAP pathways to control their flagella. The best studied and understood of these pathways is that of *E. coli* [5]. Like all HAP systems this pathway uses a HPK (CheA) and a response regulator (CheY). However

unlike canonical HPKs CheA does not sense stimuli directly, instead it interacts with transmembrane chemoreceptors termed methyl-accepting chemotaxis proteins (MCPs) [197]. This interaction is coupled by an adaptor protein, CheW. MCPs span the plasma membrane such that their sensing domains lie within the periplasmic space, thus information about chemicals within the periplasm can be transmitted across the membrane into the cytoplasm.

MCPs dimerise, and these dimers assemble into trimers of dimers. The existence of MCPs in this trimer of dimers state is not required for ligand binding or transmembrane signalling, but importantly it is required for the control of CheA activity [18]. *E. coli* has four MCPS and a redox receptor which sense a variety of chemical stimuli, such as amino acids, some sugars, dipeptides and redox potential [181]. The MCP Tar is able to sense different stimuli through multiple mechanisms, sensing aspartate directly through binding, and sensing maltose through interactions with maltose-binding-protein [118].

Ligand binding to MCPs results in signal transduction across the membrane through a shift and rotation in one of the transmembrane helices [34]. This results in changes in the interactions between the distal tip of the MCPs and CheA and CheW, which in turn changes the rate of CheA trans-autophosphorylation [77]. CheA activity determines the level of phosphorylated CheY (CheY-P) in the cell. CheY-P can bind to the flagella motor protein FliM, and when sufficient levels of CheY-P are present result in the direction of flagellar rotation to switch from CCW to CW and thus a tumbling event [205].

Given that the cell is attempting to swim towards increasing concentrations of chemoattractants it needs to reduce the frequency of tumbling events in response to increased attractants. This is achieved by inducing decreased CheA activity in response to ligands binding to MCPs.

CheY is not the only response regulator phosphorylated by CheA, CheB is also

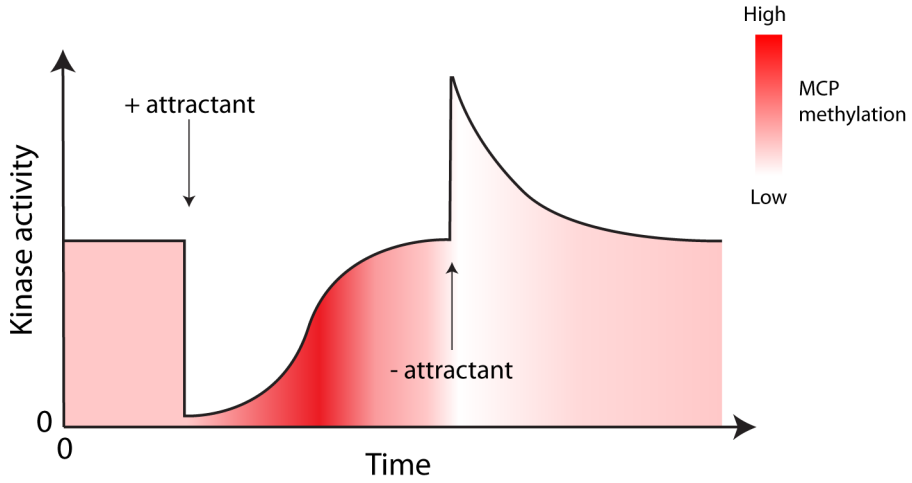

Figure 1.2: Methylation based adaptation of MCP activity. Kinase (CheA) activity drops following the addition of chemoattractant. The decrease in CheA activity decreases the levels of CheB-P, which results in increased MCP methylation (shown as red). This reduces the affinity of the MCP for ligands, which in turn increases CheA activity and therefore CheB-P levels to of that before addition of attractant. Thus the basal level of CheA activity has now been adapted to the current attractant levels. When attractant is removed CheA activity increases, which results in reduced MCP methylation (shown as white). This low methylation state increases the affinity of MCPs for ligands. The high CheA activity increases CheB-P levels and thus returns the methylation state to the pre-stimulus level.

phosphorylated. CheB is a response regulator with a methylesterase domain, and acts alongside a methyl-transferase, CheR, to form the adaptation system. An adaptation system is needed as in order for bacteria to swim up gradients they have to be able to respond to relative changes in chemical concentrations across a large range of absolute concentrations. Thus they need a mechanism by which they can determine whether current conditions are better or worse than those just previously experienced.

Both CheB and CheR act on specific glutamate residues of MCPs, demethylating and methylating them respectively; the methylation state of MCPs modulates their sensitivity to stimuli [75]. CheR is constitutively active, whereas CheB activity is increased 100 fold when phosphorylated (CheB-P) by CheA [2]. Ligand binding reduces the activity of CheA and therefore reduces the levels of CheB-P, resulting in increased MCP methylation. This in turn decreases the ligand affinity

of the MCPs and thus results in an increase in CheA activity [76]. This increased CheA activity increases levels of CheB-P, therefore reducing the levels of MCP methylation, and thus returns the MCPs to their pre-stimulus state.

Through this methylation based adaptation system the cell can continually assess current conditions relative to the previous conditions, which the chemotaxis pathway will have adapted to.

The final component of the *E. coli* chemotaxis pathway is CheZ. CheZ accelerates the rate of CheY-P dephosphorylation, reducing the half-time of CheY-P from $\sim$ 2 s to $\sim$ 200 ms [197]. This high rate of dephosphorylation is required for termination of the signal on fast enough time scales to allow bacteria to sense and respond to changes temporally whilst moving. Mutants lacking CheZ tumble excessively as the slow signal termination results in persistent signal and thus tumbling.

A schematic of the *E. coli* chemotaxis pathway is shown in fig. 1.3.

The elegant simplicity of the *E. coli* chemotaxis pathway make it an attractive paradigm. However analysis of the genomes of motile bacterial species has revealed that over 50% of them contain multiple copies of each of the core chemotaxis genes (*cheA*, *cheB*, *cheR*, *cheW* and *cheY*) [70]. Therefore models based on the study of *E. coli* chemotaxis alone may not be sufficient to describe chemotactic signalling in a large number of species. A species which has multiple homologues of the *E. coli* chemotaxis genes and whose chemotaxis has been well studied is *R. sphaeroides* .

The chemotaxis genes of *R. sphaeroides* are encoded in three operons (*che*Op$_1$, *che*Op$_2$, and *che*Op$_3$) as well as several other loci (*cheBRA* and the *cheY*$_4$-*mcpG* locus) [69]. Of these neither *che*Op$_1$ or *cheBRA* are required for chemotaxis under normal laboratory conditions [134].

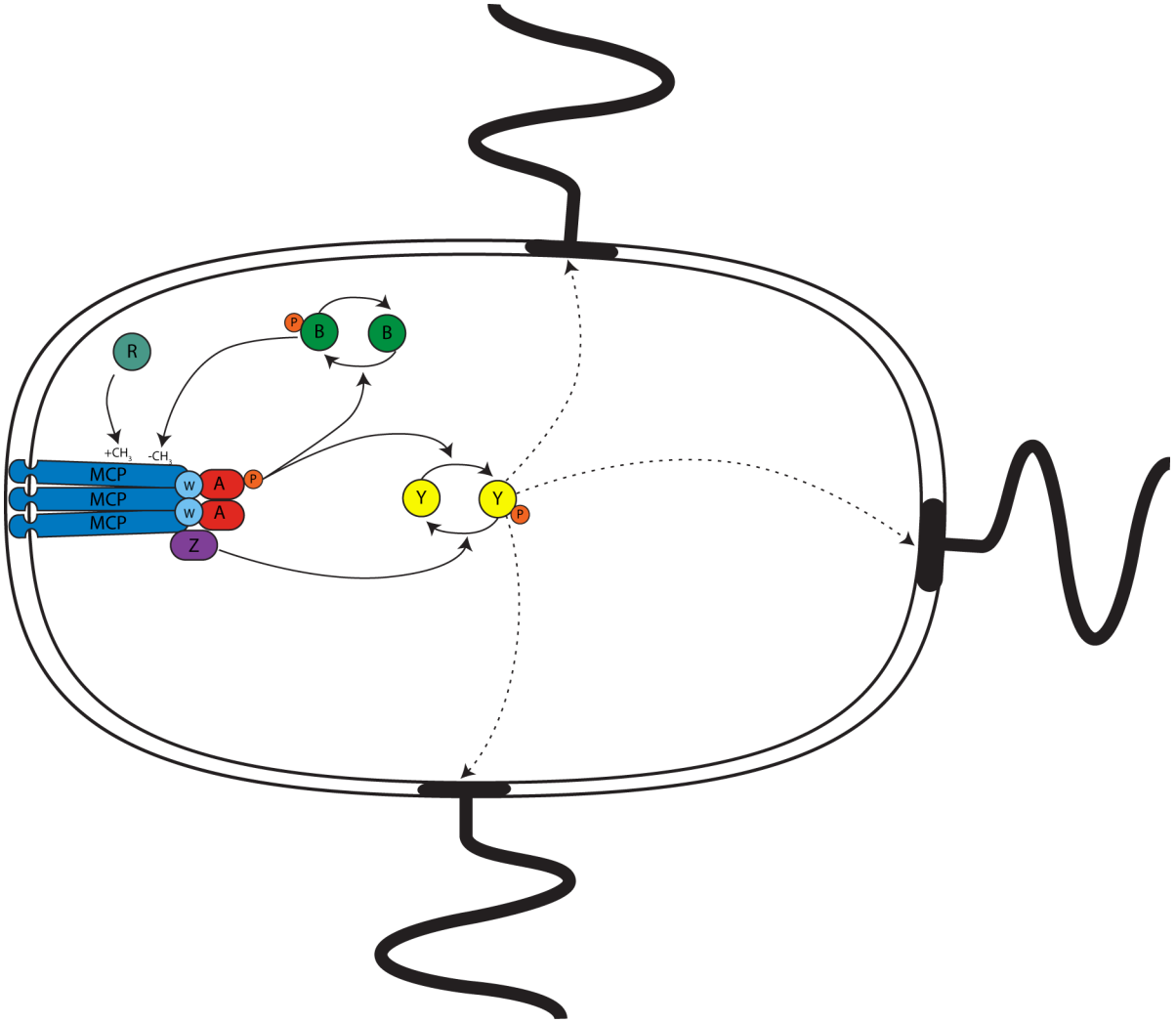

Figure 1.3: The chemotaxis pathway of *E. coli* . Transmembrane chemoreceptors, methyl-accepting chemotaxis proteins (MCPs) sense levels of chemical stimuli in the periplasmic space. Associated with them is a histidine protein kinase, CheA, and an adaptor protein, CheW. A decrease in stimuli results in an increase in trans-autophosphorylation of CheA, which then phospho-transfers to the response regulators CheY and CheB. Phosphorylated CheY is able to interact with the flagellar motor and induce rotational switching, causing a tumbling swimming event. Phosphorylated CheB removes methyl groups from the MCPs and results in adaptation. CheZ dephosphorylates CheY-P ensuring rapid signal termination.

Interestingly the *R. sphaeroides* genome also encodes two sets of flagellar genes (*fla1* and *fla2*) [132]. Under normal laboratory conditions only *fla1* is expressed (producing a single sub-polar flagellum), however by selecting for motile cells in a Δ*fla1* strain cells expressing *fla2* have been isolated [132]. Analysis of these mutants revealed that expression of *fla2* produces a tuft of polar flagella, which are controlled by proteins encoded in *che*Op$_1$ [39].

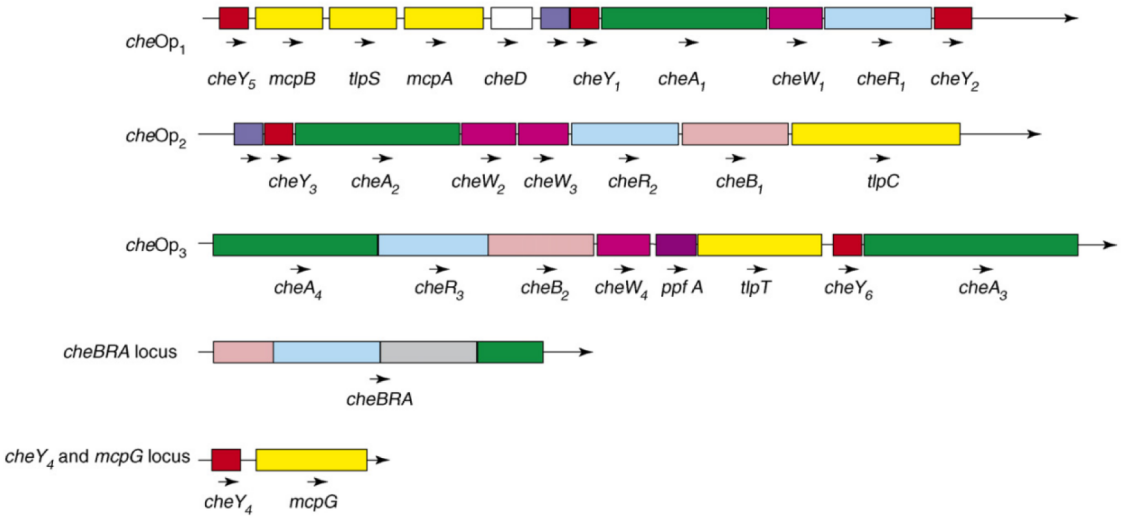

Figure 1.4: Chemotaxis operons of *R. sphaeroides* . *che*Op$_1$, *che*Op$_2$, and *che*Op$_3$ and *cheBRA* are encoded on chromosome I, the *cheY*$_4$-*mcpG* locus is encoded on chromosome II. Adapted from [134].

The signalling between *che*Op$_2$ and *che*Op$_3$ gene products and the *fla1* flagellum follows the same basic pattern as that of *E. coli* , but with several important differences. Given that *R. sphaeroides* has multiple copies of the *E. coli* chemotaxis proteins early studies investigated the organisation of these proteins in order to compare it to that of *E. coli* . The use of immuno-gold electron microscopy and fluorescent protein fusions revealed that the chemotaxis proteins of *R. sphaeroides* localise to two distinct regions within the cell [198]. *che*Op$_2$ gene products (with the exception of TlpC) localise to the pole of the cell along with the transmembrane chemoreceptors, MCPs [199], whereas proteins encoded in *che*Op$_3$ form a cluster in the cytoplasm of the cell. The chemoreceptors which localise to the cytoplasmic cluster are homologues of MCPs, but lack the transmembrane domain,

and are known as transducer-like proteins (Tlps). Both TlpT and TlpC localise to the cytoplasmic cluster [198, 201].

The polar cluster contains a single CheA homologue, $CheA_2$, and two CheW homologues, $CheW_2$ and $CheW_3$. Due to the similarity in composition to that of the *E. coli* chemotaxis cluster it is believed that signal transduction through this cluster occurs much like it does in *E. coli* , although the requirement for two CheW proteins remains unclear. $CheA_2$ auto-transphosphorylates, and has been shown to phosphotransfer *in vitro* to the response regulators $CheB_1$, $CheB_2$, $CheY_3$, $CheY_4$, and $CheY_6$. However *in vivo* the localisation suggests $CheB_2$ and $CheY_4$ are primarily associated with the cytoplasmic cluster.

The cytoplasmic cluster however is significantly different compared to both the *E. coli* cluster and the polar *R. sphaeroides* cluster, especially regarding the CheA proteins. This cluster has two CheA homologues, $CheA_3$ and $CheA_4$, however they are both atypical CheA proteins. Canonical CheAs contain five domains (P1-5), $CheA_3$ and $CheA_4$ contain different subsets of these domains (P1-P5 and P3-5 respectively). This means that they are unable to trans-autophosphorylate as homodimers, instead the kinase domain (P4) of $CheA_4$ phosphorylates the P1 domain on $CheA_3$, which then phosphotransfers to the $CheB_2$ and $CheY_6$ [134].

R. sphaeroides needs both chemosensory clusters to chemotax, and deletion of any component of these clusters results in loss of taxis. Most components will complement deletions of their *E. coli* homologues, but cannot complement deletions of homologous components within the other cluster in *R. sphaeroides* . Swapping the domains which localise CheA proteins results in switching of CheA localisation but loss of chemotaxis [166], indicating that components of these clusters must be in the correct cluster to function.

It has also been shown that the 794 amino acid linker domain between the P1 and P5 domains of $CheA_3$ is able to act as a $CheY_6$ -P phosphatase, and that

this activity is required for chemotactic ability [135]. *R. sphaeroides* lacks a CheZ homologue, and therefore has adapted a CheA protein to achieve rapid signal termination.

Both operons encode CheB and CheR homologues, and each pair is believed to be responsible for adaptation of the chemotaxis proteins they are encoded with due to their subcellular positioning. It is interesting to note that $CheA_2$ can phosphotransfer to both $CheB_1$ and $CheB_2$ suggesting possible cross-talk between the two clusters.

R. sphaeroides has multiple CheY homologues, of which a minimum of two are required for chemotaxis, $CheY_6$ and either $CheY_3$ or $CheY_4$ [136]. $CheY_6$ is the only one which has been shown to be able to stop the flagellar motor, the roles of $CheY_3$ and $CheY_4$ remain unclear.

A schematic of the chemotaxis pathway of *R. sphaeroides* is shown in fig. 1.5.

The polar cluster is proposed to sense the external environment, while the cytoplasmic one senses the metabolic state of the cell.

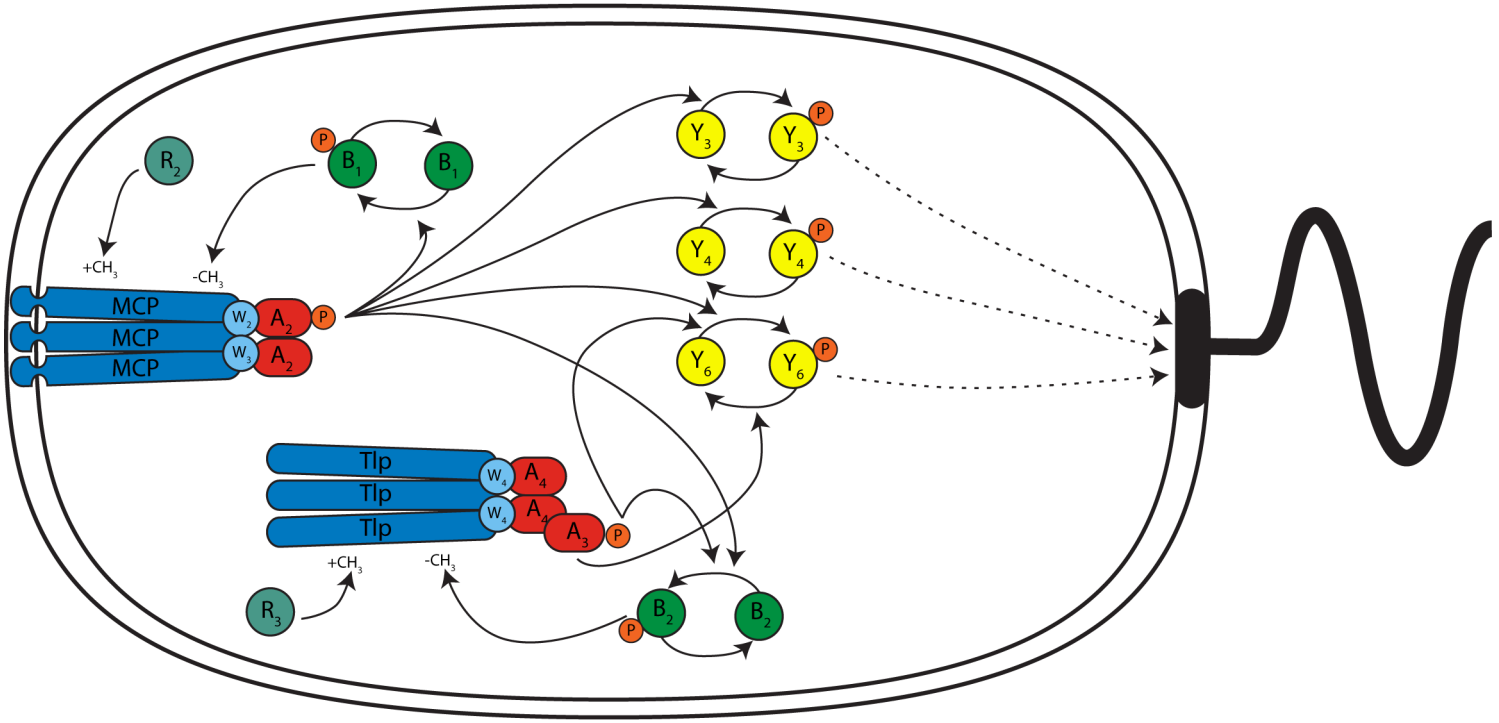

Figure 1.5: The chemotaxis pathway of *R. sphaeroides* . Transmembrane and soluble chemoreceptors (MCPs and Tlps respectively) form two spatially distinct chemosensory clusters. MCPs form a cluster at the pole, whereas Tlps form one in the cytoplasm. Each cluster has its own CheA and CheW homologues which specifically localise to that cluster. Decrease in attractant results in reduced $CheA_2$ trans-autophosphorlyation, and $CheA_3$ - $CheA_4$ transphosphorylation. A number of response regulators are then phosphorlated, with $CheY_6$ -P interacting with the motor and causing the stopping of flagellar rotation and therefore a tumbling event. Only the proteins required for chemotaxis are shown.

1.4 Chemoreceptor Arrays

Chemoreceptor clusters form incredibly large protein complexes, containing tens of thousands of copies of receptors and the associated chemotaxis proteins [106]. Given the importance of chemotaxis this large size raises several interesting questions. How are these vast numbers of proteins organised? How stable are these clusters? And how are they formed, positioned and partitioned into daughter cells? Why do the receptors along with CheW, CheA and adaptation proteins form these large ternary complexes?

1.4.1 Architecture

Electron cryo-tomography has been an invaluable tool in revealing details of the architecture of bacterial chemotaxis clusters. The use of electron cyro-tomography on intact *E. coli* cells revealed that its chemotaxis cluster is organised into a lattice of MCPs with CheA and CheW forming a base plate at the cytoplasmic side of the lattice [217]. A side view of a chemoreceptor array is shown in fig. 1.6. However this study was unable to distinguish between possible models of MCP packing.

Investigation of the *C. crescentus* chemotaxis cluster, however was able to and showed that MCPs in this species packed hexagonally into the array (see fig. 1.7) [25]. The presence of CheA and CheW is required for tight packing of the lattice, deletions strains still possess chemorecptor clusters but these are considerably more diffuse that WT [171, 94]. This shows that CheA and CheW are not just important due to their direct role in signal transduction but also structurally in the formation and maintaince of chemorecptor clusters. This approach was extended to multiple bacterial species and showed that hexagonal packing of trimers of dimers of MCPs was found across an evolutionarily diverse range of bacteria [26].

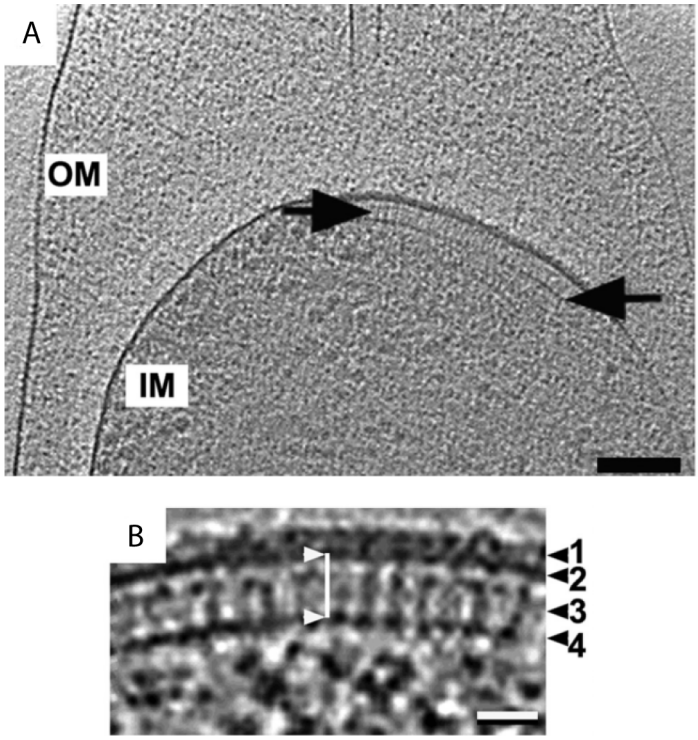

Figure 1.6: Chemoreceptor arrays. **A:** A typical tomograph of the chemoreceptor array of *Thermotoga maritima*. The outer membrane (OM) and inner membrane (IM) are visible and arrows indicate the location of the chemoreceptor array. Scale bar is 100 nm. **B:** Enlarged view of a chemoreceptor array of *Thermotoga maritima*. 1: periplasmic domain of MCPs, 2: inner membrane, 3: cytoplasmic receptor domains, 4: CheA-CheW base plate layer. Line between white arrows indicates width of the array. Scale bar is 25 nm. Both A and B adapted from [26]

The polar cluster of *R. sphaeroides* shares these characteristics [26]. The architecture of the cytoplasmic cluster is unknown, but the atypical CheAs suggests that the CheA-CheW base plate may be organised differently. The lack of a membrane to form around could also lead to different architecture.

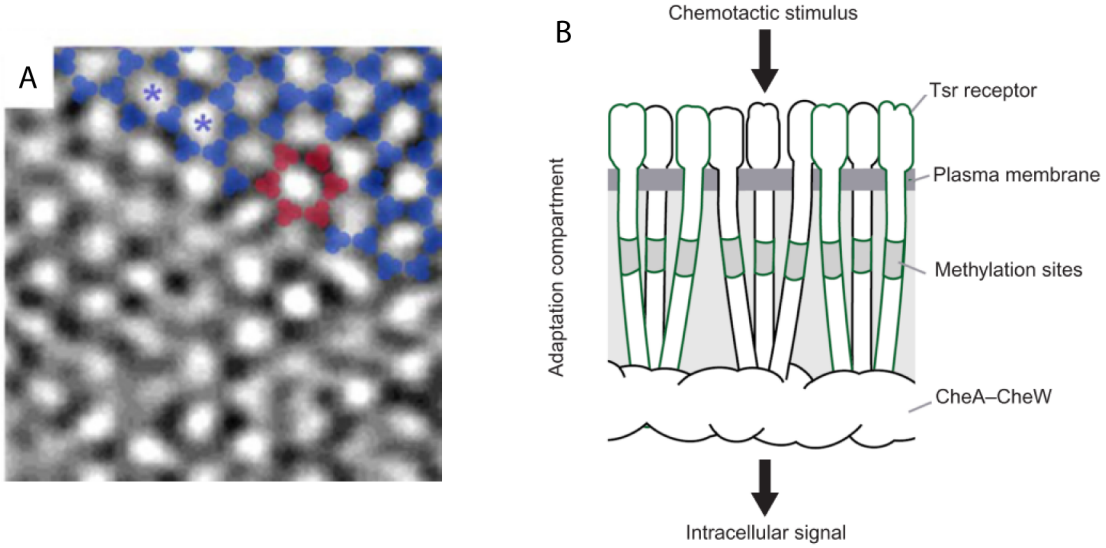

Figure 1.7: Hexagonal packing of trimers of dimers of chemoreceptors. **A:** Top down view of chemoreceptor array of *V. cholerae* . Trimers of dimers are shown in blue. The hexagonal packing is illustrated by highlighting six trimers of dimers in red. Asterisks indicate centres of hexagonal packing units. Adapted from [26]. **B:** Schematic side view of receptor packing. Adapted from [168].

1.4.2 Dynamics

Techniques such as electron cryo-tomography reveal fantastic structural details of large macromolecular assemblies, however the need to fix cells and the averaging of tomograms mean that no details about the dynamics and mobility of units within these assemblies can be determined. The use of fluorescent protein fusions on the other hand allows details of dynamics and localisation of proteins within live cells to be elucidated. A particularly powerful technique in the investigation of dynamics of proteins within assemblies is fluorescence recovery after photobleaching (FRAP). By photobleaching a region of the cell and then following the distribution of florescence in the cell following the photobleach it is possible to determine the rate at which proteins can move within the cell and how tightly held they are to their assemblies. FRAP has been performed on proteins in the chemoreceptor cluster of *E. coli* [164]. This study analysed fluorescence recovery of a number of proteins in two different strains, one with WT function-

ality and stoichiometry but increased protein levels, and a second which did not express any of the chemotaxis genes, resulting in loss of cluster formation. This meant that mobility of the proteins could be assessed both as free proteins, and when bound to the cluster. An example series of images of CheZ fluorescence recovering in both the delocalised and localised strains is shown in fig. 1.8.

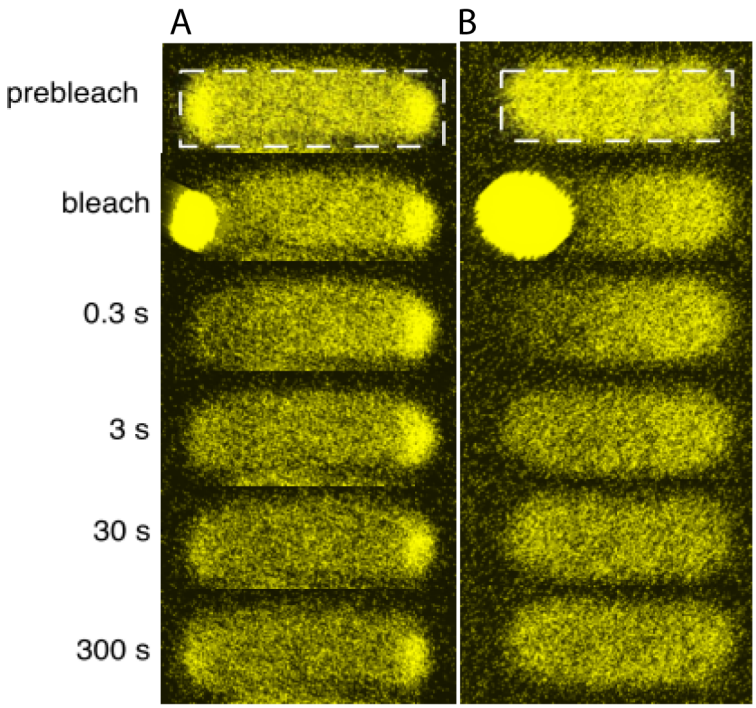

Figure 1.8: Fluorescence recovery after photobleaching of *E. coli* CheZ-YFP. **A:** Photobleaing of CheZ-YFP in a localised strain. **B:** Photobleaing of CheZ-YFP in a delocalised strain. Adapted from [164]

In the delocalised strain all proteins except for the chemoreceptor Tar displayed fast recovery times and these recovery times correlated with their molecular weight. Tar was expected to recovery slowly as it is a transmembrane protein, and its recovery is on a time scale similar to that shown for other transmembrane proteins of a similar size.

When the recovery was measured of proteins in chemoreceptor clusters all proteins except CheY showed decreased mobility. Tar recovery was very slow, ≈ 30 min, suggesting that the MCPs form a hyper-stable core of the array. CheA and

CheW also recovered slowly, though not as slowly as Tar, with recovery times of $\approx$ 12 min. CheZ was also stable, recovery time $\approx$ 8 min. Together MCPs, CheA, CheW and CheZ are proposed to form a stable core.

The adaptation proteins CheB and CheR were both less stable and showed recovery times of $\approx$ 15 s, a time scale comparable to that of adaptation.

Bleaching only part of the cluster rather than the whole cluster resulted in similar recovery rates, suggesting that the majority of exchange of CheA, CheB, CheR and CheZ proteins is due to exchange with a cytoplasmic pool rather than within the cluster.

CheY recovered very rapidly ($\approx$ 0.6 s), and is not bound tightly at the cluster as this recovery rate was independent of cluster presence. This fits with its role as signalling messenger having to rapidly transmit signals from the chemoreceptors to the flagellar motors.

1.4.3 Positioning and Partitioning

These large chemoreceptor arrays described above have been shown by electron cryo-tomography and fluorescence microscopy to preferentially localise to the polar regions of the cell across several bacterial species [26, 175]. Whilst there is a preference for the poles, it is common to find that cells with multiple clusters will have some of them localised laterally [94].

Several models have been put forward to explain the positioning of both the polar and lateral chemosensory clusters.

It was observed that the lateral clusters of *E. coli* were positioned periodically along the length of the cell. These clusters were positioned such that upon cell division lateral clusters would be positioned at the new poles of the daughter cells. This lead to the hypothesis that these lateral clusters were positioned and

anchored by a marker of pre-division sites [183]. The observation that the polar clusters were relatively mobile (within the polar regions of the cell), but that the lateral clusters immobile added further weight to the existence of a potential anchor. However no such anchor has been identified, neither cytoskeletal protein MreB or the Min system (discussed in 1.5) are required for this positioning.

A second proposed model is that of stochastic self assembly. In this model clusters form and position independently of any cellular markers or anchors. In this model clusters can stochastically nucleate and self-assemble. In a cell with an existing cluster, chemoreceptors which have just been translated and inserted into the membrane can either join the existing cluster or nucleate a new cluster. The probability of these two outcomes is dependent on the diffusion of the receptors and the nucleation rate (itself dependent on binding kinetics and amount of free receptor). If the receptor is inserted close to an existing cluster then there is a high probability that it will encounter and be absorbed into that cluster before it is able to nucleate a new one. Conversely if it inserted far from the existing cluster then probability favours nucleation, as the time required for a nucleation event to occur will be less than the time needed to encounter the existing cluster. This model has been shown in computer simulations to be able to produce periodic patterning reminiscent of that of chemosensory clusters in *E. coli* [202]. Examples of patterns generated by this simulation are shown in fig. 1.9

The authors of the pre-division anchor model adapted their model to include elements of the stochastic self assembly model [184]. Their previous model predicted between 5-9 pre-division site anchors, and that the lack of cluster occupancy at all these sites was due to insufficient levels of chemotaxis proteins. The deletion of the anti-σ factor *flgM*, essential for the regulation of flagella and chemotaxis gene expression, results in the overexpression of the chemotaxis proteins and thus allowed this hypothesis to be tested.

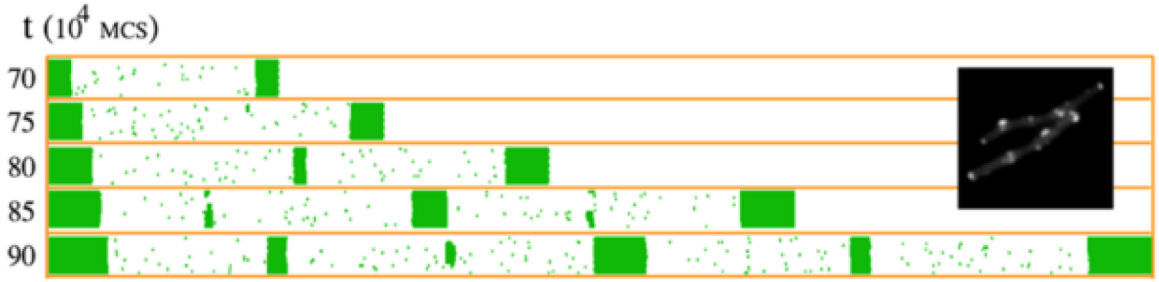

Figure 1.9: Stochastic self-assembly of chemoreceptor arrays *in silico*. The results of computer simulations of the stochastic self-assembly of chemoreceptor array formation. Green particles represent MCPs. Adapted from [202]

What was found was that the numbers of clusters initially increased with increasing protein levels. The mean maximum number of clusters per cell was 3.7, clearly lower than the predicted 5-9. Using cephalexin treatment to elongate the cells resulted in greater numbers of clusters per cell, but the cluster numbers still saturated. The average distance between clusters was found to be ~ 1 μm , indicating that there is a spatial limit relative to other clusters on cluster formation. As protein levels increased, the fluorescent intensities also increased. This increase was gradual rather than in jumps suggesting that clusters grow by gradual incorporation of receptors.

This updated model proposes that newly inserted receptors either join an existing cluster or nucleate a new one, as in the stochastic self-assembly model. Once nucleated, clusters can diffuse in the membrane until they are captured by an anchor. Once the maximum number of clusters is reached any new receptors will be captured before they can nucleate new clusters, leaving a number of anchor points unoccupied. This model is illustrated in fig. 1.10.

The use of super-resolution light microscopy has subsequently been applied to this issue [66]. Using photoactivation localisation microscopy (PALM) it was possible to localise individual chemotaxis proteins with 15 nm precision (the resolution of conventional light microscopy is $\sim$ 200 nm [79]).

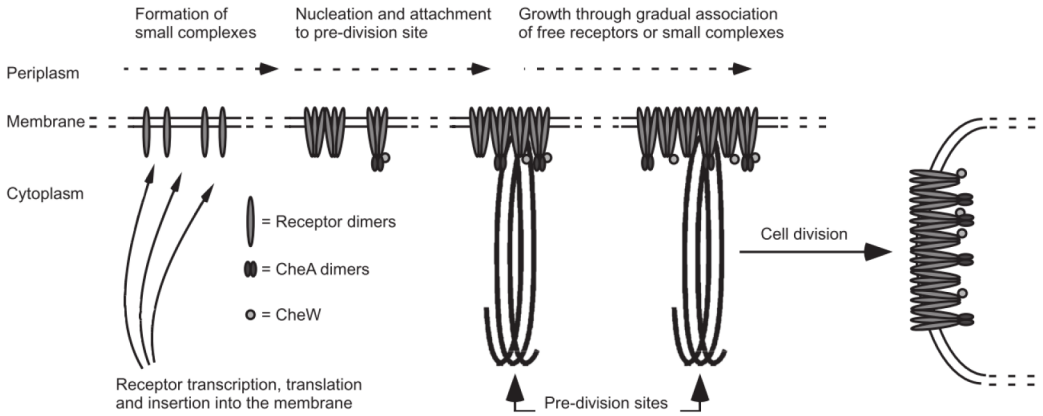

Figure 1.10: Stochastic self-assembly and capture model of chemoreceptor array formation. Receptors are inserted into the membrane, and along with CheA and CheW stochastically nucleate new clusters depending on the distance from existing clusters. These new clusters then diffuse in the membrane before being captured by a marker of the pre-division site. Adapted from [184]

The localisation patterns of the *E. coli* chemoreceptor Tar (an example of which is shown in fig. 1.11) typically consist of several large clusters which are often at the poles, a number of small lateral clusters and many even smaller clusters and single proteins. Analysis of the size of these clusters produced a continuous distribution of cluster sizes, suggesting that many small clusters form and then absorb newly expressed receptors and each other rather than a single sudden formation event from a large pool of free non-oligomeric receptors.

The fate of these small clusters is still defined by diffusion - self-assembly mechanisms: they either diffuse, encounter a large cluster and are absorbed, or are able to absorb enough new protein and other small clusters in order to grow and form a new large cluster. This is supported by analysis of the number of clusters along the long axis of the cell. In cells with one large polar cluster, the highest density of clusters is at the opposite pole, as clusters near the large one are absorbed into it. For cells with two large polar clusters the peak of cluster density is at the mid-cell.

The authors of this PALM study proposed a stochastic self assembly model which does not require any anchors or markers to achieve the spatial patterning of

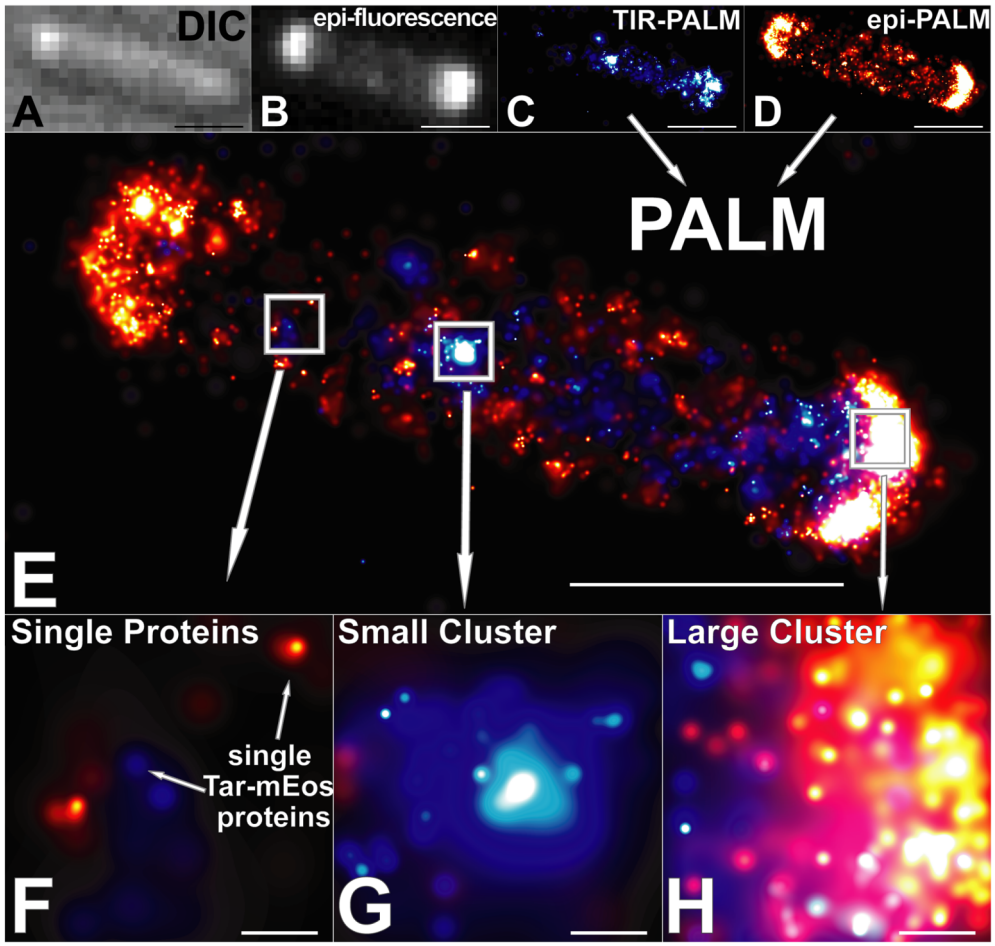

Figure 1.11: Super-resolution imaging of the chemoreceptor Tar. **A:** DIC image of the cell. **B:** Epifluorescence image of Tar-mEos. **C:** Total internal reflection PALM image of Tar molecules. **D:** Epifluorescent PALM image of Tar molecules. **E:** Composite image of TIR (in blue) and epi (in red) PALM images of Tar molecules. **F:** Single Tar molecules. **G:** Small lateral clusters. **H:** Large polar clusters. Scale bars are 50 nm. Taken from [66].

chemoreceptors seen *in vivo* .

If the anchor model was correct, then given the large number of small clusters distributed across the cell, why do none of the small clusters get captured by each predicted anchor point? Given this discrepancy and the fact that no anchor has been found yet the stochastic self assembly model is the more attractive model. It provides an elegant link between cluster formation, positioning and partitioning on division.

Other models have been suggested, such as the helical insertion of chemorecep-

tors into the membrane [169].

In *V. cholerae*, a homologue of ParA (a type I plasmid partitioning ATPase) termed ParC is responsible for the transition from a unipolar distribution of chemotaxis clusters to a bipolar distribution prior to division [150, 214], this system is discussed further in 1.8.1.

A recent study addressing the positioning of the polar transmembrane chemotaxis cluster of *R. sphaeroides* also shows divergences from the *E. coli* paradigms [35]. Like *E. coli* the membrane clusters of *R. sphaeroides* can be positioned both polarly and laterally. However unlike *E. coli* , where the lateral clusters were shown to position at pre-division sites [183], in *R. sphaeroides* the clusters positioned away from the Z-ring (a ring of FtsZ, which marks the septation site), as shown in fig. 1.12. It was also shown that the formation of a second polar cluster may be due to the movement of an existing one (either polar or lateral) to the unoccupied polar region. This does not fit with a stochastic self assembly model as the second cluster does not form furthest from the existing cluster, but suggests formation of mobile clusters of $\sim$ 800 receptors.

Re-expression of *cheW*$_2$and *cheW*$_3$in a double deletion background (both are required for proper clustering of the MCPs [200]) resulted in the formation of clusters, followed by their migration to and trapping at the poles, suggesting a preference for the curvature of the polar membrane. Together these results suggest that a combination of stochastic self assembly, diffusion-capture by the polar regions, and exclusion from regions around the Z-ring produces the positioning and partitioning of the membrane cluster of *R. sphaeroides* .

However *R. sphaeroides* also has a second cytoplasmic chemosensory cluster. This has been shown to depend on a ParA homologue, PpfA, for positioning and partition [185, 152]. This is discussed further in 1.8.2.

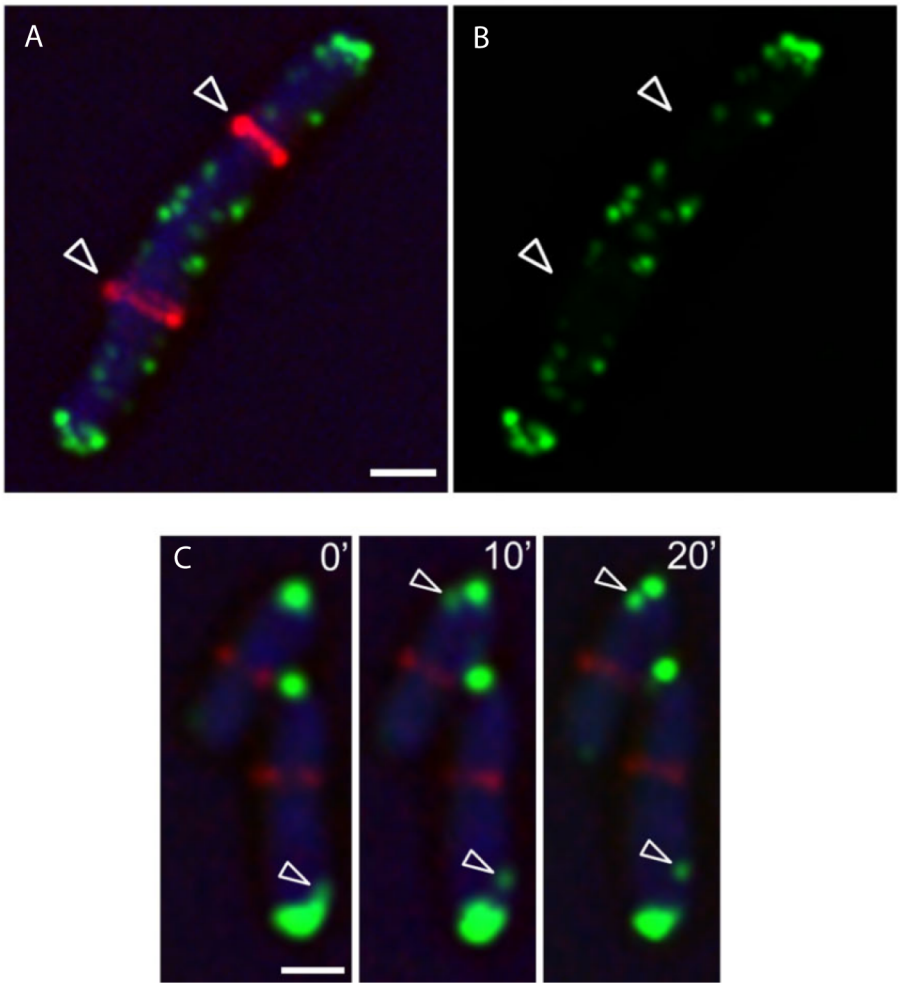

Figure 1.12: **A:** Localisations of the Z-ring and membrane chemosensory clusters in cephalexin-treated *R. sphaeroides* .White arrows indicate the positions of Z-rings. **B:** The image from A showing only the chemosensory clusters. **C:** Movement of small clusters. Arrows indicate small clusters, and the time is in minutes. Scale bars 1 μm . Adapted from [35]

1.5 Subcellular Localisation of Proteins in Bacteria

Over the last few decades there has been a dramatic shift in the understanding of bacterial intracellular organisation. Previously bacteria were considered homogeneous masses of protein and DNA bound by phospholipid bilayers. However recent advances in cellular imaging, and specifically fluorescent microscopy, have revealed that bacterial cells exhibit a staggering level of intracellular organisation. Proteins, chromosomal foci, plasmids and mRNAs across many species

have been shown to have specific localisation patterns. Use of time-lapse microscopy has shown that this high level of organisation is not just spatial but also temporal, with many proteins having dynamic patterns. A study using high throughput approaches to creating fluorescent fusions to proteins, and then imaging and analysing these fusions *in vivo* reported that over 10% of proteins expressed in *C. crescentus* showed non-uniform localisation [206].

Given both the numbers of proteins that localise and the range of subcellular localisation sites, it is clear that there cannot be a single universal mechanism for protein localisation [64]. However by comparing protein localisation strategies across species a number of general themes emerge. These include specific targeting proteins by active processes, diffusion-capture mechanisms, the use of differing physical properties of different subcellular regions, and protein self-organisation.

1.5.1 Diffusion-Capture

Diffusion-capture is an increasingly apparent theme in the localisation of many proteins [167]; its general principals are applicable to many seemingly different modes of localisation. The general model of diffusion-capture mediated localisation consists of proteins diffusing throughout the bacterial cell until they encounter a 'target', which itself is localised. This target captures the protein causing it shift from freely diffusing to localised along with the target. The target is often a protein complex which itself has been localised, but the use of diffusion-capture mechanisms means the the localisation of one protein can then be used to localise many more through passive diffusion.

Diffusion-capture is responsible for localising a number of proteins. One example is PleC, a transmembrane histidine kinase in *C. crescentus* which exhibits unipolar localisation. By tracking single molecules it was shown that molecules of PleC

are present throughout the membrane and that these molecules move through the membrane by non-directional 2D Brownian motion. Through this random diffusion they eventually reach the correct pole where they are captured and held by a target [38]. Another example is the localisation of SpoIVFB (a transmembrane protein) to the forespore membrane during sporulation in *Bacillus subtilis*. It was shown that the transmembrane protein SpoIVFA was required for correct localisation of SpoIVFB [156]. SpoIVFB is inserted into both the cytoplasmic and septal membrane and is then captured by SpoIVFA which independently localises to the septal membrane [157]. Once the forespore has been engulfed, SpoIVFA is topologically isolated from the cytoplasmic membrane, rendering any SpoIVFB inserted into the cytoplasmic membrane delocalised.

1.5.2 Association with Cytoskeletal Elements

Protein localisation in eukaryotes is often achieved by trafficking via cytoskeletal proteins. Although it was initially believed that bacteria did not possess any cytoskeletal proteins, recently homologues of the three major groups of eukaryotic cytoskeletal proteins have been found. FtsZ is a tubulin homologue; MreB and ParM are actin homologues; CreS is an intermediate filament (IM) homologue.

FtsZ

FtsZ is a bacterial homologue of the eukaryotic protein tubulin. Sequence alignments across many genomes have shown that the *ftsZ* is found in nearly all bacteria, as well as many archaea and chloroplasts [47]. It is the principle component of the cytokinetic machinery (the divisome). Just prior to cell division FtsZ forms a ring at the pre-divison site (Z-ring). This ring then recruits the other components of the divisome [49]. Upon assembly of the divisome the Z-ring contracts

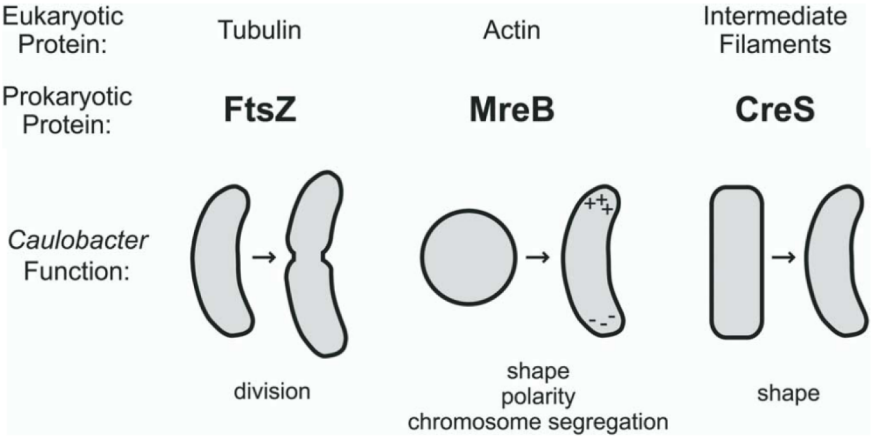

Figure 1.13: Cytoskeletal proteins of *C. crescentus* . FtsZ is a tubulin homologue and is required for septum formation. MreB is an actin homologue, and required for cell shape and polarity. CreS is an intermediate filament homologue and also require for correct cell morphology. Adapted from [62]

resulting in septation [48]. Therefore beyond its role in constriction of the cytokinetic ring, FtsZ is a target for the localisation of other divisome proteins. How the Z-ring is positioned is discussed in 1.5.3 and 1.5.5.

MreB

MreB is a bacterial actin homologue [190], which is encoded in the genomes of many rod-shaped bacteria [36]. It regulates cell shape by directing the localisation of the peptidoglycan synthesis machinery [53]. Deletion or depletion of *mreB* results in the loss of rod shape. In *C. crescentus* , *mreB* depletion also results in the loss of unipolar localisation of the proteins PleC and DivJ (amongst others) [62]. Re-expression of *mreB* results in the restoration of unipolar localisation of these two proteins, but whilst polar localisation is restored the polarity of the localisation pattern is lost. In WT cells PleC localises to the swarmer pole, whereas DivJ localises to the stalked pole. However after *mreB* re-expression this polarity is lost with $\sim$ half PleC and DivJ foci at either pole [62].

There have been a number of conflicting reports on the organisation of MreB within the cell. Early models favoured helical filaments that run the length of the

cell, while other models suggested patches associated with the membrane. Electron cryo-tomography revealed that the helical pattern is almost certainly an artefact of the N-terminal YFP tag; the placement of a mCherry tag on a loop within the protein sequence resulted in cells with no helical pattern seen in fluorescent images and significantly shorter filaments seen in tomograms [179]. Recently the use of super-resolution microscopy has suggested that MreB forms short filaments of variable length that move along straight line trajectories [126].

MreB has been shown to form a medial ring at the septal site prior to cell division, with loss of the ring structure seen post-septation in *E. coli* , *R. sphaeroides* and *C. crescentus* [193, 173, 62]. This medial ring formation is dependent on FtsZ in *C. crescentus* but not in *E. coli* and *R. sphaeroides* , and has been suggested as a mechanism to ensure segregation of MreB into both daughter cells.

CreS

CreS (cresentin) is a homologue of intermediate filaments, which has been shown to be required for the crescent cell shape of *C. crescentus* [7]. Both fluorescence microscopy and electron cyro-tomography have shown CreS to localise to the inner curve of the cell [24].

1.5.3 Self-organisation

Diffusion-capture mechanisms for protein localisation require a localised target, which then raises the question of how the target is localised. There can't be an endless list of target proteins, therefore diffusion-capture models rely on ability of some proteins to localise independently of a previously localised target. One way to achieve this target-independent localisation is through self-organisation. An example of this is the placement of the Z-ring by the Min system. As mentioned

in 1.5.2 FtsZ forms the Z-ring at the pre-division site, which then recruits the rest of the divisome proteins, presumably by diffusion-capture. This ring is always localised at the mid-cell ensuring equal distribution of genetic material between the two daughter cells. But how does FtsZ localise to the mid-cell?

Three proteins were found to be essential for the correct placement of the Z-ring, MinC, MinD and MinE; disturbing expression of these genes resulted in either misplacement of the Z-ring and therefore minicells, or the loss of Z-ring formation [37]. MinC inhibits the polymerisation of FtsZ into the Z-ring [85], and is localised to the poles of the cell by MinD and MinE [84, 146], thus only allowing the Z-ring to form at mid-cell. The polar localisation on MinC is achieved by rapid pole to pole oscillations, which are driven by MinD and MinE [145].

MinD dimerises and binds to the membrane when in the ATP bound state, and is monomeric and cytosolic when in the ADP bound state; MinE activates the ATPase activity of MinD [99, 83]. Thus MinE removes MinD from the membrane by catalysing MinD ATP hydrolysis. Once cytoplasmic, MinD can exchange ADP for ATP allowing it to bind to the membrane again, which it does so in the area with lowest MinE concentration.

This results in a pattern where MinE moves towards one pole removing MinD from the membrane, as it does this MinD rebinds the membrane at the other pole.

Once MinE has removed all the MinD at one pole it will then diffuse until it finds more MinD-ATP which is now located at the second pole, thus MinE causes MinD to oscillate from pole to pole. The directionality of MinE movement is due to the fact that the concentration of MinD-ATP is much higher in front of it than behind it where it has just previously removed all the MinD-ATP. Therefore it is always more likely to encounter MinD-ATP in front of it biasing its diffusion in a forward direction until it has removed all the MinD-ATP at a pole where it will reverse direction. MinC is not required for these oscillations [145], rather it is the

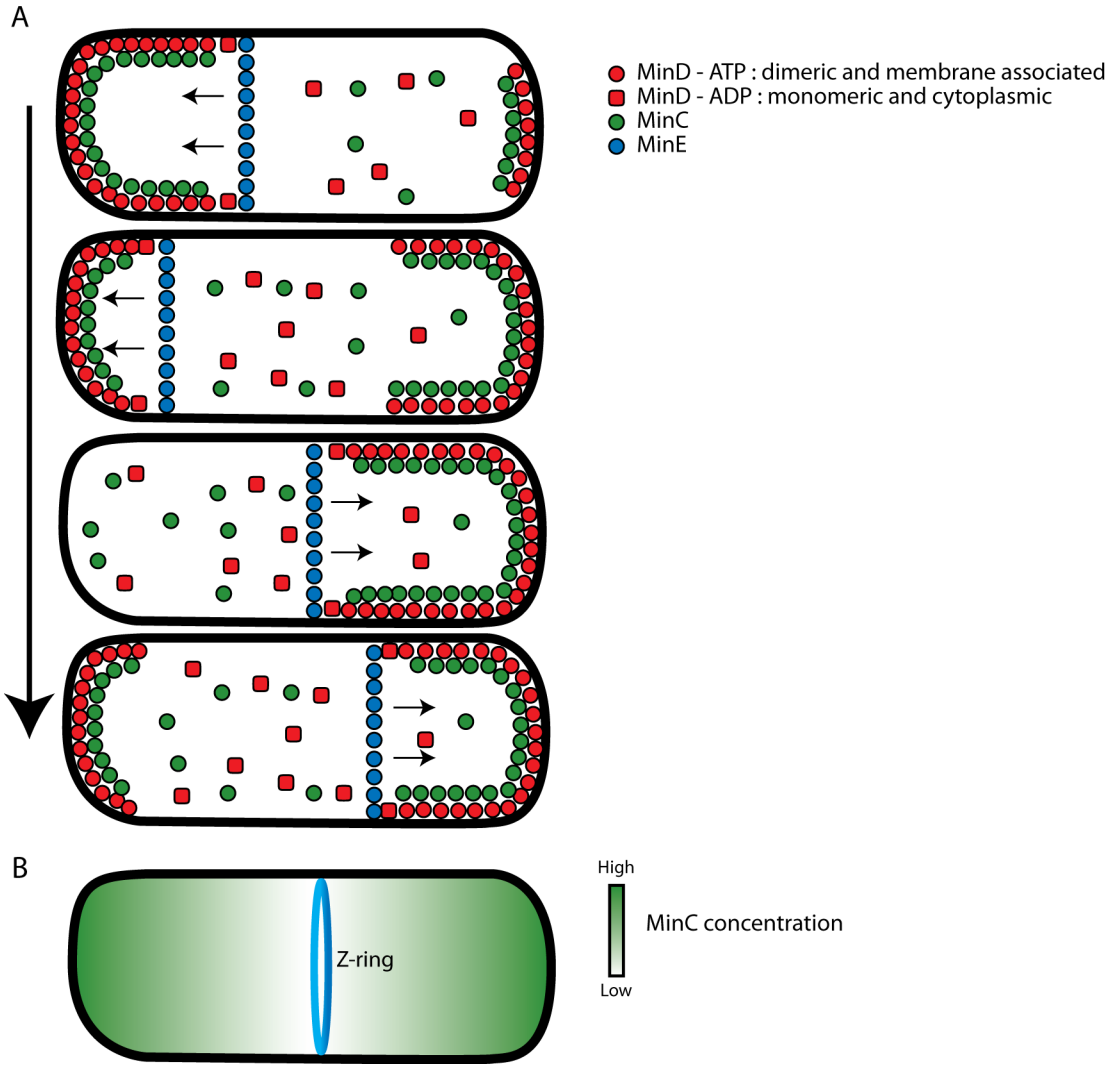

Figure 1.14: Self-organisation of the MinCDE system in *E. coli* . **A:** MinD binds ATP, allowing it to dimerise and bind the membrane. MinE activates the ATPase activity of MinD resulting in MinD removal from the membrane by MinE. As MinE progresses and removes MinD in a directional manner ADP bound MinD diffuses in the cytoplasm. MinD-ADP can exchange ADP for ATP allowing it to bind the membrane again, which it does distally from MinE. Once MinE has removed all the MinD at one pole it will diffuse until it encounters more membrane bound MinD (which has bound at the far pole) and then proceed to remove this. The resulting pattern is one with MinD localised primarily at the poles. Vertical arrow indicates progression of time. Horizontal arros indicate movement of MinE. **B:** Z-ring formation is restricted to the mid-cell due to the interaction between MinC and MinD, producing a gradient of MinC concentration.

affinity of MinC for the membrane bound MinD-ATP that results in its oscillation with MinD, as shown schematically in fig. 1.14.

This dynamic patterning has been shown to be independent of any other proteins or markers. Purified MinD and MinE will generate waves *in vitro* in the presence of ATP and a lipid bilayer [108].

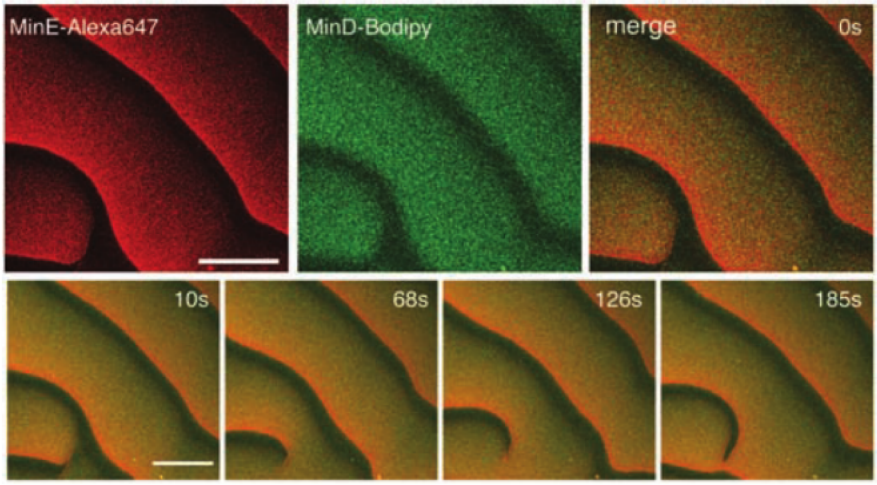

Figure 1.15: MinD and MinE form waves *in vitro* . MinD is shown in green and MinE in red. Scale bar is 50 μm . Taken from [108]

Mathematical models have also shown that these waves only require MinD, MinE, ATP and a lipid bilayer, the only further requirement for oscillations is containment [97, 82].

The result of these Min oscillations is that in a time-averaged concentration profile MinC concentration will be highest at the poles and lowest at the mid-cell, preventing Z-ring formation at positions other than the mid-cell. Another mechanism in Z-ring localisation is discussed in 1.5.5.

Whilst the Min system is the best studied example of protein self-organisation, it has been implicated in other protein localisation patterns, such as the stochastic self assembly model for chemoreceptor arrays discussed in 1.4.3.

1.5.4 Membrane Properties

Another method of directed protein localisation without the need of a previously located target protein is via the use of intrinsic variability of the membrane properties. Within each membrane there is variability in curvature and lipid composition. Examples of heterogeneity of curvature within bacterial membranes are illustrated in fig. 1.16.

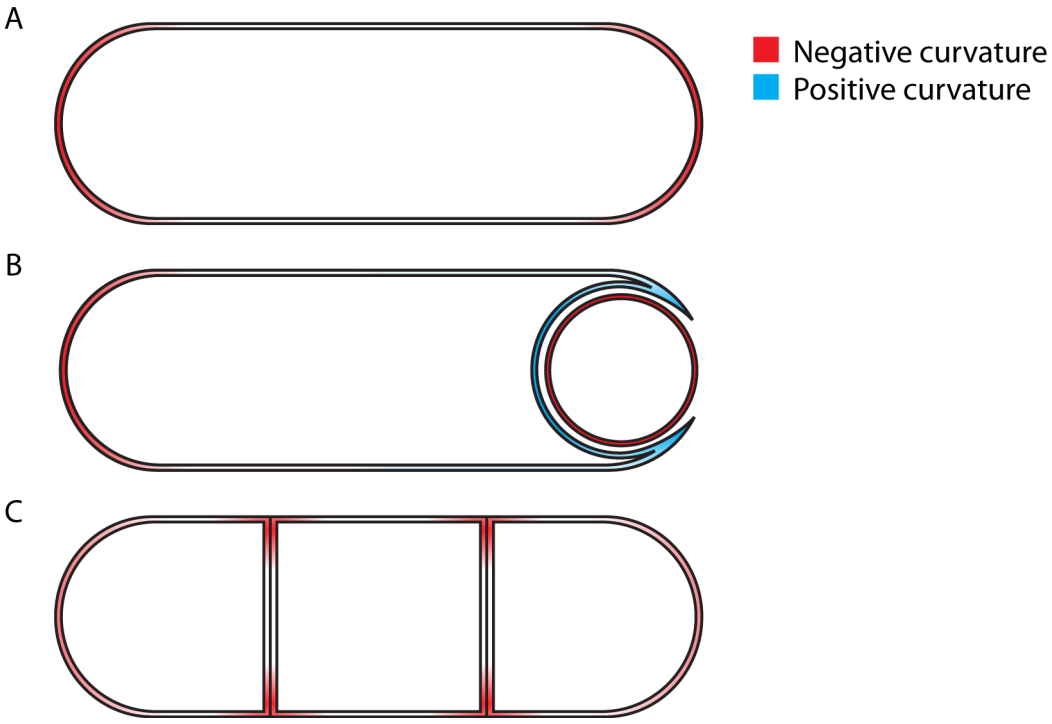

Figure 1.16: Membrane curvature in bacteria. **A:** In rod shaped cells the poles have negative curvature. **B:** In sporulating *B. subtilis* cells the membranes engulfing the forespore have positive curvature. **C:** *B. subtilis* cells growing vegetatively in chains have highly negative membranes at the septa, and less negatively curved membranes at the poles.

Proteins with specificity for both positive and negative curvature have been found in *B. subtilis* . During sporulation the mother cell engulfs the forespore [176]. During this process the protein SpoVM is localised to the membrane surrounding the forespore and not the cytoplasmic membrane of the mother cell. The basis for this localisation has been shown to be due to SpoVM preferentially localising to areas of positive (convex) membrane curvature [142]. As illustrated in fig. 1.16

B the only region of the membrane with positive curvature is the membrane surrounding the spore.

The second example for *B. subtilis* is the localisation of DivIVA, which in this species is responsible for the polar localisation of MinC (inhibitor of Z-ring formation). In vegetative growth *B. subtilis* often grows as a chain of cells which have undergone cytokinesis but have not separated [93]. This creates regularly spaced division septa within the chain of cells (illustrated in fig. 1.16 C). These septa have greater negative (concave) curvature than the poles of cells not in chains (with the exception of a single pole in both cell found at the end of the chain). DivIVA has been shown to localise to the poles and septa due to its preference for negatively curved membranes [143]. In chains DivIVA primarily localises to the septa with some localisation at the poles, whereas in single cells it is localised to the poles. This suggests that DivIVA accumulates at regions with the greatest negative curvature. Creation of spherical *B. subtilis* cells resulted in a uniform distribution of DivIVA as all of the membrane was equally curved.

Membrane curvature has also been implicated in positioning of the membrane chemosensory cluster, see 1.4.3.

Whilst this mode of localisation is exclusive to membrane proteins, these localised membrane proteins can then be used as targets for many cytoplasmic proteins.

1.5.5 Nucleoid Occlusion

Nucleoid occlusion is the process by which proteins are excluded from the regions of the cell occupied by the nucleoid. This mechanism was first seen in the positioning of the Z-ring, which does not form until the two nucleoids in the predivision cell are spatially separate, ensuring equal and complete segregation of the genome [209]. Here nucleoid occlusion works in conjunction with the Min

system.

Recently proteins which bind sequence specific sites on the chromosome have been shown to be responsible for the nucleoid occlusion of FtsZ in *B. subtilis* and *E. coli* [213, 17]. Whilst the mode of FtsZ inhibition is still being debated, it is clear that in this instance nucleoid occlusion of FtsZ is driven by the localisation of inhibitory proteins through sequence specific DNA binding. For a review on FtsZ nucleoid occlusion see [212].

Nucleoid occlusion has been shown to be the driving factor in the polar localisation of misfolded protein aggregates [208]. Distruption of the nucleoid resulted in loss of polar localisation. Mathematical models have also shown that proteins that aggregate or oligomerise into large complexes will exhibit polar localisation due to nucleoid occlusion [158]. These results suggest that in the absence of an active localisation process large structures or aggregates will localise to the poles in an entropically driven process.

1.6 Plasmid Partitioning

Plasmids have mechanisms to ensure their maintenance through indefinite rounds of cell division. High copy number plasmids are able to ensure low rates of plasmid loss simply through sheer numbers. Passive diffusion of high copy plasmids is sufficient to establish stable maintenance [178, 155]. However for low copy number plasmids (roughly 1-5 copies per chromosome equivalent) reliance on passive diffusion alone results in rapid plasmid loss [155]. Therefore plasmids have evolved a number of mechanisms to partition plasmids correctly before cell division and thus ensure stable maintenance of the plasmid. These partitioning systems are encoded in *par* loci, and to date three types of *par* loci have been discovered. Type I encodes ATPases containing a deviant Walker box, type II en-

codes actin-like ATPases, and type III encodes tubulin-like GTPases. Apart from an NTPase each locus also encodes a DNA binding protein that binds with sequence specificity to a region often in the locus; this DNA binding protein also interacts with NTPase. These tripartite systems are sufficient and necessary for plasmid segregation, and thus independent of the host, meaning that in the event of horizontal transfer to a different host species the plasmid's ability to partition remains intact.

1.6.1 Type I - Deviant Walker Box ATPases

The most commonly found *par* loci found on low copy number plasmids are Type I loci. These loci consist of three parts, *parA* and *parB* open reading frames and a *parS* sequence [125, 8].

ParA is an ATPase, which belongs to the P-loop NTPase super family. Within this super family both ParA and MinD form closely related subfamilies [104]. The proteins in the ParA/MinD subfamilies all possess a 'deviant' Walker A motif, the consensus sequence of which is -KGGXXGKT- [104]. The second lysine in this sequence is found in all Walker A motifs (deviant or otherwise), however the first lysine is specific to this subfamily. This lysine has been shown to be involved in dimerisation of the ATPase as it interacts with the ATP bound by the other subunit [105].

Within type I *par* loci there are two sub-types: type Ia and type Ib. Type Ia loci encode a 'large' ParA, which has an N-terminal helix-turn-helix DNA binding motif, type Ib encode 'small' ParAs which lack this domain [61]. The N-terminal domain of the type Ia ParAs mediate autoregulation of *par* gene expression. It has been suggested that both type Ia and Ib ParA systems operate by similar mechanisms, so both will be referred to as ParA, and, while many ParA proteins have specific names when discussing general principals the terms ParA, ParB and

parS will be used.

When ParA is in the ATP bound form it is able to dimerise [105]. This dimerised and ATP bound form of ParA ($ParA_2$-ATP_2) is then able to bind non-specifically with DNA [105, 80]. The second protein encoded by type I *par* loci is ParB. ParB is able to activate the ATPase activity of its cognate ParA [20]. ATP hydrolysis results in an ADP bound form of ParA, which monomerises and is unable to bind DNA and thus returns to a freely diffusing state in the cytoplasm [194]. How do these two proteins produce plasmid partitioning through this cycle of DNA binding and ATP hydrolysis?

ParB specifically binds the *parS* sequence of the *par* locus on the plasmid. When this ParB-*parS* complex encounters $ParA_2$-ATP_2 it triggers the hydrolysis of ATP by ParA and results in ParA release from the nucleoid. Two models have been put forward to describe how this process of ATPase stimulation and nucleoid dissociation are used to partition plasmids. These are the filament pulling model [151], and the diffusion ratchet model [194].

In the filament pulling model $ParA_2$-ATP_2 cooperatively binds the nucleoid to create a nucleating core which then rapidly polymerises into a filament. As this nucleoid associated filament polymerises it is able to explore space and will lead to it encountering a plasmid containing a *parS* sequences with ParB bound (ParB-*parS*). The interaction with ParB-*parS* activates the ATPase activity of ParA and causes the ParA molecules at the end of the filament to disassociate from the nucleoid. ParB-*parS* then interacts with the newly exposed $ParA_2$-ATP_2 end of the filament; this persistent interaction between ParB-*parS* and the ParA filament results in depolymerisation of the filament and movement of the ParB-*parS* complex in the direction of depolymerisation. After each $ParA_2$-ATP_2 hydrolysis step the ParB-*parS* complex can either continue to depolymerise the filament or it can fall away from the filament. The probability of the plasmid losing contact with

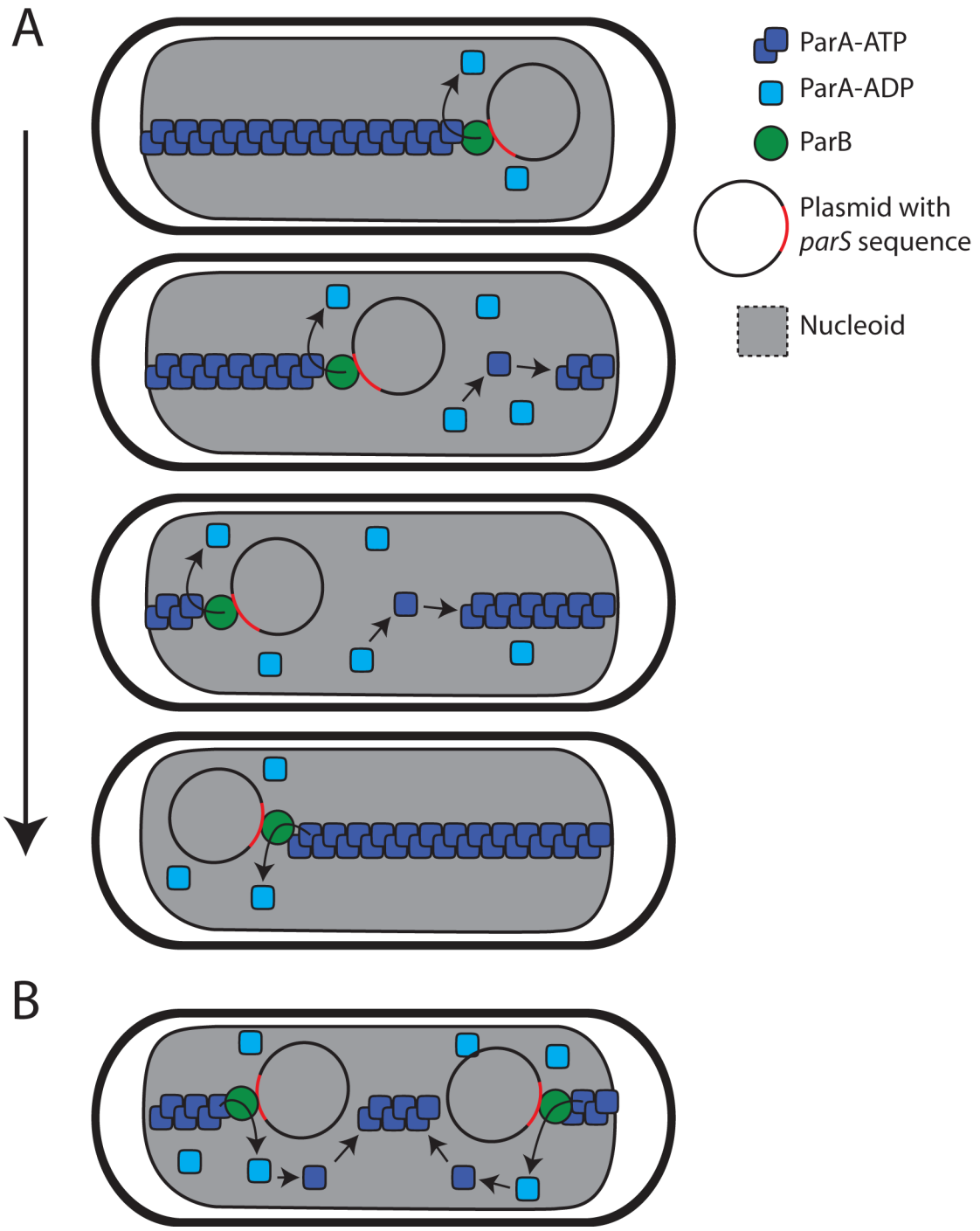

Figure 1.17: Filament pulling model of plasmid partition by ParA ATPases. **A:** Dynamic positioning of a plasmid over time (indicated by arrow). The ATP bound form of ParA forms nucleoid associated filaments. The ParB-*parS* complex stimulates the ATPase activity of ParA causing to depolymerise. The ParB-*parS* remains in contact with the retracting end of the filament resulting in the translocation of plasmid across the nucleoid. Free ADP bound ParA undergoes nucleotide exchange and re-polymerises at the far end of the nucleoid. Repeated cycles of filament depolymerisation results in plasmid oscillation across the nucleoid. **B:** When two plasmids are present they oscillate between filaments which form at the ends and middle of the nucleoid.

the filament is inversely proportional to the length of the filament.

Eventually the entire filament will have depolymerised leaving the plasmid free to diffuse. However the ParA-ADP released by filament depolymerisation will have undergone nucleotide exchange and thus been able to nucleate and polymerise into a new filament. When this new filament reaches the plasmid the ParB-*parS* complex will initiate a new round of ATP hydrolysis and filament depolymerisation. For an illustration of the filament pulling model see see fig. 1.17 A. This results in the plasmid being repeatedly pulled from one end of the nucleoid to the other, generating a time-averaged position of mid-cell. When there are two plasmids the same pattern occurs except that the plasmids will oscillate between the edges of the nucleoid and the mid point, see fig. 1.17 B.

In the diffusion ratchet model ParA also binds ATP and dimerises, but it has to undergo a slow conformational change to be in a DNA binding competent state ($ParA_2^*$-ATP_2). $ParA_2^*$-ATP_2 can reversibly non-specifically bind the nucleoid in an ATP hydrolysis independent manner. ParB-*parS* induces ParA ATPase activity causing ParA dissociation from the nucleoid. As ParA has to both exchange ADP for ATP and then undergo a slow conformational change it is unable to immediately rebind the nucleoid. This results in a zone depleted of $ParA_2^*$-ATP_2 around the ParB-*parS* complex.

The interaction between ParB-*parS* and DNA bound $ParA_2^*$-ATP_2 is made up of many interactions, as the zone is depleted of $ParA_2^*$-ATP_2 the number of these interactions decreases. This decrease in tethering interactions means that the plasmid will become increasingly mobile due to Brownian motion. As the plasmid moves out of the depletion zone it will make more interactions, but these will then decrease again as it stimulates ParA ATPase activity. The slow regeneration time of $ParA_2^*$-ATP_2 means that ParB-*parS* will continue to move in a directional manner as there will be more $ParA_2^*$-ATP_2 in front of it compared to the region

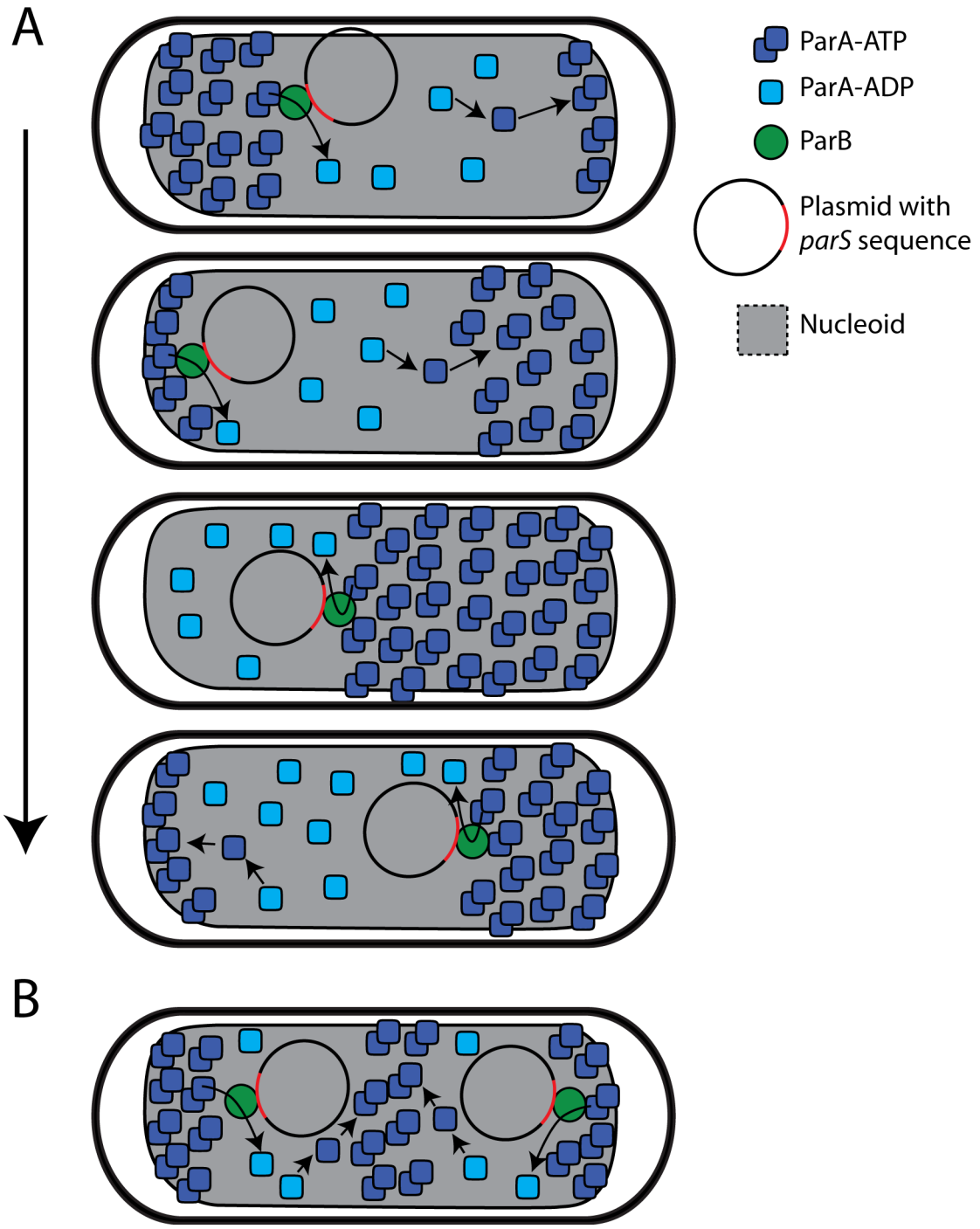

Figure 1.18: Diffusion-ratchet model of plasmid partition by ParA ATPases. **A:** Dynamic positioning of a plasmid over time (indicated by arrow). The ATP bound form of ParA binds the nucleoid as dimers. The ParB-*parS* complex stimulates the ATPase activity of ParA resulting in its release from the nucleoid. Affinity for nucleoid bound ParA bias the diffusion of the ParB-*parS* complex. Free ADP bound ParA undergoes nucleotide exchange and re-binds the nucleoid away from the ParB-*parS* complex. The resulting pattern consists of the plasmid chasing ParA dimers off the nucleoid, oscillating across it. **B:** When two plasmids are present they oscillate between multiple ParA maxima.

it has just passed over removing the $ParA_2^*$-ATP_2 from the nucleoid. Once the plasmid reaches the end of the nucleoid it will either reverse direction due to the absense of $ParA_2^*$-ATP_2 in front of it, or it will wrap around the nucleoid and travel back along a different face of the nucleoid.

This behaviour produces a pattern where the plasmid oscillates from one end of the nucleoid to the other. When plasmids are present, two plamids moving towards each other will create a large depletion zone with the lowest $ParA_2^*$-ATP_2 concentration being between them, resulting in reversal of direction.

Both models are based on the same underlying principles. ParB-*parS* destabilises ParA's interaction with the nucleoid, and due to ParB-*parS* affinity for DNA bound ParA this results in ParB-*parS* chasing ParA off the nucleoid in an oscillatory manner. The core difference between these models is the ability of ParA to form filaments.

Vecchiarelli and colleagues were unable to detect filaments of the P1 plasmid ParA, at concentrations up to 30 μM only dimers were detected [194]. Two recent studies have used *in vitro* DNA carpets to investigate the ParAs of both the P1 plasmid (ParA) [87] and the F plasmid (SopA) [195]. In both cases the ParA was seen to bind the DNA carpet as dimers or small oligomers in a dynamic and ATP hydrolysis dependent manner. ParB-*parS* complexes bound to the ParA bound to the DNA carpet via numerous tethers and were relatively immobile upon binding. Over time ParB-*parS* created a ParA depletion zone around it and ParB-*parS* displayed increasing mobility. In most cases the plasmid detached from the ParA-DNA carpet, although instances of the plasmid moving across the carpet were seen. The authors of these studies suggest that spatial confinement (i.e. the limited space between the nucleoid surface and the inner membrane) would result in the detached plasmids reattaching.

The data from both these studies strongly supports the diffusion ratchet model.

However numerous cases of ParA filaments have been reported. The ParA of the P1 plasmid forms filaments *in vivo* [42], and ParA from ChII of *V. cholerae* , SopA from the F plasmid, ParF from the TP228 plasmid, ParA from the pB171 plasmid and Soj from the *B. subtilis* chromosome have all been shown to form filaments *in vitro* [86, 19, 11, 44, 105]. It should be noted however that many of these *in vitro* filaments were formed under high concentrations of ParA.

To date the exact mechanism of plasmid segregation by type I *par* loci remains unresolved, although recent results favour the diffusion ratchet model they cannot yet rule out the filament pulling model. Given that ParAs are closely related to MinD it is tempting to envisage a similar reaction-diffusion type mechanism (i.e. the diffusion ratchet model). However a lesson to be taken from the Min system is that MinD positioning (and therefore Z-ring inhibition) is achieved by different mechanisms in different species (for a review of ParA/MinD family positioning patterns see [109]). It therefore seems entirely possible that there may be no single universal mechanism by which ParAs partition plasmids.

1.6.2 Type II - Actin-like ATPases

Type II *par* loci consist of a gene encoding an actin-like ATPase (ParM), a gene encoding a sequence specific DNA binding protein (ParR) and the centromeric site to which that protein binds (*parC*) [191].

ParM forms filaments which grow bidirectionally from ATP bound ParM subunits [58, 133]. Subunits in the filament can hydrolyse ATP, and they do so cooperatively [115] meaning that ATP hydrolysis can propagate along the filament. ADP bound subunits dissociate rapidly from the ends of the filament, thus ATP hydrolysis leads to catastrophic disassembly unless the terminal subunits are maintained in an ATP bound form [115, 58].

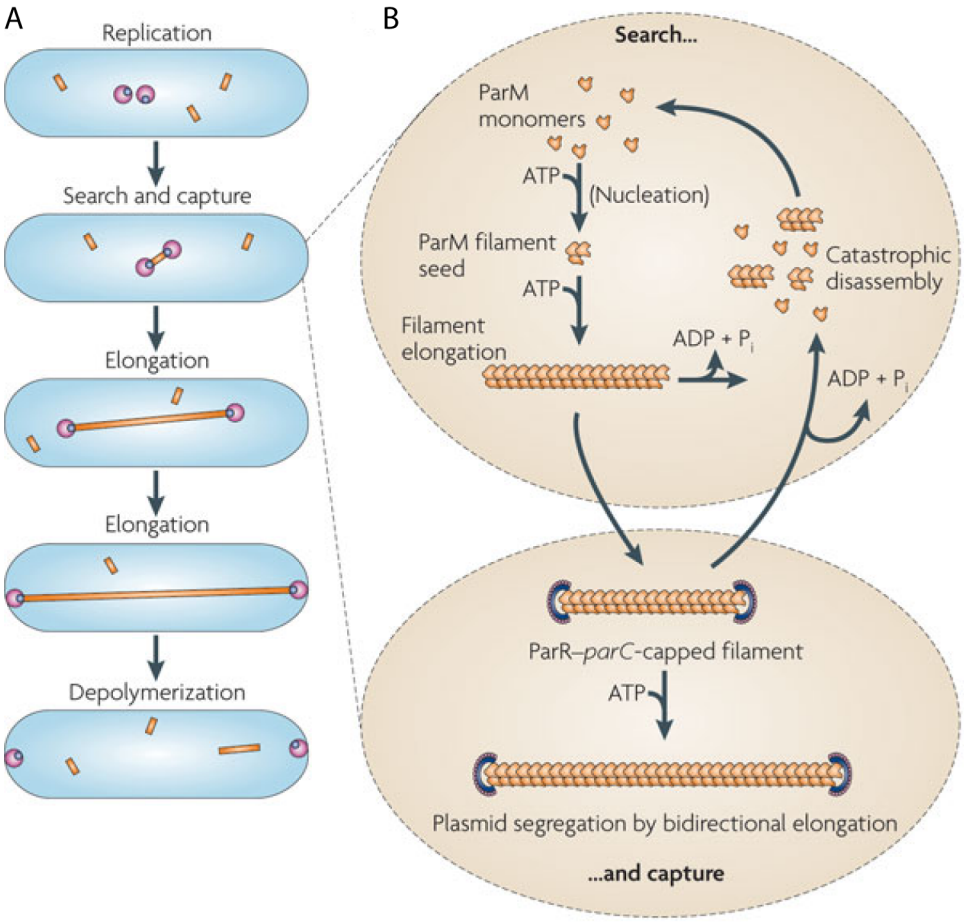

Figure 1.19: Plasmid segregation by ParMRC systems. **A:** Schematic of the mechanism of plasmid segregation by ParMRC systems in cells. Plasmids are shown in pink, ParR in blue, and ParM in orange. ParM filaments use dynamic instability to find plasmids, and once a ParR-plasmid complex is bound at both ends the filament will elongate thus segregating the plasmids. **B:** Dynamic instability of ParM filaments. Uncapped ParM filaments undergo rounds of polymerisation, ATP hydrolysis and catastrophic disassembly, allowing filaments to search space within the cell. ParM filaments are capped and stabilised by ParM-*parC* complexes allowing elongation. Adapted from [160]

This stabilisation of the ends of ParM filaments is performed by ParR-*parC* complex, which forms a cap over the end of the filament [161, 127, 165].

The ParM filaments find the plasmid (and therefore the ParR-*parC* complex) through successive rounds of polymerisation and disassembly, a process termed dynamic instability. This allows the filaments to repeatedly search space within the cell for the plasmid [58]. Both ends of the filament need to be capped by ParR-*parC* com-

plexes to prevent catastrophic disassembly, thus only once a plasmid is bound at both ends is it able to elongate. This elongation results in the plasmids being actively moved to opposite poles of the cell [114].

This model has been further validated by reconstituting it *in vitro* , with *parC* coated beads being pushed apart by ParM filament elongation [59].

1.6.3 Type III - Tubulin-like GTPases

Recently a new plasmid *par* loci was discovered encoded on low copy number plasmids in *Bacillus anthracis* and *Bacillus thuringensis*. As with other *par* loci these loci encode a NTPase, and site-specific DNA binding protein, and a centromeric DNA sequence. The NTPase is TubZ, a GTPase and homologue of FtsZ and tubulin [180, 101].

TubZ has been shown to form filaments in a GTP dependent manner [101]. Having formed the filament in the GTP bound form, TubZ subunits will hydrolyse GTP due to the high GTPase activity of TubZ. This results in most subunits within the filament being in the GDP bound state, with a growing tip in the GTP bound state stabilising polymerisation [33]. This leads to treadmilling of TubZ subunits and filament movement [101]. The DNA binding protein TubR binds to the centromeric region of the *par* loci, and this TubR-plasmid complex is able to bind TubZ filaments [122].

The model put forward based on these data (summarised in [9]) is as follows: TubZ binds GTP and assembles into a protofilament which then begins to treadmill with new GTP subunits being added at the plus end and GDP subunits being lost at the minus end. When it encounters a TubR-plasmid complex it binds it and causes the plasmid to move with it. When it gets to the cell pole the plasmid is released, resulting in segregation. How this polar release occurs is not clearly un-

derstood, but it has been suggested that the membrane curvature of the cell poles causes the TubZ filament to bend in a way which releases the plasmid [122].

1.7 Chromosome Organisation and Segregation

Advances in fluorescent microscopy have not only revealed high levels of subcellular organisation of proteins, they have also been instrumental in the exploration of the organisation and segregation of the bacterial chromosome.

1.7.1 Chromosome Organisation

Most bacteria have a single circular chromosome, though many including *V. cholerae* and *R. sphaeroides* , have two, and some species have linear chromosomes [147].

The use of techniques such as fluorescent *in situ* hybridisation, and use of fluorescent fusions to DNA-binding proteins (e.g. ParB, LacI, TetR) and the insertion of their cognate target sequence (*parS* , *lacO*, *tetO*) at specific sites has enabled the cellular positions of specific loci to be determined throughout the cell cycle. Initial studies used such methods to determine the localisation of the origin (*ori*) and terminus (*ter*) of replication, as well as the left and right replichores (the regions between the *ori* and *ter* , see fig. 1.20 A).

In *E. coli* the *ori* is positioned at the mid-cell, and the left and right replichores are positioned in separate halves of the cell, see fig. 1.20 A. The *ter* is relatively mobile and can associate with either replichore [123, 204]. *C. crescentus* however has a very different chromosomal organisation. The *ori* and *ter* are positioned at opposite poles. The *ori* is at the old pole, and *ter* at the new pole with both left and right replichores running the length of the cell [196]. The two chromosomes of *V. cholerae* display different positioning, chromosome one (ChI) has polar *ori*

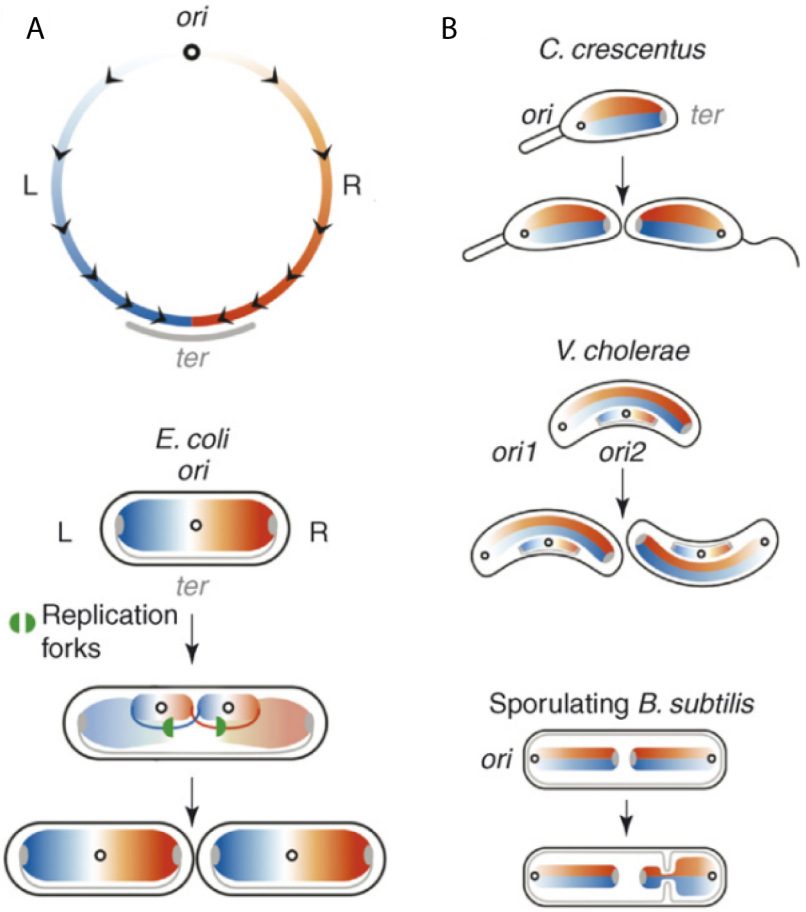

Figure 1.20: Bacterial chromosome organisation. **A:** Top: Circular bacterial chromosome. The origin of replication is shown as a black circle, left and right replichores in blue and orange respectively, and the terminus in gray. Bottom: *E. coli ori* localises to mid-cell, left and right replichores localise to separate halves of the cell, and the *ter* can localise to either replichore. During DNA replication the two origins segregate into different halves of the cell. After replication and segregation the left-right organisation is maintained in the daughter cells. **B:** Chromosome organisation in other bacteria. *C. crescentus* localises *ori* and *ter* to opposite poles of the cell. *V. cholerae* has two chromosomes, one displays polar *ori ter* organisation, whereas the other localises *ori* to mid-cell. *B. subtilis* localises *ori* to the pole during sporulation. Taken from [148].

positioning , where as the second chromosome (ChII) has its *ori* positioned at mid-cell [55]. *B. subtilis* differentially organises its chromosome depending on its growth state. During vegetative growth the *ori* is positioned at mid-cell [15]. When it enters sporulation however the origins of the two sister chromosomes exhibit polar positioning [211].

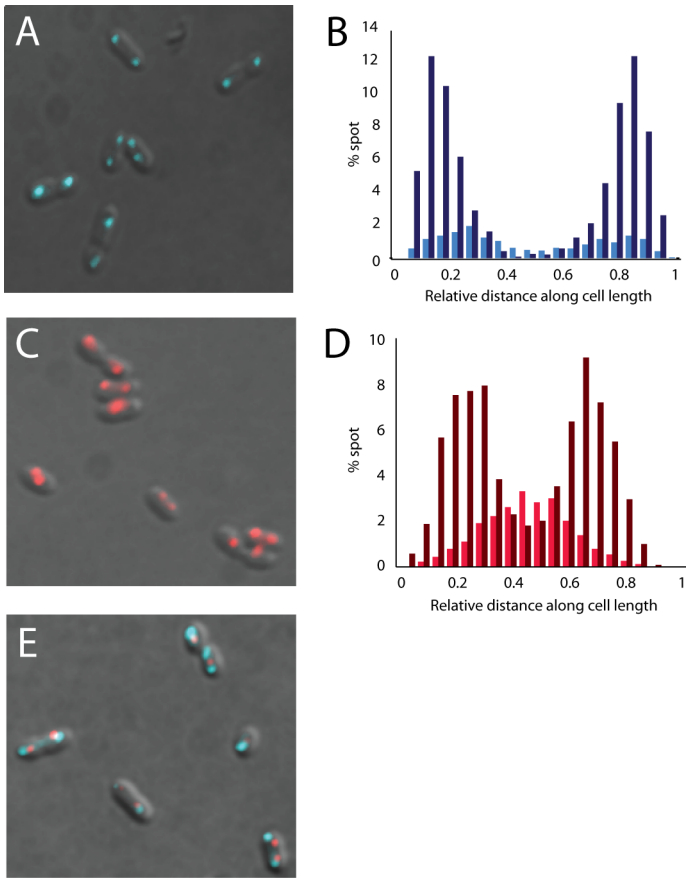

Figure 1.21: The positioning of the origins of replication of both *R. sphaeroides* chromosomes. **A:** Image showing the origin of chromosome I fluorescently tagged. **B:** Histogram of positions for ChI origin. Light blue is before orgin replication, and dark blue after. **C:** Image showing the origin of chromosome II fluorescently tagged. **D:** Histogram of positions for ChII origin. Light red is before orgin replication, and dark red after. **E:** Image showing origins of both chromosomes fluorescently tagged. ChI in blue, ChII in red.

R. sphaeroides has two chromosomes, both of which contain a *parABS* locus, deletion of the *par* locus of chromosome II results in some loss of ChII and, whilst cells appear aberrant, the locus is not essential. Several attempts at creating a Δ*parChI* strain have failed, suggesting that the *par* locus of chromosome I may be essential (Nelly Dubarry, personal communication). The origin of ChI localises to the pole, and switches from unipolar to bipolar after replication, the origin of ChII is positioned at mid-cell, and after replication moves to 1/4 & 3/4 positions (Nelly Dubarry, personal communication). The positioning of the origins of both *R. sphaeroides* chromosomes is shown in fig. 1.21.

1.7.2 Nucleoid Structure

As seen above the bacterial chromosome is a highly organised and specifically positioned molecule. Bacterial chromosomes are many times the length of the cell, and thus must be compacted $\sim$ 1000 fold [81]. These compacted chromosomes, which for *E. coli* occupies 25% of the cellular volume [218], form structures termed nucleoids. Both the structure of the nucleoid and exactly how it is compacted are still being revealed, but significant insights have been made.

The *E. coli* chromosome consists of $\sim$ 400 independently supercoiled domains (each of roughly 10kb) [40, 138], and these exist within higher order macrodomains [50]. Supercoiling alone however is not sufficient to produce the level of compaction required, and therefore other factors must be involved. A number of nucleoid associated proteins have been discovered, most of which are localised throughout the nucleoid, but one, H-NS has been shown to bring together DNA regions distal in sequence [203]. Other reports have shown that nucleoid associated proteins with different modes of sequestering DNA are expressed differentially depending on external and internal conditions [149, 28], suggesting both regulatory and structural roles of many of these proteins. The differing levels of compaction also show that the bacterial nucleoid is a dynamic structure, whose organisation can be modulated.

Loci within the nucleoid are also dynamic, and diffuse within constrained regions, until the chromosome replicates and segregates when loci move as part of bulk chromosome movement [45, 52]. Therefore whilst loci within the chromosome may have specific cellular positions which are robust through division cycles, both the macro and micro structure of the nucleoid is dynamic.

This is mirrored in a recent study which determined the force required to compact the *E. coli* chromosome to its *in vivo* size. By gently lysing the cells and then using an optical trap and bead to compress the nucleoid back to its orig-

inal size the forces required for this compression were measured. The results demonstrated that the force needed to compress the chromosome is ∼1000 fold less than the turgor pressure within the cell [130]. It was also possible to restore compaction through *in vitro* molecular crowding, a process which was reversible and repeatable with the sequential addition and removal of molecular crowding agents. Together this suggests that molecular crowding may be the primary driving force behind chromosome compaction, and nucleoid associated proteins are used to promote, modify and organise this process.

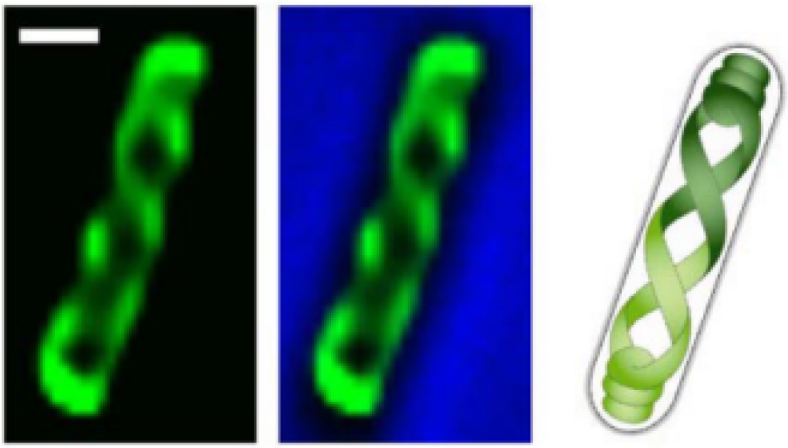

Figure 1.22: Deconvolution fluorescence image of the nucleoid. *B. subtilis* cell treated with fluorescent nucleotides. Fluorescent image shown in green, phase contrast in blue, and to the right a cartoon shematic. Scale bar 0.5 μm . Adapted from [16].

The use of both cryo-electron microscopy and fluorescence microscopy has helped to begin to resolve the shape and large scale organisation of the nucleoid. In growing cells nucleoids exhibit dense cores with multiple projections into the cytoplasmic space [46]. On a larger scale it has been observed that nucleoids can exist in a helical shape [30, 16, 54].

1.7.3 Chromosome Segregation

The tagging of a large number of loci within the *C. crescentus* chromosome demonstrated that each locus has a specific subcellular position and that this position is linearly related to its position on the chromosome [196]. The same study also used time-lapse microscopy to follow 10 of these loci through replication and segregation. The results reiterated that unlike eukaryotes, which replicate and segregate their chromosomes in temporally distinct events, the loci are segregated swiftly after their replication and before completion of replication of the whole chromosome. [196].

Fluorescent tagging of chromosomal loci enables clear descriptions of chromosome positioning and segregation both spatially and temporally, but alone it does not answer the question of what drives this positioning and segregation.

Early suggestions included the idea that the closing septum pushed the two chromosomes to either side, segregating them into different daughter cells. However it has been shown that the septum can guillotine chromosomes which have not been segregated correctly. Another suggestion was that the origins were tethered to the inner membrane of the cells, and as the cell grew the origins drifted apart with the expansion of the growing membrane, however loci are seen to segregate at speeds incompatible with this model [147].

Many proteins have been proposed to be the driver of chromosome segregation. However, for most of these, disruption of expression only leads to reduced segregation efficiency rather than complete loss of segregation. For detailed descriptions of proteins and processes that may be involved in chromosome segregation please see [147, 187].

One interesting model suggests that chromosome segregation can be achieved simply by the demixing of polymers (i.e. chromosomes) due to entropic forces

[90]. Whilst the simplicity of this model is attractive, the influence of other processes and proteins on segregation suggests that entropic forces are unlikely to be the sole driving forces. The lack of necessary and sufficient processes found for chromosome segregation in many bacterial species favours a model where a number of redundant processes work in tandem.

A system that has been shown to be required for chromosome segregation in some instances is the ParAB-*parS* system. ParAB-*parS* systems are used to segregate low copy number plasmids (ParAB-*parS* systems are described in detail in 1.6.1). An increasing number of bacterial chromosomes have been found to contain a *parABS* locus, with over 65% of sequenced genomes containing a chromosomal *par* locus (the *E. coli* chromosome however does not).

In *C. crescentus* the chromosomal ParAB-*parS* system has been shown to be responsible for segregation of one of the newly replicated sister origins to the far pole. Before the initiation of replication the *parS* locus is held at the old pole by PopZ, which binds the ParB coating the *parS* sequence [43]. ParA forms a filament-like structure which is nucleoid associated [140]. When the *parS* sequence is replicated one sister *parS* remains held by the PopZ matrix, while the other comes into contact with the ParA filament. The ParB-*parS* complex activates the ParA ATPase activity resulting in depolymerisation of the ParA filament [140]. As the ParA filament depolymerises the ParB-*parS* complex remains in contact with the retracting end of the filament thus ensuring that the ParA filament contracts all the way to the new pole and that it brings the ParB-*parS* complex and therefore the *parS* proximal region of the chromosome with it. This contraction of the ParA filament results in a local increase in ParA concentration at the new pole, which faciliates the nucleation of a second PopZ matrix [100]. This combined action of ParA to 'pull' the *parS* sequence and help nucleate a new PopZ matrix means that, as the second ParB-*parS* complex reaches the new pole

there is a PopZ matrix already formed to capture and hold it [100]. A study in which the *parS* sequence is moved to various points in the chromosome showed that no matter where the *parS* sequence was located on the chromosome it was the first locus to be segregated [186], strongly suggesting that the *par* locus is the primary driver of the segregation of the *C. crescentus* chromosome.

V. cholerae has two chromosomes, both of which have a *parABS* locus. The segregation of ChII has be shown to be dependent on its ParAB-*parS* system [215]. However for ChI the ParAB-*parS* system is only required for polar *ori* positioning and not for segregation.

The chromosome of *B. subtilis* has a *par* locus which expresses a ParA ATPase (termed Soj), a ParB homologue (Spo0J) and contains a *parS* sequence, which are also found elsewhere on the chromosome. Unlike *C. crescentus* this ParAB-*parS* system is not used for chromosome segregation during normal division. The *parS* sites are found in a chromosomal region near the origin of replication [107, 23]; Spo0J binds to these *parS* sites and then spreads over the DNA flanking the *parS* sequence [23, 120]. Soj interacts with the protein DnaA at the *ori* ; DnaA initates DNA replication, and interaction with Soj can either activate or repress this action depending on the state of Soj [119]. In the monomeric ADP or nucleotide-free form Soj inhibits DnaA, whereas in the ATP dimeric form it activates it [163]. During normal growth (i.e. before chromosome replication) Spo0J, which is bound to the *parS* sites near the *ori* , activates the ATPase activity of Soj and thus keeps it in the ADP bound monomeric form. In response to a currently unknown trigger Soj is able to overcome regulation by Spo0J; proposed models for this involve either local increases in Soj or decreases in Spo0J concentration by mechanisms such as increasing *soj* expression, or delocalisation of of Spo0J [163]. This results in a shift in the Soj population towards the dimeric ATP-bound state, activating DnaA and chromosome replication.

As well as being important in the control of chromosome replication in *B. subtilis* Spo0J is also important in the chromosomal organisation. Spo0J bound to *parS* sequences recruits the structural maintenance of chromosomes (SMC) complexes [177, 68], which play a role in condensing the chromosome [27]. Loading of SMC onto origin proximal regions of the chromosome has been shown to have an important role in chromosome segregation [177, 68]. This is believed to be of particular importance during sporulation when the chromosome reorganises, moving from mid-cell origin positioning to polar [13]. The nucleoid forms a condensed rod-like structure called the axial filament, with origins of replicated chromosomes tethered at opposite poles through the combined action of the proteins DivIVA and RacA. RacA binds specific sequences near the *ori* [13, 12], and DivIVA localises preferentially to curved regions of the membrane [143]. The interaction between the two results in polar localisation of the origins [211].

In *B. subtilis* both the ParA (Soj) and the ParB (Spo0J) perform distinct roles, in the control of replication (Soj) and promotion of chromosome segregation and compaction (Spo0J), linking these processes.

It is becoming increasingly clear that ParAB-*parS* systems are important in a number of aspects of chromosomal behaviour in many bacterial species; to date identified roles include chromosome segregation, positioning of origins of replication to specific subcellular regions, and changes in large-scale nucleoid organisation. The diversity of roles of ParA ATPases highlights the many ways the core tripartite system has been adapted by many bacterial chromosomes and plasmids.

1.8 Protein Partitioning by ParA Homologues

1.8.1 Polar Chemotaxis Cluster in *V. cholerae*

A subset of chemotaxis proteins ($CheW_1$ and $CheY_3$) in *V. cholerae* form polar foci, with young cells having a single polar focus, and pre-division cells containing foci at both poles, therefore when the cell divides each daughter cell inherits a single focus at the old pole [150]. The study by Ringgaard *et al.* then went on show that this positioning pattern is dependent on a ParA homologue, ParC. Fluorescent fusions to ParC revealed that its positioning pattern was very similar to that of the chemotaxis proteins, and time-course microscopy has shown that ParC transitioned from unipolar to bipolar before the chemotaxis proteins did so, indicating that ParC moved to the new pole and through association whith ParC the chemotaxis proteins were able to follow.

This dependence on ParC for chemotaxis protein positioning was demonstrated in Δ*parC* cells, in which $\sim 25\%$ of cells had non-polar foci.

A photoactivatable mCherry fusion to ParC was used to show that photoactivated protein in a unipolar focus exchanged with a cytoplasmic pool, which was then captured by an anchor at the new pole. Therefore the transition to bipolar foci is due to dynamic localisation of ParC, rather than the size of a single focus reaching a maximum size and newly expressed protein forming a new focus.

An ATP locked mutant of ParC showed both uni- and bipolar localisation, as well as some non-polar foci, whereas a mutant defective in ATP binding was cytoplasmic and formed non-polar foci. Both mutants were defective in positioning the chemotaxis proteins.

A subsequent study by Yamaichi *et al.* identified the protein which captures and anchors ParC. This protein, HubP, is required for correct postioning of ParC and

thus the chemotaxis proteins associtated with it [214]. HubP acts as a polar anchor for a number of ParA homologues within *V. cholerae* . It was shown to also recruit the ParA of chromosome I (ParAI) and FlhG. ParAI has been previously shown to be required for proper positioning and segregation of chromosome I [56].

1.8.2 Cytoplasmic Chemotaxis Cluster in *R. sphaeroides*

The cytoplasmic cluster of *R. sphaeroides* localises to the mid-cell. Prior to cell division the cluster is duplicated and the resulting two clusters are positioned at $^1/_4$ and $^3/_4$ positions within the cell [185]. Both the positioning and segregation of this cluster is dependent on a ParA homologue PpfA [185]. PpfA is encoded within *che*Op_3 , immediately upstream of the soluble chemoreceptor Tlpt (see fig. 1.4).

In order to confirm that PpfA acts as a ParA a CFP fusion was expressed in *E. coli* [152]. This is because DAPI doesn't condense the *R. sphaeroides* chromosomes, whereas in *E. coli* the nucleoid can be clearly distinguished from the total cytoplamsic volume. These results showed that PpfA can non-specifically bind the *E. coli* chromosome, and this binding is dependent on dimerisation and ATP binding of PpfA [152].

Genomic replacement of WT PpfA with mutants defective in dimerisation, ATP binding, ATP hydrolysis, and DNA binding, resulted in a loss of *R. sphaeroides* cytoplasmic cluster segregation in all cases [152].

The PpfA-CFP fusion expressed in *R. sphaeroides* was distributed across the nucleoid with a bright focus coinciding with the cytoplasmic cluster, this bright focus is not seen for the dimerisation, ATP binding, and DNA binding mutants, however the ATP hydrolysis mutant produced brighter foci than WT [152]. Expression in *E. coli* showed that DNA binding was dependent on ATP binding,

and dimerisation, whereas mutant PpfA locked in the ATP bound state remained co-localised with the nucleoid.

The chemoreceptor TlpT was considered a potential interaction partner due to its gene's position immediately downstream of *ppfA* in the operon. However *tlpT* deletion results in loss of cluster formation [200], meaning that this hypothesis could not be tested via the use of the Δ*tlpT* strain. Previous work has shown that proteins that activate the ATPase activity do so through N-terminal basic residues [10, 105]. The N-terminus of TlpT also contains a number of basic residues, and it was indeed shown that truncation of the 120 N-terminal amino acids of TlpT resulted in loss of cluster segregation and PpfA foci [152].

Taken together these results show that not only does the cytoplasmic cluster of *R. sphaeroides* display strikingly similar positioning to some plasmids, but its positioning and segregation is dependent on the dimerisation, ATP hydrolysis and DNA binding of a ParA protein. However no oscillations in PpfA were ever detected leaving the mechanism by which PpfA segregates the cluster unclear.

1.8.3 Carbon Fixation Complex in *Synechococcus elongatus*

Fluorescent fusions to the large subunit of ribulose-1,5-bisphosphate carboxylase-oxygenase (RbcL) and the carboxysome shell protein CcmK in the cyanobacterium *Synechococcus elongatus* revealed that carboxysomes were positioned with even spacing along the length of the cell, the size of this spacing was dependent on the length of the cell [162]. The study by Savage *et al.* then went on to use time-lapse microscopy to assess the mobility of the carboxysomes, and determined that they were constrained and not freely diffusing in the cell.

Deletion mutants of five genes annotated as encoding cytoskeletal proteins were created, and from these it was found that deletions of *mreB* and a *parA* -like gene

the authors termed *parA* result in disrupted carboxysome positioning. Δ*mreB* cells displayed a number of additional phenotypes including morphological aberrations. Δ*parA* cells on the other hand appeared WT except for carboxysome positioning.

A GFP fusion to ParA showed that it formed a cloud-like patch which moved from pole to pole in an oscillatory manner. Given that oscillations are seen in many plasmid ParAB-*parS* systems, this suggests that this dynamic relocation of ParA is positioning carboxysomes.

The loss of ParA resulted in the loss of symmetrical division of carboxysomes on cell division. Cells that inherited less carboxysomes showed reduced fitness and reduced rates of carbon fixation, clearly indicating the need to have a system to ensure equal segregation.

The mechanism behind the positioning and segregation of the carboxysomes by ParA is still unclear but the similarity of positioning and ParA distribution is strikingly similar to some plasmid segregation systems.

1.8.4 Cellulose Biosynthesis Complex in *E. coli*

In a study Le Quéré *et al.* investigated two uncharacterised genes encoded near the bacterial cellulose synthesis (*bcs*) genes in *E. coli* . One of these genes, renamed *bcsQ*, was shown to be required for cellulose biosynthesis [102]. Sequence alignment showed that BcsQ is a ParA/MinD homologue, and a fluorescent fusion to BcsQ displayed unipolar localisation. Cellulose production is also localised to a pole suggesting a potential link between BcsQ positioning and the positioning of cellulose production, although co-localisation was not tested. Cellulose biosynthesis was dependent on the ability of BcsQ to bind ATP, however its localisation was not.

This study provides another example of a ParA homologue being required for important cellular functions and exhibiting specific positioning patterns, however many questions remain regarding BcsQ's role in positioning cellulose machinery and the mechanisms behind its positioning.

1.9 Diversity Within the ParA/MinD Family

The ParA/MinD family of ATPases are involved in the subcellular positioning of cellular components, producing a diverse range of positioning patterns through a number of distinct mechanisms.

The diversity of mechanisms used is highlighted by their role in the control of the formation of the Z-ring by Min proteins. In *E. coli* the inhibitor of Z-ring formation, MinC, is positioned at the poles in order to restrict Z-ring formation to the mid-cell. This positioning pattern is created through self-organisation and oscillation of MinD and MinE (as discussed in 1.5.3). In *B. subtilis* MinC also inhibits Z-ring formation (albeit by mechanisms proposed to be distinct from that of *E. coli* MinC) [67]. The positioning of MinC in *B. subtilis* is however very different to that of *E. coli* . DivIVA localises to the curved membrane of the forming septal site [111, 141], which recruits MinJ, which recruits MinD, which then recruits MinC [129, 22, 51]. Together these proteins prevent the formation of additional Z-rings in the vicinity of the septation site through the use of targeted localisation rather than self-organisation as seen in *E. coli* .

In *C. crescentus* the Z-ring positioning is controled by a different ParA ATPase termed MipZ, which prevents FtsZ from forming the Z-ring [182]. Here the Z-ring is only permitted to form at the mid-cell due to a bipolar MipZ gradient [182], unlike MinC in *E. coli* this gradient is not an oscillatory one. The gradient of MipZ is set up through its interaction with the chromosomal ParB, which along

with the origin of replication localises to the poles [116]. ParB promotes the ATP-bound dimeric form of MipZ [95], which is then able to bind the nucleoid. The basal ATPase activity of MipZ results in its release from the nucleoid, these MipZ monomers then dimerise at the poles, where ParB is located [95]. This creates a gradient of nucleoid bound dimeric MipZ, with greatest concentrations at the poles. Interestingly ParB is also used to control the dynamic localisation of ParA, which is required for chromosome segregation [43]. ParB activates the ATPase activity of ParA, thus promoting the monomeric form of ParA [140], the opposite of the affect it has on MipZ, clearly demonstrating the versatility of these systems.

The above examples demonstrate three distinct mechanisms by which ParA/MinD family ATPases are used to prevent Z-ring formation from the polar regions of the cell.

There is also a large degree of variation in DNA positioning by ParA proteins. Low copy number plasmids are positioned equidistantly along the length of the cell [60] by a number of proposed mechanisms (discussed in 1.6.1), whereas ParAB systems encoded on primary chromosomes are implicated in a wider range of roles, including origin positioning, SMC recruitment, and control of replication initiation (discussed in 1.7.3).

Increasing numbers of ParA/MinD family proteins are being implicated in the positioning and segregation of protein complexes (as discussed in 1.8). Bioinformatic approaches have shown that ParA homologues are encoded in a large of number chemotaxis operons [71, 150], with two of these ParA homologues having been shown to position and segregate chemosensory arrays [185, 150]. ParC of *V. cholerae* positions the membrane bound chemotaxis cluster at the old pole, and then both poles just prior to division [150], and PpfA of *R. sphaeroides* positions the cytoplasmic chemosensory cluster at mid-cell, and then 1/4 & 3/4 positions before division [185, 152]. These two examples alone suggest that the diversity seen

in DNA positioning and segregation by ParA proteins is mirrored in their roles in protein complex positioning.

Segregation of DNA by ParA ATPases is not limited to bacteria. A recent study showed that a ParA homologue, SegA, is required for chromosome segregation in the archaeon *Sulfolobus solfataricus* [92], further highlighting the widespread use of ParA/MinD family proteins. In this system the protein that modulates SegA polymerisation, SegB, is unrelated to ParB or any other bacterial protein [92], indicating that the ParA partner protein is also variable.

This use of proteins other than ParB homologues to partner ParA proteins is also seen in bacteria. The plasmid TP228 contains a *par* locus encoding a ParA homologue *parF* and a second gene *parG* whose gene product has no homology to ParB proteins [74]. ParG however performs the same role as ParB, activating the ATPase of its cognate ParA [10]. In *R. sphaeroides* the chemoreceptor TlpT has been proposed to act as the ParB for PpfA.

The use of proteins beyond to ParB homologues to control ParA ATPases has a number of benefits. It has been suggested that it represents a mechanism by which to reduce cross-talk between ParA segregation systems [57], something especially important for plasmids which may find themselves in a number of host species alongside various other plasmids which may contain *parABS* loci themselves. It also suggests a way by which ParA/MinD proteins can further diversify the positioning patterns they generate and the mechanisms by which they achieve these.

The diversity of the roles and mechanisms of ParA/MinD proteins suggest that they represent a core system in bacteria in positioning and segregating many cellular components. Despite the apparent complexity of these systems the core mechanism they are all based around is elegantly simple. They consist of an ATPase whose nucleotide state acts as switch between different localisation be-

haviours, and interactions with partner proteins modulate this switch to create dynamically localised patterns, which in turn controls the position of its cargo.

1.10 Aims of the Project

The aims of this project were to investigate the cytoplasmic chemosensory cluster of *R. sphaeroides* and the mechanisms used to ensure stable inheritance of this cluster through cell division, specifically:

- Quantification of the turnover of proteins within the cytoplasmic cluster for comparison with known data for membrane associated chemoreceptor clusters in *E. coli* .
- Use a range of fluorescence microscopy techniques to address the role of PpfA in the segregation of the cytoplasmic cluster, building up an understanding of the process from the molecular to cellular level.
- Analyse imaging data to of the cytoplasmic cluster and PpfA to quantify results.
- Test known models of partitioning by ParA ATPases to determine if any of these adequately describe the data acquired for PpfA and the cytoplasmic cluster.
- Generate a model of how the cytoplasmic cluster is segregated and positioned by PpfA.

Chapter 2

Materials and methods

2.1 Strains and Plasmids

2.1.1 Strains

Strain	Species	Genotype/description	Source
XL1-Blue	*E. coli*	General cloning strain, used for plasmid creation and modification. Tetracycline resistant.	Stratagene
S17-λ pir	*E. coli*	Plasmid mobilising strain, used for introducing plasmids into *R. sphaeroides* strains. Streptomycin resistant	[131]
RP437	*E. coli*	Wild-type strain	[128]
WS8N	*R. sphaeroides*	Spontaneous naladixic acid resistant strain of the wild-type strain WS8	[174]
JPA543	*R. sphaeroides*	*tlpC-gfp*	[201]
JPA1215	*R. sphaeroides*	$\Delta cheY_1 - 5$ $cheY_6$D57N. Non-motile	[152]
JPA1331	*R. sphaeroides*	$\Delta tlpT$	[137]
JPA1425	*R. sphaeroides*	*yfp-cheA3*	[198]
JPA1438	*R. sphaeroides*	*yfp-cheA4*	[198]
JPA1456	*R. sphaeroides*	*cfp-cheW*$_4$	[198]
JPA1457	*R. sphaeroides*	*yfp-cheW4*	[198]
JPA1519	*R. sphaeroides*	*yfp-cheW4* $\Delta tlpT$	[200]
JPA1558	*R. sphaeroides*	*tlpT-yfp*	[200]
JPA2290	*R. sphaeroides*	$\Delta tlpT$ $\Delta ppfA$	This study
JPA2291	*R. sphaeroides*	$\Delta tlpT$ $\Delta ppfA$ *cfp-cheW*$_4$	This study

Table 2.1: Strains

2.1.2 Plasmids

Plasmid Name	Description	Source
pBAD33-*yfp-tlpT*	pBAD33 containing the *tlpT* with an N-terminal *yfp* fusion	David Zollman
pIND4	IPTG inducible plasmid for gene expression in *R. sphaeroides* . Kanamycin resistance.	[88]
pIND-*tlpT*	pIND4 containing the *tlpT* gene.	This study
pIND-*ppfA-cfp*	pIND4 containing a C-terminal *cfp* fusion to *ppfA*	[152]
pIND-*ppfA-PAmCherry*	pIND4 containing a C-terminal *PAmCherry* fusion to *ppfA*	This study
pK18*mobsacB*	Kanamycin resistance suicide plasmid, sucrose sensitive.	[131]
pK18*mobsacB*:Δ*tlpT*Δ*ppfA*	pK18*mobsacB* containing 500bp flanking regions up and down stream of the adjacent *ppfA* and *tlpT* genes.	This study
pROD-*PAmCherry*	pROD containing the *PAmCherry* gene	Rodrigo Reyes-Lamothe

Table 2.2: Plasmids

2.2 Growth conditions

2.2.1 Antibiotics

Antibiotic	Concentration for *E. coli*	Concentration for *R. sphaeroides*
Kanamycin	25 μg/ml	25 μg/ml
Nalidixic acid	25 μg/ml	25 μg/ml
Ampicillin	100 μg/ml	–
Tetracycline	25 μg/ml	–

Table 2.3: Antibiotic concentrations

2.2.2 Liquid Cultures of *E. coli*

Liquid cultures of *E. coli* were grown in LB, see Appendix A,containing the appropriate antibiotic/s at 37°C with shaking.

2.2.3 Agar Plates for *E. coli*

E. coli was grown on solid agar plates made from LB, see Appendix A, and 2% agar containing the appropiate antibiotic/s.

2.2.4 Aerobically Grown *R. sphaeroides*

R. sphaeroides was grown aerobically in succinate media, see Appendix A, containing the appropriate antibiotic/s with shaking at 30°C .

2.2.5 Photoheterotrophically Grown *R. sphaeroides*

R. sphaeroides was photoheterotrophically grown in succinate media, see Appendix A, containing the appropriate antibiotic/s in sealed bottles with minimal air space and incubated at 30°C under white light.

2.2.6 Agar Plates for *R. sphaeroides*

R. sphaerodies was grown on solid agar plates,made as described in 2.2.3, and incubated at 30°C .

2.2.7 Agar Plates for Sucrose Selection

Plates for sucrose selection were made using M22 minimal media, see Appendix A, 10% sucrose and 2% agar.

2.3 Genetic Techniques

2.3.1 Extraction of *R. sphaeroides* Chromosomal DNA.

Cultures were grown aerobically to stationary phase (48hrs). 1.5ml of culture was centrifuged and the pellet was snap frozen in liquid nitrogen, the frozen pellet was then resuspended in 0.5ml lysis buffer, see Appendix A, heated to 65°C . 100μg of proteinase K was added before incubation at 45°C for 2 hours. The chromosomal DNA was then extracted twice with 0.5ml phenol:chloroform:isoamyl-alcohol (25:24:1), and precipitated with 100% ethanol and incubated at -20°C for 30 minutes. Following incubation the sample was centrifuged at 16000 x g for 15 min, the pellet was then washed with 70% ethanol and spun again as above. The pellet was then dried at 37°C overnight and resuspended in 50 μl sterile water and stored at -20°C .

2.3.2 Polymerase Chain Reaction (PCR)

Standard PCR

PCR was carried out with reaction mixture composition as described in table 2.4. Reaction mixtures were then placed in a thermocycler and subjected to the program described in table 2.5, annealing temperature was dependent on the T_M of the primers used in each reaction.

Component	Quantity
Template DNA	0.5 μl
Primers	1 μl of each at 100 μM
Pfu DNA polymerase (Promega)	1 μl
10x *Pfu* polymerase buffer (Promega)	5 μl
dNTPs	5μl at 2.5 mM
DMSO	0μl for 0% 2.5 μl for 5% 5 μl for 10%
MilliQ	Make up to total volume of 50 μl

Table 2.4: PCR reaction mixture composition

Stage	Number of cycles	Temperature	Time
Initial denaturation	1	98°C	10 min
Denaturation		98°C	1 min
Annealing	30	Annealing temperature	1 min
Extension		72°C	2 min per 1kb product
Final Extension	1	72°C	5 min

Table 2.5: PCR reaction program

Overlap Extension PCR

Overlap extension PCR was used to create constructs for generating deletion strains and genomic replacement strains. A schematic of the process is shown in fig. 2.1.

2.3.3 Restriction Enzyme Digests

Restriction enzyme digest reaction mixtures (as described in tables 2.6 and 2.7) were incubated at 37°C for at least 2 hours or overnight.

2.3.4 De-phosphorylation

Restriction digests of plasmids were stopped by heating them to 80°C for 20 min, and then cooling to 4°C . 1 μl of calf intestinal alkaline phosphatase (CIP) (New

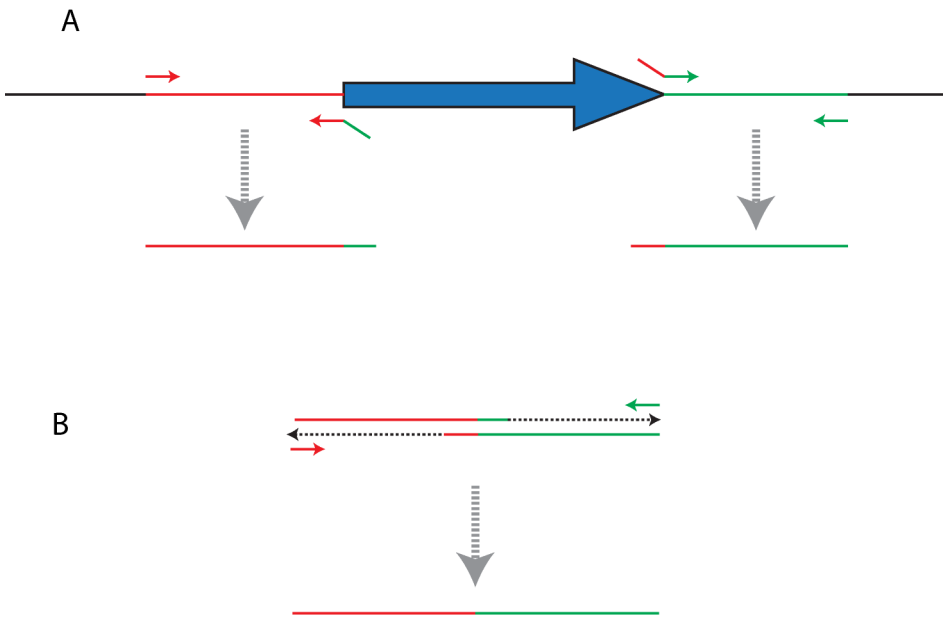

Figure 2.1: Overlap extension PCR to create deletion construct. **A:** First round of PCR. Two reactions (grey arrows) are run using primers designed to amplify the flanking regions (green and red) of the gene to be deleted (blue). The inner primers contain a region of overlap with other flanking region. The products created contain a region of complementarity. **B:** Second round of PCR. Both products and the outside primers are used in a single reaction. The regions of complementarity between the two products of the first round allow them to act as primers and this results in elongation of a single fused sequence.

Component	Quantity
DNA	25 μl for PCR products 10 μl for plasmids
10 x buffer	5 μl
Bovine serum albumin	0.5 μl
Enzyme	1 μl each
MilliQ	make up to 50 μl total volume

Table 2.6: Restriction enzyme digest reaction mixture composition

Component	Quantity
Plasmid	5 μl
10 x buffer	2 μl
Bovine serum albumin	0.2 μl
Enzyme	0.5 μl each
MilliQ	make up to 20 μl total volume

Table 2.7: Restriction enzyme digest reaction mixture for confirmation of ligation

England Biolabs) was added and the mixture incubated at 37°C for 1 hour.

2.3.5 Gel Electrophoresis

DNA framents were separated using gel electrophoresis. Gels were made using between 0.8% and 2% multi-purpose agarose (Roche) in 0.5 x TBE, see Appendix A, depending on the fragment sizes that required separation. Fragments were electrophoresed at voltages between 80-140 V. Visualisation of gels was achieved by staining them in 1 ng/ml ethidium bromide for 15 minutes and viewing on a UV transiluminator.

2.3.6 Purification of DNA Fragments

DNA fragments were purified from agarose gels and solution using the Gel Extraction Kit (QIAGEN), following the provided protocol.

2.3.7 DNA Ligation

DNA ligation mixtures were made up as described in table 2.8, the volume of plasmid and insert DNA was adjusted to give a specific molar ratio of insert to plasmid, usually 3:1.

Component	Quantity
Digested plasmid	10 μl
Digested insert	24 μl
T4 DNA ligase (Invitrogen)	1 μl
T4 DNA ligase buffer (Invitrogen)	10 μl
MilliQ	5 μl

Table 2.8: DNA ligation reaction mixture

2.3.8 Competent Cells

E. coli cells were made chemically competent using rubidium chloride method as follows.

50 ml of LB-broth was inoculated with 1 ml of stationary phase *E. coli* and then incubated at 37°C until it reached an OD_{600nm} of 0.4. The culture was then transferred to a 50 ml falcon tube and incubated on ice for 15-30 minutes, before being centrifuged at 1000 x g for 10 minutes at 4°C . The pellet was resuspended in 16 ml ice cold TFB-I, see Appendix A, and incubated on ice for 1 hour, before being centrifuged at 750 x g for 10 minutes at 4°C . This pellet is then resuspended in 4 ml ice cold TFB-II, see Appendix A,. 200 μl aliquots of the resuspended cells were then flash frozen in liquid nitrogen and stored at -80°C .

2.3.9 Transformation of Plasmids into Competent Cells

100 μl competent *E. coli* XL-1 cells were defrosted on ice, and then incubated on ice with plasmid DNA for 45 min. For ligations 25 μl of ligation mixture was

added, for purified plasmid 1 μl was added. The cells were then heat shocked by incubating them at 43°C for 45s and then immediately on ice for 45s. 1ml of soc medium was then added and incubated at 37°C for 1 hour before being plated on LB agar plates with the appropriate selective antibiotic.

2.3.10 Plasmid Purification

E. coli cultures containing the plasmid of interest were grown overnight in LB-broth and the appropriate antibiotic at 37°C . The plasmid was then extracted using the QIAGEN QIAfilter plasmid mini or midi kit according to the manufacture's instructions.

2.3.11 DNA Sequencing

DNA sequencing was done using the Automated DNA Sequencing Service from Geneservice (Source BioScience). The BigDye termination method (PE Biosystems) was used on on a 3730 DNA sequencer (Applied Biosystems). Contigs were generated using the Staden software package and analysed using Clone Manager (Sci Ed Central).

2.3.12 Conjugation of Plasmids into *R. sphaeroides*

R. sphaeroides cannot be made competent therefore plasmids were introduced via conjugation from *E. coli* S17-1λ*pir* cells. These cells were made competent as described in 2.3.8 and plasmids transformed into them as described in 2.3.9. 1 ml of mid-log phase *E. coli* cells and 1 ml of photoheterotrophic phase *R. sphaeroides* were centrifuged at 3500 x g. Pellets of both *E. coli* and *R. sphaeroides* were washed in 1 ml LB-broth (without any antibiotics), before being finally resuspended in

100 μl LB-broth. Special care was taken when resuspending the *E. coli* S17-1λ*pir* cells as to not shear the pili. 10 μl of *E. coli* were gently mixed with 100 μl of *R. sphaeroides* , and this mixture was pipetted onto a sterile nitrocellulose filter on an LB agar plate with no antibiotic. This plate was then incubated to 30°C overnight, before the cells were washed off the filter in LB-broth and spread onto LB agar plates containing nalidixic acid and the appropriate selective antibiotic for the plasmid.

2.3.13 Recombination for Genomic Replacement and Deletion Mutants in *R. sphaeroides*

Recombination was used in order to delete genes from the genome or replace genomic genes with fluorescently labelled mutants. This was done using the suicide plasmid pK18*mobsacB*. For genomic deletion mutants constructs were created that contained the 500bp regions flanking the gene upstream and downstream but not the gene itself, see fig. 2.1. For N terminally tagged genomic replacements constructs contained the upstream 500bp, the tag and 500bp of the gene, for C terminally tagged replacements they contained the final 500bp of the gene, the tag and the downstream 500bp.

These plasmid constructs were transferred into the background *R. sphaeroides* strain by conjugation, described in 2.3.13, and spread onto LB agar plates containing kanamycin and naladixic acid. *R. sphaeroides* is unable to replicate pK18*mobsacB* and thus the only way the cells can pass the kanamycin resistance encoded on pK18*mobsacB* is by integrating the plasmid into their genome by homologous recombination. This is the first round of recombination.

Colonies from the first round of recombination were grown in succinate media with naladixic acid for 48 hours. The absence of kanamycin allows the second

recombination event to occur as this excises the vector backbone, including the *kan*^{r} and *sacB* genes, from the genome. The second round of recombination is selected for by plating cells from the first round of recombination onto M22 10% sucrose plates. Replica plates were also used to confirm the loss of the *kan*^{r} gene. This second recombination event also results in the excision of either the parental gene or the mutation construct, and thus two possible end results; the desired mutant strain or reversion to the wild type genotype.

PCR screens were used to distinguish between the two possible double recombinants.

2.4 Phenotypic Analysis of *R. sphaeroides* Strains

2.4.1 Swim Plates

Swim plates were used to asses the chemotactic ability of *R. sphaeroides* strains.

Semi-solid agar plates were made using 0.25% agar (BiTek) in M22 minimal media, see Appendix A. The plates contained naladixic acid and a chemoattractant (100 μM proprionate), which was the only carbon source available on the plate. 5 μl of stationary photoheterotrophic culture was pipetted onto spots. Plates are incubated at 30°C for 48 hours. As the cells grow they consume the proprionate and thus create a concentration gradient, which if the cells are motile and chemotactic they will swim up. The area of the rings formed around the inoculation site is measured and used as a measure of chemotactic ability relative to control strains.

2.5 Microscopy

2.5.1 Preparing Cells for Microscopy

R. sphaeroides

R. sphaeroides cells were grown aerobically, as described in 2.2.4, to mid-log phase (OD_{700nm} 0.4-0.6).

E. coli

E. coli cells were grow as described in 2.2.2 to mid-log phase (OD_{600nm} 0.5-0.6), unless otherwise stated. Cells were then washed in M9 minimal media,, see Appendix A, to remove LB broth and therefore a highly autoflourescent background.

Elongated cell preparation

R. sphaeroides cells were grown aerobically, as described in 2.2.4, to OD_{700nm} 0.2, then treated with 1μg/ml cephalexin and grown for a further 2 hours.

E. coli cells were grown to OD_{600nm} 0.2, and then treated with 100 μg/ml cephalexin and grown for a further 2 hours.

2.5.2 Preparing Slides

Agarose Pad Slides

Agarose pad slides were created by adding a thin layer of 1% agarose in succinate medium to a slide and then applying 2 μ l of cells to the agarose before adding a cover slip.

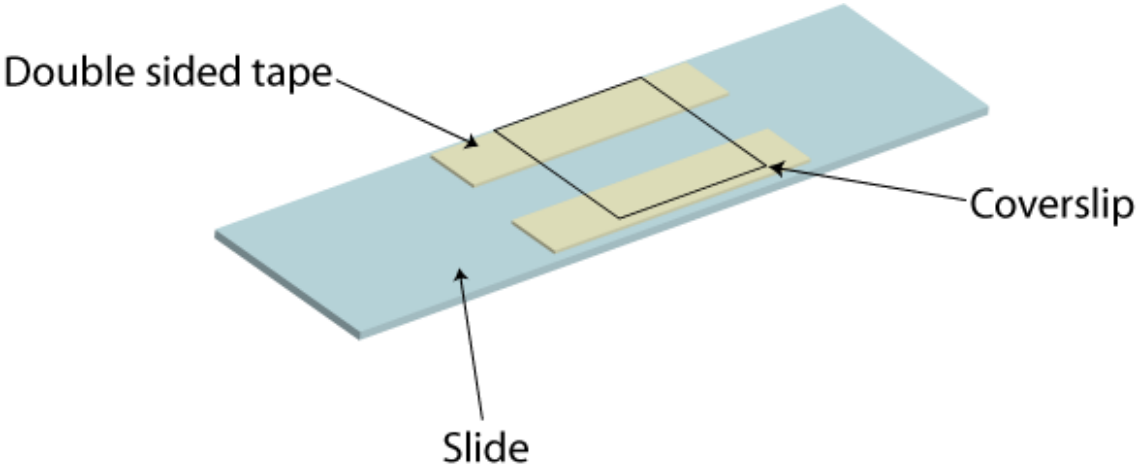

Figure 2.2: Tunnel slide

Tunnel Slides

Tunnel slides were created by applying two strips of double sided tape (3M) to the slide and affixing a cover slip to these strips, as shown in fig. 2.2 to create a small space between the slide and the cover slip of 25 μl. A solution of poly-L-lysine (0.01% w/v in water) is then wicked through this space and the slide is incubated upside down for 2 min. This solution is then was washed out twice with 100 μl of the media the cells will be in when imaged. 100 μ l of the media containing the cells is then wicked through and incubated with the slide upside down for 10 min. Any non-stuck cells are removed by washing the slide with 100 μl of media three times. The open ends of the tunnel are then sealed with nail varnish to prevent evaporation.

2.5.3 Microscopes

Nikon Eclipse Ti

The system used to acquire fluorescence images of cells consisted of an inverted Nikon Eclipse Ti microscope using differential interference contrast (DIC) enhancement. Either 60X or 100X oil objectives (Nikon) were most commonly used,

with an additional 1.5X magnification applied within the microscope also commonly used. The microscope was controlled using NIS Elements software (Nikon). The Perfect Focus System (PFS) was used when time courses or multiple fields of view were captured in order to maintain focus. This microscope could be used either in confocal mode or epifluorescence mode (see below).

Nikon Eclipse Ti - Epifluorescence Mode

For epifluorescence image acquisition the Nikon Eclipse Ti microscope was used with a mercury lamp and appropriate excitation and emission filters for YFP and CFP. Brigtfield images used a halogen lamp for illumination. The images were captured using an Andor iXON CCD camera.

Nikon Eclipse Ti - Confocal Mode

For confocal image acquisition the Nikon Eclipse Ti microscope was used with a Nikon A1R module. Images were captured using a photon multiplier tube, which was also controlled by NIS elements software.

Nikon Eclipse TE200

In addition to the Nikon Eclipse Ti a Nikon Eclipse TE200 microscope was also used. Samples were illuminated with a mercury lamp with the appropriate excitation and emission filters (Chroma) for YFP, CFP, GFP, RFP and DAPI. Brightfield images used a halogen lamp for illumination, and contrast was enhanced using a DIC set up. Images were captured using a Hamamatsu ORCA-ER CCD camera. The microscope was controlled using the Simple PCI 6 software package.

Photoactivation Localisation microscope

For photoactivation localisation microscopy (PALM) a custom built microscope was used. YFP fusion proteins were excited with a 473 nm laser, PAmCherry fusion proteins were photoactivated with a 405 nm laser (CNI), and excited with a 561 nm laser (Oxxius). Brightfield images were aquired using a LED light source (coolLED) and an Olympus condenser. The objective used was 100x oil immersion Olympus objective with 1.4 numerical aperture. For futher details please see [189].

Chapter 3

Image Analysis

3.1 Epifluorescence Images of Bacterial Cells

In order to gain information about the localisation of proteins within cells by epifluorescence microscopy several pieces of data must be acquired and stored within the output image. These include (i) the signal from the fluorescently tagged protein/s and (ii) a signal which indicates the boundaries of the cell body. This is normally done through the acquisition of a non-fluorescence brightfield image, although it can also be done by using a fluorescent dye or tag that marks the cell membrane. These data are acquired as individual greyscale images, the bit-depth of which will depend on the camera. These greyscale images are then compiled and stored as an individual image or file. The two file types used in this study are detailed below.

3.1.1 RGB .tif files

The RGB .tif format is a lossless image format which consists of three channels which are displayed visually as red, green and blue, thus coming together to

form an RGB image. Due to the RGB format no more than three channels can be stored within an single .tif file. The colours seen in the RGB.tif file are false and are simply the greyscale images displayed in the colour of the channel to which they have been assigned, which is arbitrary. It is also possible to save a single channel as a greyscale .tif file.

This results in an image where each pixel has 5 pieces of information associated with it, an X coordinate, a Y coordinate, a R pixel value, a G pixel value and a B pixel value. Thus each image is an m x n x 3 matrix where m and n are the number of pixels in X and Y respectively.

Images acquired using the Nikon Eclipse TE200 (see 2.5.3) were saved as RGB.tif files.

3.1.2 .nd2 files

When using the Nikon Eclipse Ti microscope (see 2.5.3) the images were saved in the Nikon proprietary format .nd2. This file format had several advantages over .tif files. There is no limit on the number of channels which can be stored within a single file, and when capturing time course or Z-stack data all the images are stored within a single file. The file also saves meta data about the image including microscope and camera settings used to acquire all the images within the file.

However a major disadvantage of the .nd2 file format is that these files cannot be viewed or processed outside the NIS Elements software package. Therefore in order to process the images they must be exported as individual greyscale .tif files for each channel. Once exported as .tif files the meta data are lost, so after exporting both .nd2 and .tif files were retained.

3.2 Contrast Enhancement Techniques

As bacterial cells are aqueous and are viewed embedded on or within aqueous media (such as agarose pads - see 2.5.2, or tunnel slides - see 2.5.2) simply illuminating the sample with white light produces very little contrast between the cells and the background medium. Various techniques have been created in order to increase the contrast between biological samples and the background. Whilst this can be done with the use of stains, it is preferential to use optical techniques which do not perturb the sample. Phase contrast and differential interference contrast (DIC) are two of the most commonly used optical contrast enhancement techniques, both of which utilise the changes in the phase of light as it passes through matter.

3.2.1 Phase Contrast

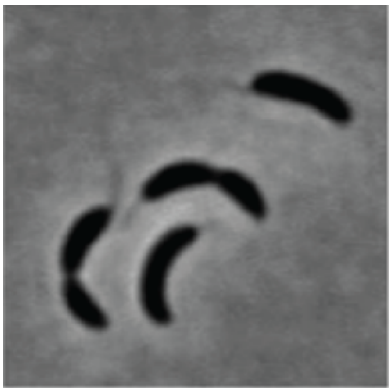

Figure 3.1: Typical phase contrast image of *C. crescentus* . Adapted from [100]

Phase contrast works through the addition of two elements to a traditional bright-field set up, these are a phase annulus and a phase plate (see fig. 3.2). The phase annulus is an opaque plate containing a transparent ring and is placed between the light source and the condenser lens. This results in two parallel wavefronts illuminating the specimen. When light passes through the biological sample some of the light will be scattered and have its phase retarded by one quarter of the

wavelength ($\frac{1}{4}\lambda$). The light then passes through the objective and the phase plate. The phase plate consists of a transparent plate with a ring (which corresponds to the ring in the annulus) which has been treated such that it will advance the phase of the light by $\frac{1}{4}\lambda$ as well as attenuate the amplitude of the light. Light which has not passed through the sample and thus not had its phase altered is focussed onto this region of the phase plate, where as light that has had its phase altered passed through other regions of the plate. Therefore the light that has passed through the sample has been retarded by $\frac{1}{4}\lambda$ and the light that has not has been advanced by $\frac{1}{4}\lambda$, resulting in a $\frac{1}{2}\lambda$ difference between them. When these waves interfere it will produce a wave with decreased amplitude due to destructive interference compared to light which has passed through regions of the slide with no biological sample. Thus the resultant image will have darker regions where the cells are compared to where they are not, hence images such as fig. 3.1 showing dark cells on a light background.

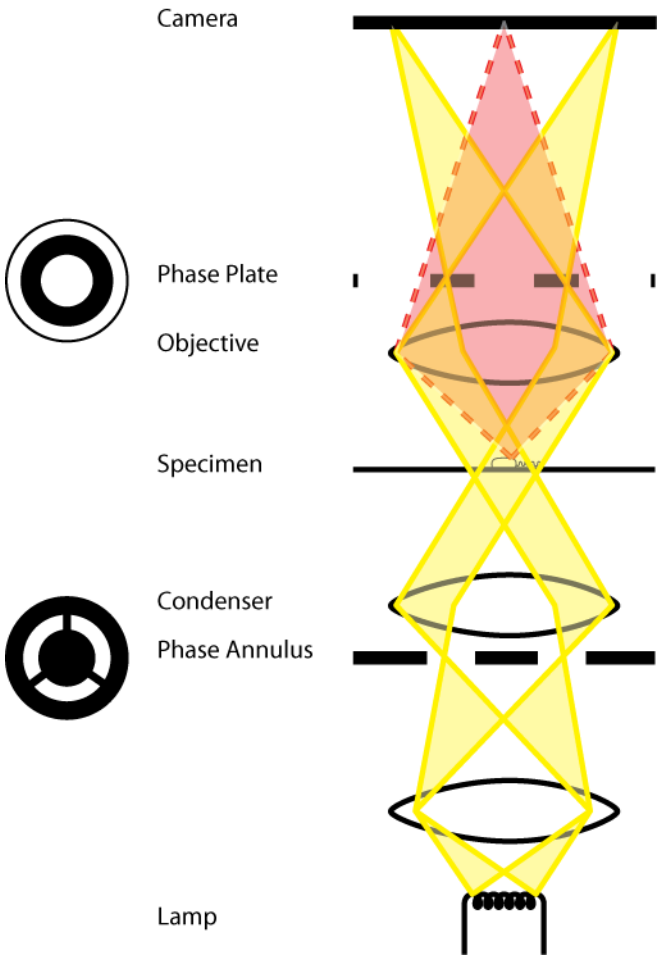

Figure 3.2: Phase contrast microscope light path schematic. Yellow paths show light that has not had its phase altered by the specimen and therefore passes exclusively through the coated region of the phase plate, shown in black. Light which has had its phase altered is shown in red and is able to pass through uncoated regions of the phase plate.

3.2.2 Differential Interference Contrast

In a DIC set up (shown in fig. 3.2.2) light first passes through a polariser, this polarised light then enters a Wollaston prism. The Wollaston prism splits the beam into two beams polarised at 90°C relative to each other, as the beams are polarised orthogonally to each other they cannot interfere. These two beams are then focused by the condenser such that they pass through specimen plane adjacent to each other rather than coincidently, this offset is referred to as the shear.

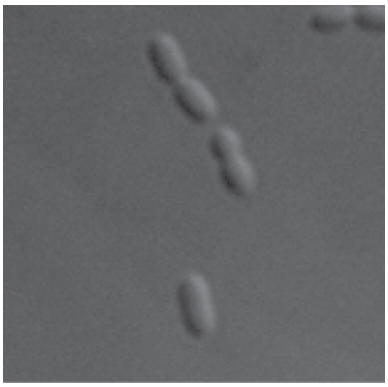

Figure 3.3: Typical DIC image of *R. sphaeroides* .

The beams then pass through the objective which focuses them onto a second Wollaston prism. Here the two beams are recombined into a single beam with one polarisation state, before passing through a second polariser and hitting the camera.

If when the two beams pass through the specimen plane they both pass through material of the same depth and refractive index then they will remain in phase with each other. However if one of the beams passes through a cell, for example, then its phase will be retarded. When the beams are recombined by the second Wollaston prism the difference in phase will produce interference, either constructive or destructive creating brighter or darker regions of the image. If both beams pass through the cell they will both have their phase altered equally and thus remain in phase with each other, and there will be no interference.

This creates images where regions with differences in refractive index or depth relative to the media will have a light edge, a dark edge and a middle with the same intensity as the background, creating a pseudo-3D effect as seen in fig. 3.3.

The position of the light and dark edges of the objects is related to the angle of the shear and independent of the objects.

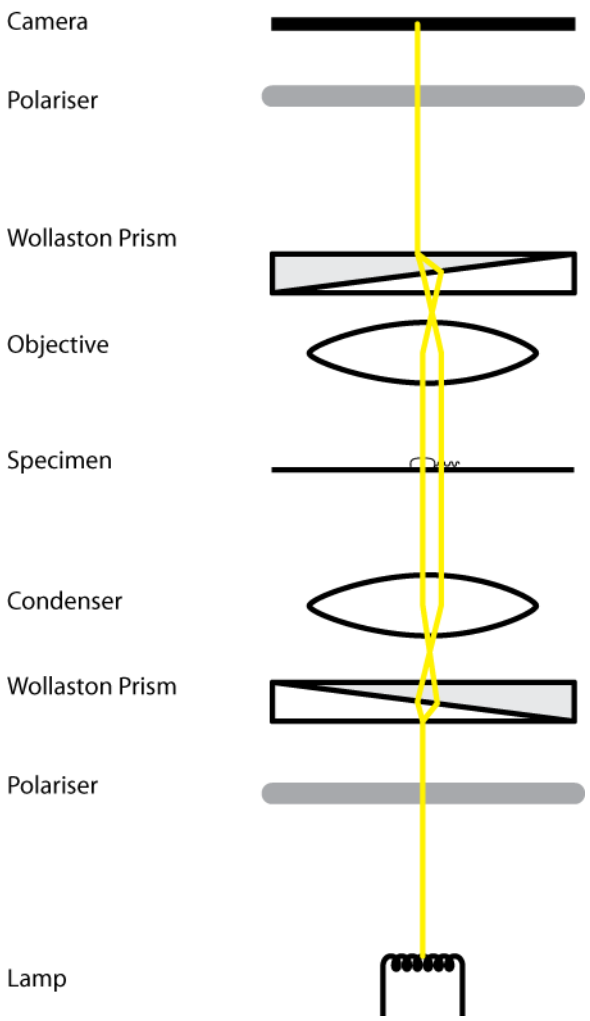

Figure 3.4: Differential interference contrast microscope light path schematic. The yellow line represents a single beam, which is split into two adjacent beams with orthogonal polarisations by a Wollaston prism. These beams pass through the specimen before being focused onto a second Wollaston prism which recombines them before the light reaches the camera.

3.2.3 Comparison of DIC and Phase Contrast

Both phase contrast and DIC have advantages and disadvantages, listed in table 3.1. Based primarily on the fact that DIC can capture greater amounts of fluorescent light than phase contrast both the Nikon Eclipse Ti and the Nikon Eclipse TE200 are equipped with a DIC set up. Greater fluorescent light captured means that in order to acquire the same strength of fluorescent signal less excitation

light is needed in a DIC set up compared to a phase contrast one. This reduces the amount of photobleaching, something especially advantageous in time course experiments.

Technique	Disadvantages	Advantages
Phase contrast	The phase annulus reduces the amount of light able to illuminate the sample.	Not dependent on the use of polarised light and therefore can be used with materials that affect the polarisation of light such as plastics.
	Presence of halos around objects. Some of the defracted light will pass through the treated region of the phase plate and create a reversal of contrast around objects	
	The phase plate reduces the maximum numerical aperture objective that can be used.	
DIC	The contrast is directional, with maximum contrast parallel to the shear angle, and no contrast perpendicular to it.	Can work with higher numerical aperture objectives, and therefore can collect more fluorescent light.
	Dependent of polarised light, and therefore can't be used with plastics.	Good for use with thick specimens.

Table 3.1: Comparison of phase contrast and DIC microscopy

3.3 Current Image Analysis Approaches

Where as previously it was common for images to be analysed in a qualitative manner it has become increasingly important and possible to do so quantitatively. Doing so allows better definition of fluorescent protein positioning and cell morphology. Importantly it removes a significant amount of bias that can be introduced by subjectively defining features. It also gives greater insight into variation within populations.

Quantifying images means that statistical measures can be used, allowing for a more rigorous comparison of strains and species. However this requires a large enough number of data points, hence the increasing desire to create high throughput semi-automated methods for image analysis.

3.3.1 Mean Grey Level Analysis

Mean grey level analysis has been used to determine whether proteins within bacterial cells are clustered or diffuse, it has also been used to determine the dependence of a protein's clustering ability on the presence of other proteins. [200, 198]. In order to perform this analysis strains to be compared are grown on the same day and imaged using identical microscope and camera settings. The fluorescent channels from the resultant images are then thresholded. The threshold value is determined by imaging non-fluorescent cells using identical settings and determining the maximum pixel value within these non-fluorescent cells. Using a threshold generated like this means that any pixel values above the threshold are due to the presence of a fluorescently tagged protein and not simply autofluorescence. Once this threshold has been determined then objects are defined as adjacent pixels within the image that above the threshold value. For each of these objects mean grey values are then calculated. If the protein of interest forms clusters then these objects will be smaller than the cells, however if the protein is diffuse the objects will occupy the whole of the cell body. When trying to determine which proteins are required for clustering of a specific protein the mean grey values can be compared. Assuming that the expression level and therefore the amount of protein is the same across the strains then the more clustered a protein the higher the concentration of fluorophore, and therefore mean grey level, in the defined objects.

This approach has its drawbacks. The determining of a threshold level is arbitrary

and subject to bias. As only the fluorescent channel is being analysed it gives you no quantitative information about the level of clustering within single cells, just across the whole image and therefore information about cell to cell variation is averaged out.

3.3.2 Manual Object Position and Cell Morphology Analysis

Using software such as NIS Elements, Simple PCI or ImageJ (`http://rsbweb.nih.gov/ij/`) it is possible to measure distances between two points. This is done by drawing a line between those two points and outputting the length of the line drawn in pixels. This distance is then converted to μm using a pixel to μm scale factor created by imaging a 100 μm graticule and calculating the distance occupied by one pixel.

In order to gain cell morphology information a line must be drawn for each piece of information required, for example measuring the length and width of cells requires lines spanning the length and width of the cells to be drawn and measured sequentially.

Measuring the position of fluorescent objects within cells, typically done relative to the long axis of the cell requires measuring the length of the cell and then the distance between the object and a cell pole. To measure the position relative to the short axis of the cell then the width of the cell and the distance of the object from one edge of the cell must also be measured.

As the technique is entirely dependent on user input to define the point between which the distances are measured it is prone to user error and care must be taken to ensure consistent placement of points at cell poles and edges, across multiple measurements within an individual cell and across all cells in the study. Due to the number of points that have to be manually defined for each cell this technique

is very time consuming, limiting the number of cells feasibly possible to analyse.

3.3.3 Semi-automated Image Analysis Approaches

Due to the limitations for the approaches described above groups have been increasingly trying to develop higher throughput methods with a greater level of automation. In order for high throughput method to analyse images at a single cell level the first step required is to segment the image into regions that correspond to individual cells. Once these regions have been defined they can be applied to the fluorescent channels and information about the fluorescence within each individual region can then be extracted.

The difficulty in this approach is being able to reliably, rapidly and accurately define the cell outlines from the images. Several methods for segmenting images of cells are discussed below.

Whilst semi-automated image processing software can be written in virtually any programming language, two of the most commonly used environments are ImageJ and MATLAB, both of which are discussed in 3.5.1.

3.4 Image Segmentation

3.4.1 Phase Contrast and fluorescent Image Segmentation

The methods used to segment phase contrast images take advantage of the fact that the cells are dark objects on a light background (see 3.2.1). The simplest method for segmenting phase contrast images involves a one step threshold algorithm. Firstly the image is inverted so that the cells now appear light on a dark background and then the image is thresholded, this is illustrated in fig. 3.5.

The threshold value used is arbitrary and usually chosen to give the best results across all the images. It is often advantageous to apply median or Gaussian filters to reduce noise before the threshold step.

Another method for defining cell regions is edge detection. It is possible to use built in functions in both MATLAB and ImageJ to find edges within images and use the resultant image to create a binary mask similar to that shown in fig. 3.5 C.

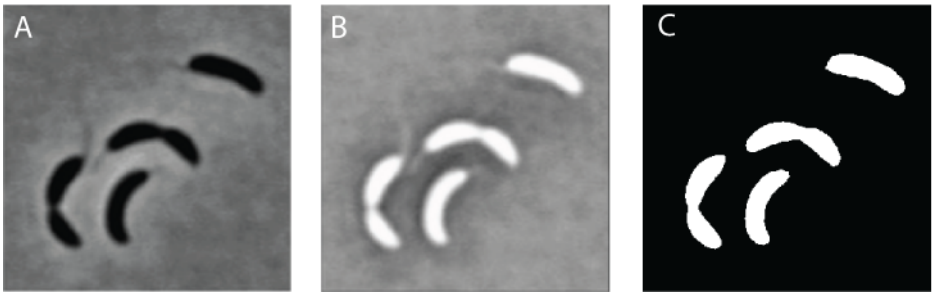

Figure 3.5: Phase contrast image thresholding. **A** Phase contrast image of *C. crescentus* , adapted from [100]. **B** The image from A inverted so that they cell body now appears light on a dark background. **C** A binary image created by applying a threshold to the inverted image in B. This binary image contains regions of white corresponding to the cell bodies.

The same methodologies can be used to segment fluorescent images where the fluorescent signal either fills the cell volume evenly or where it stains the cell membrane (this will require some additional steps to fill the regions so that they correspond to the whole of the cell body and not just the membrane). As the fluorescent signal is light against a dark background there is no need to invert the image before applying the threshold.

For both threshold and edge detection analysis some post processing will be required. This is because it is very unlikely that every object identified in an image will be a cell. Individual pixels may have a high pixel intensity due to noise, especially in images acquired with long exposure times and/or high camera gain settings. Also dust particles within the light path may visible in the image and be above the threshold cut-off. Any cells overlapping will have no definable edge between them and thus will be interpreted as one large region. The best solu-

tion is to manually determine a range of acceptable cell sizes (in px^2) and then exclude all regions that do not fit within this range. Care must be taken to ensure this range is appropriate and is not biassing the data. In some cases further post-processing has been to the binary image created by thresholding [172], and is discussed later.

3.4.2 DIC Image Segmentation

Segmenting DIC images is not as straight forward as segmenting phase contrast images. This is due to images having a pseudo-3D appearance (see 3.2.2). Objects having both light and dark edges means that simply applying a single threshold (as can be done for phase contrast images) will produce images containing only either the light or dark areas(see fig. 3.6 B and C). The presence of light and dark edges to objects also precludes the use of edge detection algorithms as this will only extract the two contrasting edges and not the object as a whole. Therefore more complicated approaches must be considered.

A simple approach is to threshold at two levels, one to extract the dark areas and one to extract the light areas. This is done by initially thresholding the image to create regions from the light areas, and then inverting the original image and thresholding again, creating regions which are dark in the original image (and light in the inverted image). Whilst this method has been used previously [170], it is not ideal. This is due to the lack of contrast perpendicular to the shear angle meaning at this angle the edge of the cell will be the same intensity as both the centre of the cell body and the background. Thus when combining binary images created with thresholds for dark and light regions the resulting regions will not correspond to the complete cell boundary (see fig 3.6 D).

More complex approaches include the fitting of templates to the image [216] and imaging objects multiple times at different shear angles and reconstructing the

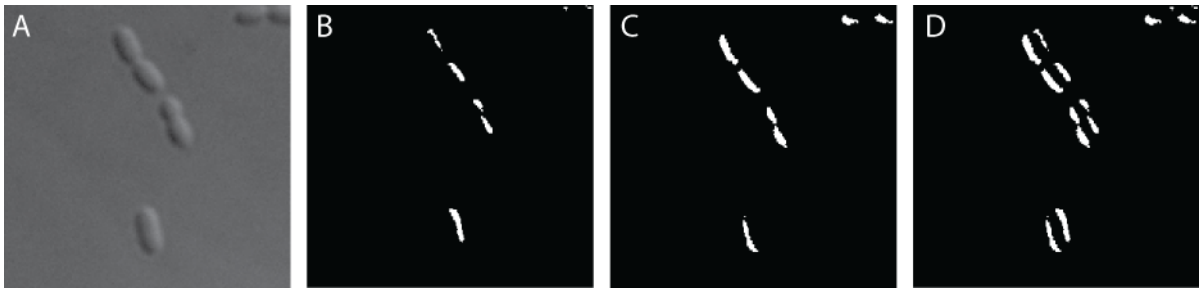

Figure 3.6: DIC image thresholding. **A** DIC image of *R. sphaeroides* cells. **B** The image in A. thresholded to create a binary image containing the light regions of the original image. **C** The image in A. thresholded to create a binary image containing the dark regions of the original image. **D** Binary images B and C combined to create a binary with both the light and dark regions of the DIC image. Both single level and bi-level thresholds are insufficient to create binary images with regions that encompass the entire cell body, this is due to the lack in contrast in the direction perpendicular to the shear angle.

object [139]. Template fitting was not feasible for images of bacterial cells as it requires a relatively constant cell size, and is not suitable for the large number of cells within a single image. The rotational approach is also not feasible here as it requires either the rotation of the sample or the Wollaston prisms, both of which are not possible on microscope set ups used.

Approaches which attempt to reconstruct the object from a single DIC image (i.e. without the need to rotate the shear angle) are more appropriate for the types of images collected and microscope set ups used in this study. These approaches seek to transform the DIC image to an image where the objects within resemble objects seen in phase contrast images, i.e. made up of uni-directional contrast against the background. These reconstructed images can then be subjected to the techniques used for phase contrast image segmentation (discussed above). These methods are discussed and compared in [78] and [6], both of which determine that the use of the Hilbert transform gives the best results.

An example of a simulation of a 1D Hilbert transform on a the cross-section of a model object is shown in fig. 3.7. In effect the Hilbert transform renders asymmetric features (such as DIC objects) symmetric. In a 1D example the asymmetry

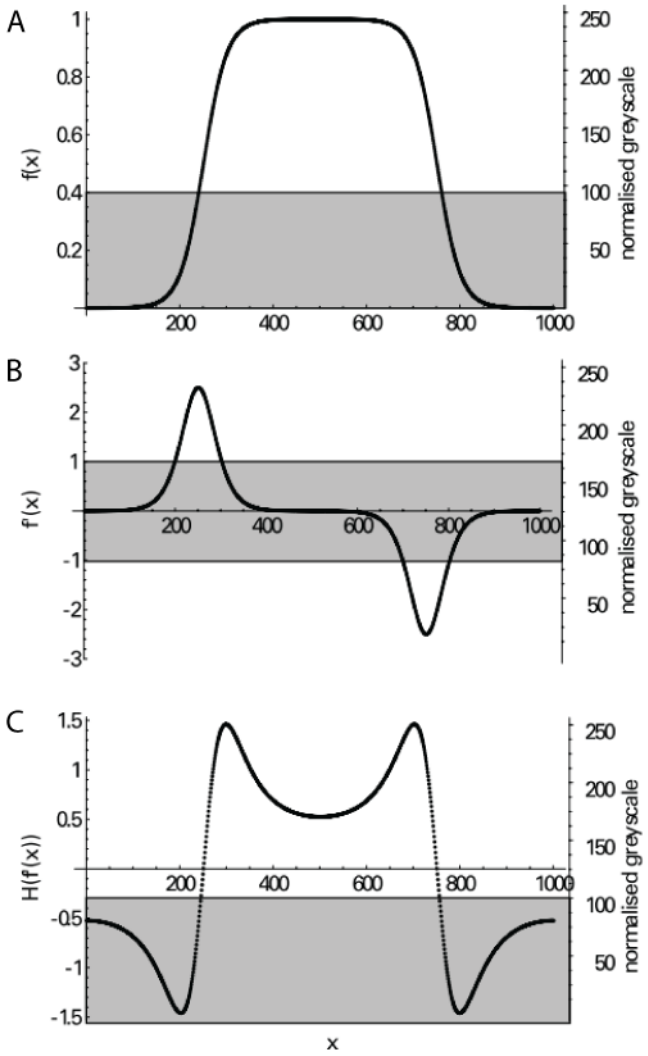

Figure 3.7: Hilbert transform of a 1D model of a DIC object. **A** A 1D model of an object. **B** The object in A having been imaged by DIC where the shear angle is along the x-axis. Where there will be differences in the path length on one beam relative to the other (i.e. at the edges of the object) deviations in amplitude are present. The positve and negative peaks correspond to the light and dark edges of DIC object respectively. **C** The Hilbert transform of the signal in B. Whereas in B the object was asymmetric, symmetry has now been restored. In all three the shaded region represents a threshold level that could be used to distinguish the object from the background, in B the centre of the object is indistinguishable from the background. Taken from [6].

is along the x-axis, however in a 2D example the asymmetry can be along any axis, and thus the 2D Hilbert transform requires an angular argument. In the case of a DIC image the asymmetry is along the angle of greatest contrast, the shear angle.

3.5 Semi-automated Image Analysis Software Packages

3.5.1 ImageJ and MATLAB

ImageJ is a free java-based software package, which comes with a number of image processing and analysis functions. It also has a larger number of plugins created by third-party developers creating an extensive library of tools available for image analysis. Whilst ImageJ is primarily GUI-based it is possible to create macros and automate the processing of multiple images through a single work flow.

MATLAB is a software package from Mathworks (`http://www.mathworks.co.uk/`) designed for matrix manipulation and mathematical treatment of data. An additional image processing toolbox contains a large number of additional functions created specifically for the manipulation and analysis of images. MATLAB has its own programming language and environment in which new functions and programmes can be created. Two examples of software packages which run within the MATLAB environment are detailed below.

3.5.2 Microbe Tracker

MicrobeTracker ([172],`http://www.microbetracker.org/`) is a MATLAB based software package designed to segment phase contrast images, and analyse the fluorescent signal within the segmented cells. The segmentation process starts with a thresholding step as described in 3.4.1, which is coupled with an edge detection algorithm to create a binary image. Regions in this binary image are then assessed according to pixel area, if a region's area does not fall within a user-defined range of areas it is disregarded. The second stage consists of applying

contour which describes the model shape of an individual cell to the remaining regions. This outline is adjusted until it converges with the shape of the region in the binary image using an active contour algorithm. These contours have a number of internal constraints based on parameters defined by the user such as the typical length, width and curvature of the bacterial species under investigation and magnification used to acquire the image. If the object's shape is sufficiently different from that described by the parameters then the algorithm will be unable to converge the contour and the outline of the binary region. This means that objects in the image which are not cells but fall within the area range are excluded.

If analysing time-lapse image sequences MicrobeTracker segments the inital frame as above, but for subsequent frames it uses the contours from the previous frame as its initial guess for the contour of the cell in the new frame, significantly reducing the time required to define the contours. Doing so also allows it to retain the identity of each cell through a time-course meaning that it is easy to investigate the changes in fluorescent signal in individual cells over time.

Having created the contour MicrobeTracker extracts and saves a number of data, both morphological and regarding the fluorescence signal. It however has an additional feature to determine the presence of clustered protein within the fluorescent image, this can be done manually (SpotFinderM) or automatically (SpotFinderZ). SpotFinderZ defines spots automatically through an algorithm which fits a 2D Gaussian to the fluorescent signal, this fitting is dependent on user defined parameters such as the width and intensity of the spot. Once the 2D Gaussian has been fitted data is extracted. These data included magnitude (total intensity) of the spot, its position in x and y within the image, and its distance along the centreline of the cell.

Together these features make MicrobeTracker a powerful tool for extracting data from images of bacterial cells. However the dependence on user-defined param-

eters means that care must be taken not to introduce bias.

The main drawback concerning MicrobeTracker's use in this study is that it has been designed to process phase contrast images, and whilst it does have a tool to process DIC images it rarely produces satisfactory results.

3.5.3 DIC Bacterial Cell Image Analysis Toolbox

The DIC Bacterial Cell Image Analyis Toolbox (DICbc toolbox) [124] is a MATLAB based software package specifically designed to segment and analyse DIC images of bacterial cells. It does so through the use of the 2D Hilbert transform (see 3.4.2) in order to reconstruct the DIC image. Segmentation is then done through a single step by applying a threshold. The resultant binary image is then filtered to remove regions below a user-defined threshold size.

A local thresholding algorithm is then applied to the fluorescence image in order to define fluorescent protein clusters. The software then outputs and saves data on cell length, cell area, total cell fluorescence intensity, fluorescence intensity of define clusters, and positional information about the cluster.

This software package has some limitations. Whilst there is a step to remove regions below a certain size, there is no maximum value meaning that overlapping or touching cells have to be removed manually, and as there is no cell shape criteria non cell objects also have to be removed manually. The methodology used to define clusters of protein is the use of a threshold which requires input values, and may result in false positives where a slightly brighter areas in an diffuse fluorescent signal are defined as clusters. Compared to MicrobeTracker it lacks many features including tools to help analyse the output data.

3.6 Processing Images for use with the Microbe Tracker Suite

Given the strengths and weaknesses of both MicrobeTracker and the DICbc toolbox, custom software was written in MATLAB to adapt the 2D Hilbert transform step used in the DICbc toolbox to process DIC images so that they can be segmented by MicrobeTracker. Thus MicrobeTracker's superior segmentation process and analytical tools could be used on the DIC images collected in this study.

The processing steps used to create images suitable for MicrobeTracker use are as follows. Firstly the image undergoes a 2D Hilbert transform, this image is then subjected to a top-hat filtering step. The MATLAB top-hat filter performs an opening by a structuring element of user defined shape and size (here a disk of variable size was used). The opening performs a morphological erosion followed by a dilation of the image by the structuring element, this results in objects smaller than the structuring element being removed. The top-hat filter then subtracts the image created by the opening from the original image. As the opening step results in an image with only large features remaining the subtraction of this serves to remove large features from the image. This proved especially useful at removing the effects of uneven illumination on the image whilst preserving the details of the cells. The image was then inverted so that the cells appeared dark on a light background, and rescaled between the minimum and maximum pixel intensities. The final step was to apply a low-pass filter to remove noise from the image. This was done by creating a mask which was applied to the Fourier transform of the image such that it removed information near the edges of the transform. In Fourier space regions furthest from the origin represent high frequency information, such as noise. Having masked off this area an inverse Fourier transform was applied. This process is shown with an example image in

fig. 3.8.

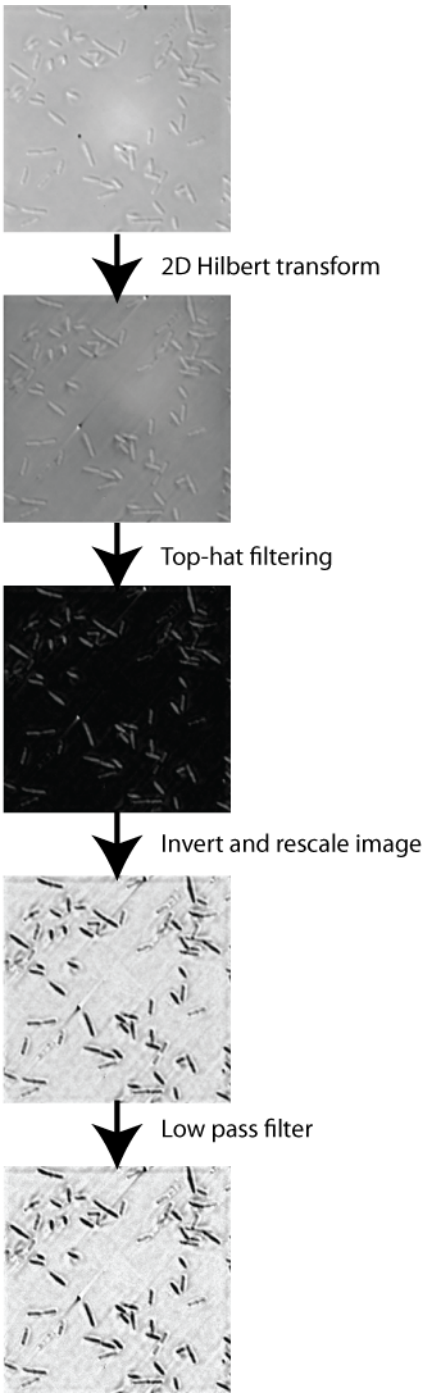

Figure 3.8: Image sequence showing the processing steps in DIC image reconstruction for use with MicrobeTracker. Top shows a DIC image of *R. sphaeroides* cells. Subsequent images show the result of the processing step indicated by the arrows preceeding them. The final result is shown at the bottom, in which cell bodies appear dark against a light background.

The processed DIC can now be segmented by MicrobeTracker. Fig. 3.9 shows

that the cell outline MicrobeTracker creates from the processed DIC image is a good fit for the cell bodies as seen in both DIC and fluorescence. It was therefore possible to analyse DIC images and time-courses in a high throughput manner using MicrobeTracker.

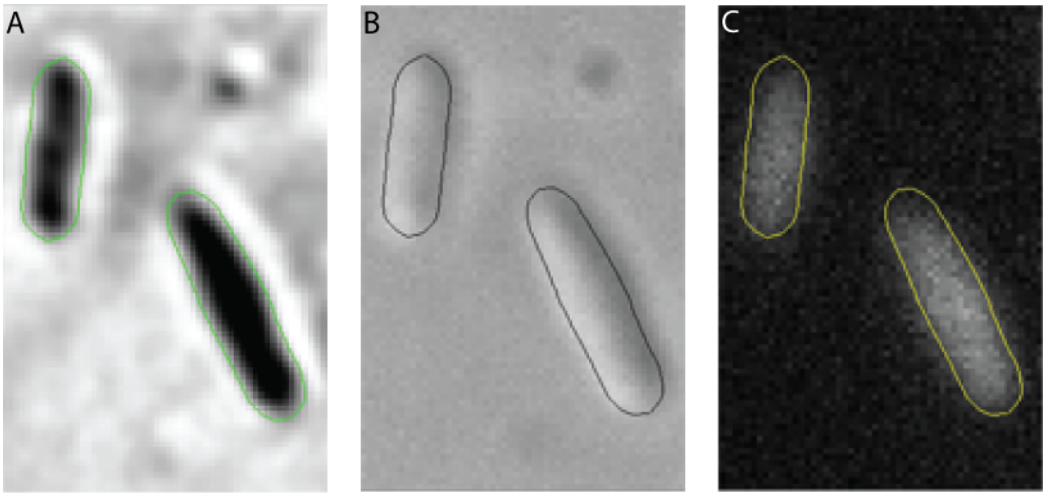

Figure 3.9: MicrobeTracker segmentation of a processed DIC image. **A:** The processed DIC image with the MicrobeTracker defined cell outline shown in green. **B:** The original DIC image overlaid with the cell outline defined from the processed image in black. **C:** The fluorescent image of a labelled protein occupying the entire cytoplasmic volume overlaid with the cell outline defined from the processed image in yellow. In both cases the cell outline defined from the processed DIC is seen to be a good fit for the cell body.

Chapter 4

Cluster Numbers and Positioning

In order to validate the analysis method described in 3.6 a number of strains were chosen for analysis, specifically a strain with *tlpT* tagged with *yfp* (JPA1558) and the same genotype with *ppfA* deleted. This allowed the results produced to be compared against results from previous studies, and were also directly relevant to this study. Further results produced in this study using this approach could therefore be directly compared to that of these strains.

4.1 *tlpT -yfp*

Images of cells containing *tlpT -yfp* expressed from the native promoter from the chromosome (JPA1558) were acquired. The DIC component of these images was then processes and segmented as described in 3.6. The segmentation produced cell outlines with a mean length of 2.2 μm and a standard deviation of 0.5 μm , this is similar to previously produced data (David Wilkinson, unpublished data), and suggesting that the cell outlines produced by MicrobeTracker following the Hilbert transformation and additional processing steps accurately describe *R. sphaeroides* cells.

The segmented images were then subjected to MicrobeTracker's spot finding algorithm. These results were then analysed to determine the percentages of cells within the population with different numbers of clusters. The results of this analysis are shown in fig. 4.1. They show that 7% of cells contain no visible cluster, 78% contain one, 14% two and 1% three. A comparison of this data with previously published data is shown in table 4.1.

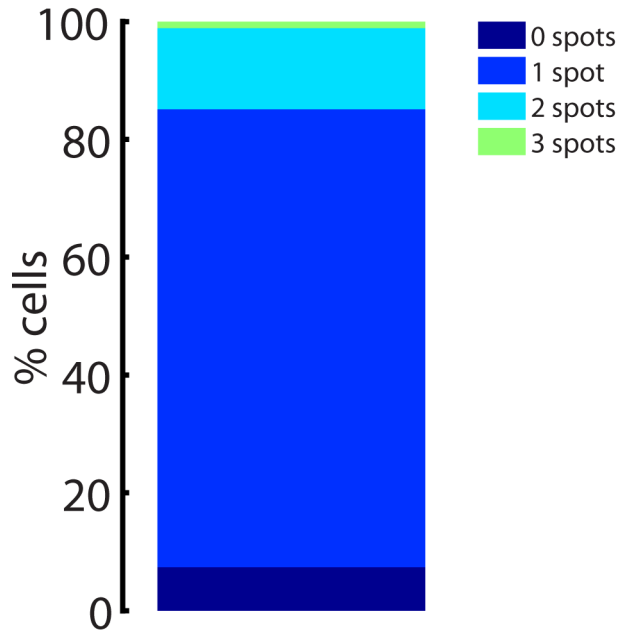

Figure 4.1: Percent of *tlpT -yfp* cells with 0, 1, 2, and 3 clusters. 7% are seen with 0 clusters, 78% are seen with 1, 14% with 2, and 1% with three. 1517 cells were analysed. Refer to legend for colouring.

	Number of clusters			
Data source	0	1	2	3
This study	7%	78%	14%	1%
Thompson *et al.* [185]	0.1%	72%	26.6%	0.7%

Table 4.1: Comparison of cluster numbers in a *tlpT -yfp* strain with previously published data

Whilst not identical these two sets of results are in close agreement, especially regarding the number of cells containing a single cluster. Given the different microscope and updated analysis routines an exact agreement was unlikely.

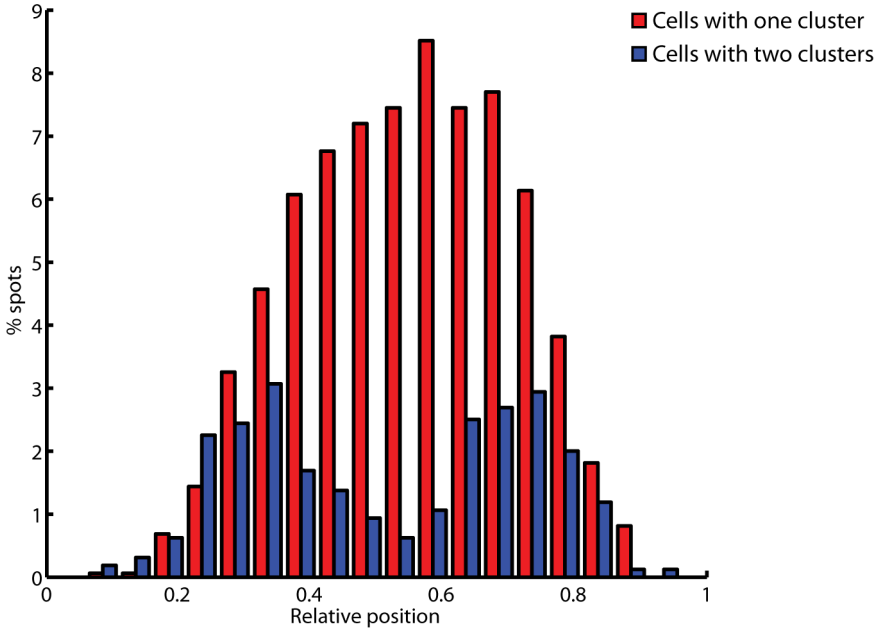

Figure 4.2: The position of clusters within *tlpT -yfp* cells relative to cell length were binned into 20 equally spaced bins between 0 and 1. The number of clusters in each bin was then expressed as a percentage of the total number of cluster across both 1 and 2 cluster populations. The results for clusters in cells with 1 cluster are shown in red, and those in cells with 2 in blue. 1649 clusters were analysed.

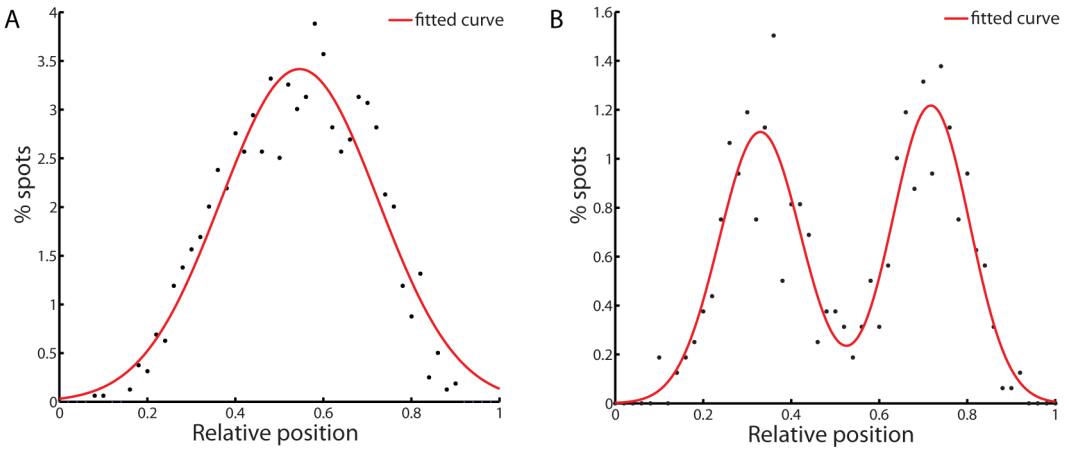

Figure 4.3: **A:** Gaussian fit of the distributions of cluster positions in cells with a single cluster. The peak of the fitted Gaussian is 0.55 and and standard deviation is 0.25. **B:** Gaussian fit with two terms to the distributions of clusters in cells with two clusters. The peaks of the fit are 0.33 and 0.72, both with standard deviations of 0.12

In the cells with detectable clusters, the positions of these clusters were extracted

and calculated relative to cell length. The relative positions were then binned into 20 equally spaced bins. The histograms produced for cells containing one and two clusters are shown in fig. 4.2.

In order to extract quantitative information from the histogram shown in fig. 4.2, Gaussian curves were fitted to the data (fig. 4.3) showing that the mean one cluster position relative to cell length is 0.55 with a standard deviation of 0.25. Fitting a two term Gaussian curve to the two cluster distribution allowed information about each sub-population in the distribution, giving mean positions 0.33 and 0.72, both with standard deviations of 0.12.

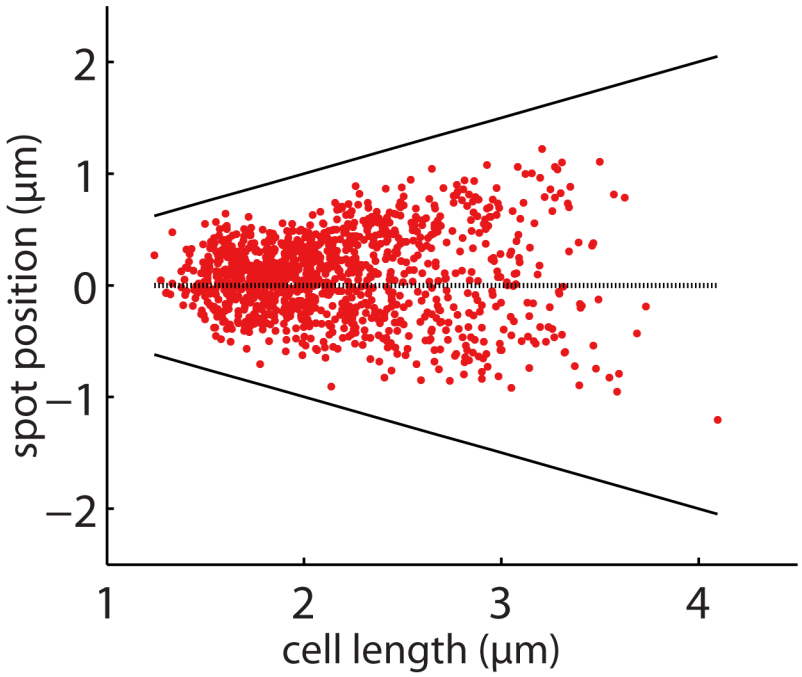

Figure 4.4: Positions of clusters in *tlpT -yfp* cells containing 1 cluster plotted against cell length. Solid lines represent the position of the poles, and the dashed line that of the mid-cell

The position of clusters can be further explored by plotting their positions within the cell against cell length, the resulting plot for one cluster cells is shown in fig. 4.4, and two cluster cells in fig. 4.5. These figures show that there are a greater

number of small cells with one cluster than two, and that in cells with one cluster the cluster can occupy most positions within the cell with exception of the poles. In cells with two clusters it can be seen that the clusters tend to occupy regions around the 1/4 and 3/4 positions of the cell. However some clusters are seen to be positioned around the mid-cell, suggesting that there is not something specific about the mid-cell with repels clusters.

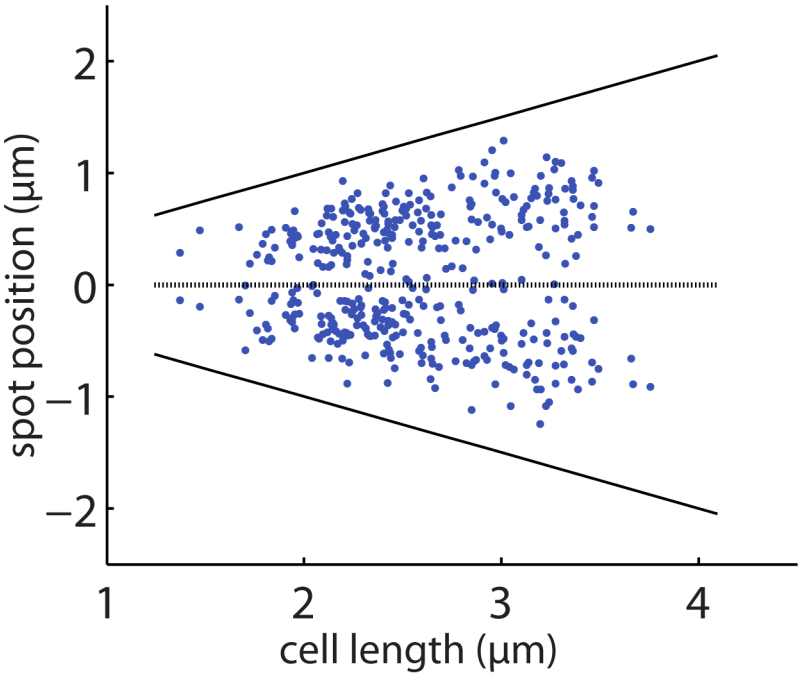

Figure 4.5: Positions of clusters in *tlpT -yfp* cells containing 2 clusters plotted against cell length. Solid lines represent the position of the poles, and the dashed line that of the mid-cell

4.2 Filamentous *tlpT -yfp*

Treating cells with cephalexin (as described in 2.5.1) results in elongated cells. Whilst these cells are unable to divide they do replicate and segregate the cytoplasmic chemosensory cluster, resulting in greater numbers of clusters than in untreated cells. By applying the same analysis as described above, the numbers

of clusters in these cells was determined and is shown in fig. 4.6. These results show that 11% of cells are seen with zero clusters, 19% with one, 40% with two, 19% with three, 9% with four, 2% with five, and 1% with more than five.

The positions of these spots relative to the cell length for clusters in cells with one, two, three and four clusters were calculated. For clarity these results were displayed across two figures, one and two cluster positions are show in fig. 4.7 and those for three and four clusters shown in fig. 4.8. The results for single cluster cells show a distribution about the mid-cell, and those for two clusters show peaks at the mid-cell, 1/4 and 3/4 positions. The distributions of cluster positions in three and four cluster cells show less distinct patterns.

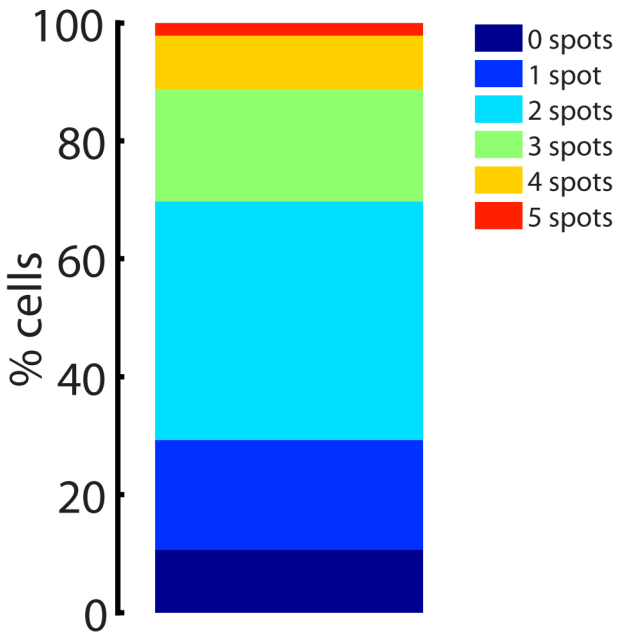

Figure 4.6: Percent of filamentous *tlpT -yfp* cells with 0, 1, 2, 3, 4 and 5 clusters. 11% are seen with 0 clusters, 19% with 1, 40% with 2, 19% with 3, 9% with 4, 2% with 5, and 1% with more than 5. Refer to legend for colouring.

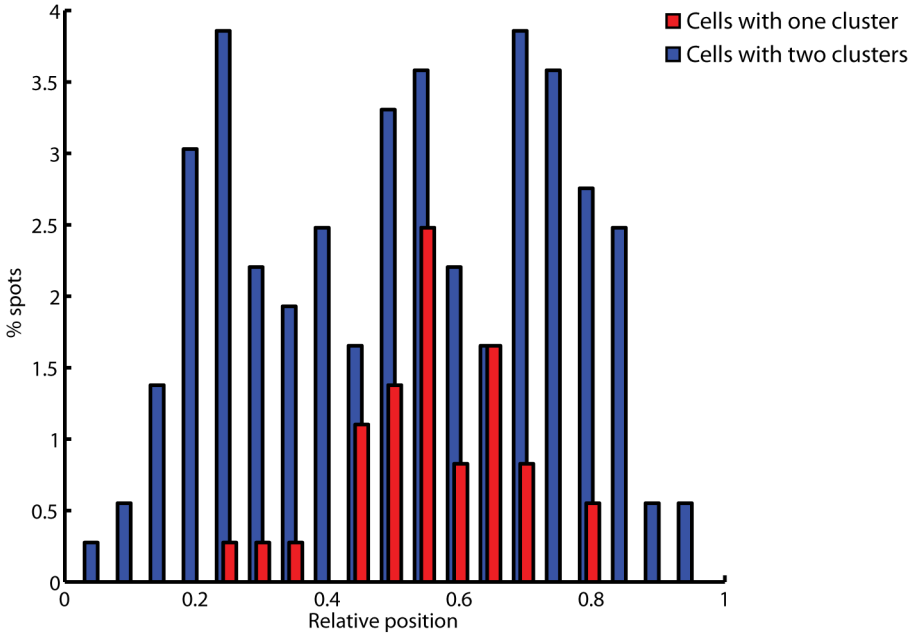

Figure 4.7: The position of clusters within filamentous *tlpT -yfp* cells relative to cell length were binned into 20 equally spaced bins between 0 and 1. The number of clusters in each bin was then expressed as a percentage of the total number of cluster across both 1, 2, 3 and 4 cluster populations. The results for clusters in cells with 1 cluster are shown in red, and those in cells with 2 in blue. 384 clusters were analysed.

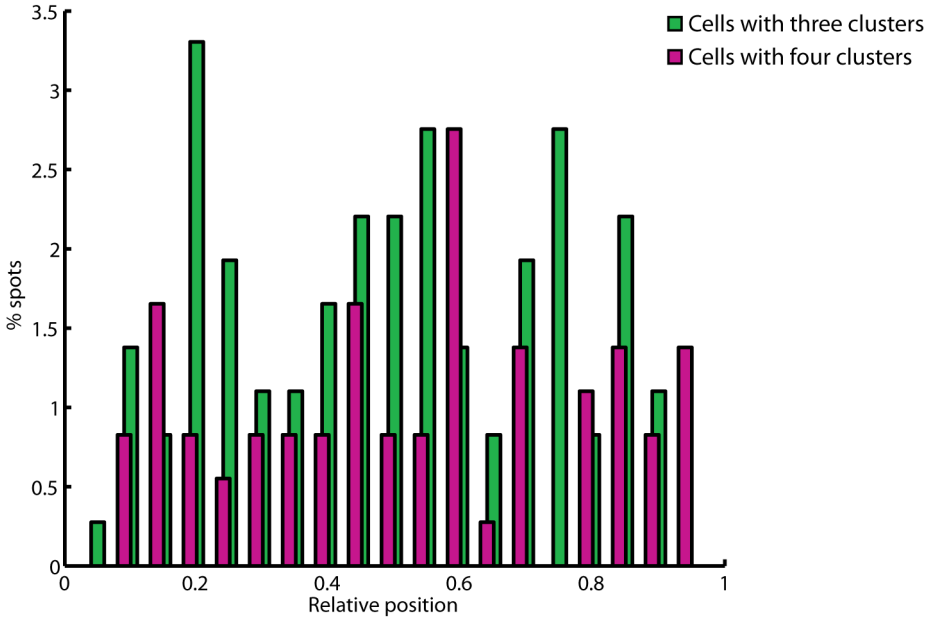

Figure 4.8: The position of clusters within filamentous *tlpT -yfp* cells relative to cell length were binned into 20 equally spaced bins between 0 and 1. The number of clusters in each bin was then expressed as a percentage of the total number of cluster across both 1, 2, 3 and 4 cluster populations. The results for clusters in cells with 3 cluster are shown in green, and those in cells with 4 in magenta. 384 clusters were analysed.

4.3 *tlpT -yfp* Δ*ppfa*

As seen in 1.8.2 deletion of *ppfA* results in the loss of the segregation of the cytoplasmic chemosensory cluster on cell division, resulting in only one daughter cell inheriting a cluster. Therefore at any one time a percentage of the population exists without a cluster, before it is able to form a new one from the continuously expressed chemotaxis proteins. Analysis of the number of clusters in cells with *ppfA* deleted and *tlpT* tagged with *yfp* expressed under native control from the genome (JPA1553), shown in fig. 4.9.

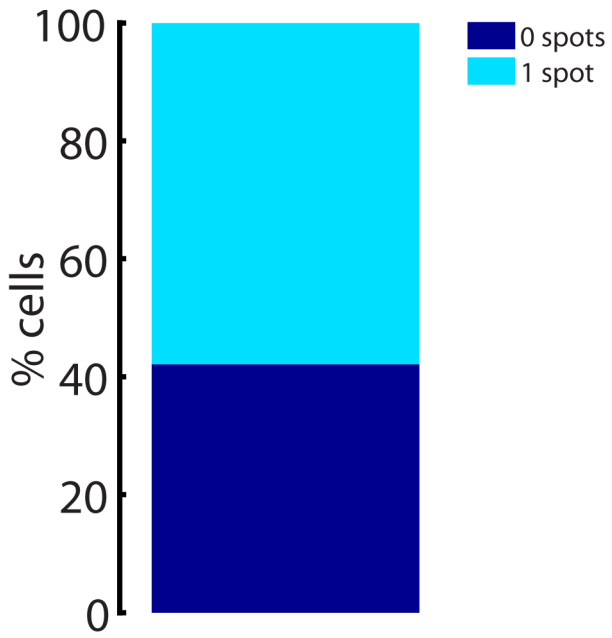

Figure 4.9: Percent of Δ*ppfA tlpT -yfp* cells with 0 and 1 clusters. 42% are seen with 0 clusters,and 58% with 1. 235 cell were analysed. Refer to legend for colouring.

These results show that 42% of cells have no visible cluster, while the remaining 58% have one cluster. No cells are seen with two clusters. These results are compared with those previously published in table 4.2.

	Number of clusters		
Data source	0	1	2
This study	42%	58%	0%
Thompson *et al.* [185]	28%	72%	0%

Table 4.2: Comparison of cluster numbers in aΔ*ppfA tlpT -yfp* strain with previously published data

There are differences in the proportions of cells with zero and one clusters, this is probably due to differences in imaging and analysis. However what is clear across both studies is that no cells with two clusters are ever seen.

Plotting the positions of these clusters relative to cell length (fig. 4.10) produces a distribution that centres on mid-cell, which is similar to that of *tlpT -yfp* cells with single clusters. When this distribution is examined in the context of cell length (fig. 4.11) the only clear pattern that can be observed is that clusters remain away

from the cell poles.

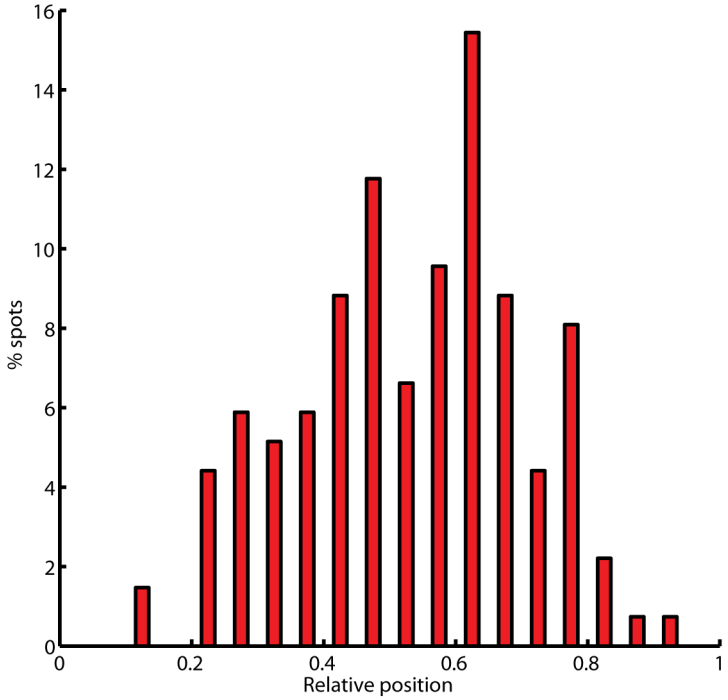

Figure 4.10: The position of clusters within Δ*ppfA tlpT -yfp* cells relative to cell length were binned into 20 equally spaced bins between 0 and 1. The number of clusters in each bin was then expressed as a percentage of the total number of clusters. 136 clusters were analysed.

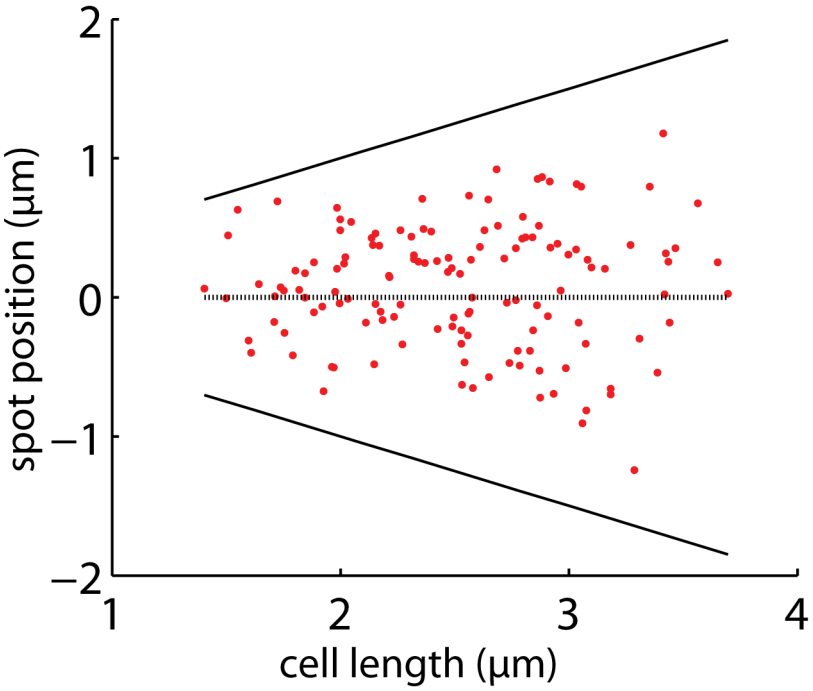

Figure 4.11: Positions of clusters in Δ*ppfA tlpT -yfp* cells plotted against cell length. Solid lines represent the position of the poles, and the dashed line that of the mid-cell

4.4 Filamentous Δ*ppfA tlpT -yfp*

Elongation of cells lacking *ppfA* by cephalexin treatment does not result in the increase in cluster numbers seen in 4.2. Quantitative analysis of the numbers of clusters in cells is shown in fig. 4.12. These results show that, in the absence of *ppfA* , cells are still unable to form more than one cluster irrespective of cell length. There is an increase in the proportion of cells with a single cluster, because after the addition of cephalexin cells will no longer divide, and therefore no new daughter cells, which would lack clusters, will be produced. Those cells lacking clusters at the point of cephalexin addition will be able to form new clusters over time.

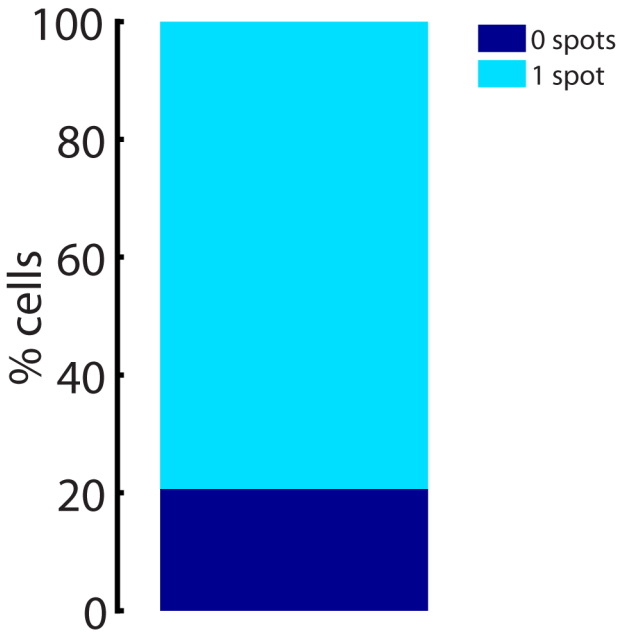

Figure 4.12: Percent of filamentous Δ*ppfA tlpT -yfp* cells with 0 and 1 clusters. 42& are seen with 0 clusters,and 58% with 1. 63 cell were analysed. Refer to legend for colouring.

The relative positions of these clusters are shown in fig. 4.13, the resulting distribution is similar to that of the non-filamentous cells.

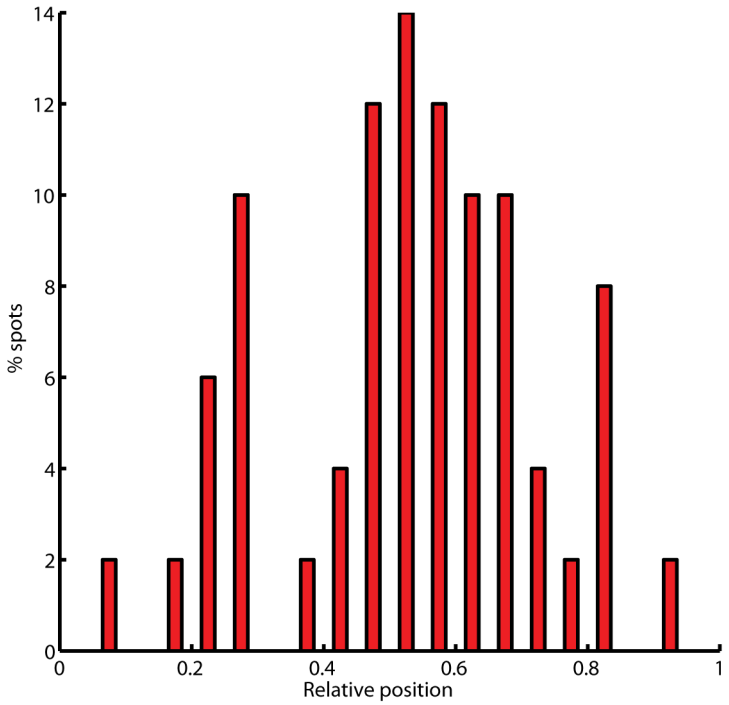

Figure 4.13: The position of clusters within filamentouss Δ*ppfA tlpT -yfp* cells relative to cell length were binned into 20 equally spaced bins between 0 and 1. The number of clusters in each bin was then expressed as a percentage of the total number of clusters. 50 clusters were analysed.

4.5 Inter Cluster Distances

Having extracted the positional information of clusters in *tlpT -yfp* cells, it was possible, by looking at cells with more than one cluster, to investigate the distance between clusters. Inter-cluster distances for non-filamentous cells are shown in fig. 4.14. This shows that as cells increase in length the distances between clusters increases, it also shows an increase in the spread of distances. This suggests that there is not a clear fixed distance between clusters, in absolute distance or relative to cell length, simply that the two cluster are kept apart.

Filamentous *tlpT -yfp* cells with two, three and four clusters were also analysed, the results are shown in fig. 4.15. As with the non-filamentous cells no clear pat-

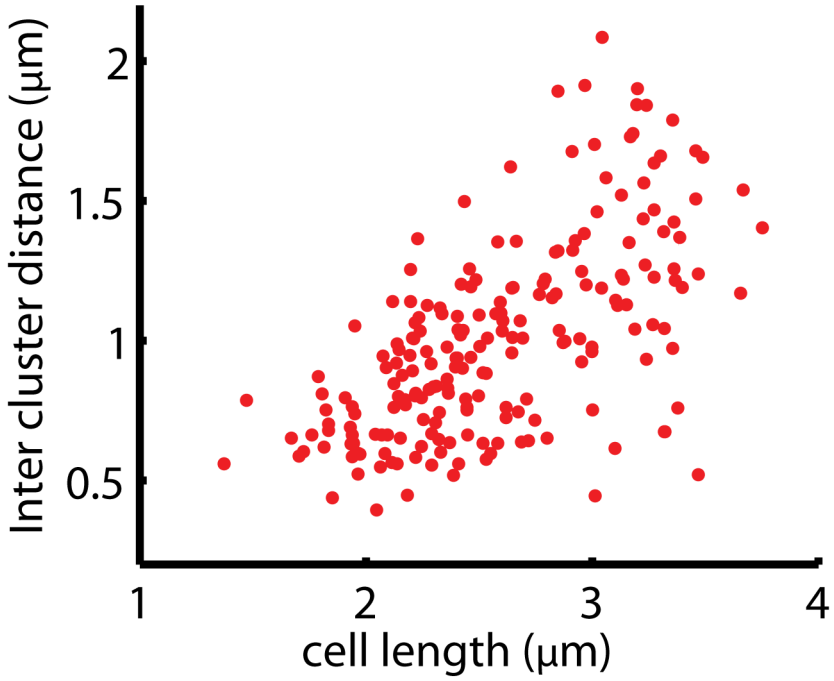

Figure 4.14: Distances between clusters in *tlpT -yfp* cells plotted against cell length.

tern is seen other than that in longer cells clusters are further apart, and that there is a large overlap between the distances between two, three and four clusters. So whilst clusters in a single filamentous cell appear regularly spaced there is not a set spacing between clusters seen across multiple cells.

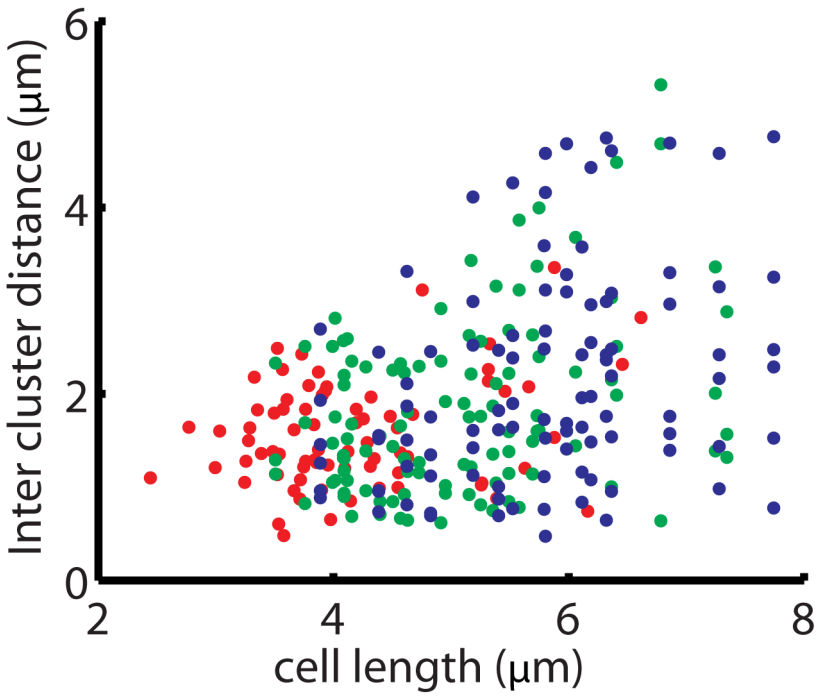

Figure 4.15: Distances between clusters in filamentous *tlpT -yfp* cells plotted against cell length. Distances in cells with two clusters are shown in red, those in cells with three in green, and in cells with four in blue.

4.6 Discussion

Results presented in this chapter show that the combined use of the Hilbert transformation and MicrobeTracker produce segmented images that give cell outline which fall within the range of previously reported results. MicrobeTracker's spot finding algorithm produces results which are comparable to those previously published, validating its use for determining the numbers and positions of the cytoplasmic chemosensory cluster. The analysis of the positioning of clusters in cells with either one or two clusters also closely matches published results, further validating this approach, which is higher throughput than the previous manual approaches used to analyse DIC images of *R. sphaeroides* cells.

Positions of clusters in cells with one cluster are distributed broadly about the mid-cell, however clusters in two cluster cells are positioned around the 0.7 and

0.3 positions (relative to cell length) with narrower distributions. When *ppfA* is deleted cells have no more than a single cluster, with a distribution of positions similar to that of the single cluster cells with *ppfA* .

The use of cephalexin to create elongated cells further highlights the importance of *ppfA* in segregating the cytoplasmic cluster. In filamentous *tlpT -yfp* cells a greater number of clusters are seen when compared to non-filamentous cells. This is because despite the inability of cells to septate, they still undergo successive rounds of replication and segregation of cellular components, including the chromosomes and cytoplasmic chemosensory cluster. However in cells with *ppfA* deleted only a single cluster is formed in filamentous cells showing that the formation of additional clusters is not simply limited spatially. The distributions of cluster positions in filamentous *tlpT -yfp* cells show that in one cluster cells the cluster still tends to position around the mid-cell, and for two cluster cells the most common positions are the mid-cell, $^1/_4$ and $^3/_4$ positions. For three and four cluster cells the distributions produced no clear patterns suggesting there was large variability of both the length of these cells, and the positions of the clusters within them.

To explore the spacing of clusters the distances between clusters was calculated. For non-filamentous *tlpT -yfp* cells the results of this analysis show that there is no fixed distance between the clusters, either in absolute terms or relative to the cell length. A similar result is seen with filamentous cells, albeit with a larger range of distances due to the increase cell lengths. Both these results show a minimum distance between clusters, suggesting that it is important to keep clusters apart but not at a constant distance from each other. This fits with the notion that in order for each daughter cell to inherit a single cluster the clusters need to be positioned either side of the septation site, but it is not important how far on either side they are positioned.

Chapter 5

Cluster Formation

As seen in 1.8.2 Δ*ppfA* strains are unable to segregate the cytoplasmic chemosensory cluster upon cell division. One daughter cell inherits the cluster and the other does not. The cell with no cluster is however able to form a new one *de novo*. This suggests that whilst *ppfA* is required for cluster segregation it is not for cluster formation.

In this chapter investigations into *de novo* cluster formation will be described. Specifically whether new clusters can be formed simply re-expressing core cluster components. The system used to investigate this was the strain JPA1519 (Δ*tlpT yfp-cheW*$_4$) and a plasmid containing *tlpT* under the control of an inducible promoter (pIND4).

Filamentous cells were used to determine the positioning of newly formed clusters, and how this compares to WT positioning of clusters.

In both normal and filamentous cells, the effect of *ppfA* on the formation and positioning of new clusters was investigated using a Δ*tlpT* Δ*ppfA cfp-cheW*$_4$ strain.

5.1 Creation of pIND-*tlpT*

tlpT was amplified from the WS8N genome by PCR using the primers TlpT-F and TlpT-R (see Appendix B for primer sequences). PCR products were purified and their size confirmed by gel electrophoresis. *tlpT* PCR products were then digested with BspHI and HindIII restriction enzymes, and pIND4 digested with NcoI and HindIII (BspHI and NcoI have compatible sticky ends). *tlpT* was inserted into pIND by ligation and the presence of the insert was identified by 5 μl digestion of mini-preps from transformed cells. Those plasmids containing the correct size insert were then sequenced to confirm the insertion of *tlpT* and that the sequence was free from PCR errors.

Once the sequence of the plasmid had been confirmed as correct, the plasmid was transformed into *E. coli* S17-1λ*pir* cells, which were then used to conjugate the plasmid into the background *R. sphaeroides* strains WS8N (WT), JPA1215 (non-motile), JPA1519 (Δ*tlpT yfp-cheW*$_4$), JPA1331 (Δ*tlpT*) and Δ*tlpT* Δ*ppfA* strains.

5.2 Creation of Δ*tlpT* Δ*ppfA* strains

Testing the effect of *ppfA* on new cluster formation required the creation of strains with both *tlpT* and *ppfA* deleted. As both *tlpT* and *ppfA* genes are adjacent to each other on the genome a single deletion construct was designed to delete both genes in tandem. This was done by amplifying 500 bp regions up and downstream of the *tlpT ppfA* region (using primers PpfATlpT-del-UF, PpfATlpT-del-UR, PpfATlpT-del-DF, PpfATlpT-del-DR, see Appendix B for sequences) and fusing them using overlap extension PCR. This fragment was then cloned into the suicide vector pK18*mobsacB* . 5 μl digests were used to confirm presence of insert, and sequencing to confirm correct DNA sequence. The plasmid was then transformed into *E. coli* S17-1λ*pir* cells, which were then used to conjugate the plasmid

into the background *R. sphaeroides* strains WS8N and JPA1456 (*cfp-cheW*$_4$).

pK18*mobsacB* : Δ*tlpT* Δ*ppfA* was then used to delete the two genes through two rounds of recombination (detailed in 2.3.13). The deletion was confirmed by PCR screen using primers (see Appendix B for primer sequences) binding outside the cloning region.

5.3 Re-expression of *tlpT* on swim plates

Swim plate assays were carried out to determine whether expression of *tlpT* from a plasmid would restore chemotactic ability. Swim plates were created as described in 2.4.1, with the addition of varying amounts of IPTG. IPTG concentrations of 0 μM , 10 μM , 50 μM , and 100 μM were used.

To ensure that any restored chemotactic ability was due solely to the re-expression of *tlpT* a number of controls were used. JPA1215 is a non-motile strain, JPA1331 (Δ*tlpT*) is non-chemotactic, all strains were tested with 0 μM IPTG, and with empty pIND4 rather than pIND-*tlpT* at all IPTG concentrations. A representative swim plate is shown in fig. 5.1.

The results of the swim plate assays are shown in fig. 5.2. These results show that the expression of *tlpT* from plasmid in Δ*tlpT* strains results in the restoration of chemotaxis. JPA1331 pIND-*tlpT* shows levels of chemotaxis just above that of WS8N at IPTG concentrations of 50 μM and 100 μM . This result is mirrored by JPA1519 (Δ*tlpT yfp-cheW*$_4$) pIND-*tlpT* , showing that the YFP tag on CheW$_4$ does not effect chemotactic ability. The Δ*tlpT* Δ*ppfA* strain shows near WT levels of chemotaxis at 50 μM , and levels just above it at 100 μM . The Δ*tlpT* Δ*ppfA* *cfp-cheW*$_4$ strain shows near WT levels at both 50 μM and 100 μM , showing that both the absence of *ppfA* and the CFP on CheW$_4$ have no significant effect on chemotaxis. All four of the above strains showed no response to all IPTG concen-

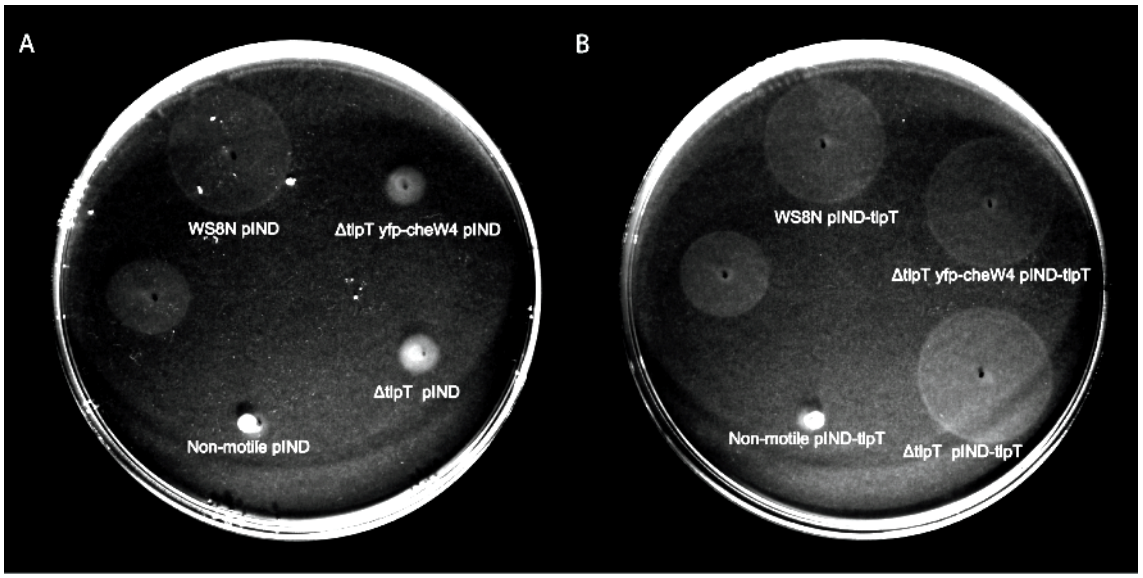

Figure 5.1: **A:** A representative swim plate with 50 μM IPTG showing WS8N, Δ*tlpT yfp-cheW*$_4$ (JPA1519), Δ*tlpT* (JPA1331) and the non-motile control (JPA1215) all containing pIND4 .**B:** A representative swim plate with 50 μM IPTG showing WS8N, Δ*tlpT yfp-cheW*$_4$ (JPA1519), Δ*tlpT* (JPA1331) and the non-motile control (JPA1215) all containing pIND-*tlpT* . These plates show that when in the presence of IPTG but only empty plasmid both JPA1519 and JPA1331 remain non-motile. However when these strains contain pIND-*tlpT* and are in the presence of IPTG their chemotactic ability is restored to that of WT. They also show that the expression of *tlpT* has no effect on the non-motile control or WS8N.

trations when they contained empty pIND4, and the non-motile control (JPA1215) showed no response irrespective of whether it contained pIND4 or pIND-*tlpT*.

In all the responding strains the results for 50 μM and 100 μM were either not significantly different or 50 μM gave results closer to WT. In light of this it was decided to use 50 μM IPTG to test whether re-expression of *tlpT* is able to form cytoplasmic chemosensory clusters *de novo*.

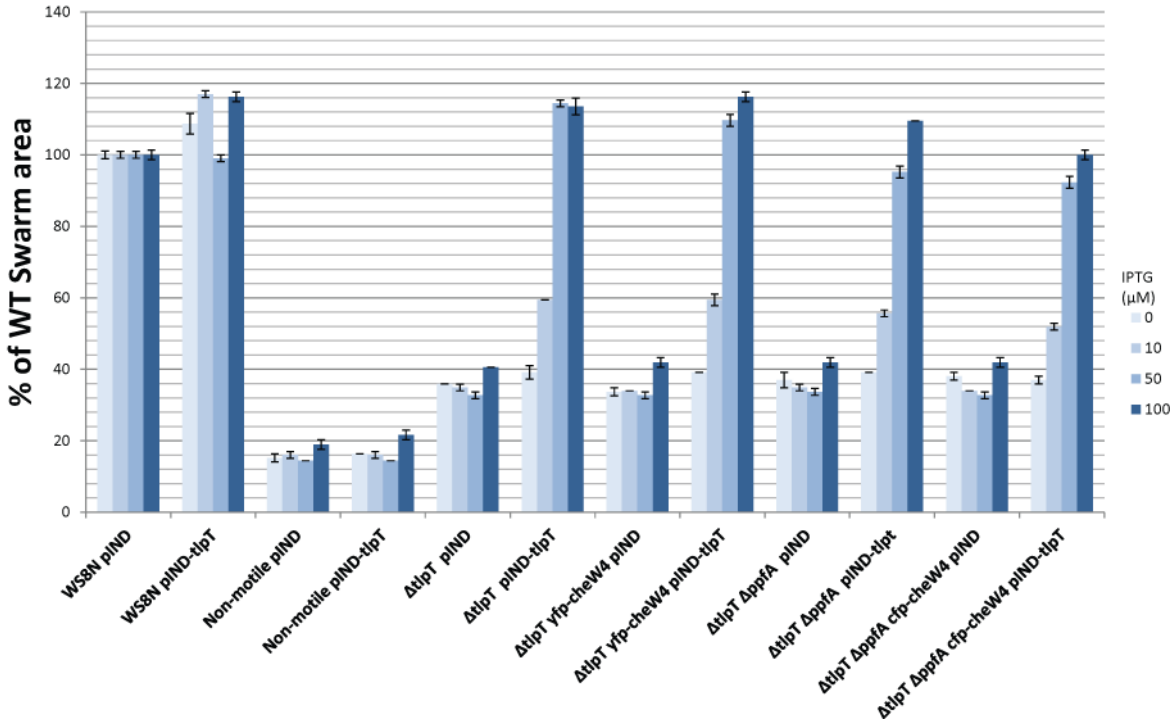

Figure 5.2: The effect of IPTG concentration on chemotactic ability in combination with either pIND4 or pIND-*tlpT* . Increasing IPTG concentrations show increasing chemotactic ability in all the strains lacking *tlpT* . None of the strains containing pIND4 respond to IPTG across all concentrations. The non-motile strain is also non-responsive to IPTG, both with pIND4 and pIND-*tlpT* . Results are the average of three swim plate experiments, and error bars represent standard error.

5.4 Cluster formation through re-expression of *tlpT*

In order to investigate whether the re-expression of *tlpT* would result in *de novo* cytoplasmic cluster formation, cells were immobilised in tunnel slides as described in 2.5.2. With a final wash with succinate media containing 50 μM IPTG. The ends of the tunnel were then sealed and the slide immediately placed on the microscope to be imaged. The final wash also contained 25 μM kanamycin to ensure the retention of the plasmid.

Once on the microscope both DIC and fluorescent images were captured every 5 minutes for 3 hours.

5.4.1 Re-expression of *tlpT* Results in Cluster Formation

Re-expressing *tlpT* in Δ*tlpT yfp-cheW*$_4$ background (JPA1519) results in the shift in YFP-CheW$_4$ from diffuse to clustered. The fluorescent signal from a cell following IPTG addition can be seen in fig. 5.3. Cluster formation happens rapidly after *tlpT* induction, with changes in YFP-CheW$_4$ distribution visible within 5 minutes, and discrete clusters visible from 15 minutes.

This results shows that TlpT is able to bring together the other cytoplasmic cluster components and form clusters *de novo*.

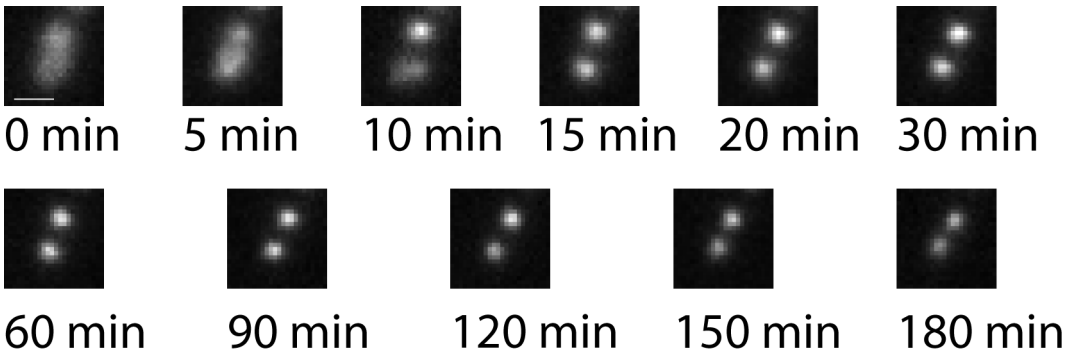

Figure 5.3: Fluorescent images of JPA1519 (Δ*tlpT yfp-cheW*$_4$) pIND-*tlpT* with 50 μM IPTG. Following the addition of IPTG the distribution of YFP-CheW$_4$ goes from diffuse throughout the cell to two discrete clusters. Time is from addition of IPTG. Scale bar is 1 μm .

In order to quantify these results images from the time course were analysed using MicrobeTracker (as described in 3.6). Cells were then further analysed using MicrobeTracker's spot detection algorithm to determine the number of spots within each cell. The cells at each time point were then binned depending on the number of spots. The percentage of cells with 0, 1 and 2 spots at each time point was then plotted. The resultant plot for JPA1519 pIND-*tlpT* with 50 μM IPTG is shown in fig. 5.4.

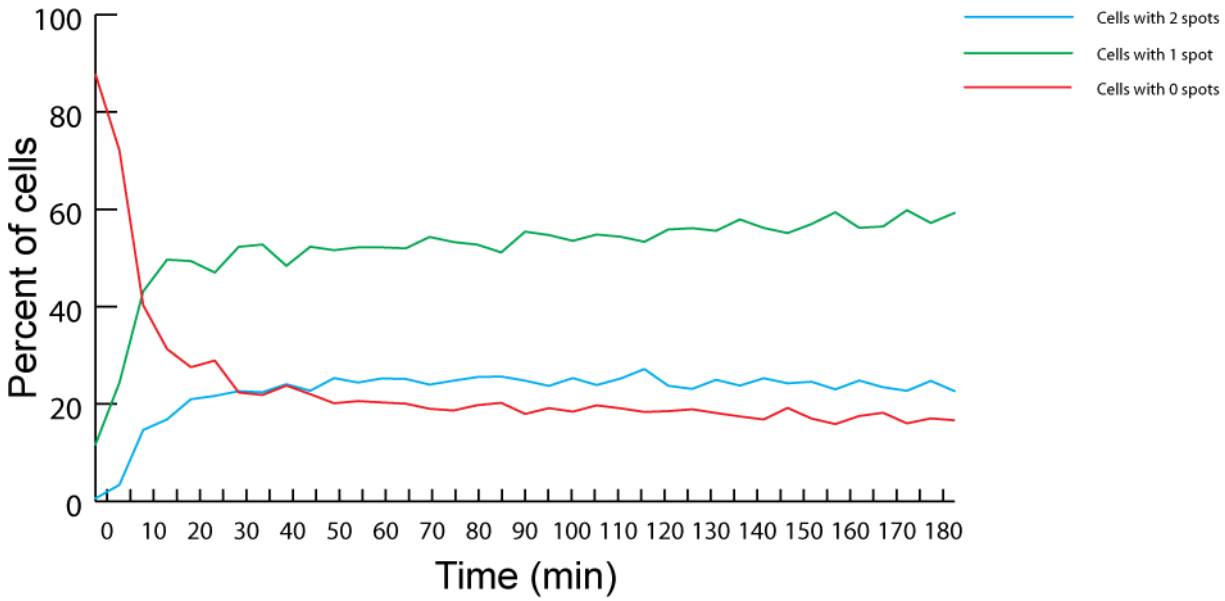

Figure 5.4: Expression of *tlpT* results in cluster formation. The number of cells containing 0 spots is shown in red, cells containing 1 spot in green and cells containing two spots in blue. Following the addition of IPTG the number of cells with 0 spots decreases, while the number containing 1 and 2 increases, showing that the expression of *tlpT* results in the clustering of YFP-CheW$_4$. The x axis represents time after induction with IPTG. The average number of cells at each time point is 620 cells.

At 0 minutes 88% of the cells contain no detectable spot, 11.5% contain 1 and 0.5% contain 2. By the end of the time course (180 minutes post induction) 17% of cells contain 0 spots, 60% contain 1 spot, and 23% contain 2. This shows that across a population of cells the reintroduction of TlpT is able to cause cluster formation in the majority of cells, and results in either one or two clusters within cells.

The results show that within 15 minutes of induction there is a rapid drop in the number of cells with 0 spots, and an increase in those with 1 and 2. The increase in the number of cells with 2 spots is slower than that for cells with 1. This may be due to that in cells forming 2 clusters one becomes more distinct first and therefore is called as a cell with 1 cluster by the analysis and only when the second cluster becomes clear is it identified as a 2 cluster cell. It may also be possible that the clusters take longer to form when the newly expressed TlpT protein is split into two clusters rather than one.

By 50 minutes the percentage of cells in each category has stabilised with a slight upward trend remaining in 1 spot cells, and a slight downward trend in 0 spot cells. This says that there is a limit on the number of cytoplasmic chemosensory clusters within a cell as the continued expression of *tlpT* over the 180 minutes does not result in ever increasing numbers of cluster, or a secondary trend where cells with one cluster form second clusters due to continued *tlpT* expression. This would be seen as a decrease in cells with one cluster and an increase of cells with two after the initial increase in cells with one, this is clearly not seen in the data.

The distribution of WT cells with zero, one and two clusters is 7%, 78% and 14% respectively. Comparing this with the distribution of cell in the final image of the time course (17%, 60% and 23% for cells with zero, one and two clusters respectively) it can be seen that whilst in both instances cells with one cluster are in the majority, the population with newly formed clusters has a greater number of cells with zero and two clusters.

5.4.2 Cluster Formation is Independent of both pIND4 and IPTG

In order to ensure that the formation of *de novo* cytoplasmic clusters was due solely to the re-expression of *tlpT* two controls were tested. The first control was JPA1519 (Δ*tlpT yfp-cheW*$_4$) pIND-*tlpT* with no IPTG added, and the second was JPA1519 pIND4 with 50 μM IPTG added. For both cases no change in the distribution of YFP-CheW$_4$ was seen over time. Thus the cluster formation seen in 5.4.1 is not an artefact due to the presence of pIND4, IPTG or any part of the cell preparation or image acquisition. Fluorescent images for both controls are shown in fig. 5.5.

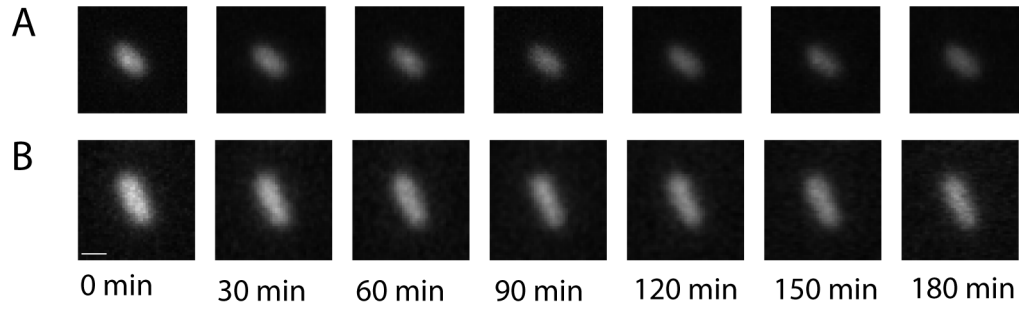

Figure 5.5: **A:** Fluorescent images of JPA1519 (Δ*tlpT yfp-cheW*$_4$) pIND-*tlpT* without the addition of IPTG. **B:** Fluorescent images of 1519 pIND4 following the addition of 50 μM IPTG. Both cases show no change in the cellular distribution of YFP-Wiv . Scale bar is 1 μm .

By calculating the percentage of cells with zero and one spots over time for JPA1519 (Δ*tlpT yfp-cheW*$_4$) pIND following the addition of 50 μM IPTG, as shown in fig. 5.7, it can be seen that not only is there no change in the distribution of cells over time, but also virtually all the cells have no distinct spots.

Applying the same treatment to JPA1519 (Δ*tlpT yfp-cheW*$_4$) cells with pIND-*tlpT* but no IPTG also shows no change in the distribution of cells over time. However it does show that even in the absence of IPTG there is a basal level of cluster formation in these cells, as over time approximately 12% of cells have a single detectable spot. This value matches the percentage of cells with one spot at the 0 minute time point following the addition of IPTG to JPA1519 pIND-*tlpT* (11.5%). The fact that this level of cells with spots is seen throughout the zero IPTG experiment, and at the start of the experiment with IPTG, but not in the experiment with empty pIND4 suggests that these spots are due to some leak in the expression of pIND-*tlpT* and not due an artefact in the analysis of the images.

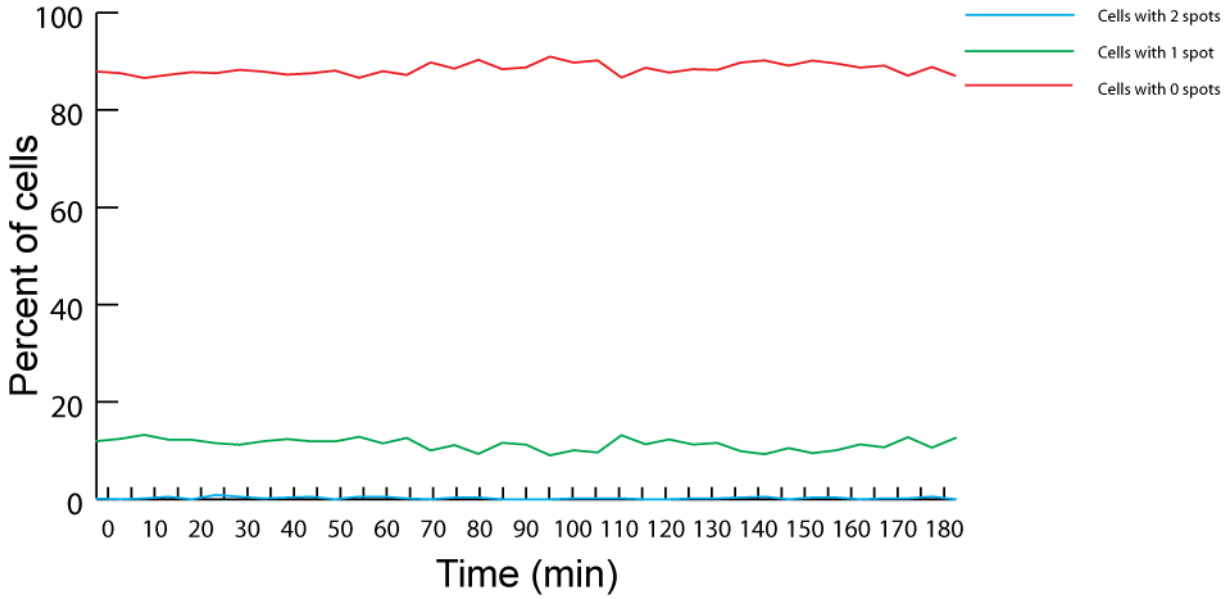

Figure 5.6: In the absence of IPTG the number of JPA1519 (Δ*tlpT yfp-che*W_4) pIND-*tlpT* cells containing clusters does not change over time. The average number of cells at each time point is 567 cells.

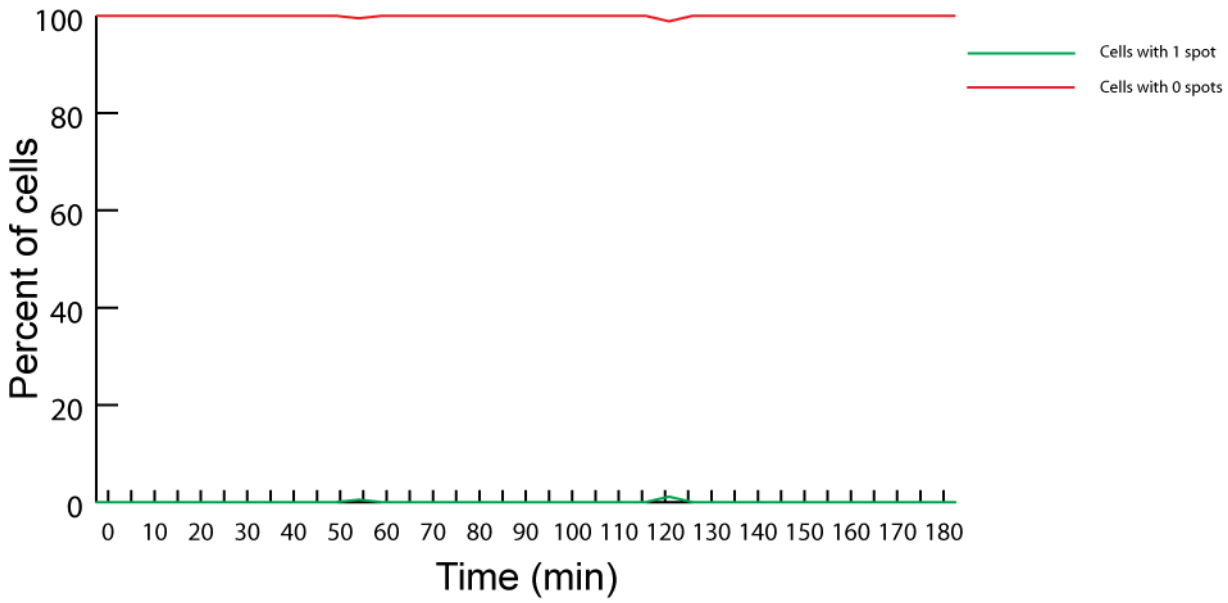

Figure 5.7: In the presence of 50 μM IPTG JPA1519 (Δ*tlpT yfp-che*W_4) cells containing empty pIND4 there is no change over time in the number of cells containing zero detectable spots. The average number of cells at each time point is 187 cells.

5.4.3 Re-expression in Δ*tlpT yfp-cheW*$_4$ filamentous cells

Investigating the positioning and spacing of these newly formed clusters is limited by the small size of *R. sphaeroides* cells. Therefore cells were treated with cephalexin (as described in 2.5.1) prior to being immobilised on slides and *tlpT* expression induced.

Fluorescent images of a filamentous JPA1519 (Δ*tlpT yfp-cheW*$_4$) pIND-*tlpT* cell following expression of *tlpT* is shown in fig. 5.8. As with the non-filamentous case the cell starts with a diffuse distribution of YFP-CheW$_4$ throughout the cell, and subsequently distinct spots are seen to form over time. What is especially striking in these images is that many more clusters are able to form in these filamentous cells compared to normal cells.

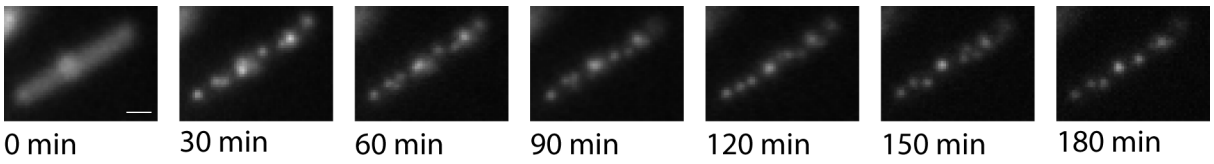

Figure 5.8: Fluorescent images of filamentous JPA1519 (Δ*tlpT yfp-cheW*$_4$) pIND-*tlpT* with 50 μM IPTG. Following the addition of IPTG the distribution of YFP-CheW$_4$ goes from diffuse throughout the cell to multiple discrete clusters. Time is from addition of IPTG. Scale bar is 1 μm .

Analysing a population of cells, shown in fig. 5.9, it can be seen that as with non-filamentous cells the number of cells not containing a cluster rapidly decreases following IPTG addition. However at the 0 minute time point there is a higher percentage of cells with a single cluster than in the non-filamentous cells. Within the first thirty minutes this value decreases slightly. This is due to the fact that many of the cells which begin with a visible cluster will form many more once *tlpT* has been expressed. The loss in cells with one cluster is countered by the loss of cells with none which will result in cells which previously had no clusters now having one or more, thus the net result is a small decrease in the percentage of cells with one cluster. The number of cells with two and three clusters shows

increases at a rate similar to that of the number of cells with two clusters in non-filamentous cells (fig. 5.4). The increase in number of cells with four and five clusters is similar, both being slower than that of cells containing two or three.

Like the non-filamentous cells by 50 minutes the number of cells in each category has stabilised, suggesting that as with the non-filamentous cells there is a maximum number of clusters which are able to produced by the expression of *tlpT*

.

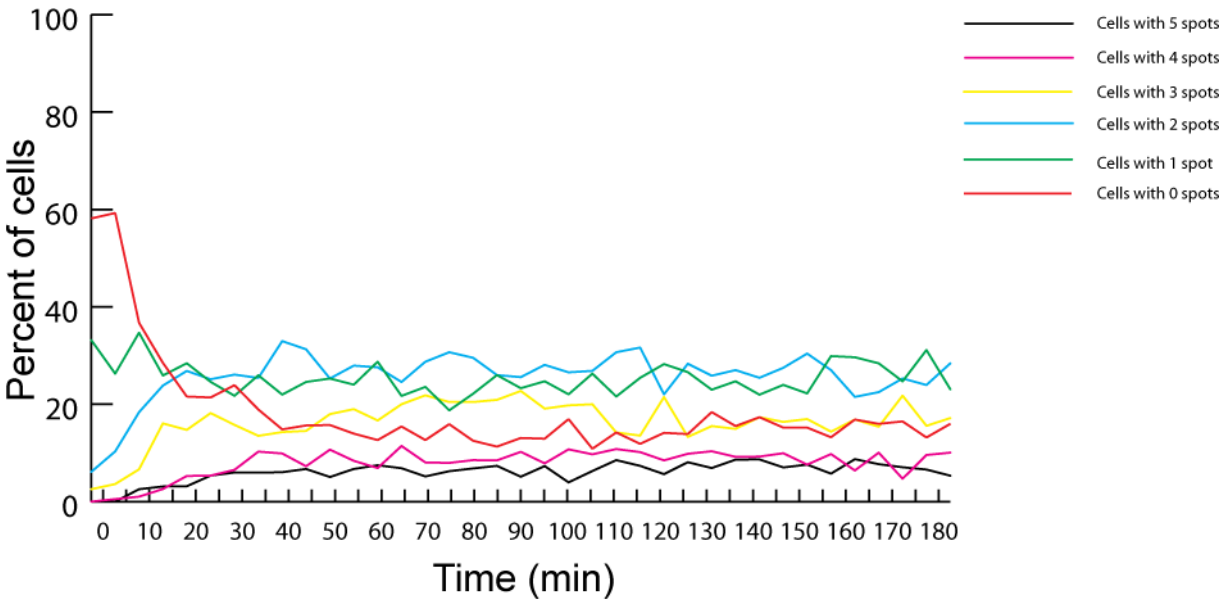

Figure 5.9: The number of cells containing 0 spots is shown in red, 1 in green, 2 in blue, 3 in yellow, 4 in magenta, and 5 in black. Following the addition of IPTG the number of cells with 0 spots decreases, while the number containing 2, 3, 4 and 5 increases. The number of cells containing 1 spot starts at 33% and decreases slightly in the first 30 mins. The x axis represents time after induction with IPTG. The average number of cells at each time point is 178 cells

The greater proportion of cells with one cluster at the start of the time course may be due to the greater number of plasmids within cells due to plasmid replication and lack of cell division. Given that leak from pIND-*tlpT* in non-filamentous cell results in cluster formation in 12% of cells in the absence of IPTG, then it is plausible that in cells which have undergone several rounds of plasmid duplication the combined leak of *tlpT* expression could result in the 33% of cells which possess

one cluster at the start of the time course.

A comparison of the proportion of cells with different numbers of clusters from populations of filamentous JPA1457 (YFP-CheW$_4$) and filamentous JPA1519 (Δ*tlpT yfp-cheW*$_4$) pIND-*tlpT* 50 μM IPTG at the end of the time course is shown in table 5.1. This shows that as with the non-filamentous cells there is a greater proportion with no clusters when compared to WT. There is also a general skew of proportions towards lower numbers of cluster compared to WT.

Number of clusters	JPA1457	JPA1519 pIND-*tlpT* 50 μM IPTG
0	0%	12%
1	5%	23%
2	16%	28%
3	36%	17%
4	29%	10%
5	13%	6%
6	1%	0%

Table 5.1: Comparison of the percentage of cells with 0 to 6 clusters in filamentous JPA1457 and JPA1519 (Δ*tlpT yfp-cheW*$_4$) pIND-*tlpT* treated with 50 μM IPTG.

5.4.4 Re-expression in Δ*tlpT* Δ*ppfA cfp-cheW*$_4$ background

This approach was extended to investigate the re-expression of *tlpT* in cells lacking both *tlpT* and *ppfA* , to identify whether PpfA might influence the formation of new clusters despite it not being required for formation.

As expected the expression of *tlpT* in this double deletion strain does result in the formation of clusters, fluorescent images are shown in fig. 5.10.

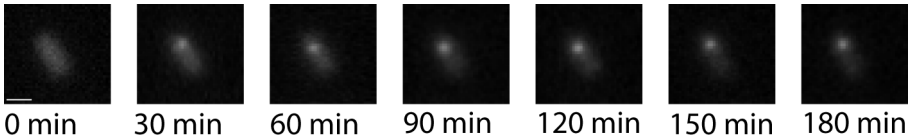

Figure 5.10: Fluorescent images of Δ*tlpT* Δ*ppfA cfp-cheW*$_4$ pIND-*tlpT* with 50 μM IPTG. Following the addition of IPTG the distribution of CFP-CheW$_4$ goes from diffuse throughout the cell to a single discrete cluster. Time is from addition of IPTG. Scale bar is 1 μm .

Looking at the percentage of cells with zero, one and two clusters over time following IPTG addition, shown in fig. 5.11, there are several clear differences when compared to that of JPA1519 (Δ*tlpT yfp-cheW*$_4$) pIND-*tlpT* (fig. 5.4).

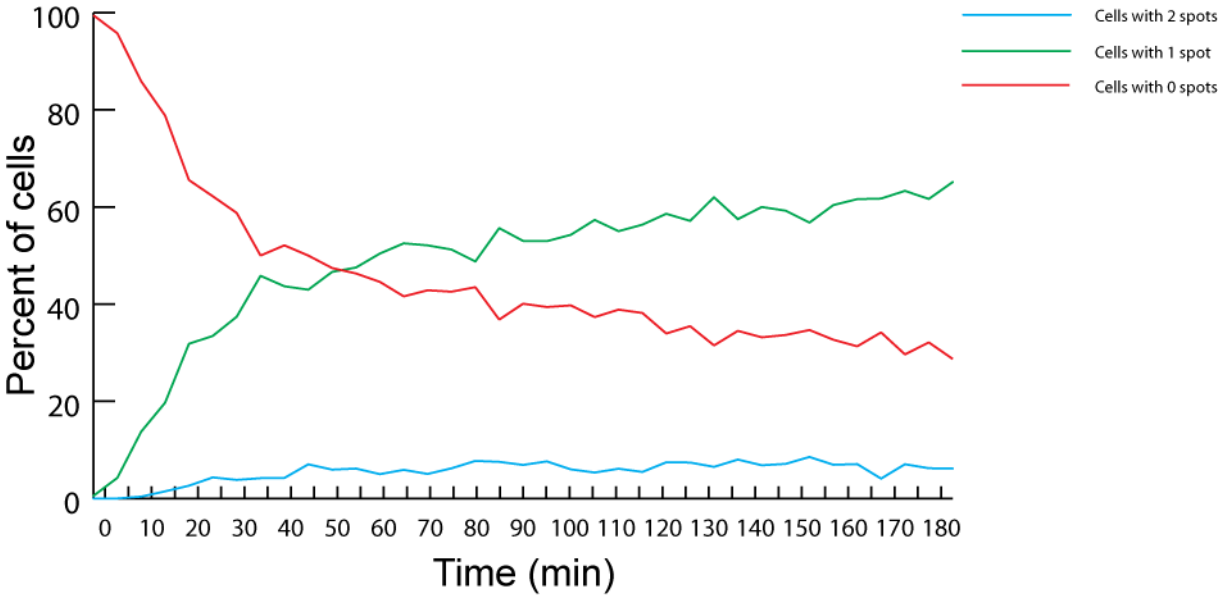

Figure 5.11: Expression of *tlpT* results in cluster formation in the absence of *ppfA* . The number of cells containing 0 spots is shown in red, cells containing 1 spot in green and cells containing two spots in blue. Following the addition of IPTG the number of cells with 0 spots decreases, while the number containing 1 and 2 increases. The x axis represents time after induction with IPTG. The average number of cells at each time point is 235 cells.

Firstly the decrease in the number of cells with no clusters, and corresponding increase in cells with one cluster is much slower than in JPA1519 (Δ*tlpT yfp-cheW*$_4$). So slow in fact that by the end of the time course (180 minutes) the number of cells in each category has yet to stabilise, compared to the 50 minutes needed in JPA1519. Secondly the distribution of cells at the end of the time course is different. Similar numbers of cells have one cluster (65% and 60% for Δ*tlpT* Δ*ppfA cfp-cheW*$_4$ and JPA1519 respectively), however in the absence of *ppfA* only 6% of cells are able to form two clusters. As a result of this there are more cells with no clusters (28% compared to 17%).

Also striking is that unlike JPA1519 (Δ*tlpT yfp-cheW*$_4$) at the beginning of the time

course none of the cells have any clusters. This is also seen when analysing a 0 μM IPTG control, shown in fig. 5.12. Virtually all of the cells have no clusters, whereas in JPA1519 (Δ*tlpT yfp-cheW*$_4$) pIND-*tlpT* even in the absence of IPTG $\sim$ 12% of cells have one cluster. Together these two results suggest that PpfA lowers the threshold level of TlpT needed to trigger the self-assembly of the cytoplasmic cluster.

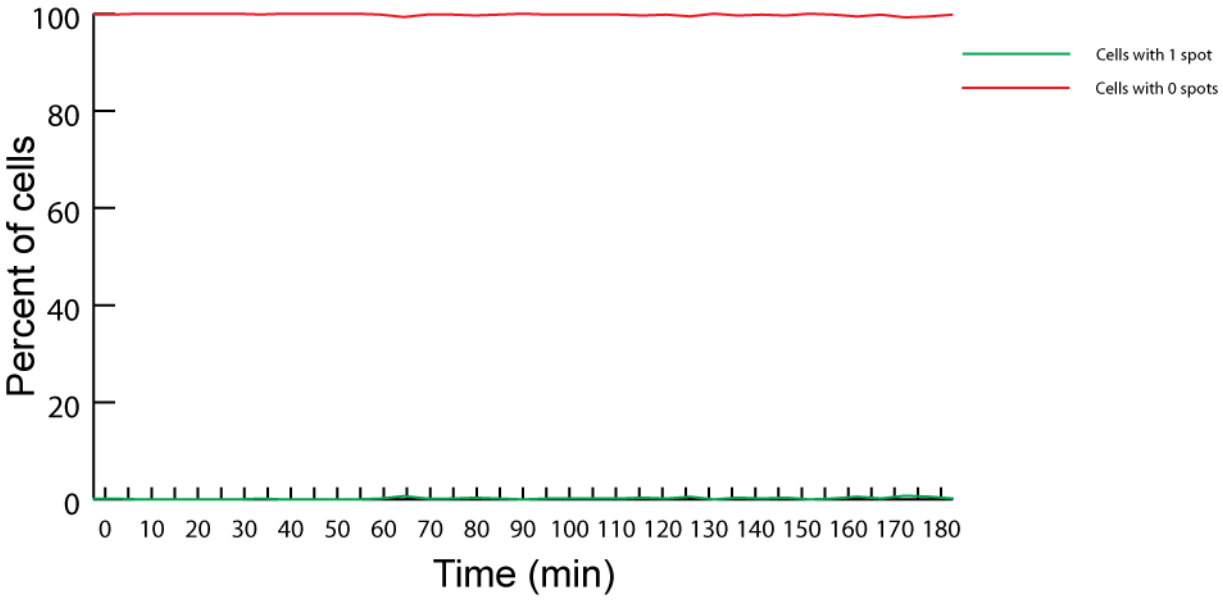

Figure 5.12: Distribution of cells with 0, and 1 clusters in Δ*tlpT* Δ*ppfA cfp-cheW*$_4$ pIND-*tlpT* 0 μm IPTG over time. The red line represents cells with 0 clusters and then green those with 1. The average number of cells at each time point is 577 cells.

5.4.5 Re-expression in Δ*tlpT* Δ*ppfA cfp-cheW*$_4$ filamentous cells

As with JPA1519 (Δ*tlpT yfp-cheW*$_4$) pIND-*tlpT* , cephalexin was used to elongate the cells in order to investigate any effect PpfA has on the positioning and spacing of the newly formed clusters.

Fluorescent images of a cell following IPTG addition is shown in fig. 5.13.

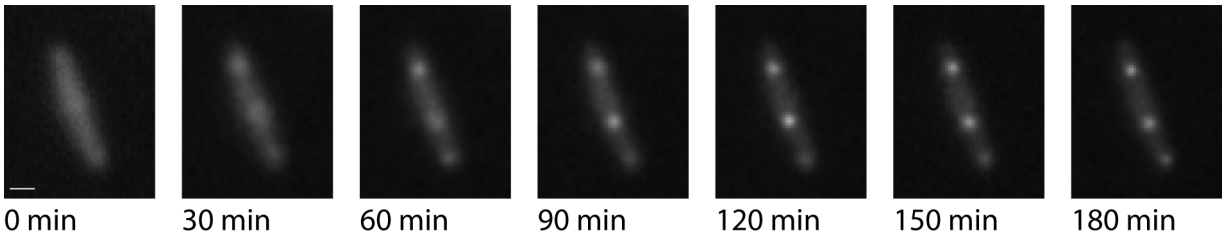

Figure 5.13: Fluorescent images of filamentous Δ*tlpT* Δ*ppfA cfp-cheW*$_4$ pIND-*tlpT* cells with 50 μM IPTG. Following the addition of IPTG the distribution of CFP-CheW$_4$ goes from diffuse throughout the cell to multiple discrete clusters. Time is from addition of IPTG. Scale bar is 1 μm .

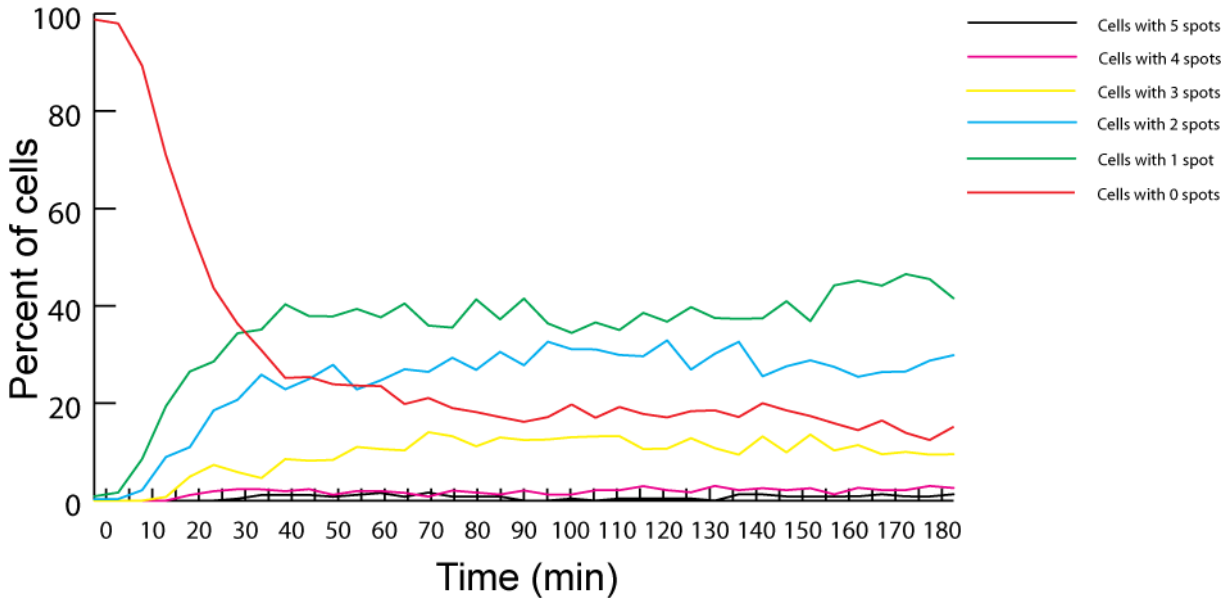

Figure 5.14: The number of cells containing 0 spots is shown in red, 1 in green, 2 in blue, 3 in yellow, 4 in magenta, and 5 in black. Following the addition of IPTG the number of cells with 0 spots decreases, while the number containing 1, 2, 3, 4 and 5 increases. The x axis represents time after induction with IPTG. The average number of cells at each time point is 248 cells

The change in the number of cells with different numbers of clusters following IPTG addition is shown in fig. 5.14. Comparing this to the result obtained expressing *tlpT* in filamentous JPA1519 (Δ*tlpT yfp-cheW*$_4$) cells, it can be seen that by the end of the time course fewer proportions of cells have three, four and five clusters. The percentage of cells from the final image of the time course with different numbers of cluster is shown in table 5.2. This clearly shows that the absence of PpfA results in fewer cells forming larger numbers of clusters.

Interestingly unlike the non-filamentous Δ*tlpT* Δ*ppfA cfp-cheW*$_4$ pIND-*tlpT* the number of cells in each category stabilises, and does so in a time similar to that of both filamentous and non-filamentous JPA1519 (Δ*tlpT yfp-cheW*$_4$) pIND-*tlpT* cells ($\sim$ 50 minutes).

Number of clusters	JPA1519 pIND-*tlpT*	Δ*tlpT* Δ*ppfA cfp-cheW*$_4$ pIND-*tlpT*
0	12%	15%
1	23%	42%
2	28%	30%
3	17%	9%
4	10%	3%
5	6%	1%
6	0%	0%

Table 5.2: Comparison of the percentage of cells with 0 to 6 clusters in filamentous JPA1519 (Δ*tlpT yfp-cheW*$_4$) pIND-*tlpT* and Δ*tlpT* Δ*ppfA cfp-cheW*$_4$ pIND-*tlpT* treated with 50 μM IPTG.

5.5 Positioning of Newly Formed Clusters

Having assessed the number of clusters within cells as a result of re-expression of *tlpT* , the data from these time courses was then analysed to investigate the positioning of these newly formed clusters. The positioning of the new clusters could then be compared to the WT cluster positions. It could also be used to determine whether PpfA has a role in positioning these new clusters. It was also hoped that this would reveal whether the new clusters form first and then are positioned, or if they form at their positions, and what effect PpfA has upon this process.

5.5.1 JPA1519 (Δ*tlpT yfp-cheW*$_4$) pIND-*tlpT*

In order to investigate the positioning and movement of new clusters within individual cells kymographs were created. A kymograph for a JPA1519 (Δ*tlpT yfp-*

cheW$_4$) pIND-*tlpT* cell following expression of *tlpT* (the same cell as in fig. 5.3) is shown in fig. 5.15.

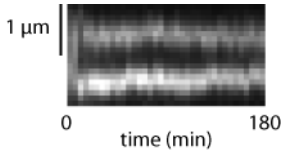

Figure 5.15: Kymograph of cluster formation in JPA1519 (Δ*tlpT yfp-cheW*$_4$) pIND-*tlpT* . Each unit in the x axis is 5 min.

What this kymograph shows is that, as seen 5.4.1, clusters form rapidly. It also shows that once the clusters form they remain positioned. The clusters do not form, and then search for a position.

To assess this across the population cells with zero, one and two clusters were separated. Then within the one and two cluster sub-populations the distribution of cluster positions within cells were determined at each time point. The resulting histograms for JPA1519 (Δ*tlpT yfp-cheW*$_4$) pIND-*tlpT* cells with one cluster and two cluster are shown in fig. 5.16 and fig. 5.17 respectively.

Both these histograms show that once clusters have formed they're positioned with the cell in a manner very similar to that of JPA1558 (*tlpT -yfp*). With cells with one cluster showing a broad distribution centred around midcell, and cells with two clusters showing a distribution with two narrow peaks at one and three quarter positions.

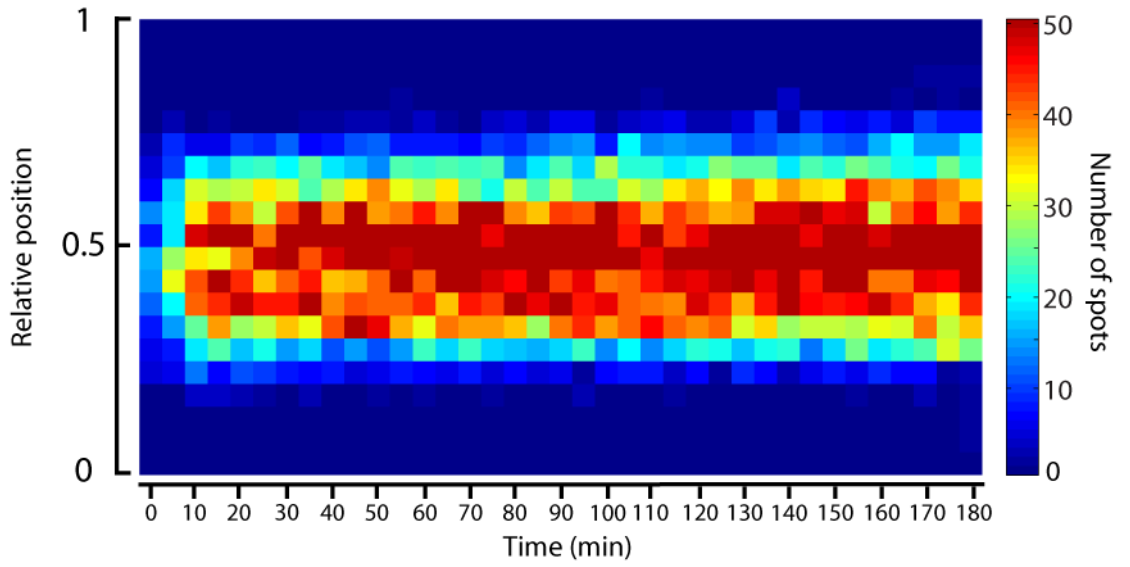

Figure 5.16: Histogram showing positions of clusters in cells with only one cluster following expression of *tlpT* in JPA1519 (Δ*tlpT yfp-cheW*$_4$) pIND-*tlpT* . x axis represents time after IPTG addition, the y axis the position of clusters relative to the cell length. The number of spots at each position is given by the colour scale.

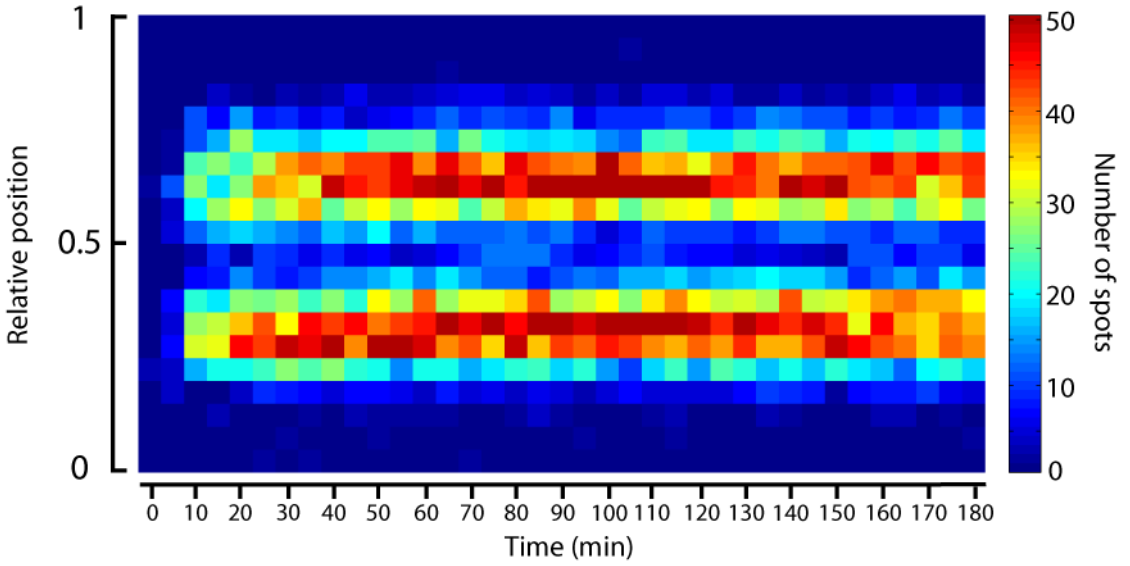

Figure 5.17: Histogram showing positions of clusters in cells with two clusters following expression of *tlpT* in JPA1519 (Δ*tlpT yfp-cheW*$_4$) pIND-*tlpT* . x axis represents time after IPTG addition, the y axis the position of clusters relative to the cell length. The number of spots at each position is given by the colour scale.

These histograms also show that once the cluster is of sufficient size to be detected by this analysis it is positioned. If the clusters formed and then searched for positions the histograms would show broader distributions at early time points,

and tightening as they found positions. Such an effect cannot be seen.

5.5.2 Filamentous JPA1519 pIND-*tlpT*

Kymographs for filamentous JPA1519 (Δ*tlpT yfp-cheW*$_4$) pIND-*tlpT* , an example is shown in fig. 5.18, show results similar to that of the non-filamentous cells, with the obvious exception of having more cluster formed. Clusters are formed rapidly and do so at relatively fixed positions.

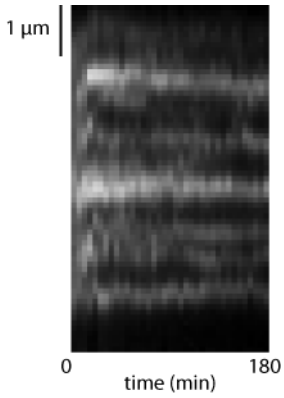

Figure 5.18: Kymograph of cluster formation in filamentous JPA1519 (Δ*tlpT yfp-cheW*$_4$) pIND-*tlpT* . Each unit in the x axis is 5 min.

However one notable difference is seen in fig. 5.18 and fig. 5.8, which is two clusters forming out of a region of semi-diffuse YFP-CheW$_4$. The fact that two smaller clusters form in close proximity suggests that the formation of clusters seen here is not simply stochastic self-assembly based.

5.5.3 JPA1519 (Δ*tlpT yfp-cheW*$_4$) pIND-*tlpT* 0 μM IPTG

In JPA1519 (Δ*tlpT yfp-cheW*$_4$) pIND-*tlpT* cells with no IPTG $\sim$ 12% of cells are identified as having one cluster. The histogram of their positions over time is shown in fig. 5.19. This distribution matches that of the cells with one cluster when IPTG is added, further suggesting that the presence of cells with one cluster

in this population is due to leaky expression of *tlpT* from pIND-*tlpT* rather an artefact introduced by the analysis.

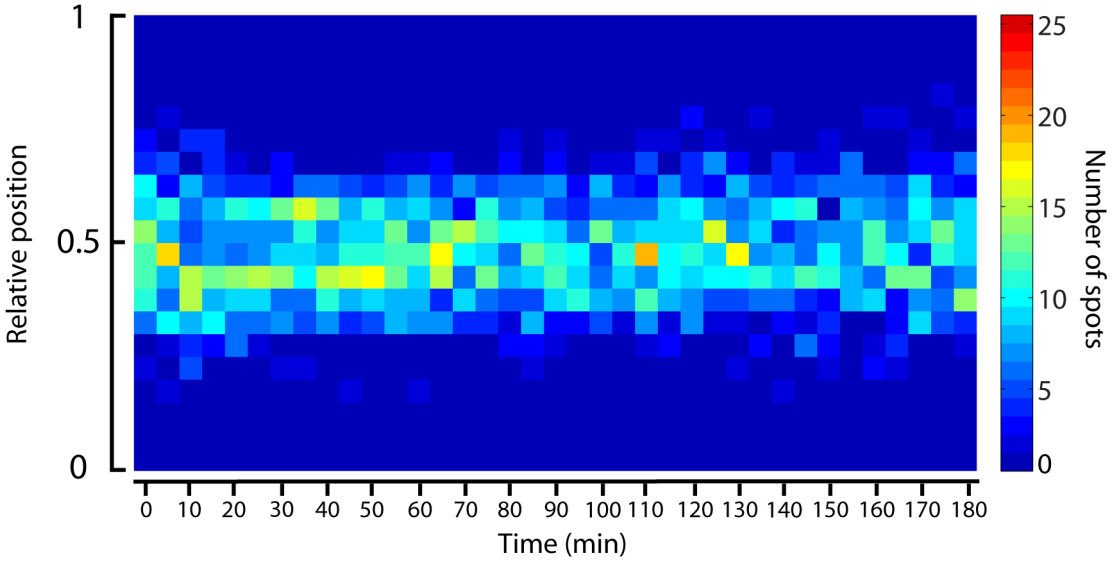

Figure 5.19: Histogram showing positions of single clusters in JPA1519 (Δ*tlpT yfp-cheW*$_4$) pIND-*tlpT* in the absence of IPTG. x axis represents time after IPTG addition, the y axis the position of clusters relative to the cell length. The number of spots at each position is given by the colour scale.

5.5.4 Δ*tlpT* Δ*ppfA cfp-cheW*$_4$ pIND-*tlpT*

A kymograph for a typical Δ*tlpT* Δ*ppfA cfp-cheW*$_4$ pIND-*tlpT* cell is shown in fig. 5.20. As seen with the previous cluster number based analysis the formation of clusters is slower than JPA1519 (Δ*tlpT yfp-cheW*$_4$) pIND-*tlpT* . However like JPA1519 pIND-*tlpT* once the cluster has formed it seems to remain in position.

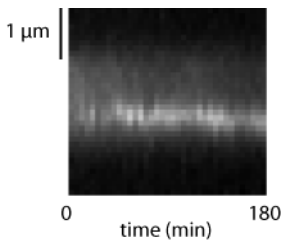

Figure 5.20: Kymograph of cluster formation in Δ*tlpT* Δ*ppfA cfp-cheW*$_4$ pIND-*tlpT* . Each unit in the x axis is 5 min.

The histogram of spot positions in cells with one cluster formed, shown in fig. 5.20 shows a similar distribution to that of JPA1553 (*tlpT -yfp ΔppfA*), centred around midcell and broader than in cells with PpfA.

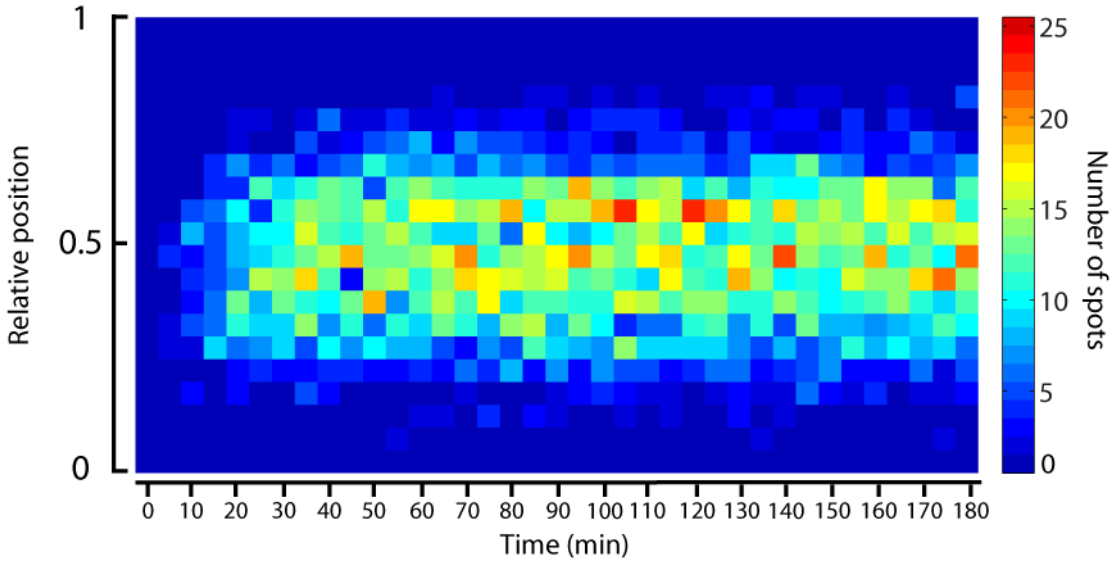

Figure 5.21: Histogram showing positions of clusters in cells with only one cluster following expression of *tlpT* in Δ*tlpT* Δ*ppfA cfp-cheW*$_4$ pIND-*tlpT* . x axis represents time after IPTG addition, the y axis the position of clusters relative to the cell length. The number of spots at each position is given by the colour scale.

Δ*ppfA* cells are never observed with more than a single cluster. Thus it is therefore not possible to compare positions of two clusters between these two strains. However the positioning of two clusters does show similarity to that of JPA1558 (*tlpT -yfp*), two narrow peaks at one and three quarter positions. This shows that in the few cells which can form two clusters, these form at spatially separate points. It also shows that these cells aren't simply cells with one real cluster and a second false positive as that would produce a distribution similar to that of cells with one cluster.

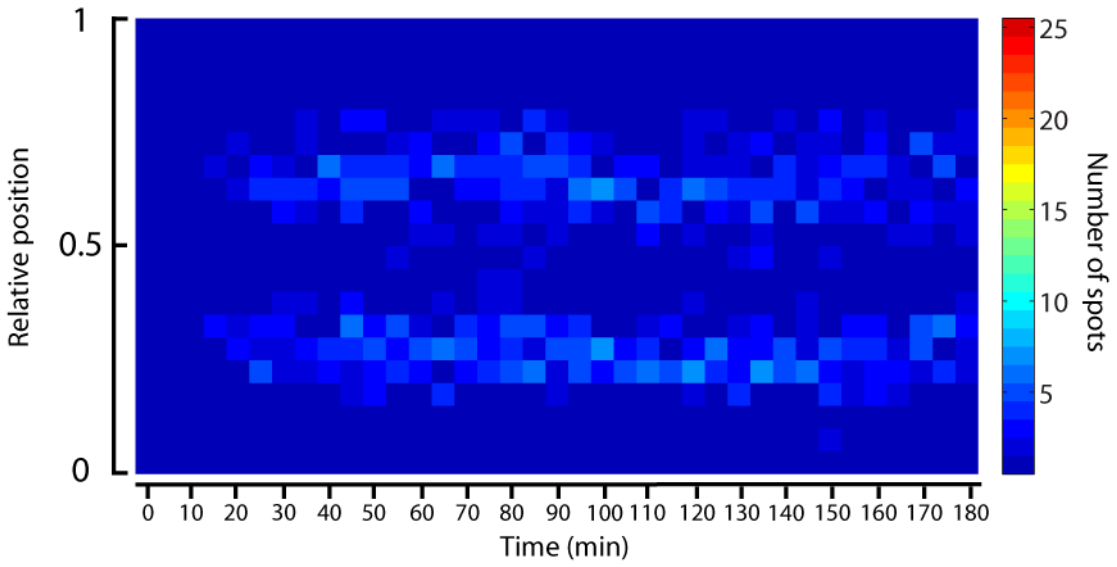

Figure 5.22: Histogram showing positions of clusters in cells with two clusters following expression of *tlpT* in Δ*tlpT* Δ*ppfA cfp-cheW*$_4$ pIND-*tlpT* . x axis represents time after IPTG addition, the y axis the position of clusters relative to the cell length. The number of spots at each position is given by the colour scale.

5.5.5 Filamentous Δ*tlpT* Δ*ppfA cfp-cheW*$_4$ pIND-*tlpT*

A kymograph for a filamentous Δ*tlpT* Δ*ppfA cfp-cheW*$_4$ pIND-*tlpT* cell is shown in fig. 5.23. Compared with kymographs for filamentous JPA1519 (Δ*tlpT yfp-cheW*$_4$) pIND-*tlpT* cells fewer clusters are seen. What is also not seen is multiple clusters forming out of a single semi-diffuse region of CheW$_4$, as is seen in filamentous JPA1519. However what is often seen is clusters merging, something rarely seen in cells with *ppfA* .

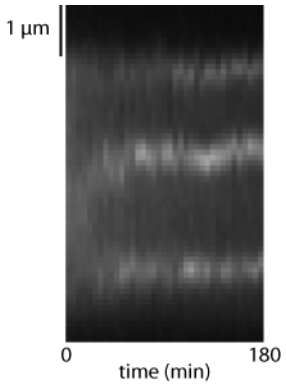

Figure 5.23: Kymograph of cluster formation in filamentous Δ*tlpT* Δ*ppfA cfp-cheW*$_4$ pIND-*tlpT* . Each unit in the x axis is 5 min.

5.6 Cell Length Affects the Number of Clusters Formed

Given the range of numbers of clusters which are able to form in cells, especially when filamentous, the effect of the length of the cell on the number of clusters was investigated. This was done by binning cells based on their length, and then calculating the percentages of cells in each bin with different numbers of clusters. Using the graphs in 5.4 to determine at which point the number of cells in each category had stabilised, only images after this time point were used so as to compare stable sub-populations.

5.6.1 JPA1519 (Δ*tlpT yfp-cheW*$_4$) pIND-*tlpT*

From fig. 5.4 it was determined that time point by which the number of cells within each cluster number category had stabilised was 50 minutes. Cells from this time point onwards were binned based on their length. The bins used were 0.5 μm wide and ranged from 1.25 μm to 3.75 μm . The percentage of cells within each bin containing either zero, one, two, three or four spots was then calculated. The result of this analysis is show in fig. 5.24. These results show that with increasing cell length the proportion of cells with zero and one clusters

decreases, and the proportion of cells with two and three clusters increases. The small percentage of cells with four clusters in the two bins of longest length is most likely due to a small number of instances where the analysis has segmented two cells end to end as if they were a single cell.

These data show that longer cells have a greater ability to form multiple clusters.

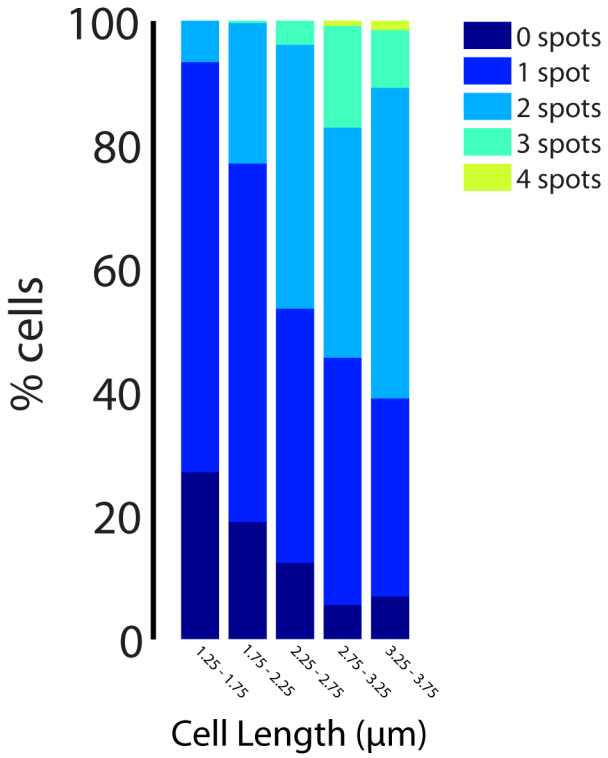

Figure 5.24: The proportion of cells in each cell length bin with 0, 1, 2, 3 and 4 spots. The colour for each spot number is given by the legend.

5.6.2 Filamentous JPA1519 (Δ*tlpT yfp-cheW*$_4$) pIND-*tlpT*

Filamentous cells were analysed in the same manner in order to explore the relationship between the number of clusters formed and cell length across a greater range of cell sizes. Using fig. 5.9 a time point of 50 minutes was chosen to use as a start point analyse to from. The bins used were 0.5 μm wide and ranged from 1.75 μm to 7.25 μm .

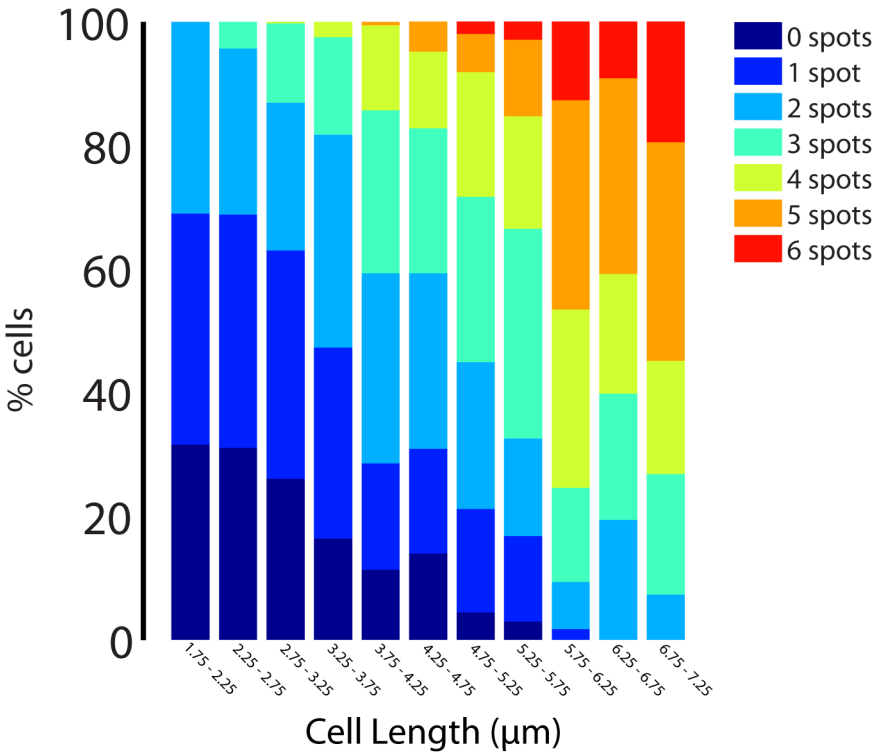

Figure 5.25: The proportion of cells in each cell length bin with 0, 1, 2, 3, 4, 5 and 6 spots. The colour for each spot number is given by the legend.

The results, fig. 5.25, show that for the shortest cell length bin the proportion of cells with zero, one and two clusters is near equal, but with increasing cell length the proportion of these decreases as the number of cells with three or more clusters increases. Whilst the proportion of zero and one cluster cells decreases quickly, the proportion of two cluster cells only starts to decrease when cell lengths are greater than 4.75 μm . Initially the proportion of three cluster cells increases, however beyond cell lengths of 5.75 μm it decreases as cells with four, five and six clusters have increasing proportions. The proportions of cells with three, four, five and six clusters increase with cell size sequentially, suggesting a clear relationship between cell size and the maximum number of cluster that can be formed.

5.6.3 Δ*tlpT* Δ*ppfA cfp-cheW*$_4$ pIND-*tlpT*

In order to determine the effect *ppfA* has on the relationship between cell size and the number of clusters formed Δ*tlpT* Δ*ppfA cfp-cheW*$_4$ pIND-*tlpT* were analysed using the same bins as used in 5.6.1. As the cluster formation is slower than in JPA1519 (Δ*tlpT yfp-cheW*$_4$) pIND-*tlpT* (see fig. 5.11) only cells from 80 minutes onwards were analysed.

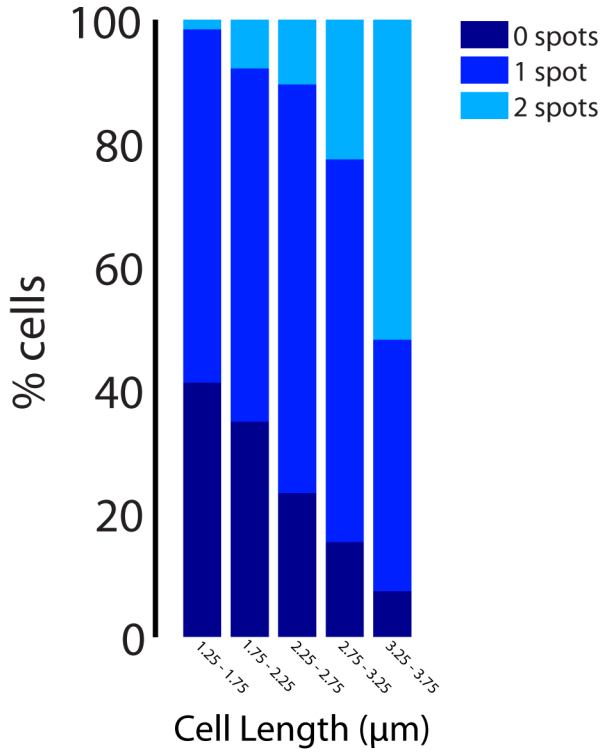

Figure 5.26: The proportion of Δ*tlpT* Δ*ppfA cfp-cheW*$_4$ pIND-*tlpT* cells in each cell length bin with 0, 1, and 2 spots. The colour for each spot number is given by the legend.

Like JPA1519 (Δ*tlpT yfp-cheW*$_4$) pIND-*tlpT* the results for Δ*tlpT* Δ*ppfA cfp-cheW*$_4$ pIND-*tlpT* (see fig. 5.26) show that as cell size increases the percentage of cells with zero clusters decreases. The proportion of cells with one cluster remains reasonably constant, with a slight decrease in the longest bin. That of cells with two clusters increases with cell length. This shows that in the absence of *ppfA* there is still a relationship between cell size and the maximum number of clusters

formed.

However comparing these results to that of JPA1519 pIND-*tlpT* , it is interesting to see that, for a given cell length, populations of cells with *ppfA* have a higher proportion of cells with larger numbers of clusters.

5.6.4 Filamentous Δ*tlpT* Δ*ppfA cfp-cheW*$_4$ pIND-*tlpT*

To further explore the differences in the relationship between cell size and cluster formation in cells with and without *ppfA* , filamentous Δ*tlpT* Δ*ppfA cfp-cheW*$_4$ pIND-*tlpT* cells were analysed as described in 5.6.2 but using a starting time point of 80mins.

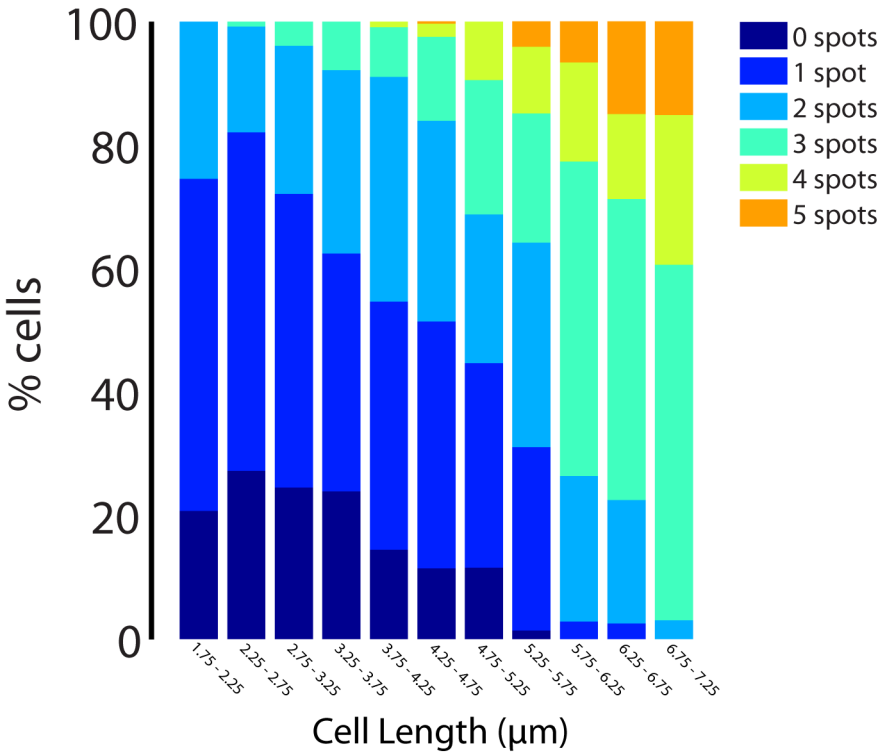

Figure 5.27: The proportion of Δ*tlpT* Δ*ppfA cfp-cheW*$_4$ pIND-*tlpT* cells in each cell length bin with 0, 1, 2, 3, 4 and 5 spots. The colour for each spot number is given by the legend.

The results (fig. 5.27) show similar trends to that seen in filamentous JPA1519 (Δ*tlpT yfp-cheW*$_4$) pIND-*tlpT* cells (see fig. 5.25). With increasing cell length the

proportions of cells with zero and one clusters decreases, while the proportion of those with three, four, and five increases. The proportion of cells with two clusters only decreases in the longest bin. As with non-filamentous cells lacking *ppfA* these results show that the tendency for longer cells to form more clusters is not dependent on *ppfA* . However as with the non-filamentous cells, when compared to cells with *ppfA* (fig. 5.25) at each cell length have higher proportions of cells with larger numbers of spots. Showing that whilst the relationship between cell length and numbers of clusters formed is not dependent on *ppfA* , it is influenced by it, with cells containing *ppfA* being able to form more clusters for a given cell length.

5.7 Discussion

Whilst it was previously shown that TlpT is required for the cytoplasmic chemosensory proteins to form into a cluster, it was not known if these proteins could be brought back together by simply reintroducing TlpT into the cell. Here it has been shown that this is the case, expressing *tlpT* in a Δ*tlpT* background with YFP-$CheW_4$ used as a marker for the cytoplasmic cluster results in the self-assembly of the cluster.

This *de novo* formation of the cluster is particularly interesting as it involves the coming together of several different proteins all with copy numbers in the thousands. These results show that when TlpT is reintroduced into the system it is able to bring all these proteins together triggering the self-assembly of the cluster. This explains how in Δ*ppfA* strains the daughter cell which does not inherit the cluster is then able to subsequently form a new cluster, as expression of the cluster components will result in self-assembly of a new cluster once sufficient levels of the proteins are present within the cell.

By analysing this formation in multiple cells over time, it shows that, following expression of *tlpT* there is a rapid decrease in the number of cells with no clusters (i.e. a diffuse localisation of YFP-CheW$_4$), coupled with a rapid increase in those with one cluster. Cells with two identifiable clusters show a slower increase compared to those with with just one, suggesting that when all the newly expressed TlpT is pooled into a single cluster, the cluster is able to assemble faster than when distributed between two. This may be a result of either sequential cluster nucleation, or two clusters forming at the same time but growing in size slower, thus taking longer to become identifiable. Also in cells with two clusters often one becomes more distinct before the other (as seen in fig. 5.3), indicating that first of the clusters to begin forming is able to incorporate more TlpT initially. This fits with the idea that the formation mechanism may be similar to a reaction-diffusion mechanism where cluster formation is a balance between incorporation into existing clusters and nucleation of new clusters.

PpfA is not required for cluster formation, but it does influence it. Cells without PpfA are slower to form clusters, and fewer of them form two clusters. This suggests that PpfA is able to stabilise newly formed clusters, both speeding up the formation and increasing the chance that free TlpT molecules will be able to nucleate a new cluster rather than be incorporated into an existing one. This is supported by one of the control experiments. In cells with pIND-*tlpT* but without the addition of IPTG there is a striking difference between cells with and without PpfA. In JPA1519 (Δ*tlpT yfp-cheW*$_4$) pIND-*tlpT* cells $\sim$ 12% of cells form clusters as a result of leaky *tlpT* expression, however in Δ*tlpT* Δ*ppfA cfp-cheW*$_4$ pIND-*tlpT* no cells formed clusters. This suggests that PpfA is able to lower the threshold level of TlpT required to form clusters.

The results of analysing the positions of the newly formed clusters show that once the form they remain positioned, indicating that they do not form and po-

sition sequentially. Instead this results suggest that either the clusters form at a position or they are positioned before they are large enough to be detected above the free YFP-CheW$_4$ background signal in which case they must be positioned rapidly after forming. Interesting this pattern is also seen in Δ*ppfA* cells. Cells which form a single cluster show a similar distribution of cluster positions to that of JPA1553 (Δ*ppfA tlpT -yfp*, see 4.3), being centred about mid-cell and with a slightly wider distribution that that of JPA1558. In the Δ*ppfA* no cells are seen with more than one cluster, however a small proportion of Δ*ppfA* Δ*tlpT* cells with *tlpT* re-expressed form two clusters. So the fact that the positioning of two clusters within these cells shows a $^1/_4$ and $^3/_4$ pattern, suggests that when two clusters form they do so spatially separate within the cell.

These results are mirrored in those of cells made filamentous by cephalexin treatment. Both JPA1519 (Δ*tlpT yfp-cheW*$_4$) pIND-*tlpT* and Δ*tlpT* Δ*ppfA cfp-cheW*$_4$ pIND-*tlpT* cells are able to form more clusters when elongated compared to untreated cells. In both strains theses clusters tend to remain at that position after they have formed. However there are some instances of cluster movement. Occasionally in JPA1519 pIND-*tlpT* multiple clusters are seen to form in close proximity to each other before moving apart, and clusters in Δ*tlpT* Δ*ppfA cfp-cheW*$_4$ pIND-*tlpT* cells are sometimes seen merging. This supports the proposed role of PpfA in helping stabilise cluster formation and in segregating clusters, whereas in the absence of PpfA clusters in close proximity simply merge through a reaction-diffusion like mechanism.

By analysing the relationship between the length of cells and the number of clusters which form within them when *tlpT* is re-expressed it was seen that in all cases more clusters are able to form in larger cells. The relationship could be due either to greater cell volume allowing more clusters to form if they do so by a reaction-diffusion type mechanism, or the presence of pre-segregated sites. In the

latter scenario the existence of multiple sites would be dependent on the position of the cell within the cell cycle and therefore cell length, or for filamentous cells dependent on the number of replicative cycles the cell has undergone without septation, which would also result in increasing cell length. However given that it is known that PpfA is responsible for segregating the cluster it seems unlikely that pre-defined sites exist in the Δ*ppfa* cells, and therefore for the Δ*ppfA* cells positioning may depend on a reaction-diffusion mechanism. What this analysis shows is that while cells lacking *ppfA* have the ability to form greater number of clusters in larger cells, at a given cell length they form fewer than cells with PpfA. The observation that PpfA allows the formation of more clusters suggests that it is able to stabilise the nucleation of greater numbers of clusters in cells than would otherwise be possible without it.

Together these results highlight the key role TlpT plays in the cytoplasmic cluster, not just in terms of signalling but in the overall super-structure of the cluster. The importance of TlpT in the super-structure of the cluster further enhances its candidacy as the segregation partner for PpfA, with it acting as a bridge between the cluster and the segregation machinery. The results also provide information key to the understanding of PpfA's role in cluster formation. The cells with PpfA are able to form more clusters, form them more quickly, and form them with lower amount of TlpT than those without PpfA, suggesting that PpfA enhances the nucleation of new clusters.

Chapter 6

Following PpfA and the Cytoplasmic Cluster Through the Cell Cycle

A number of models have been put forward as to how ParA ATPases segregate their cargo. These range from movement from one pole to the other of filaments or cloud-like ParA structures [140], oscillations of ParA [73], and ParA foci assembly and disassembly [72].

In order to determine how the cytoplasmic chemosensory cluster is segregated, and how this compares to previously published models for other ParA segregation systems, time-lapse microscopy was used. Both the cluster (marked by TlpT-YFP) and PpfA-CFP distributions within the cell were followed over the course of 3 hours to capture cluster duplication and segregation events.

6.1 Co-localisation of PpfA and TlpT

Expression of *ppfA-cfp* from the inducible plasmid pIND in a *tlpT-yfp* background results in PpfA-CFP foci which coincide with the cytoplasmic chemosensory cluster. The formation of these foci was shown not to be a result of interaction between fluorescent proteins as the foci were also present when *ppfA-cfp* was expressed in a WT (WS8N) background [152]. An example of the co-localisation of PpfA-CFP and TlpT-YFP is shown in fig. 6.1. Beyond this focus, PpfA localises to the nucleoid, which fills the cytoplasm [152].

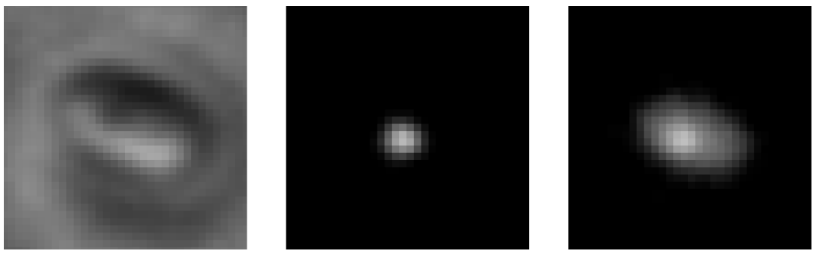

Figure 6.1: Co-localisation of TlpT-YFP and PpfA-CFP focus. The left panel shows the DIC image, middle panel the TlpT-YFP and right panel the PpfA-CFP.

The profiles of fluorescence intensity along the cell length for TlpT-YFP and PpfA-CFP for a typical cell with two clusters are shown in fig. 6.2. Bimodal Gaussian functions were fitted to both profiles, shown as solid lines in fig. 6.2, from these fits it was confirmed that the centres of the clusters and PpfA foci were in the same positions.

However single snapshot images do not address a key feature of ParA ATPases: dynamic positioning. Therefore cells were followed by time-lapse microscopy in order to ascertain the distribution of PpfA-CFP and TlpT-YFP through the cell cycle.

Kymographs of cells with both one and two clusters are shown in fig. 6.3. These results show that the PpfA-CFP focus remains co-localised with the cluster over

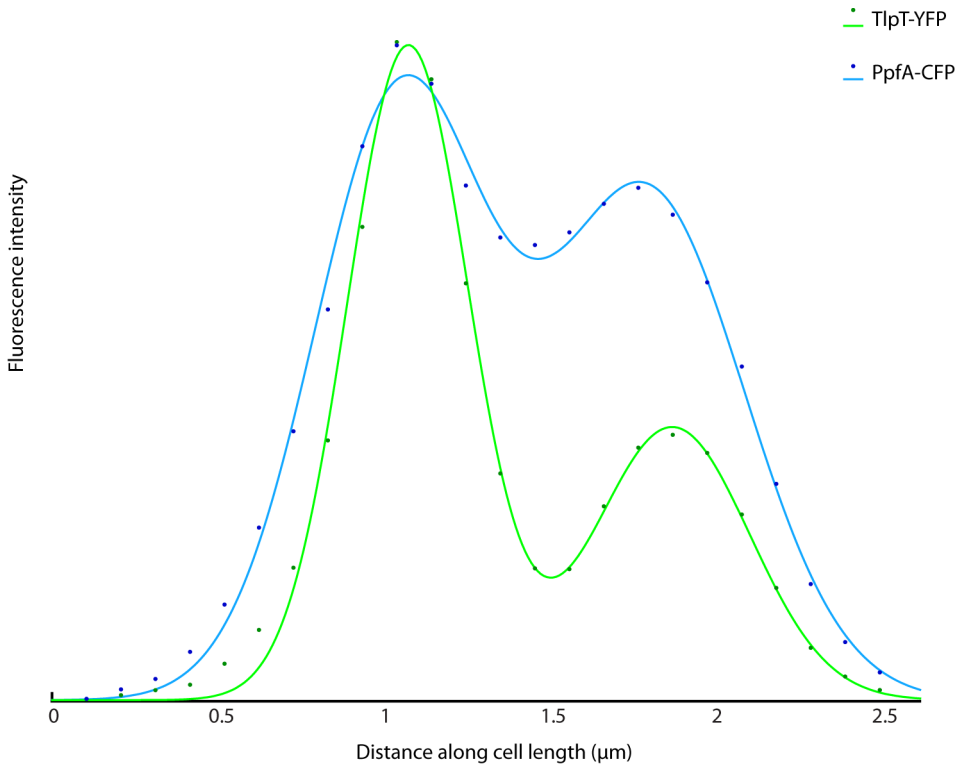

Figure 6.2: Profile of fluorescent TlpT-YFP and PpfA-CFP signals in typical cell. TlpT-YFP signal shown in green, PpfA-CFP signal shown in blue. Circles represent actual data, solid lines represent fits of bimodal Gaussian equations to data.

long time periods, with movement of the cluster being mirrored by the movement of the PpfA-CFP foci. No oscillations of PpfA-CFP are seen in these kymographs, confirming previously reported results [152]. There were no 'blinking' events (disassembly and reassembly of foci) seen for PpfA-CFP as seen for ParA of the P1 plamid [72].

Over these long time scales (3 hours) both the cluster and the PpfA foci are relatively mobile (as seen in fig. 6.3 B & C) within the cell, suggesting that they are not tethered to a tightly held anchor. What can also been seen from these results is that in cells with two clusters there is no fixed distance between them, clusters move both toward and away from each other.

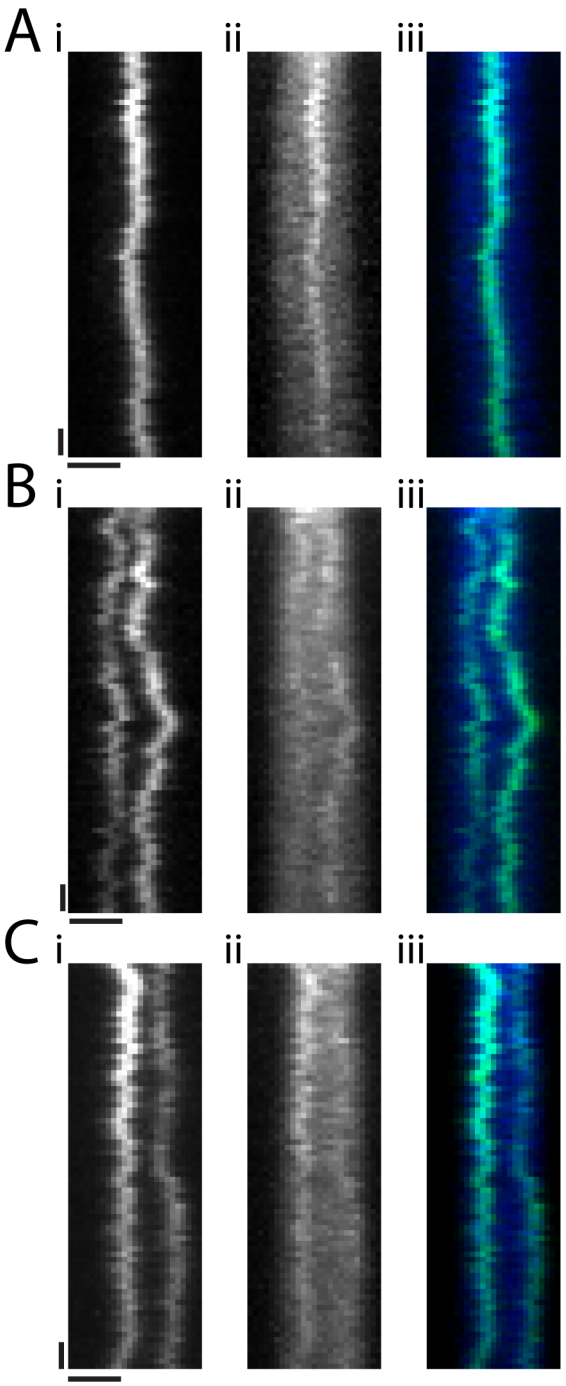

Figure 6.3: Kymographs of TlpT-YFP and PpfA-CFP. **A** Typical cell with a single cytoplasmic cluster. **i:** TlpT-YFP, **ii:** PpfA-CFP, **iii:** Merge, TlpT-YFP shown in green, PpfA-CFP shown in blue. **B-C** Typical cell with two cytoplasmic clusters. **i:** TlpT-YFP, **ii:** PpfA-CFP, **iii:** Merge of both signals, TlpT-YFP shown in green, PpfA-CFP shown in blue. Horizontal scale bar is 1 μm , vertical scale bar is 10 min.

6.2 The Cytoplasmic Cluster is Replicated by Splitting, Not *de novo* Formation

Two possible hypotheses were proposed for how the second cluster is formed before division. The first was that PpfA formed a second focus, which then allowed the nucleation of a second cluster. The second involved PpfA pulling apart a single cluster into two then segregating them. In order to distinguish between these two hypotheses cells which formed a second cluster during the course of the time-lapse were analysed.

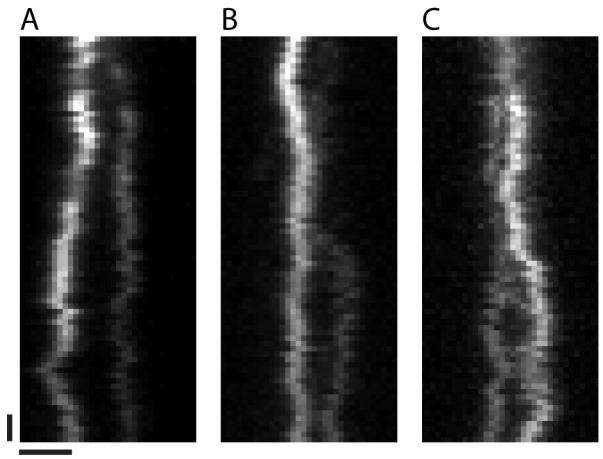

Figure 6.4: Kymographs of TlpT-YFP showing the cytoplasmic cluster splitting. **A-C:** TlpT-YFP fluorescent signal in cells in which the formation of two clusters is seen. Horizontal scale bar is 1 μm , vertical scale bar is 10 min.

Kymographs of the TlpT-YFP signal from example cells which demonstrated such cluster formation are shown in fig. 6.4. It can be clearly seen from these results that the second cluster is formed by splitting off from the first, and not *de novo* nucleation and formation of a second cluster at a site distal from the first.

The PpfA-CFP fluorescent signal in cells with splitting clusters were analysed to determine the distribution of PpfA-CFP before, during and after cluster splitting, thus revealing whether the splitting and segregation were due to changes in the distribution of PpfA within the cell. Kymographs generated from cells with split-

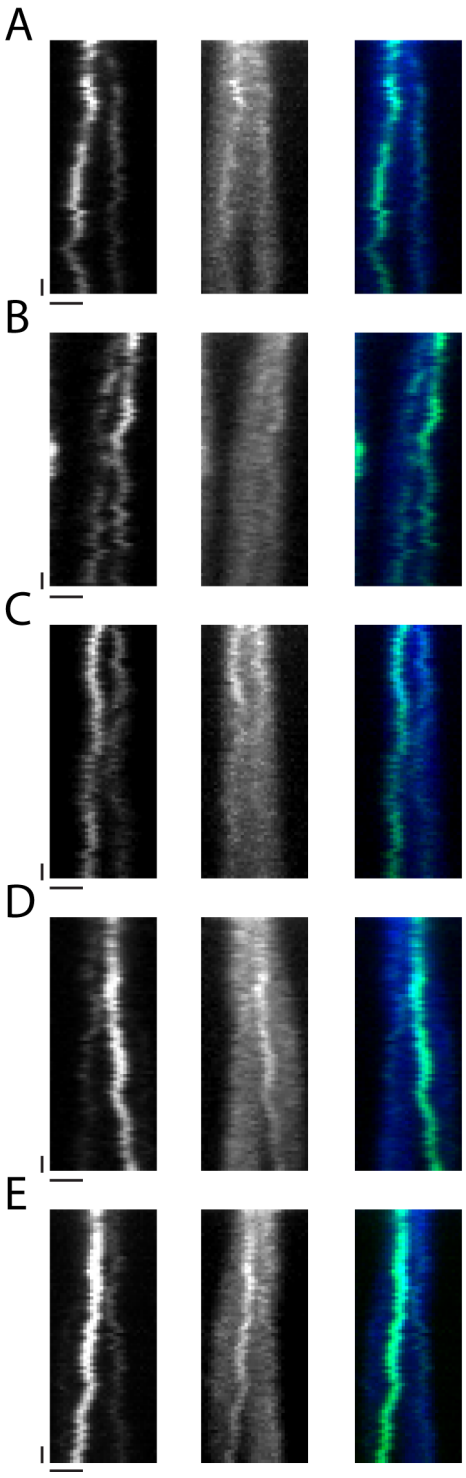

Figure 6.5: Kymographs of TlpT-YFP and PpfA-CFP in cells showing the cytoplasmic cluster splitting. **A-E:** Left panel: TlpT-YFP fluorescent signal. Middle panel: PpfA-CFP fluorescent signal. Right panel: merge of both signals, TlpT-YFP shown in blue, PpfA-CFP shown in green. Horizontal scale bar is 1 μm , vertical scale bar is 10 min.

ting clusters are shown in fig. 6.5. These results show that there is no detectable reorganisation of PpfA-CFP distribution within the cell as the cluster splits and segregates. As the cluster splits so does the PpfA-CFP focus.

It is also interesting to note that often after cluster splitting the clusters begin to segregate but then come back closer together before segregating fully. This suggests that there is not a rapid segregation event that swiftly pulls the two clusters apart.

These kymographs also make it clear that clusters are not split equally. One cluster is often much larger (of greater fluorescence intensity) then the other.

6.3 Discussion

Various models have been presented in the literature as to how ParA ATPases partition their cargo (be it plasmid, chromosome, or protein complex). The results presented in this chapter suggest that PpfA partitions the cytoplasmic chemosensory cluster by a mechanism not hitherto described.

In *C. crescentus* the origin of replication of the chromosome is positioned at the cell pole, and after replication of the *parS* sequence ParA segregates one of the sister *parS* sequences (and thus the rest of the chromosome) to the other pole [186]. This is achieved by the ParB-*parS* complex of one chromosome causing the depolymerisation of a nucleoid associated ParA filament, the persistent interaction between ParB-*parS* and the retracting ParA filament results in translocation of the ParB-*parS* complex to the distal pole where it is captured by a matrix of PopZ protein [186, 43, 140]. The PopZ matrix is itself formed at the new pole due to the increased local ParA concentration (due to the contraction of the ParA filament), with which it interacts enabling the nucleation of a second matrix [100]. Therefore in this system both the ParB-*parS* complex and PopZ are partitioned by

ParA, but through different mechanisms. However both these mechanisms rely on the transition of ParA distribution from one in which ParA is spread over all of the nucleoid to one in which it is removed from the nucleoid in a directional manner until the nucleoid is stripped of ParA. No such changes in PpfA distribution were seen in any time courses.

The ParA of the F plasmid, known as SopA, has been suggested to position and partition the plasmid through a reaction-diffusion mechanism in which oscillations of nucleoid bound ParA are driven by SopB-*sopC* (ParB-*parS*) [73]. In this model it is these oscillations that result in plasmid positioning and thus partition. No oscillation of PpfA were observed.

A contrasting model is one presented for the P1 plasmid. This system shares some similarities with PpfA and the cluster, P1 ParA is found diffuse across the nucleoid and forms a focus at the position of the plasmid [72], this mirrors the PpfA which also is diffuse across the nucleoid except where the cluster is positioned where it forms a focus. There are however several key differences. The results presented by Hatano *et al.* showed the ParA focus to 'blink' due to disassembling and reassembling of the focus, and the authors also reported that two ParA foci would form before sister plasmids segregated to these positions. In the profiles of PpfA-CFP over time no such blinking is observed, and the positions of the cluster and the PpfA-CFP foci are also co-localised.

From these data it is clear that PpfA does not segregate the cytoplasmic cluster by mechanism which can be described by the models mentioned above.

From these results it is possible to distinguish between two hypothesised models for cluster duplication. A second PpfA focus does not form and then nucleate the formation of second cluster (at least within the resolution of conventional light microscopy). Instead the current cluster splits along with the PpfA focus and then segregated. Interestingly after splitting, clusters are often seen to either remain

in close proximity to each other for some time (fig. 6.5 D & E), or move apart before coming closer again (fig. 6.5 A, B & C). This indicates that segregation does not occur through a sudden rapid motion, and that there is no set distance between clusters, a result also seen in measuring positions of clusters in invidual snap-shot images (see 4.5).

Another observation previously made (David Wilkinson, unpublished data) is that the splitting of the cluster is not equal. After splitting one cluster is demonstrably larger (of greater fluorescence intensity) than the other, indicating that the stoichiometry of proteins within the cluster may be more important than absolute numbers for proper chemotactic signalling.

Chapter 7

Turnover of Cytoplasmic Chemosensory Cluster Proteins

After the cytoplasmic cluster segregates the two resultant clusters are not of equal size (see Chapter 6). This raises the question how does the smaller cluster grow in size? Is it simply the case that newly expressed protein is incorporated into both large and small clusters, or does protein exchange between the two clusters allowing their sizes to equilibrate?

In order to investigate whether proteins exchange between clusters fluorescence recovery after photobleaching (FRAP) was used on cytoplasmic cluster components tagged with fluorescent proteins. The proteins investigated were TlpT-YFP (JPA1558), TlpC-GFP (JPA543), YFP-CheW$_4$ (JPA1457), YFP-CheA$_3$ (JPA1425), and YFP-CheA$_4$ (JPA1438).

Given that only a small percentage of the cells in a population have two clusters (see 4.1), cells were treated with cephalexin to elongate them and thus increase the number of clusters within cells (see 4.2).

7.1 Photobleaching Cluster Proteins

The turnover of proteins within the cytoplasmic chemosensory cluster was investigated by using fluorescent fusions of TlpT, TlpC, $CheW_4$, $CheA_3$, $CheA_4$, and photobleaching them and following the fluorescent recovery (FRAP). FRAP was performed on cephalexin treated cells using the Nikon Eclipse Ti in confocal mode, using the 405 nm laser to photobleach a single point for 1 s. Cells were imaged every second for 10 s prior to bleaching to establish the pre-bleach level of fluorescence. After bleaching they were imaged every second for 30 s, then every 3 s for 5 minutes, and finally every 16 s for 10 minutes. These time points were chosen to capture details of potential fast recovery as well as being able to establish the final levels of recovery, whilst minimising photobleaching due to acquisition.

Example images of clusters in each strain being bleached are shown in fig. 7.1.

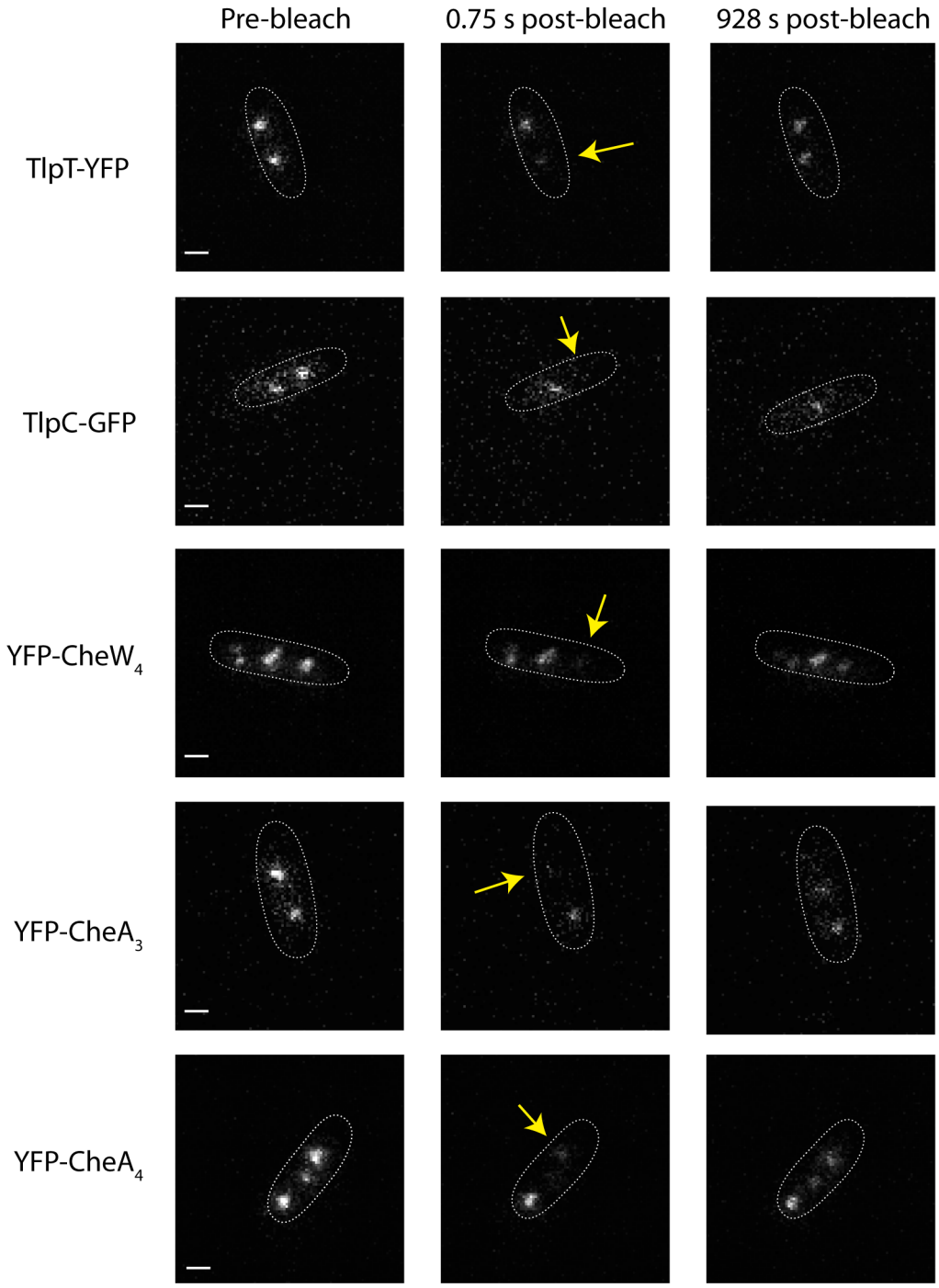

Figure 7.1: Fluorescence recovery after photobleaching of TlpT-YFP, TlpC-GFP, YFP-CheW$_4$, YFP-CheA$_3$, and YFP-CheA$_4$. The first image show the cell before bleaching, the second immediately after bleaching and the third shows the cell 928 seconds after bleaching. The yellow arrow indicates area of the cell which has been bleached. Dashed lines represent cell outlines. Scale bars are 1 μm .

7.2 Quantitative Analysis of Recovery

In order to quantify the recovery of fluorescence, and therefore turnover of protein, the fluorescence intensity of clusters was measured at each time point. The levels of fluorescence over time gave an initial indication of recovery, and made it possible to distinguish between clusters which showed recovery and those which did not. The percentage of clusters which showed recovery for each strain investigated is shown in the 2nd column of table 7.1. The fluorescence intensities of the clusters which did show some recovery were then averaged to generate a mean recovery curve. Curves were then fitted to the mean curves for each strain. The equation fitted is given by equation 7.1, where I_{fit} is the fitted curve, I_0 is the fluorescence intensity at the first time point post-bleach, t is time, and a and b are constants.

$$I_{fit} = I_0 - a.e^{(-b.t)} \tag{7.1}$$

By fitting equation 7.1 to the data the half-time of recovery ($t_{1/2}$) mobile fraction of each protein could be determined. These results are presented in table 7.1. The generation of mean fluorescence intensity values and curve fitting was done through the use of the easyFRAP software package [144].

The mean and standard deviation of data from clusters which showed recovery for TlpT-YFP and the fitted curves are shown in fig. 7.2, those for YFP-CheW$_4$ in fig. 7.4, those for YFP-CheA$_3$ in fig. 7.5, and those for YFP-CheA$_4$ in fig. 7.6. No clusters in the TlpC-GFP strain showed any recovery and therefore curve fitting was not possible, the mean and standard deviation of all of the TlpC-GFP data are shown in fig. 7.3.

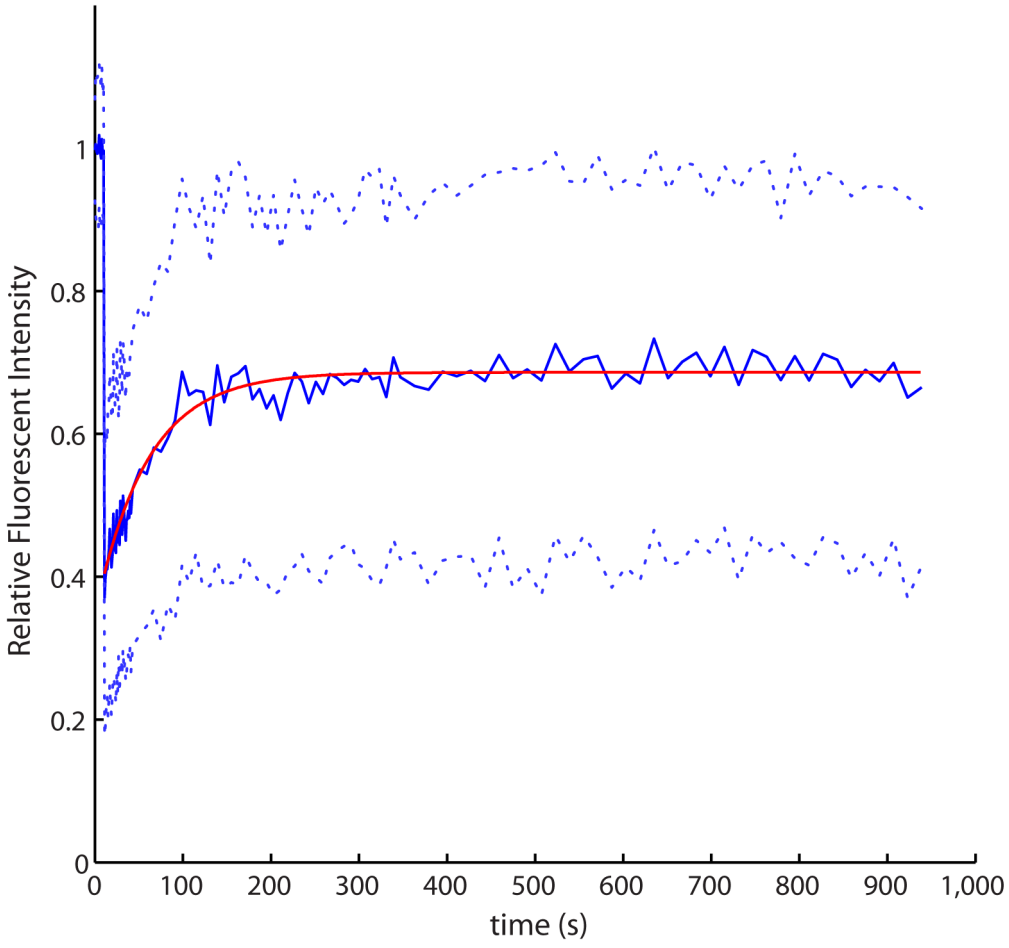

Figure 7.2: Fluorescence recovery after photobleaching of TlpT-YFP. The solid blue line represents the mean relative fluorescence intensity at each time point of the 20 clusters which showed recovery, and the dashed blue lines indicate $\pm$ one standard deviation. The solid red line represents the fitted curve. The R^2 of the fit was 0.95.

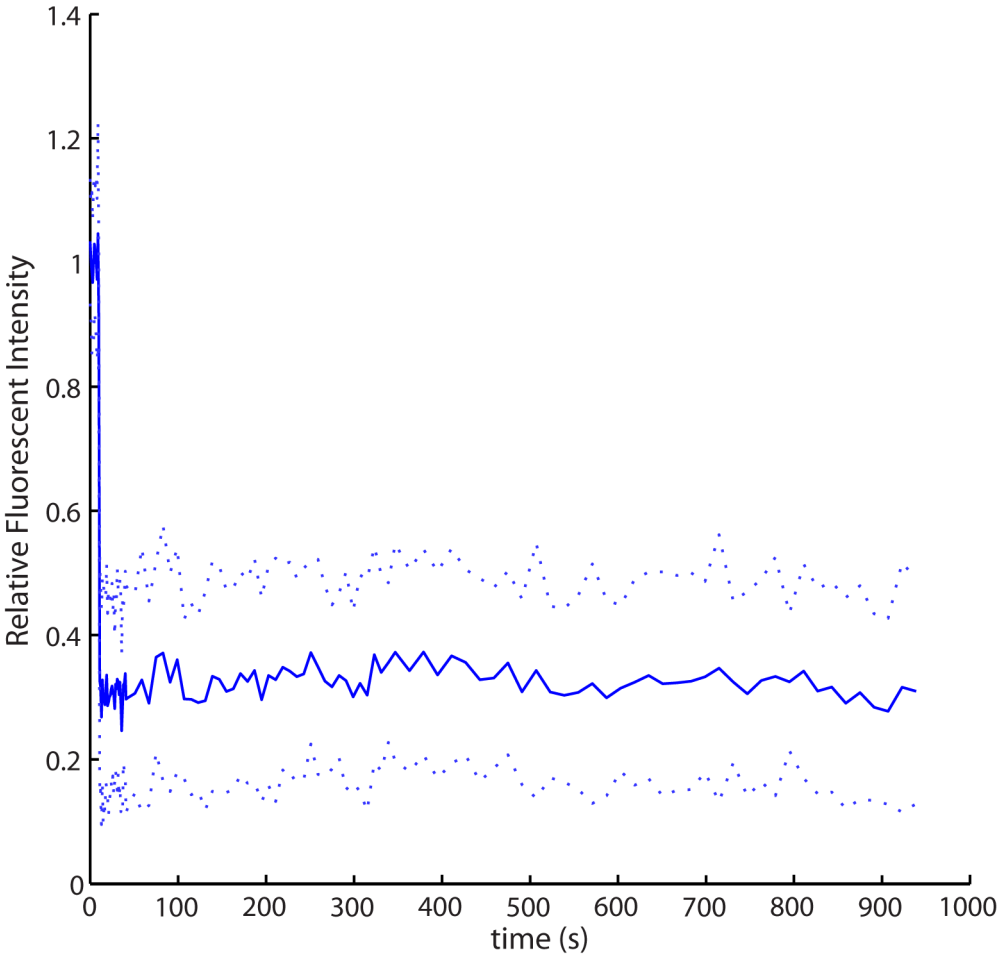

Figure 7.3: Fluorescence recovery after photobleaching of TlpC-GFP. The blue line represents the mean relative fluorescence intensity at each time point, and the dashed blue lines indicate $\pm$ one standard deviation.

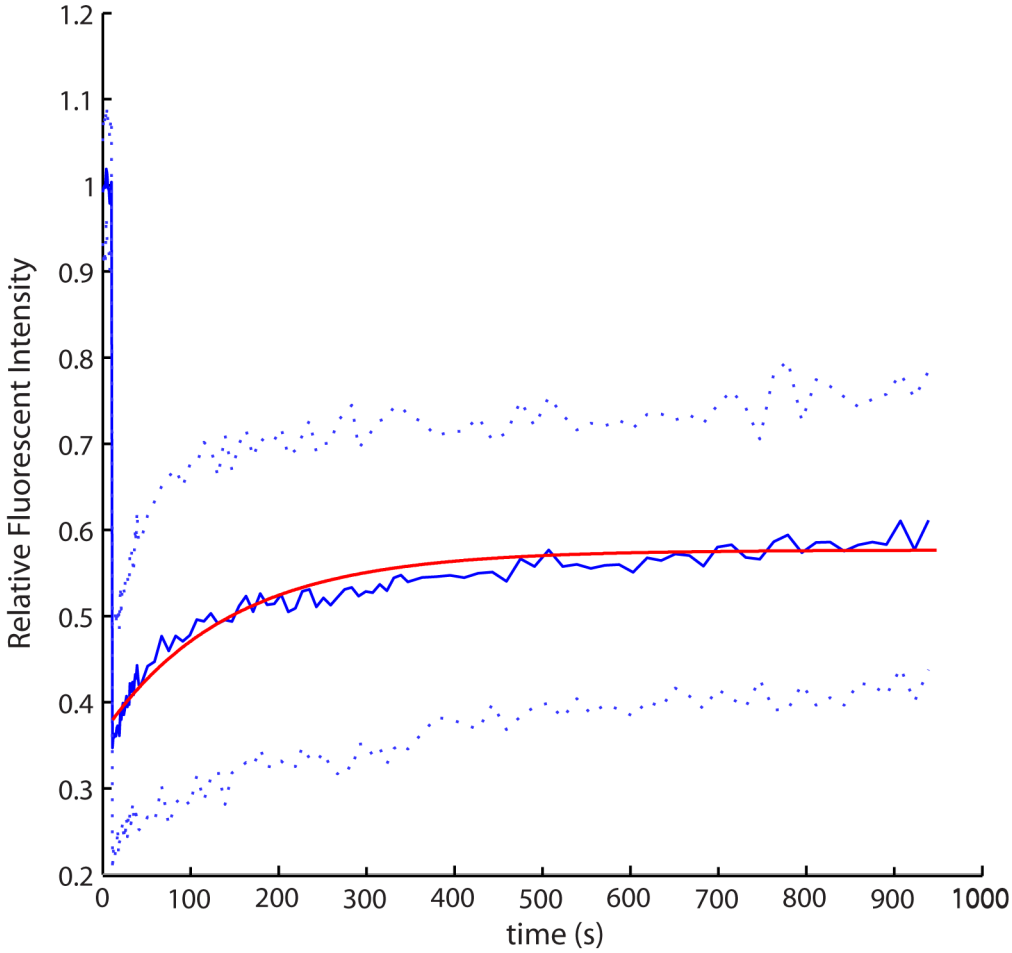

Figure 7.4: Fluorescence recovery after photobleaching of YFP-CheW$_4$. The blue line represents the mean relative fluorescence intensity at each time point, and the dashed blue lines indicate $\pm$ one standard deviation. The solid red line represents the fitted curve. The R^2 of the fit was 0.96

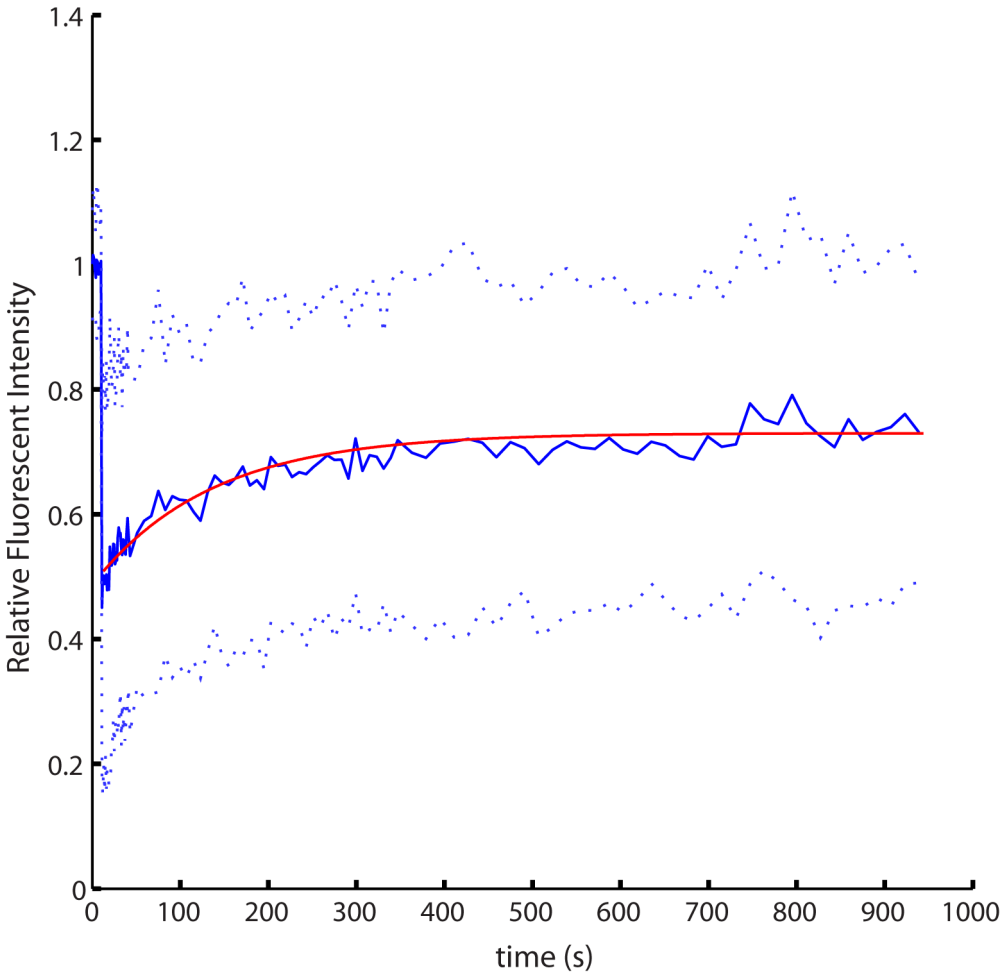

Figure 7.5: Fluorescence recovery after photobleaching of YFP-CheA$_3$. The blue line represents the mean relative fluorescence intensity at each time point, and the dashed blue lines indicate $\pm$ one standard deviation. The solid red line represents the fitted curve. The R^2 of the fit was 0.93

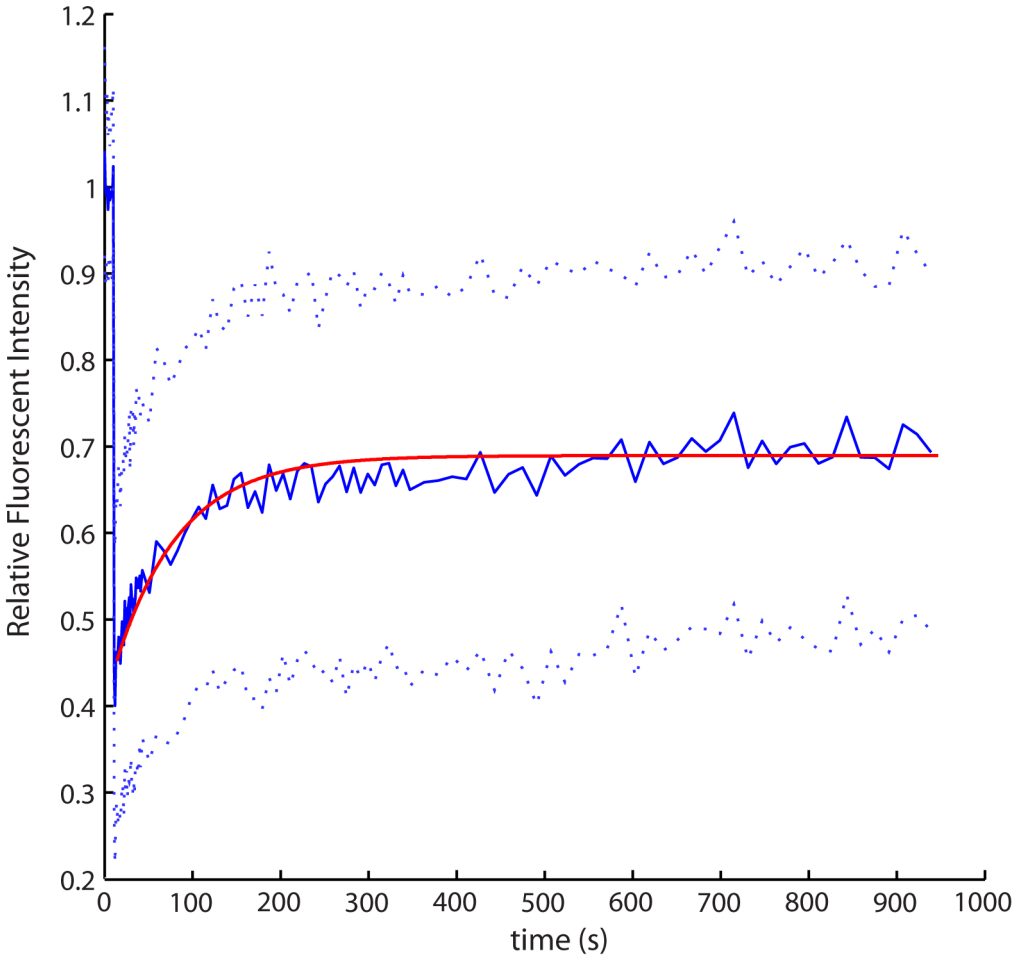

Figure 7.6: Fluorescence recovery after photobleaching of YFP-CheA$_4$. The blue line represents the mean relative fluorescence intensity at each time point, and the dashed blue lines indicate $\pm$ one standard deviation. The solid red line represents the fitted curve. The R^2 of the fit was 0.94

Protein	% of clusters exhibiting recovery	$t_{1/2}$ (s)	Mobile fraction
TlpT-YFP	55.6	40.94	0.48
TlpC-GFP	0	N/A	N/A
YFP-$CheW_4$	62.2	97.91	0.31
YFP-$CheA_3$	76.9	93.08	0.43
YFP-$CheA_4$	65.2	50.97	0.41

Table 7.1: Fluorescence recovery after photobleaching results

It is clear that there is a large variation in fluorescence intensity across all data. However for all of the proteins the standard deviation does not greatly increase over time following the photobleaching, i.e. the variation seen is primarily due to variation in the intensities of clusters after being bleached. Given that photobleaching laser settings were kept constant this variation must be due to the number of proteins within the clusters and thus the proportion of fluorophores bleached. This suggests that the large standard deviation is primarily due to variation in cluster size rather than recovery behaviour, as this would result in increasing standard deviation over time.

The results (summarised in table 7.1) show that with the exception of TlpC-GFP the other cytoplasmic cluster proteins tested can undergo some turnover. However the number of incidences of non-recovery and the small mobile fractions suggest that this turnover is limited. $CheW_4$ has both the lowest mobile fraction and the slowest half-time of recovery, $CheA_3$ and $CheA_4$ both have similar mobile fractions, but have differing half-times of recovery. TlpT has the highest mobile fraction and the fastest half-time, whereas an other chemoreceptor TlpC appears completely immobile. However despite differences in turnover behaviour these results show that large proportions of the molecules in the cytoplasmic cluster do not exchange either with a free pool or with other clusters.

7.3 Discussion

The results presented in this chapter show that the cytoplasmic chemosensory cluster of *R. sphaeroides* is a relatively stable structure which does not undergo large scale exchange of components with pools of proteins either free in the cytoplasm or within other clusters in the cell. For YFP fusions to TlpT, $CheW_4$, $CheA_3$, and $CheA_4$ significant proportions of the tested population showed no measurable turnover; and for the cases where turnover was seen the recovery was only partial. TlpC-GFP exhibited no turnover in any of the measured cases. For all the proteins that did exhibit recovery the $t_{1/2}$ values indicate that this exchange is slow. Interestingly TlpT-YFP had the fastest $t_{1/2}$ and largest mobile fraction, a result which strikingly contrasts with FRAP experiments performed on the polar chemosensory cluster in *E. coli* [164].

In the *E. coli* study it was reported that Tar (the MCP chosen for study) formed a stable core to the polar chemosensory cluster, CheA and CheW demonstrated slow exchange albeit faster than that of Tar. Like TlpT there was a large immobile fraction of Tar molecules, however exchange of Tar molecules is far slower than that of Tlpt, with Tar taking $\approx$ 700 s to reach maximal recovery and TlpT taking $\approx$ 250 s. Tar in the polar cluster of *E. coli* is membrane spanning, which therefore makes an ideal candidate as a central stable core to the complex as its diffusion will be slower than that of cytoplasmic proteins and it is only able to diffuse in two dimensions. The cytoplasmic cluser of *R. sphaeroides* however does not span any membranes which gives rises to the potential for chemoreceptors to be more mobile, but also to the need to generate cluster stability in the absence of a structure such as the plasma membrane. This is what is seen with TlpT, as whilst it also has a large immobile fraction its exchange is faster than Tar suggesting that in this cluster chemoreceptors do not by default form a stable core. However no exchange of TlpC molecules is seen, indicating that the dynamic

behaviour of chemoreceptors within the cluster can be different. Another striking difference between results for the cytoplasmic *R. sphaeroides* cluster and the polar *E. coli* cluster is the behaviour of the CheA and CheW molecules. In both cases CheA and CheW molecules demonstrate similar slow levels of exchange, however in *E. coli* CheA and CheW have fully mobile fractions, whereas in *R. sphaeroides* $CheW_4$, $CheA_3$, and $CheA_4$ have mobile fractions of 0.31, 0.43 and 0.41 respectively. This reduction in the mobile population may be how stability within the cluster is generated without a membrane to immobilise around. The authors of the *E. coli* FRAP study suggested that presence of some slow exchange of cluster components may be important in ensuring that clusters maintain similar stoichiometries, this may be why the components of the cytoplasmic cluster in *R. sphaeroides* , with the exception of TlpC, exhibit some exchange, helping to generate similar stoichiometries of proteins in clusters after cluster segregation.

These results suggest that exchange between clusters is not sufficiently fast to be the primary driver in the growth in size of the smaller of the two clusters after segregation; whilst the exchange might be able to adjust stoichiometries of proteins the speed of exchange and size of the mobile fraction does not fit with the suggestion of the bulk flow of protein to equilibrate cluster size.

A theory tested by [164] was that cluster components are able to diffuse within the cluster. They tested this by both bleaching whole clusters and part bleaching them, these produce similar recovery kinetics suggesting that the majority of exchange is with a free pool of proteins rather than within the cluster itself. Unfortunately due to the smaller size of *R. sphaeroides* compared to *E. coli* and smaller area occupied by the cytoplasmic cluster compared to the polar one it was not possible to bleach part of a cluster, and therefore it was not possible to investigate intra-cluster exchange.

Chapter 8

PpfA Controls the Mobility of the Cytoplasmic Chemosensory Cluster

The positioning of the cytoplasmic chemosensory cluster is strikingly similar to the positioning of low copy number plasmids which require an active segregation mechanism; before duplication at the mid-cell and after duplication at the 1/4 and 3/4 positions. However the distribution of PpfA in the cell relative to the cluster is very different to that of ParA and plasmids, suggesting significant differences in the mechanisms used. Given that most models for both type I and II plasmid segregation systems require the dynamic positioning of the plasmids for segregation, the mobility of the cluster was investigated, both with and without PpfA, in order to determine PpfA's influence over the mobility of the cluster and to help elucidate possible mechanisms by which PpfA segregates and positions the cluster.

8.1 Cluster Movement

Analysis of the positions and numbers of clusters in Chapter 4 shows that whilst a *tlpT -yfp* Δ*ppfA* (JPA1553) cannot form more than one cluster, the positions of these single clusters is similar to that of *tlpT -yfp* (JPA1558) cells with just one cluster. This raises the question as to whether the primary role of PpfA is segregating and positioning two clusters, rather than positioning a single cluster. In order to address this, the movement of clusters in cells with and without *ppfA* was analysed. The time scale of 10 minutes was chosen as it is significantly shorter than the cell cycle of *R. sphaeroides* and would therefore make it easier to exclude any clusters undergoing active segregation.

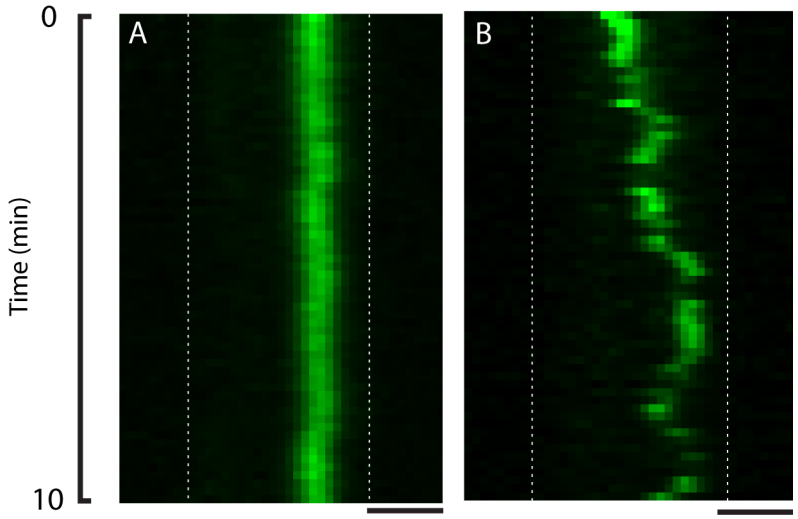

Figure 8.1: **A:** Kymograph of the cytoplasmic cluster (TlpT-YFP) over 10 minutes. **B:** Kymograph of the cluster (TlpT-YFP) in a Δ*ppfA* strain. For both pictures were taken every 10 s over 10 mins, dashed lines represent cell poles, and scale bars represent 1 μm .

These time courses show that when *ppfA* is deleted the cluster is highly mobile within the cell when compared to clusters in the presence of PpfA. This is seen in kymographs of *tlpT -yfp* and *tlpT -yfp* Δ*ppfA* cells, fig. 8.1.

In order to quantify this difference in mobility between the two strains the position of each cluster at each time point over 10 minutes was determined using the

ImageJ plugin View5D (`http://www.nanoimaging.uni-jena.de/View5D/`). An example of tracks of positions of clusters for both strains are shown in fig. 8.2.

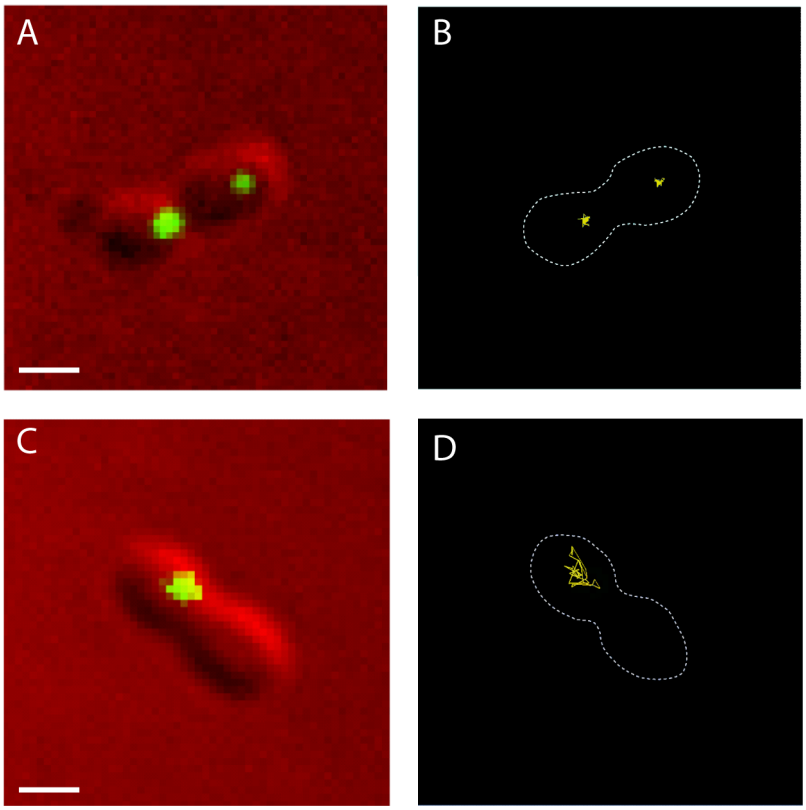

Figure 8.2: **A:** DIC and fluorescent image of a *tlpT -yfp* cell at the start of the time course. **B:** The outline of the cell shown in A represented as a dashed white line, and the tracks of the cluster over the time course shown as a solid yellow line. **C:** DIC and fluorescent image of a *tlpT -yfp* Δ*ppfA* cell at the start of the time course. **D:** The outline of the cell shown in A represented as a dashed white line, and the tracks of the cluster over 10 min shown as a solid yellow line. Scale bars represent 1 μm .

8.2 Mean Square Displacement of Clusters

From the positions of clusters the mean square displacement (MSD) can be calculated. The equation for the mean squared displacement in one dimension is given by equation 8.1, which states that the mean square displacement for a given time window (t) is the mean of the square of the displacement in that dimension in each possible instance of that time window. For example if the time window was

10 s, then the squared distance between the position of the cluster at each time point (x_0) and its position 10 s later ($x(10)$) is measured and averaged.

$$MSD_x(t) = \langle (x(t) - x_0)^2) \rangle \tag{8.1}$$

The mean square displacement in more than one dimension is the sum of the mean square displacements in each dimension, the mean square displacement for two dimensions is given by the equation 8.2.

$$MSD_{xy} = MSD_x + MSD_y \tag{8.2}$$

The mean MSD values were calculated for each time window for clusters in *tlpT -yfp* and *tlpT -yfp* Δ*ppfA* cells (113 and 164 clusters respectively). Then a curve, equation 8.3, was fitted to both data sets. Both the data and the fitted curves are shown in fig. 8.3.

$$f(x) = ae^{(-bx)} + c \tag{8.3}$$

If clusters underwent completely free diffusion then the MSD results would be linear, however for both strains the relationship between time window and MSD quickly deviates from linearity and begins to plateau. This is not unexpected as even if the clusters were able to move completely unhindered, they would still be confined within the cell and therefore, no matter how large the time window used, the maximum displacement could never be greater than the area of the cell. The mean square displacement value of this plateau is therefore the maximum distance the cluster can move in two dimensions, and the square root of this plateau is termed the radius of confinement. In order to extract the MSD values of the plateaus of both data sets the equation 8.3 was fitted, with the value of c

giving the height of the plateau of the mean square displacement data.

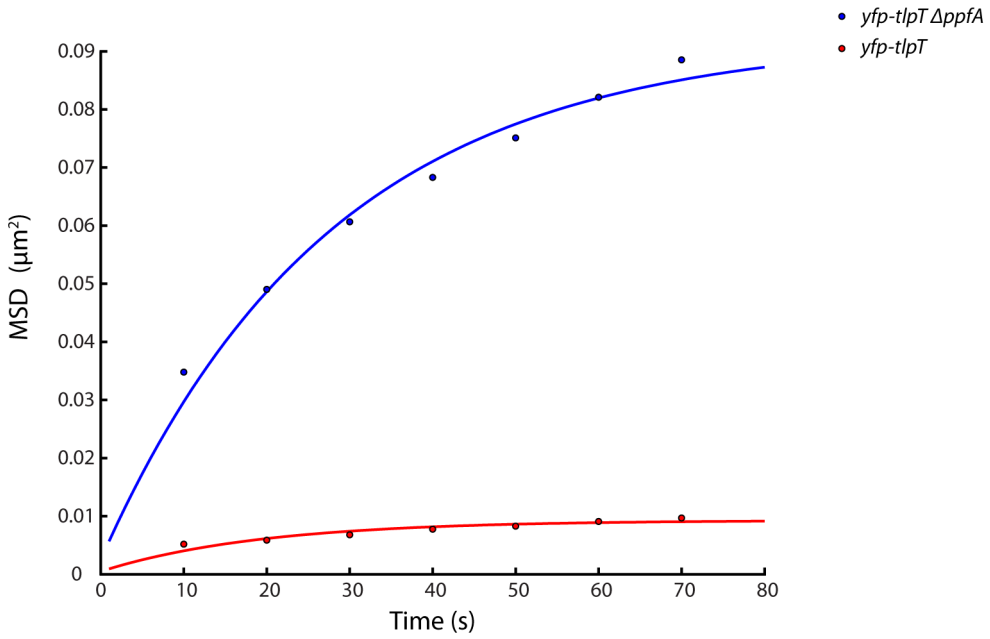

Figure 8.3: Mean squared displacement of clusters in *tlpT -yfp* (in red) and *tlpT -yfp* Δ*ppfA* strains (in blue). Dots represent the mean values for MSD at each time window, and the solid lines the fitted curve. 113 traces were analysed for for *tlpT -yfp* , and 164 for *tlpT -yfp* Δ*ppfA* .

The average confinement radius of the cluster in cells with PpfA is 0.096 μm , whereas that of cells without PpfA is 0.30 μm . These results show that PpfA restricts the area within which the cytoplasmic cluster is able to move.

8.3 Diffusion coefficient of the Cluster

In order to determine whether this is the sole effect of PpfA on movement of the clusters, or whether the rate of movement is also affected, the apparent diffusion coefficients for clusters in cells with and without *ppfA* were calculated. The relationship between the diffusion coefficient and the mean square displacement in two dimensions is shown in equation 8.4, where D is the apparent diffusion coefficient and t is time.

$$MSD_{xy} = 4Dt \tag{8.4}$$

In order to determine the diffusion coefficient of clusters within their confined area the linear region of the mean square displacement curve was needed, therefore only the initial gradient was used to calculate the diffusion coefficients. Box plots of the diffusion coefficients for clusters in *tlpT -yfp* and *tlpT -yfp* Δ*ppfA* cells. The median diffusion coefficient for clusters in *tlpT -yfp* cells is 6.64×10^{-5} $\mu m^2 \cdot s^{-1}$, and that of clusters in *tlpT -yfp* Δ*ppfA* cells is 6.91×10^{-4} $\mu m^2 \cdot s^{-1}$. In order to determine if the difference between the two strains was statistically different a Wilcoxon rank sum test was applied. This showed that the probability of these two populations being the same was < 0.001, and therefore the effect of PpfA on diffusion of the cluster is significant.

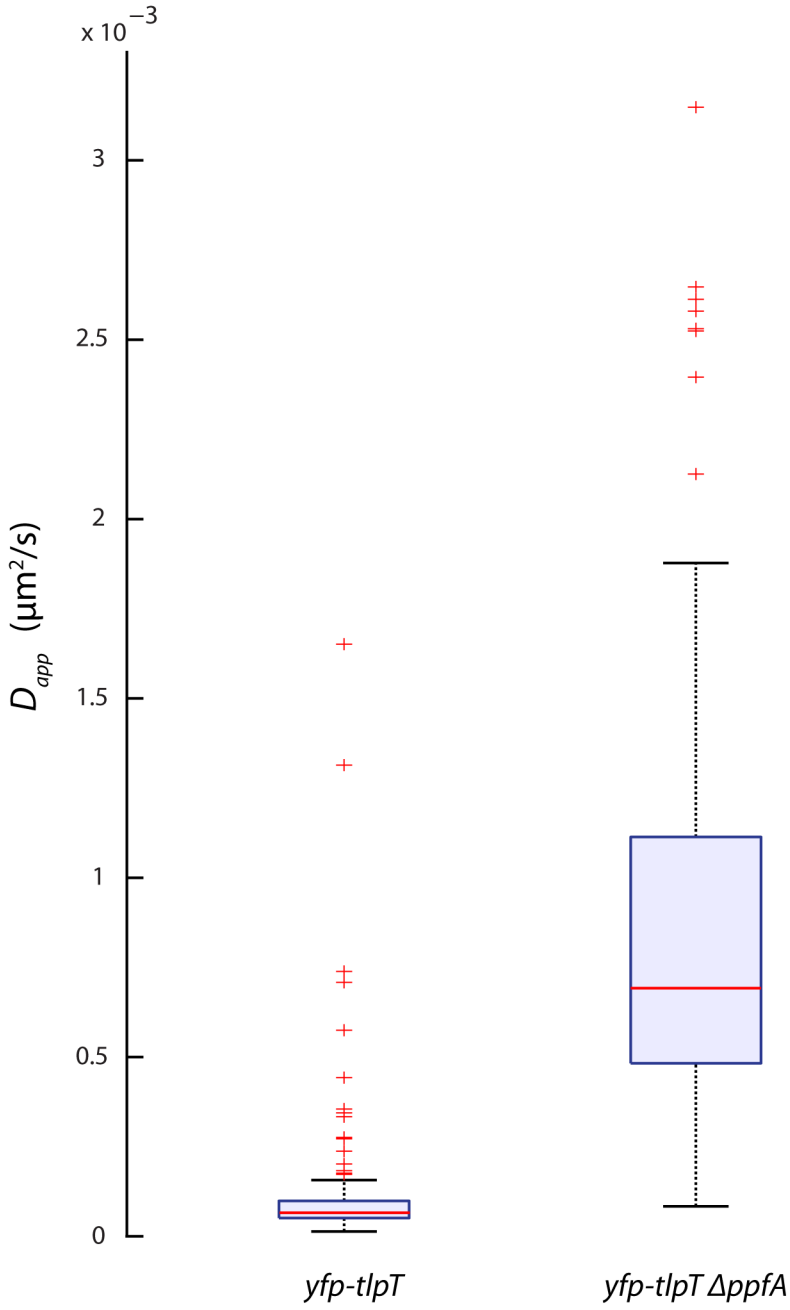

Figure 8.4: Box plot of diffusion coefficients of clusters in *tlpT -yfp* and *tlpT -yfp* Δ*ppfA* strains. Red lines represent the median values, the blue boxes the interquartile range, and the ends of the whiskers 1.5 time the interquartile range beyond the first and third quartiles. Red crosses represent outliers. For *tlpT -yfp* n=113, for *tlpT -yfp* Δ*ppfA* n=164.

8.4 Discussion

The results presented in this chapter show that PpfA controls two aspects of the movement of the cytoplasmic chemosensory cluster. PpfA reduces both the rate of diffusion of the cluster within in the cell, and the size of the area in which the cluster can diffuse.

This mirrors results from a study of the plasmid RK2 [41]. It was shown that the deletion of the type I *par* locus resulted in increased mobility of the plasmid within the cells, the *par* - plasmids diffused rapidly and were able to explore the entire cell volume. Introduction of the F plasmid partition locus onto the *par* - RK2 resulted in restoration of the restriction in mobility. Taken with the results presented in this chapter it is possible that both positioning and maintaining the position of their cargo are common features of type I *par* systems.

This contrasts with results from a type II plasmid segregation system (ParMRC), in which the deletion of the Par operon from the plasmid results in an decrease in the rate of diffusion and the radius of confinement [31]. The model presented for this plasmid segregation system depended upon the dynamic instability of the ParM polymers, which push plasmids apart from each other towards the cell poles. Here the ParM filaments, unable to separate the plasmids any further collapse, allowing the plasmids to undergo free diffusion again, once the two plasmids are in close enough proximity to each other they will again be segregated by ParM filaments. This process results in the active and repeated movement of the plasmids to ensure that on septation they will be spatially separate. Deletion of the segregation machinery results in plasmids just undergoing free diffusion, and loss of active movement. It is clear that the cluster, and RK2 and SopAB plasmid systems discussed above, are positioned by a mechanism which reduces its movement, rather than one which relies upon actively moving it and increasing its mobility.

Chapter 9

Photoactivation Localisation Microscopy of PpfA

Many models of segregation of protein complexes, chromosomes and plasmids by ParA ATPases require the ATP dependent switching of mobility states of the ParA protein. To visualise these sub-populations of molecules single molecule tracking photoactivation localisation microscopy was used. A photoactivatable mCherry fusion was used to track the movement of individual PpfA molecules within living *R. sphaeroides* cells. Combining this technique with epifluorescence imaging of TlpT-YFP made it possible to distinguish between those PpfA molecules interacting with the cluster and those which are not. Therefore the effects of TlpT on individual PpfA molecules could be measured.

9.1 Creation of *ppfA-PAmCherry* fusion constuct in the plasmid pIND4

The *PAmCherry* was amplified from the pROD-*PAmCherry* plasmid by PCR using primers PpfA-PAmCherry-F andPpfA-PAmCherry-R. The PCR product was purified and digested with *BamHI* and *HindIII* restriction enzymes. The plasmid pIND-*ppfA-cfp* was also digested with *BamHI* and *HindIII*, which removed the *cfp* gene. The remaining plasmid was purified from the *cfp* gene using gel electrophoresis. The linearised plasmid lacking *cfp* was then ligated with the digested *PAmCherry* PCR product. The ligation product was transformed into XL-1 *E. coli* cells, which were grown on kanamycin selection plates. Purified pIND-*ppfA-PAmCherry* plasmid from individual clones was then sequenced to confirm correct insertion of the *PAmCherry* gene and absence of PCR errors.

The plasmid was then transformed into the *E. coli* strain S17-λ pir so that it could be conjugated into the *R. sphaeroides* strains *tlpT -yfp* (JPA1558), and Δ*tlpT yfp-cheW*$_4$ (JPA1519).

9.2 Tracking of PpfA-PAmCherry Molecules in Live Cells

Cells containing the plasmid pIND-*ppfA-PAmCherry* were subcultured into succinate media containing 25 μM IPTG and grown to an OD_{700nm} of 0.4. The cells were then immobilised on 1% agarose in succinate media. TlpT-YFP and YFP-CheW$_4$ signals were captured using the 473 nm laser. Single molecules of PpfA-PAmCherry were imaged using simultaneous illumination from 405 nm and 561 nm lasers, for activation and excitation respectively, and imaged using an expo-

sure time of 15 ms for 10000 frames. In order to ensure accuracy of localisation the 405 nm laser illumination was adjusted such that only single molecules of PAmCherry were activated within individual cells at any point in time.

A custom built MATLAB software package, created by [189], was used to fit point spread functions (PSFs) in each frame so that the centre of each PSF could be determined. The same software package was then used to analyse all the localisations in each image set in order to generate tracks of PpfA-PAmCherry molecules.

9.3 The Absence of TlpT Results In Changes In the Diffusion Characteristics of PpfA Molecules

By imaging single PpfA-PAmCherry molecules and generating tracks of their positions over time the behaviour of PpfA in cells with and without TlpT can be compared. Images of PpfA-PAmCherry in TlpT-YFP and Δ*tlpT* YFP-CheW$_4$ cells were acquired across multiple days, and the tracks from each strain were pooled so that mean square displacement values could be calculated. MSD curves for PpfA-PAmCherry in TlpT-YFP, and Δ*tlpT* YFP-CheW$_4$ cells are shown in fig. 9.1. These curves show that the presence of TlpT has an effect on the movement of PpfA molecules, the most striking difference being the MSD values at which they plateau. The values of these plateaux were determined by fitting equation 9.1 to the curves, in this equation a, b, and c are constants, with c being the y axis value of the plateau.

$$f(x) = ae^{(-bx)} + c \tag{9.1}$$

The curve fitting gave values for the plateaus of 0.096 $\mu m^2$and 0.173 $\mu m^2$for PpfA-PAmCherry in TlpT-YFP, and Δ*tlpT* YFP-CheW$_4$ cells respectively. From these

values the mean radii of confinement were calculated, and are 0.31 μm for TlpT-YFP cells, and 0.42 μm for Δ*tlpT* YFP-CheW$_4$ cells.

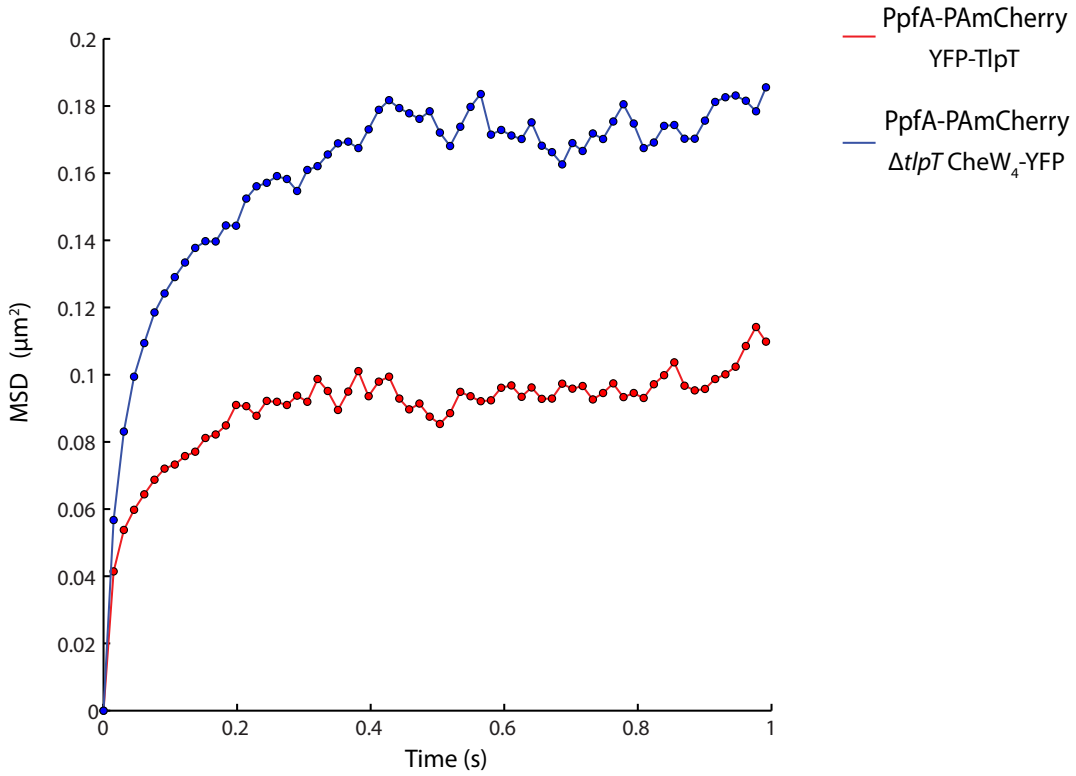

Figure 9.1: Mean square displacement (MSD) of PAmCherry-PpfA molecules. The MSD of PAmCherry-PpfA molecule in TlpT-YFP cells are shown in blue (n=38937), and those in Δ*tlpT yfp-cheW*$_4$ are shown in red (n=16687).

The apparent diffusion coefficient (D_{app}) of single PpfA-PAmCherry molecules was determined by applying the MSD and time window values in the linear region of the MSD curve to equation 9.2. For the comparison and analysis of D_{app} values only tracks of 4 or more steps were analysed, as the error of localisation results in D_{app} values for tracks with fewer than 4 steps being highly variable and unsuitable for comparison.

$$MSD_{xy} = 4D_{app}t \tag{9.2}$$

The spread of apparent diffusion coefficients for each strain is shown in fig. 9.2. These results show that in the absence of TlpT D_{app} values for PpfA-PAmCherry are shifted upward, with the median, lower and upper quartiles all increasing in the absence of TlpT. This difference in distribution of PpfA-PAmCherry D_{app} values was shown to be statistically significant through the application of a Wilcoxon rank sum test, which gave the probability of the two distributions being from the same population as < 0.001.

Previous analysis of FRAP data from PpfA and various PpfA mutants expressed both in *E. coli* and *R. sphaeroides* suggested different possible states of PpfA mobility [152]. Expression of PpfA-CFP in *E. coli* resulted in co-localisation with the nucleoid and a $t_{1/2}$ of recovery of 16 ± 2 s, whereas mutants in both Walker box and putative DNA binding regions resulted in loss of co-localisation with the nucleoid and $t_{1/2}$ values of < 1 s. These results represent diffusion on the chromosome, and free diffusion within the cytoplasm. An ATP locked mutant showed the slowest recovery suggesting that ATP hydrolysis increases the rate of PpfA disassociation from the nucleoid.

Based on this tracks were binned into three categories based on their D_{app} values, one to represent free diffusion in the cytoplasm, one for diffusion on the nucleoid surface, and one for further restricted diffusion. Analysis of the mobility of proteins within the cytoplasm of *E. coli* showed that there is a dependency of D_{app} on the molecular weight of the protein [98]. Diffusion coefficients were determined for a number of proteins in that study, the one with the closest molecular weight to PpfA-PAmCherry (52.8 kDa) was Crr-YFP (45 kDa). The value of D_{app} for Crr-YFP determined was $2 \pm 0.05\ \mu m^2 \cdot s^{-1}$. The D_{app} of a fluorescent fusion to a ParA homologue (SopA-GFP) on an *in vitro* DNA carpet was determined to be $0.85 \pm 0.14\ \mu m^2 \cdot s^{-1}$[195]. Based on the above results two threshold D_{app} values were used, 0.4 and 1.4 $\mu m^2 \cdot s^{-1}$. Molecules with a $D_{app} > 1.4\ \mu m^2 \cdot s^{-1}$display

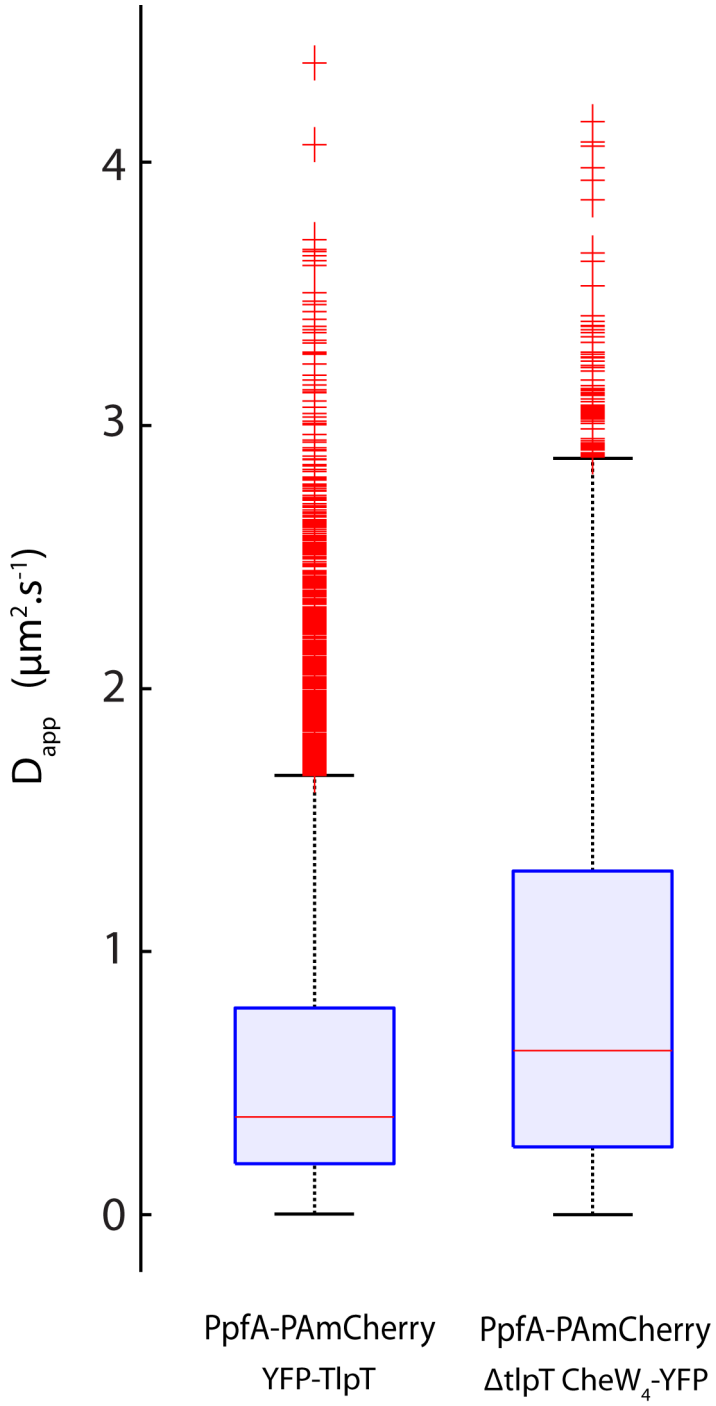

Figure 9.2: Box plot of diffusion coefficients of PpfA-PAmCherry, in TlpT-YFP cells (left) and in Δ*tlpT* YFP-CheW$_4$ cells (right).Red lines represent the median values, the blue boxes the interquartile range, and the ends of the whiskers 1.5 time the interquartile range beyond the first and third quartiles. Red crosses represent outliers. For TlpT-YFP cells 12805 tracks were analysed, and 8268 for Δ*tlpT* YFP-CheW$_4$ cells.

behaviour consistent with a freely diffusing protein of PpfA-PAmCherry's size. D_{app} values below 1.4 $\mu m^2 \cdot s^{-1}$suggest restrained diffusion, such as the diffusion of SopA-GFP on DNA where the rate of diffusion is limited by the protein's interaction with DNA. Values below 0.4 $\mu m^2 \cdot s^{-1}$suggest an even greater restraint on free diffusion, such as tighter binding to DNA or interactions with a third party.

The proportion of tracks which fall between or either side of these two threshold values are shown in fig. 9.3 and summarised in table 9.1.

	Strain		
D_{app} ($\mu m^2 \cdot s^{-1}$)	TlpT-YFP	Δ*tlpT*	YFP-CheW$_4$
$D_{app} < 0.4$	48%		34%
$0.4 \leq D_{app} < 1.4$	42%		43%
$D_{app} \geq 1.4$	10%		23%

Table 9.1: Distributions of diffusion coefficients of PpfA-PAmCherry molecules in TlpT-YFP and Δ*tlpT* YFP-CheW$_4$ cells.

These results show that in TlpT-YFP cells the majority (90%) of PpfA-PAmCherry molecules have D_{app} values below 1.4 $\mu m^2 \cdot s^{-1}$. However in cells lacking TlpT this value is reduced to 77%. The percentage of tracks with D_{app} values between 0.4 and 1.4 $\mu m^2 \cdot s^{-1}$remains consistent between the two strains (42% and 43% for cells with and without TlpT respectively). The proportion of PpfA molecules with D_{app} values below 0.4 $\mu m^2 \cdot s^{-1}$shifts from 47% to 34% in the absence of TlpT. Together these results suggest that TlpT is able to stabilise the slowest diffusing form of PpfA, whilst having no effect on the PpfA molecules proposed to be diffusing on the nucleoid, and decreasing the numbers of PpfA molecules diffusing freely in the cytoplasm.

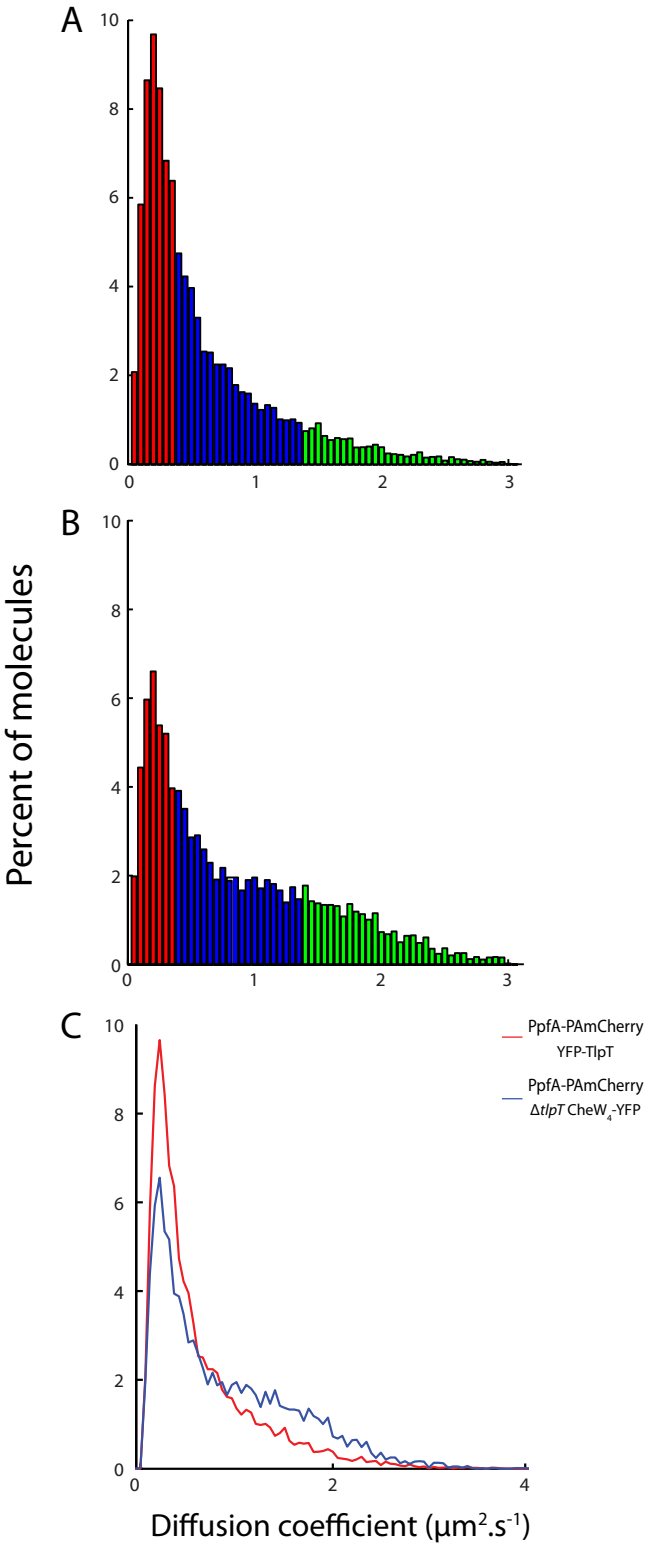

Figure 9.3: Histograms of diffusion coefficients of PpfA-PAmCherry. **A:** Histogram of diffusion coefficients of PpfA-PAmCherry in TlpT-YFP cells. 12805 tracks were analysed. **B:** Histogram of diffusion coefficients of PpfA-PAmCherry in Δ*tlpT* YFP-CheW$_4$ cells. 8268 tracks were analysed. **C:** An overlay of the two histograms for comparison. Diffusion coefficients of PpfA-PAmCherry in TlpT-YFP cells are shown in red, and those in Δ*tlpT* YFP-CheW$_4$ cells are shown in blue.

9.4 Slower PpfA Molecules Co-localise with TlpT

As seen above the presence of TlpT increases the proportion of PpfA-PAmCherry molecules with slow ($< 0.4\ \mu m^2 \cdot s^{-1}$) diffusion coefficients. In order to investigate the spatial distribution of PpfA-PAmCherry molecules with different D_{app} values, and to compare this distribution with the position of the cytoplasmic chemosensory cluster, tracks were displayed over both brightfield and TlpT-YFP fluorescent images of cells. The tracks were coloured based on their D_{app}, with the same bins and colours used as in fig. 9.3. Fig. 9.4 shows images and tracks from representative TlpT-YFP and Δ*tlpT* YFP-CheW$_4$ cells. These results show that slow moving PpfA-PAmCherry molecules co-localise with the cytoplasmic cluster, although not exclusively as slow moving molecules are both seen away from the cluster and in Δ*tlpT* cells. This suggests that TlpT stabilises the slow moving sub-population of PpfA.

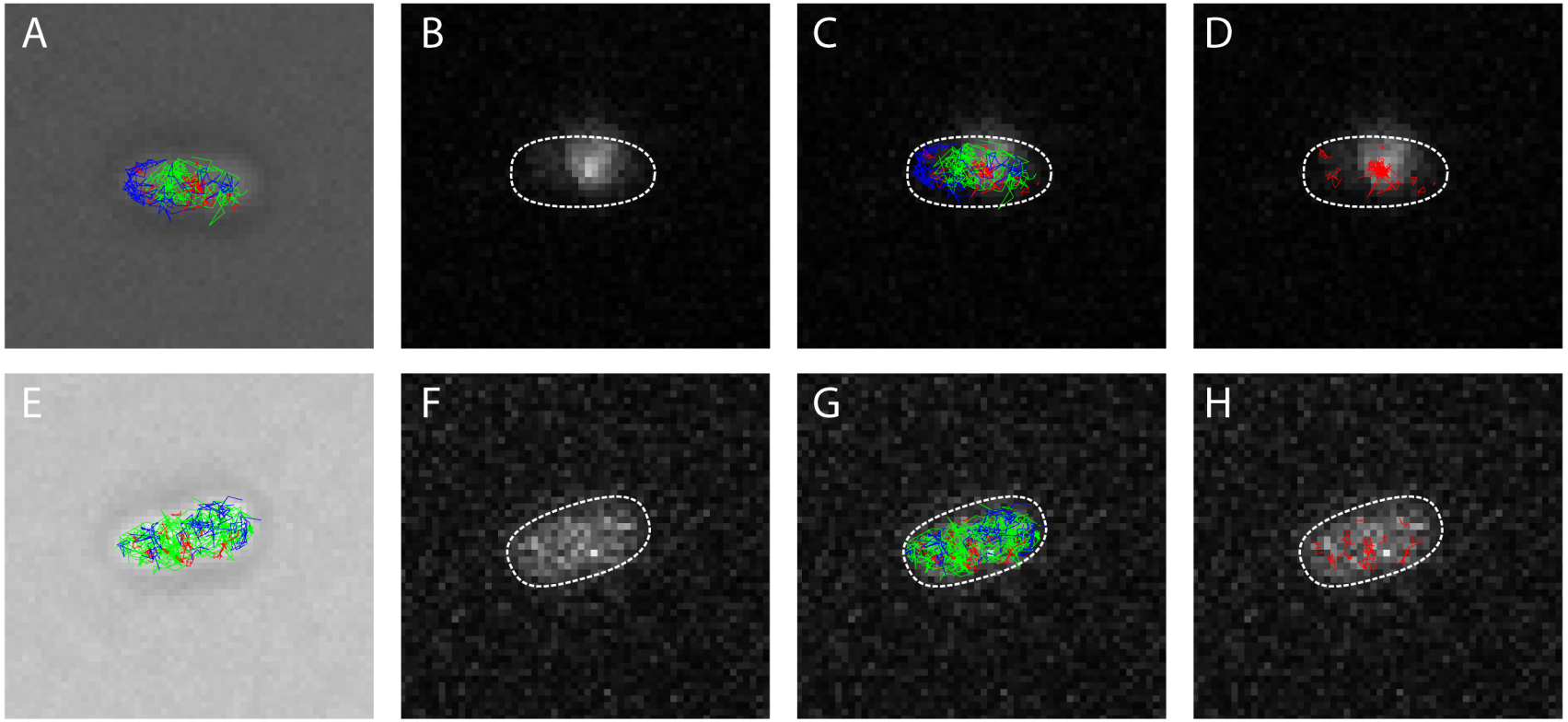

Figure 9.4: Tracking of PpfA molecules in cells with (A-D) and without (E-H) TlpT. **A:** Tracks of PpfA-PAmCherry shown over the transmitted light image of a *tlpT -yfp* cell. **B:** Fluorescent TlpT-YFP of the cell shown in A. **C:** Tracks of PpfA-PAmCherry shown over the transmitted TlpT-YFP image. **D:** Slow tracks of PpfA-PAmCherry shown over the transmitted TlpT-YFP image. **E:** Tracks of PpfA-PAmCherry shown over the transmitted light image of a *yfp-cheW*$_4$ Δ*tlpT* cell. **F:** Fluorescent YFP-CheW$_4$ of the cell shown in E. **G:** Tracks of PpfA-PAmCherry shown over the transmitted YFP-CheW$_4$ image. **H:** Slow tracks of PpfA-PAmCherry shown over the transmitted YFP-CheW$_4$ image. Red tracks are those with diffusion coefficients less than 0.4 $\mu m^2 \cdot s^{-1}$, those in blue between 0.4 and 1.4 $\mu m^2 \cdot s^{-1}$, and those in green greater than 1.4 $\mu m^2 \cdot s^{-1}$.

9.5 Discussion

Results presented in this chapter provide insights into the dynamic behaviour of individual PpfA molecules. They show that PpfA has a range of diffusive states, and that the proportion of molecules in these states is altered by the presence of TlpT. The slower diffusing molecules have a tendency to co-localise with the cytoplasmic chemosensory cluster, indicating that the PpfA foci seen in epifluorescence images are not just due to a higher local concentration of PpfA but also due to decreased mobility of the PpfA molecules in the foci. The formation of ParA foci which co-localise with their cargo is also seen for the P1 plasmid ParA [72], suggesting two states of DNA bound ParA, one spread over the nucleoid and the other co-localised with the plasmid. The presence of multiple DNA bound states of PpfA as well as a freely diffusing cytoplasmic state is supported by both these results and those from previous FRAP experiments performed on PpfA and various PpfA mutants from [152], which are summarised in table 9.2. Whilst the FRAP results provide information about the mobility of a population of PpfA molecules, rather than individual ones, the use of mutants to trap PpfA in various states results in information about the mobility of PpfA molecules in these different states. Mutants defective in dimerisation, ATP binding and DNA binding all displayed rapid exchange and loss of co-localisation with the nucleoid, both in *E. coli* and *R. sphaeroides* , indicating the existence of a rapidly diffusing state of PpfA in the cytoplasm. The recovery rate of PpfA expressed in *E. coli* and in a *R. sphaeroides* strain with the N-terminus of TlpT deleted, which in both cases co-localises with the nucleoid, suggests a state dependent of DNA binding, dimerisation and ATP binding, but independent of TlpT in which PpfA diffuses across the surface of the nucleoid. In order to confirm the differing mobilities of PpfA molecules in these different states the PALM experiments should be repeated with the mutants tested in [152].

Mutant	Description	$t_{1/2}$ (s) of PpfA-CFP expressed in...	
		E. coli	*R. sphaeroides*
WT		16 ± 2	10 ± 2 (foci) 8 ± 1 (diffuse)
G10V	Inhibition of dimerisation	< 1	< 1
K14A	Inhibition of ATP binding	< 1	< 1
D39A	ATP locked	19 ± 3	22 ± 3
R167E, K196E	Distribution of DNA binding	< 1	< 1
WT	in *tlpT* ΔN background		16 ± 1

Table 9.2: Summary of PpfA FRAP data from [152]

By bleaching both PpfA in regions corresponding to the position of the cluster and positions away from the cluster it was shown that PpfA molecules which co-localise with the cluster turnover slower than those distal from it. This is mirrored in the results presented here which show that TlpT and the cluster stabilise the slow moving PpfA molecules. When the N-terminus of TlpT is deleted PpfA turnover slower in the FRAP experiments, however in the data presented here a full-length deletion of *tlpT* resulted in PpfA molecules with faster diffusion coefficients. The basis for this difference is uncertain; FRAP experiments on a full length *tlpT* strain and single molecule PALM tracking on the *tlpT* ΔN would reveal whether the difference is in PpfA mobility or a result of the experimental technique used.

Recent studies performing FRAP on ParA proteins on DNA carpets have shown that related plasmid segregation ParA proteins display different shifts in dynamic behaviour when their cognate ParB protein is present. The P1 plasmid ParA exchanges slower on *in vitro* DNA carpets when ParB is also present [87], suggesting that ParB may be able to temporarily stabilise the ParA-ATP interaction with DNA before inducing ATP hydrolysis. However the F plasmid ParA (SopA) exchanges faster on a DNA carpet in the presence of SopB [195], clearly contrasting the results for P1 ParA, suggesting that SopB both increases the rate of SopA dissociation from the nucleoid and inhibits its re-association with it. This highlights

the variation in type I plasmid partition systems, present even in systems proposed to use the same underlying mechanisms. The co-localisation of the cluster and slowly diffusing PpfA molecules could be explained by TlpT possessing a similar ability to that of P1 ParB, stabilising the interaction between PpfA and the nucleoid.

The use of single molecule PALM tracking in live cells reveals the clear diversity of mobilities of PpfA.

Chapter 10

Expression of *tlpT* and *ppfA* in *E. coli*

It has been previously shown that when expressed in *E. coli* PpfA co-localises with the nucleoid [152]. In order to investigate the interaction between TlpT and PpfA inducible plasmids containing fluorescent fusions to both genes were transformed into a WT *E. coli* strain (RP437). Both constructs were expressed, both together and individually, to investigate their localisation patterns.

10.1 Co-expression of TlpT-YFP and PpfA-CFP

Plasmids containing *tlpT-yfp* (pBAD33-*tlpT-yfp*) and *ppfA-cfp* (pIND-*ppfA-cfp*) were transformed into *E. coli* (strain RP437). Cells were grown overnight at 30°C , then subcultured and expression induced with 200 μm IPTG and 0.2 % W/V arabinose.

Example cells are shown in fig. 10.1. As expected from previously published results (in which it co-localises with DAPI stained nucleoid [152]) PpfA-CFP produces a distribution of a nucleoid bound protein. Interestingly a very similar distribution is seen for TlpT-YFP, which clearly is localised to the nucleoid and absent from inter-nucleoid spaces. Unexpectedly TlpT-YFP is also able to form

foci in many cells (fig. 10.1 lower middle panel). The positioning of these foci on the nucleoid suggests that they are not simply the result of misfolding and aggregation as misfolded aggregates localise to the cell poles and internucleoid spaces [208], the exact opposite distribution to that seen for TlpT-YFP.

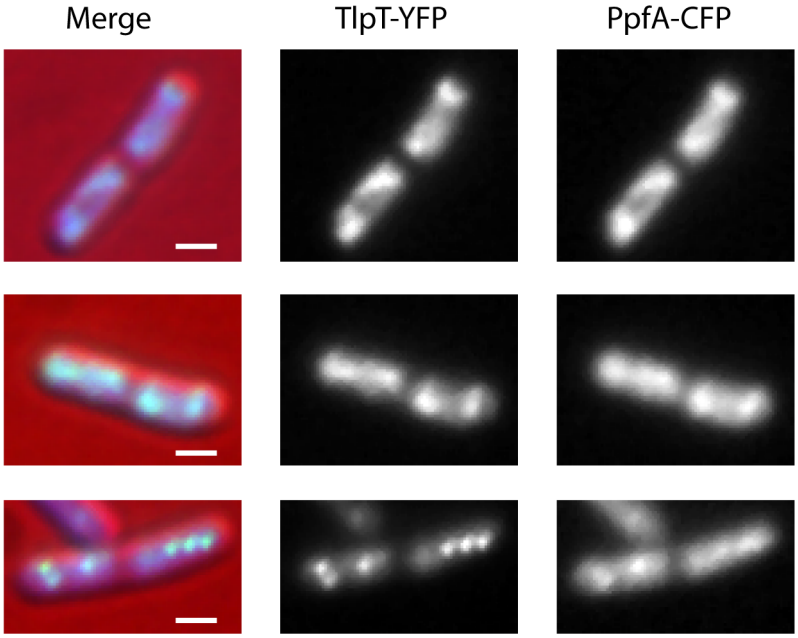

Figure 10.1: Images of TlpT-YFP and PpfA-CFP co-expressed in *E. coli* . Left panel shows a merge of the DIC image (in red), TlpT-YFP image (in green) and the PpfA-CFP image (in blue). Middle panel shows TlpT-YFP images, and the right panel show the PpfA-CFP images. Scale bars are 1 μm .

To confirm this pattern of TlpT-YFP and PpfA-CFP distribution, cells were treated with cephalexin (as described in 2.5.1) resulting in filamentous cells with clearly distinct nucleoids. Images of *E. coli* cells expressing TlpT-YFP and PpfA-CFP which have been treated with cephalexin are show in fig. 10.2. As with non-filamentous cells PpfA-CFP can be seen binding the nucleoid, and TlpT-YFP co-localising with it, forming foci and absent from the internucleoid spaces. The absence of TlpT-YFP from the internucleoid spaces indicates that it is not diffusing freely in the cytoplasm.

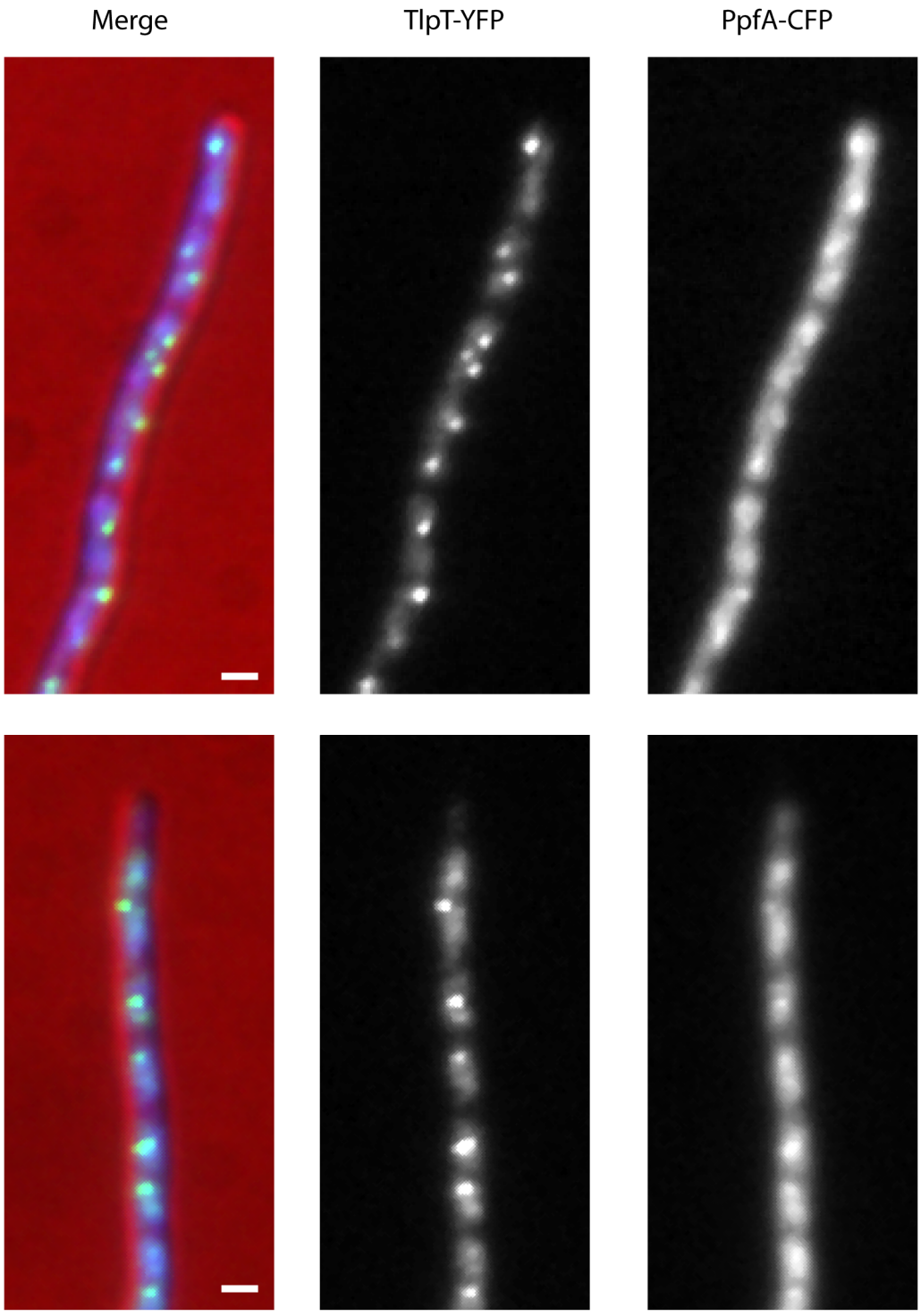

Figure 10.2: Images of TlpT-YFP and PpfA-CFP co-expressed in cephalexin treated *E. coli* . Left panel shows a merge of the DIC image (in red), TlpT-YFP image (in green) and the PpfA-CFP image (in blue). Middle panel shows TlpT-YFP images, and the right panel show the PpfA-CFP images. Scale bars are 1 μm .

10.2 Expression of TlpT-YFP

To test whether the localisation of TlpT-YFP to the nucleoid was due to the presence of PpfA, pBAD33-*tlpT-yfp* alone was transformed into *E. coli* , and grown and expressed as above (omitting IPTG). Surprisingly the localisation of TlpT-YFP in *E. coli* is very similar in both the presence and absence of PpfA. Images of cells expressing just TlpT-YFP are shown in fig. 10.3. These show that TlpT-YFP still appears to co-localise with the nucleoid.

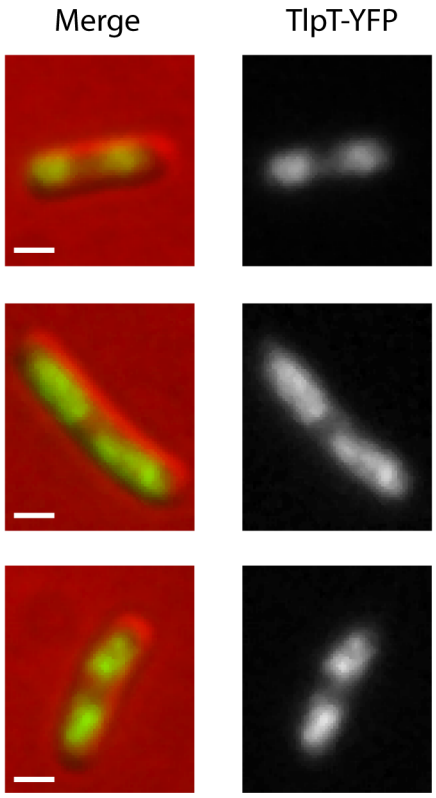

Figure 10.3: Images of TlpT-YFP expressed in *E. coli* . Left panel shows a merge of the DIC image (in red), and the TlpT-YFP image (in green), right panel shows TlpT-YFP images. Scale bars are 1 μm .

As previously this pattern was confirmed by cephalexin treatment of the cells (see fig. 10.4.

The co-localisation of TlpT-YFP with the *E. coli* nucleoid was confirmed by DAPI staining the cells, as seen in fig. 10.5 (David Zollman, unpublished data). These results clearly show that the TlpT-YFP foci are positioned in the nucleoid.

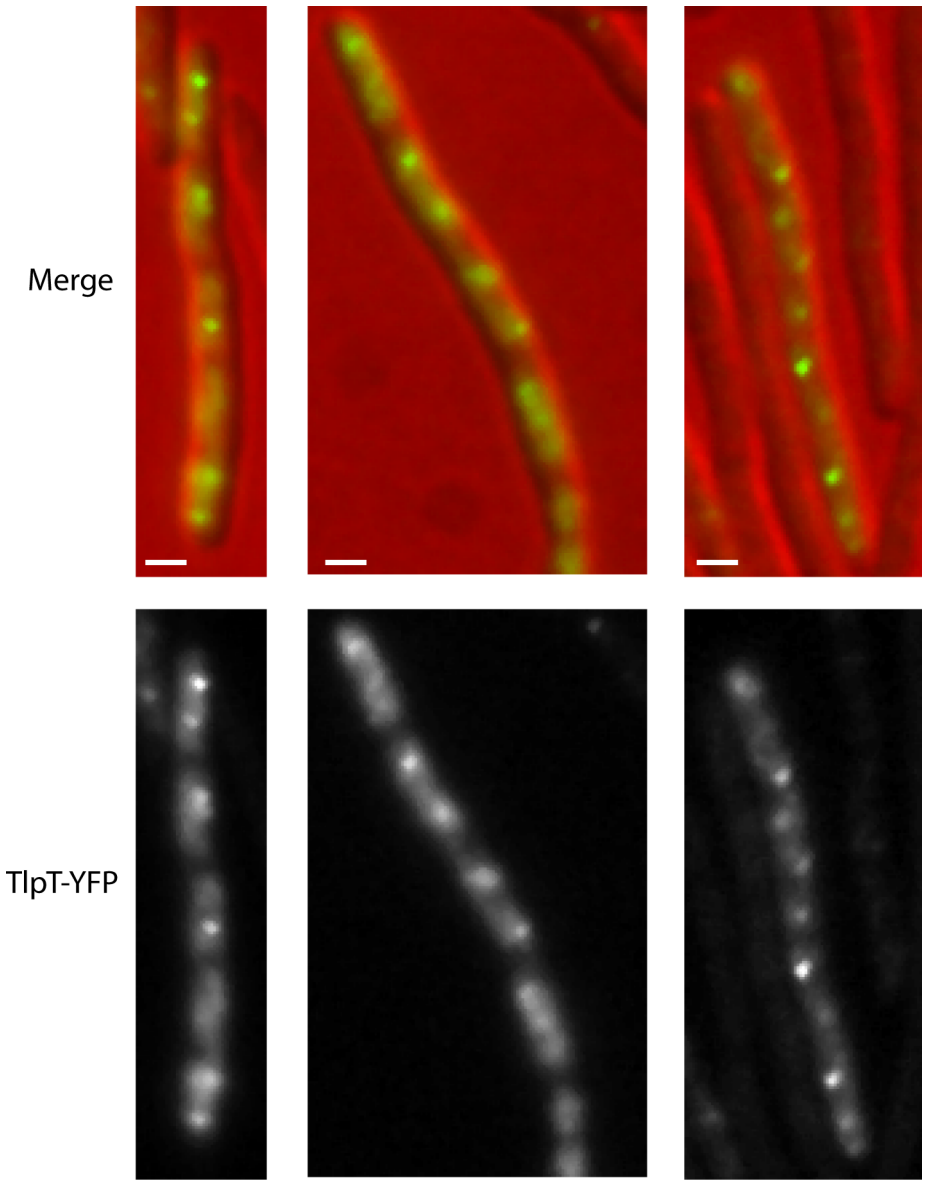

Figure 10.4: Images of TlpT-YFP expressed in cephalexin treated *E. coli* . Left panel shows a merge of the DIC image (in red), and the TlpT-YFP image (in green), right panel shows TlpT-YFP images. Scale bars are 1 μm .

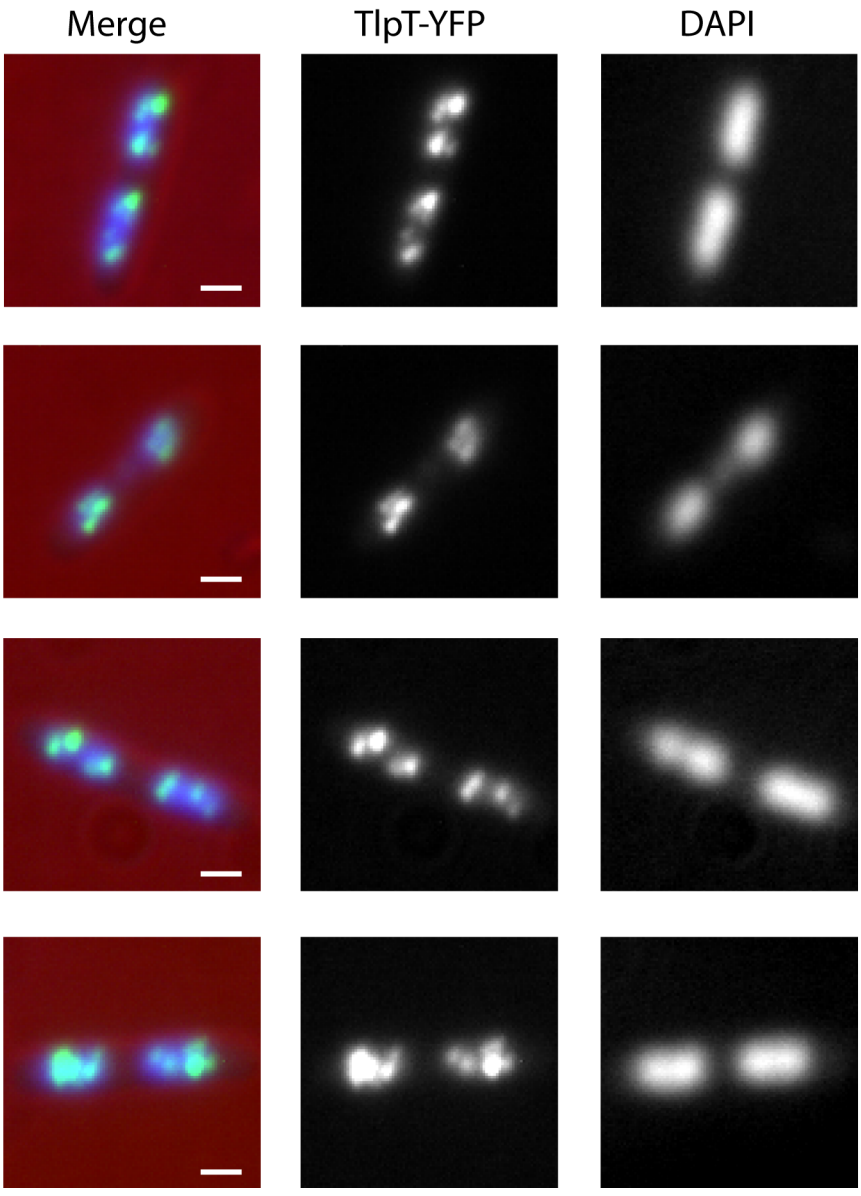

Figure 10.5: Images of TlpT-YFP expressed in *E. coli* cells stained with DAPI. Left panel shows a merge of the DIC image (in red), and the TlpT-YFP image (in green), middle panel shows TlpT-YFP images, and right panel DAPI images. Scale bars are 1 μm . Courtesy of David Zollman

10.3 Discussion

The results presented in this chapter, while very preliminary, suggest that TlpT-YFP may be able to bind the nucleoid. This result was unexpected and warrants further investigation to confirm whether this interaction is real or just an artefact of expressing TlpT in *E. coli* . The *E. coli* chromosome is not dependent on a *parABS* loci for segregation, however there are several loci present, therefore interaction with a host ParA can not be ruled out.

It was also interesting to see TlpT-YFP form foci in *E. coli* despite the absence of of any *R. sphaeroides* cytoplasmic cluster proteins. Further work has to be done to determine if TlpT is interacting with any of the *E. coli* chemotaxis proteins to form these foci, or if these foci are solely TlpT, or indeed if they are artefactual. Variation in expression levels of both *tlpT* and *ppfA* should be used to determine any potential dependency of focus formation. The nucleoid in *R. sphaeroides* fills the whole cell therefore it is not possible to determine whether TlpT is able to bind DNA in *R. sphaeroides* through epifluorescence microscopy

Chapter 11

Discussion

11.1 Comparison of the cytoplasmic chemosensory cluster with membrane associated chemoreceptor arrays

Compared to membrane bound chemoreceptor clusters very little is known about the cytoplasmic chemoreceptor cluster of *R. sphaeroides* . The architecture, formation, dynamics, positioning, partitioning have all been investigated for membrane bound chemosensory clusters, however there is very little information regarding these aspects of the cytoplasmic chemosensory cluster of *R. sphaeroides* or indeed any bacterial cytoplasmic chemosensory cluster.

A great deal is known about the polar membrane bound chemosensory cluster of *E. coli* , which is used as the primary paradigm for bacterial chemoreceptor arrays. A study investigated the dynamics of chemoreceptor arrays used fluorescent fusions to chemosensory proteins in the polar cluster and FRAP to determine the levels of turn-over of proteins within the *E. coli* polar cluster. The results from this study show that the transmembrane chemoreceptors are the most stable

component of the array [164], given that they can only diffuse in two dimensions through lipids this is not unexpected. CheW and CheA were also stable, although less stable than the receptor, and proteins such as CheB and CheR were less stable again. Therefore the core the array is made up of transmembrane receptors whose inherently reduced mobility is further reduced through interactions with CheA and CheW. Given that these results present the membrane as a key scaffold around which the array is built and maintained, they raised a number of questions regarding how the cytoplasmic cluster is organised and held together.

FRAP experiments were performed on cytoplasmic chemosenory proteins in order to determine the turn-over of proteins within this array and compare them to membrane bound cluster of *E. coli* . The results presented in Chapter 7 showed that the the receptors, CheA proteins and CheW protein of the cytoplasmic cluster of *R. sphaeroides* all have low levels of turn-over, suggesting that like the array of *E. coli* the cytoplasmic array is relatively stable structure with limited turnover. There were however some key differences in exchange rates. The turn-over of TlpT proteins might be slow, but it is much faster than that seen for Tar (the transmembrane chemoreceptor tested by Schulmeister *et al.*). The turn-over rates of $CheA_3$ and $CheA_4$ are similar to that of *E. coli* CheA, as is that of $CheW_4$ compared to *E. coli* CheW. However for all three of these proteins the fraction of proteins which are able to undergo exchange is considerably less than their *E. coli* homologues, which both have mobile fractions of 100%.

The difference in receptor turnover can be explained by the lack of membrane to restrict TlpT movement, although another chemoreceptor, TlpC, displayed no turn-over at all. The reduced mobile fraction for the CheA and CheW proteins compared to *E. coli* may be due to the need for the array components to be highly stable in order to compensate to the increased mobility of some receptors.

After clusters split the two resultant cluster are often not of equal size (as shown

in Chapter 6). It was hypothesised that in these cells with two clusters of unequal size exchange of protein between them could result in equilibration of sizes before cell division. However the rate of exchange exhibited by all the proteins investigated here is too slow to drive such equilibration on the time scale of cell division, therefore suggesting that growth of the new cluster is due to incorporation of newly expressed protein. How this newly expressed protein is divided by the old (larger) and new (smaller) clusters has yet to be investigated, and would reveal interesting details regarding whether clusters grow equally, in proportion to their size, or if new protein is specifically directed to the smaller cluster.

A system in which *tlpT* was expressed in cells lacking the genomic copy of *tlpT* was used to follow the *de novo* formation of clusters, and is described in Chapter 5. These results show that the cluster is able to self-assemble once all the required proteins are present. The number of clusters formed increases with cell length in both normal and cephalexin treated cells which suggests two possible mechanisms for this formation: targeted formation at a cellular 'landmark', or stochastic self-assembly. The results presented favour a stochastic self-assembly model of formation similar to that proposed for the membrane bound chemoreceptor array of *E. coli* [184, 66, 202]. This is based on a number of observations, firstly despite the apparent regular spacing of clusters within cells, this spacing is not consistent between cells of the same length. PpfA does not act as a landmark for cluster formation, as cephalexin treated cells also form multiple clusters with apparent regular spacing, PpfA only forms a focus when TlpT is formed into a cluster, and PpfA binds DNA non-specifically. Therefore a stochastic self-assembly model for the formation of the cytoplasmic cluster is proposed, in which the formation of clusters is dependent on the diffusion of TlpT molecules and the cytoplasmic volume of the cell. In small cells which have formed a single cluster any newly expressed TlpT molecules will encounter the existing cluster before they are able to stochastically nucleate a new cluster, larger cells allow additional nucleation

events to occur.

Whilst PpfA does not act as a landmark results suggest that it does bias the stochastic self-assembly. Cells with PpfA were able to form a greater number of clusters at a given cell length, and less TlpT was needed to form clusters compared to Δ*ppfA* cells. Together these data suggest that PpfA stabilises the formation of new clusters, reducing the threshold of cell size and TlpT concentration for cluster nucleation.

Our understanding of how the cluster is positioned and segregated is somewhat limited by the lack of knowledge regarding its architecture. A greater understanding of this would allow greater speculation on the nature of the nucleoid-PpfA-TlpT interface.

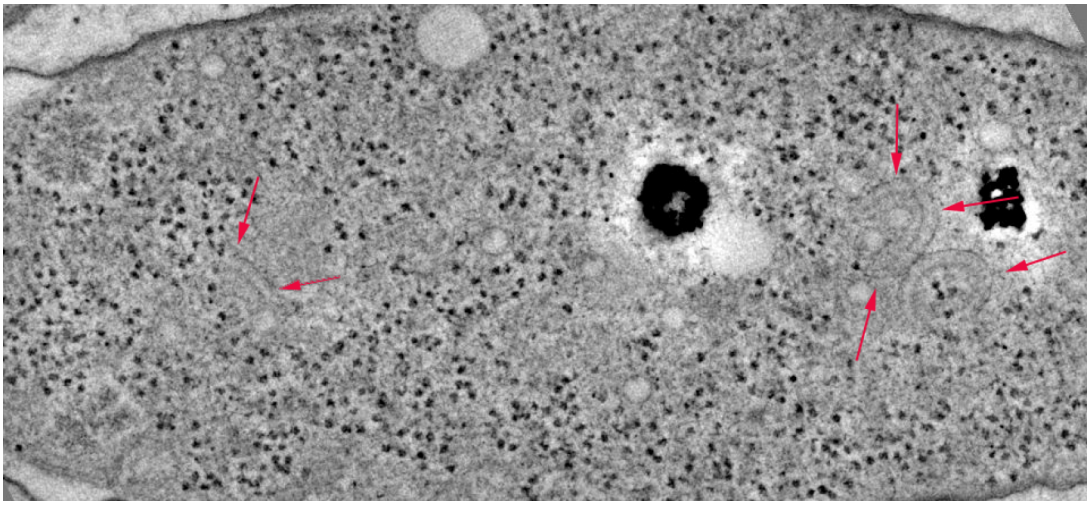

Figure 11.1: Electron cyro-tomograph of *R. sphaeroides* showing the cytoplasmic chemosensory cluster. Red arrows indicate cytoplasmic clusters. Image courtesy of Ariane Briegel (California Institute of Technology).

Recent results from a collaboration with Ariane Briegel and Grant Jensen (California Institute of Technology) have provided the first details on the structure of the cytoplasmic chemoreceptor array. Structures seen in electron cryo-tomographs were proposed to be the cluster, but results were ambiguous. Strains in which the chemotaxis proteins are overexpressed produce a greater number of cluster than WT and electron cryo-tomographs of these strains confirmed an increase in the

structures proposed to be the cluster. The final confirmation that these were indeed the cytoplasmic cluster was through immunogold staining with a anti-GFP antibody and a TlpC-GFP strain.

The structures confirmed to be the cytoplasmic chemosensory array are shown in fig. 11.1. The distance between the inner membrane and the CheA/CheW base plate of the *R. sphaeroides* polar cluster is 21nm [26], the corresponding distance for the cytoplasmic cluster has been measured at 21.5nm (Ariane Brigel, personal communication). Top down views of the array were captured and used to investigate the packing of the chemoreceptors, an example is shown in fig. 11.2 A. Power spectra from these images were used to determine the symmetry of packing (shown in fig. 11.2 B), and showed that like the *R. sphaeroides* polar cluster and indeed all bacterial chemoreceptor arrays trimers of dimers of the chemoreceptors are packed into a hexagonal array (Ariane Brigel, personal communication). The spacing of this array is 12nm, the same as that for the *R. sphaeroides* polar cluster and all membrane bound clusters investigated by Briegel *et al.*

These results suggest that the chemoreceptors pack in the same manner as other transmembrane chemoreceptors, however questions remain as to how these structures interface with PpfA and the nucleoid.

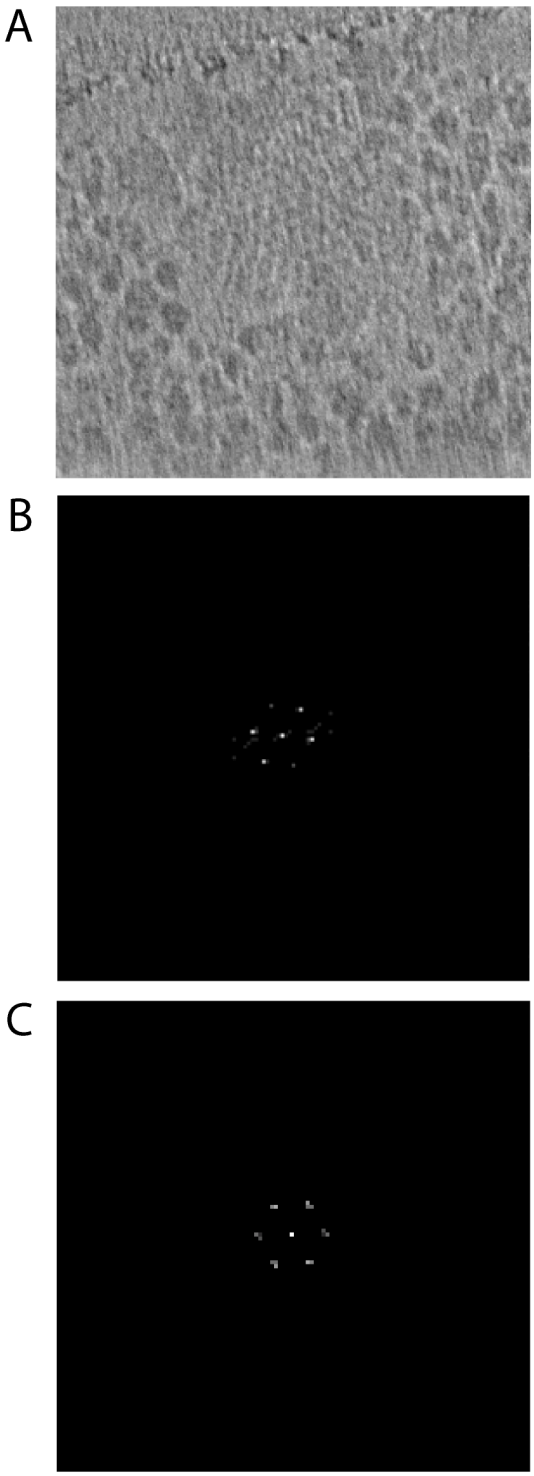

Figure 11.2: Hexagonal packing of the *R. sphaeroides* cytoplasmic chemosensory cluster. **A:** A top down view of the cytoplasmic chemoreceptor array. **B:** Power spectrum of the array in A showing the packing arrangement. **C:** Power spectrum of the polar chemoreceptor cluster from the same cell, showing identical packing pattern. Images courtesy of Ariane Briegel.

11.2 The role of PpfA in cluster segregation

Time-lapse microscopy was used to follow both PpfA and TlpT localisation during the cell cycle. These results (presented in Chapter 6) were then used to compare the segregation of the cytoplasmic cluster with that of both protein and plasmid complexes by ParA ATPase. The results showed that the PpfA focus which coincides with the cytoplasmic cluster in single snap-shot images remains with the cluster throughout the cell cycle. No oscillations of PpfA localisation were observed, which rules out the oscillatory self-organisation model proposed for the F plasmid [73]. The results also rule out a model proposed for the P1 plasmid in which the ParA is spread over the nucleoid with brighter foci which coincide with the plasmids [72], as while the co-localisation of the cluster and the PpfA focus is reminiscent of this pattern there are several clear differences. The P1 ParA focus sporadically disassembles and assembles producing a blinking effect, plasmid segregation is produced by a single P1 ParA focus disassembling and reassembling into two foci to which the plasmids then move. No blinking of PpfA foci was observed, nor did the PpfA foci split before the cluster, both the cluster and the PpfA foci split and segregated simultaneously.

In systems where plasmids are positioned through rapid and dynamic relocalisation by a Par system the majority of the movement of the plasmid is due to the Par system. Thus in the absence of the Par system the plasmid's movement should be solely due to Brownian motion and therefore have reduced mobility compared to when in the presence of the Par system. Such an effect has been demonstrated for the type II plasmid partitioning system, a plasmid is less mobile when the *par* locus has been deleted [31]. However for type I plasmid partition systems it has been shown the the partition system significantly reduceds the mobility of the plasid [41].

When *ppfA* is deleted the cytoplasmic cluster dramatically increases in mobility

(as seen in the results presented in Chapter 8), showing that PpfA restrains the mobility of the cytoplasmic cluster. The results showed that PpfA both reduced the apparent diffusion coefficient of the cluster and reduced its radius of confinement, suggesting that PpfA not only reduces the speed at which the cluster can move but also contains its movement to a small subcellular region. This suggests that both plamids ParAs and PpfA both restrain as well as position their cargo indicating that they mechanism for partitioning is not dependent on rapid repositioning as is the case for type II par systems.

Previous results had shown that PpfA non-specifically binds DNA in an ATP dependent and TlpT independent manner [152]. What then causes the formation of PpfA foci? It could be due to an increased concentration of PpfA due to the nucleoid and TlpT providing an increased capacity for the binding of PpfA molecules, or the increased concentration could be due to decreased mobility of PpfA molecules in the focus. In order to address this question single molecule tracking PALM was used. The results shown in Chapter 9 show that the slower PpfA molecules tended to co-localise with the cytoplasmic cluster, and that cells without *ppfA* had a higher median apparent diffusion coefficient. These results suggest that TlpT may stabilise PpfA's interaction with the nucleoid.

A collaboration with Molly Allen and Suckjun Joon (University of California, San Diego) was initiated to investigate the interactions between the nucleoid, PpfA and TlpT. Cells were trapped in microfluidic channels and then gently lysed (as described in [130]) and the nucleoid, PpfA and TlpT were followed during this process. The results showed that PpfA remained with the chromosomes as they escaped the cell during lysis, occasionally the cytoplasmic cluster also remained with PpfA and the DNA. However in the majority of cases the cluster is retained within the shell of the cell. These results show that whilst the cluster can interact with PpfA and the nucleoid, outside the cell the interaction is relatively weak as

in most cases the chromosomes rapidly escaping the cell cause the cluster to be stripped off.

11.3 Relationship between segregation of the cytoplasmic cluster and the chromosomes of *R. sphaeroides*

Recent work determining the timings of the replication and segregation of origin and termini of the chromosomes of *R. sphaeroides* has revealed details about the relationship between chromosome and cluster replication and segregation.

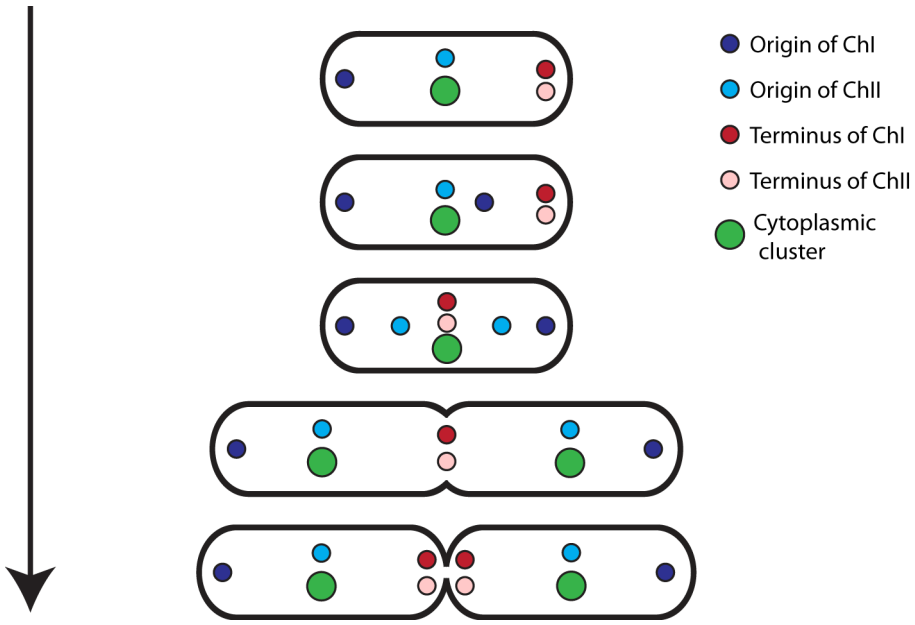

Figure 11.3: Chromosome and cytoplasmic cluster segregation in *R. sphaeroides* . Arrow indicates progression through the cell cycle. Vertical displacement of positions is for clarity and does not represent actual differences in positioning. ChI - chromosome I, ChII - chromosome II.

These results show that the origin of chromosome I (*oriCI*) relpicates and segregates first, shortly followed by the origin of chromosome II (*oriCII*). Following this the cytoplasmic cluster segregates, and finally the termini of both chromosomes replicate and segregate (Nelly Dubarry, unpublished data). These results are sumarised in fig. 11.3. It is clear that chromosome replication occurs before

cluster segregation; 95% of cells with two clusters also have two *oriCI*. It is currently unclear what influence the replication and segregation of the chromosomes has on cluster segregation. It is possible that the segregating chromosomes pull the cluster apart as they move in opposite directions, it may play a more passive role with a larger nucleoid surface allowing PpfA to segregate the cluster, or the two may be unrelated and the timings coincidental.

11.4 Possible models for segregation of the cytoplasmic cluster and future work

No current models of segregation of chromosomes, plasmids or protein complexes adequately describe the results observed for the segregation of the cytoplasmic chemosensory cluster of *R. sphaeroides* . However the ATP dependent interaction of PpfA with the nucleoid suggest that like many ParA systems the nucleoid is used as a surface on which ParA proteins can generate localisation patterns.

There are possible preliminary models which require further work. One model is that PpfA is able to form filaments which nucleate from the cluster and push against both the other cluster and the cell membranes. In this model TlpT would have to promote the formation of PpfA filaments, which would nucleate around it thus explaining the less mobile focus of PpfA at the cluster. Investigations into the possible *in vivo* presence of PpfA filaments, and the effect of TlpT on these filaments are needed to test this model.

It is also possible that rather than acting as a conventional ParB and activating ATPase activity TlpT may act to stabilise the dimeric ATP bound form of PpfA. There is precedent for such a role in the chromosomal ParB of *C. crescentus* which activates the ATPase activity of ParA but promotes ATP binding and dimerisa-

tion of MipZ (a ParA/MinD homologue). This would explain the local increase in stable PpfA molecules at the cluster but does not suggest a mechanism for segregation.

The force of the segregating chromosomes is also a possible driver of cluster splitting and segregation. However this does not explain the slow segregation and often seen movement of clusters towards and away from each other before final segregation. Origin replication occurring soon after cell division and termini replication happens just prior, therefore chromosome replication and segregation is happening during most of the cell cycle. Thus care must be taken to differentiate between causation and correlation.

Results suggesting that TlpT may also bind DNA were unexpected and require further work. If verified consideration must be taken as to what role this may play in cluster segregation.

Taken together these data suggest that a ParA/MinD ATPases have evolved to use a range of mechanisms to control the correct positioning of macromolecules during cell development and division. The PpfA dependent segregation of the cytoplasmic chemosensory cluster of *R. sphaeroides* uses a novel mechanism and understanding the mechanism in more detail has implications for the organisation of protein complexes in other systems.

Chapter 12

Appendices

A Media and Reagents

Luria broth

Ingredient	Quantity per litre
Yeast extract	5 g
Tryptone	10 g
NaCl	5 g

Made up to 1 litre with MilliQ water. Adjusted to pH 7.0. Autoclave.

Succinate media

Ingredient	Quantity per litre
1M Phosphate buffer pH 7.0	20 ml
Concentrated base (see below)	20 ml
Growth factors (see below)	2 ml
$(NH_4)_2\ SO_4$	0.5 g
NaCl	0.5 g
Sodium succinate	2 g
Casamino acids	1 g

Made up to 1 litre with MilliQ water, pH adjust to 7.2 with KOH, autoclave.

1M Phosphate buffer pH 7.0

Ingredient	Quantity per litre
K_2HPO_4 1M	174.18 g
KH_2PO_4 1M	136.09 g

Adjust to ph 7.0 with KOH, autoclave and store at 4°C .

Concentrated base

Ingredient	Quantity per litre
Nitrilotiracetic acid (diNa salt)	5.94 g
Metals 44 solution	25 ml
$MgSO_4$ $7H_2O$	14.5 g
$CaCl_2$ $2H_2O$	1.67 g
$FeSO_4$ $7H_2O$	50 mg
Ammonium molybdate $4H_2O$	4.6 mg or 0.2 ml of 23 mg/ml

Dissolve diNa first and pH with KOH to pH 5.0, it won't dissolve until very near pH 5. This allows $FeSO_4$ to dissolve. Don't worry if you over pH it, adding the other ingredients with bring the pH back down. Add all the other ingredients. pH to 6.8 with KOH. Autoclave and store a 4°C .

Metals 44 solution

Ingredient	Quantity per litre
Tetrasodium versenate (EDTA)	2.5 g
$ZnSO_4$ $7H_2O$	11 g
$FeSO_4$ $7H_2O$	5 g
3M sulphuric acid	1.5 ml
$MnSO_4$ $4H_2O$	3 g
$CuSO_4$ $5H_2O$	0.39 g
H_3BO_3	0.12 g
$CoCl_2$ $6H_2O$	0.2 g

Filter sterilise and store at 4°C .

Growth factor

Ingredient	Quantity per litre
Biotin	20 mg
$NaHCO_3$	500 mg
Niacin	1 g
Thiamine HCL	500 mg

Autoclave and store at 4°C .

M22

Ingredient	Quantity
1 M phosphate buffer	20 ml
Conc. base	20 ml
Growth factor	2 ml
$(NH_4)_2\ SO_4$	0.5 g
NaCl	0.5 g

Made up to 1 litre with MilliQ water, pH adjust to 7.2 with KOH, autoclave.

10 x M9

Ingredients	Quantity
$NaHPO_4\ 2H_2O$	75.2 g
KH_2PO_4	30 g
NaCl	5 g
NH_4Cl	10 g

Made up to 1 litre with MilliQ water.

SOC media

Ingredient	Concentration
Glucose	20 mM
MgCl	10 mM
$MgSO_4$	10 mM
NaCl	10 mM
Tryptone	20 g/l
Yeast extract	5 g/l

5 x DNA loading dye

Ingredient	Quantity (W/v)
Glycerol	70%
Bromophenol blue	0.25%
Xylene cyanol	0.25&
MilliQ water	29.5&

10 x TBE

Ingredient	Quantity
Tris base	108 g
Boric acid	55 g
EDTA pH 8.0	7.4 g

Made up to 1 litre with MilliQ water. pH adjusted to pH 8.3.

TFB I

Ingredient	Concentration
Potassiun acetate	30 mM
$RbCl_2$	100 mM
$CaCl_2$ $2H_2O$	10mM
$MnCl_2$ $4H_2O$	50 mM
Glycerol	15% (v/v)

Adjust pH to 5.8 with 0.2 M acetic acid. Filter sterilise.

TFB II

Ingredient	Concentration
PIPES	10 mM
$CaCl_2$ $2H_2O$	75mM
$RbCl_2$	10 mM
Glycerol	15 % (v/v)

Adjust pH to 6.8 with HCl. Filter sterilise.

Lysis buffer

Ingredient	Quantity
Tris-HCl pH. 8.0	10 mM
EDTA	1 mM
SDS	1%

Dissolved in MilliQ water.

B Primers

Name	Sequence (5′ - 3′)	Feature
TlpT-F	CGTCATGACACGCCGCCCCAAGACG	*bspHI* site
TlpT-R	CTAAGCTTCAGAAGTCGCCGAAGCC	*hindIII* site
PpfATlpT-del-UF	CTCTCTAGAGAAGACCTGACCCGCACCGC	*xbaI* site
PpfATlpT-del-UR	CGGCCGGCCGCGTCTCACATCGCCCGCAAGGCTC	Overlap with downstream region
PpfATlpT-del-DF	GCCTTGCGGGCGATGTGAGACGCGGCCGGC	Overlap with upstream region
PpfATlpT-del-DR	CTCAAGCTTGAGCCCGAGACGGCGACCGAGG	*hindIII* site
PpfATlpT-del-screen-F	CATGCCGCTTGCAGCACGC	
PpfATlpT-del-screen-R	CCATCTCGTCGAATGCGTC	
PpfA-PAmCherry-F	CGAGGATCCAGATCTCGTGAGCAAGGGCGAGGAGGATAAC	*bamHI* site
PpfA-PAmCherry-R	TCGAAGCTTTTACTTGTACAGCTCGTCCATGCC	*hindIII* site

Bibliography

[1] Alexandre, G., Aug. 2010. Coupling metabolism and chemotaxis-dependent behaviours by energy taxis receptors. Microbiology (Reading, England) 156 (Pt 8), 2283–93.
URL http://www.ncbi.nlm.nih.gov/pubmed/20558508

[2] Anand, G. S., Goudreau, P. N., Stock, a. M., Oct. 1998. Activation of methylesterase CheB: evidence of a dual role for the regulatory domain. Biochemistry 37 (40), 14038–47.
URL http://www.ncbi.nlm.nih.gov/pubmed/9760239

[3] Anderson, J. K., Smith, T. G., Hoover, T. R., Jan. 2010. Sense and sensibility: flagellum-mediated gene regulation. Trends in microbiology 18 (1), 30–7.
URL http://www.pubmedcentral.nih.gov/articlerender.fcgi?artid=2818477&tool=pmcentrez&rendertype=abstract

[4] Armitage, J. P., 1992. Bacterial motility and chemotaxis. SciProg 76, 451–477.
URL http://www.scopus.com/inward/record.url?eid=2-s2.0-0026513441&partnerID=40

[5] Armitage, J. P., 1999. Bacterial tactic responses. Advances In Microbial Physiology 41, 229–289.
URL http://www.ncbi.nlm.nih.gov/pubmed/10500847

[6] Arnison, M. R., Cogswell, C. J., Smith, N. I., Fekete, P. W., Larkin, K. G., Jul. 2000. Using the Hilbert transform for 3D visualization of differential interference contrast microscope images. Journal of microscopy 199 (Pt 1), 79–84.
URL http://www.ncbi.nlm.nih.gov/pubmed/10886531

[7] Ausmees, N., Kuhn, J. R., Jacobs-Wagner, C., Dec. 2003. The bacterial cytoskeleton: an intermediate filament-like function in cell shape. Cell 115 (6), 705–13.
URL http://www.ncbi.nlm.nih.gov/pubmed/14675535

[8] Austin, S., Abeles, A., 1983. Partition of unit-copy miniplasmids to daughter cells: I. P1 and F miniplasmids contain discrete, interchangeable sequences sufficient to promote equipartition. Journal of molecular biology, 353–372.
URL http://www.sciencedirect.com/science/article/pii/S0022283683800552

[9] Barillà, D., Jul. 2010. One-way ticket to the cell pole: plasmid transport by the prokaryotic tubulin homolog TubZ. Proceedings of the National Academy of Sciences of the United States of America 107 (27), 12061–2.

URL http://www.pubmedcentral.nih.gov/articlerender.fcgi?artid=2901473&tool=pmcentrez&rendertype=abstract

[10] Barillà, D., Carmelo, E., Hayes, F., Feb. 2007. The tail of the ParG DNA segregation protein remodels ParF polymers and enhances ATP hydrolysis via an arginine finger-like motif. Proceedings of the National Academy of Sciences of the United States of America 104 (6), 1811–6.
URL http://www.pubmedcentral.nih.gov/articlerender.fcgi?artid=1794263&tool=pmcentrez&rendertype=abstract

[11] Barillà, D., Rosenberg, M. F., Nobbmann, U., Hayes, F., Apr. 2005. Bacterial DNA segregation dynamics mediated by the polymerizing protein ParF. The EMBO journal 24 (7), 1453–64.
URL http://www.pubmedcentral.nih.gov/articlerender.fcgi?artid=1142544&tool=pmcentrez&rendertype=abstract

[12] Ben-Yehuda, S., Fujita, M., Liu, X. S., Gorbatyuk, B., Skoko, D., Yan, J., Marko, J. F., Liu, J. S., Eichenberger, P., Rudner, D. Z., Losick, R., Mar. 2005. Defining a centromere-like element in Bacillus subtilis by Identifying the binding sites for the chromosome-anchoring protein RacA. Molecular cell 17 (6), 773–82.
URL http://www.ncbi.nlm.nih.gov/pubmed/15780934

[13] Ben-Yehuda, S., Rudner, D. Z., Losick, R., Jan. 2003. RacA, a bacterial protein that anchors chromosomes to the cell poles. Science (New York, N.Y.) 299 (5606), 532–6.
URL http://www.ncbi.nlm.nih.gov/pubmed/12493822

[14] Berg, H. C., Brown, D. A., 1972. Chemotaxis in Escherichia coli analysed by three-dimensional tracking. Nature 239, 500–504.
URL http://www.menem.com/~ilya/wiki/images/f/f8/Berg-brown-1972.pdf

[15] Berkmen, M. B., Grossman, A. D., Jan. 2007. Subcellular positioning of the origin region of the Bacillus subtilis chromosome is independent of sequences within oriC, the site of replication initiation, and the replication initiator DnaA. Molecular microbiology 63 (1), 150–65.
URL http://www.ncbi.nlm.nih.gov/pubmed/17140409

[16] Berlatzky, I. A., Rouvinski, A., Ben-Yehuda, S., Sep. 2008. Spatial organization of a replicating bacterial chromosome. Proceedings of the National Academy of Sciences of the United States of America 105 (37), 14136–40.
URL http://www.pubmedcentral.nih.gov/articlerender.fcgi?artid=2544591&tool=pmcentrez&rendertype=abstract

[17] Bernhardt, T. G., de Boer, P. a. J., May 2005. SlmA, a nucleoid-associated, FtsZ binding protein required for blocking septal ring assembly over Chromosomes in E. coli. Molecular cell 18 (5), 555–64.
URL http://www.ncbi.nlm.nih.gov/pubmed/15916962

[18] Boldog, T., Grimme, S., Li, M., Sligar, S. G., Hazelbauer, G. L., Aug. 2006. Nanodiscs separate chemoreceptor oligomeric states and reveal their signaling properties. Proceedings of the National Academy of Sciences of the United States of America 103 (31), 11509–14.

URL http://www.pubmedcentral.nih.gov/articlerender.fcgi?artid=1544200&tool=pmcentrez&rendertype=abstract

[19] Bouet, J.-Y., Ah-Seng, Y., Benmeradi, N., Lane, D., Jan. 2007. Polymerization of SopA partition ATPase: regulation by DNA binding and SopB. Molecular microbiology 63 (2), 468–81.
URL http://www.ncbi.nlm.nih.gov/pubmed/17166176

[20] Bouet, J. Y., Funnell, B. E., Mar. 1999. P1 ParA interacts with the P1 partition complex at parS and an ATP-ADP switch controls ParA activities. The EMBO journal 18 (5), 1415–24.
URL http://www.pubmedcentral.nih.gov/articlerender.fcgi?artid=1171231&tool=pmcentrez&rendertype=abstract

[21] Bourret, R. B., Silversmith, R. E., Apr. 2010. Two-component signal transduction. Current opinion in microbiology 13 (2), 113–5.
URL http://www.pubmedcentral.nih.gov/articlerender.fcgi?artid=2847671&tool=pmcentrez&rendertype=abstract

[22] Bramkamp, M., Emmins, R., Weston, L., Donovan, C., Daniel, R. a., Errington, J., Dec. 2008. A novel component of the division-site selection system of Bacillus subtilis and a new mode of action for the division inhibitor MinCD. Molecular microbiology 70 (6), 1556–69.
URL http://www.ncbi.nlm.nih.gov/pubmed/19019154

[23] Breier, A. M., Grossman, A. D., May 2007. Whole-genome analysis of the chromosome partitioning and sporulation protein Spo0J (ParB) reveals spreading and origin-distal sites on the Bacillus subtilis chromosome. Molecular microbiology 64 (3), 703–18.
URL http://www.ncbi.nlm.nih.gov/pubmed/17462018

[24] Briegel, A., Dias, D. P., Li, Z., Jensen, R. B., Frangakis, A. S., Jensen, G. J., Oct. 2006. Multiple large filament bundles observed in Caulobacter crescentus by electron cryotomography. Molecular microbiology 62 (1), 5–14.
URL http://www.ncbi.nlm.nih.gov/pubmed/16987173

[25] Briegel, A., Ding, H. J., Li, Z., Werner, J., Gitai, Z., Dias, D. P., Jensen, R. B., Jensen, G. J., Jul. 2008. Location and architecture of the Caulobacter crescentus chemoreceptor array. Molecular microbiology 69 (1), 30–41.
URL http://www.pubmedcentral.nih.gov/articlerender.fcgi?artid=3090075&tool=pmcentrez&rendertype=abstract

[26] Briegel, A., Ortega, D. R., Tocheva, E. I., Wuichet, K., Li, Z., Chen, S., Müller, A., Iancu, C. V., Murphy, G. E., Dobro, M. J., Zhulin, I. B., Jensen, G. J., Oct. 2009. Universal architecture of bacterial chemoreceptor arrays. Proceedings of the National Academy of Sciences of the United States of America 106 (40), 17181–6.
URL http://www.ncbi.nlm.nih.gov/pubmed/19805102

[27] Britton, R., Lin, D., Grossman, A., 1998. Characterization of a prokaryotic SMC protein involved in chromosome partitioning. Genes & development, 1254–1259.
URL http://genesdev.cshlp.org/content/12/9/1254.short

[28] Browning, D. F., Grainger, D. C., Busby, S. J., Dec. 2010. Effects of nucleoid-associated proteins on bacterial chromosome structure and gene expression. Current opinion in microbi-

ology 13 (6), 773–80.
URL http://www.ncbi.nlm.nih.gov/pubmed/20951079

[29] Bulyha, I., Schmidt, C., Lenz, P., Jakovljevic, V., Höne, A., Maier, B., Hoppert, M., Sø gaard Andersen, L., Nov. 2009. Regulation of the type IV pili molecular machine by dynamic localization of two motor proteins. Molecular microbiology 74 (3), 691–706.
URL http://www.pubmedcentral.nih.gov/articlerender.fcgi?artid=2784877&tool=pmcentrez&rendertype=abstract

[30] Butan, C., Hartnell, L. M., Fenton, A. K., Bliss, D., Sockett, R. E., Subramaniam, S., Milne, J. L. S., Mar. 2011. Spiral architecture of the nucleoid in Bdellovibrio bacteriovorus. Journal of bacteriology 193 (6), 1341–50.
URL http://www.pubmedcentral.nih.gov/articlerender.fcgi?artid=3067633&tool=pmcentrez&rendertype=abstract

[31] Campbell, C. S., Mullins, R. D., Dec. 2007. In vivo visualization of type II plasmid segregation: bacterial actin filaments pushing plasmids. The Journal of cell biology 179 (5), 1059–66.
URL http://www.pubmedcentral.nih.gov/articlerender.fcgi?artid=2099209&tool=pmcentrez&rendertype=abstract

[32] Charon, N. W., Greenberg, E. P., Koopman, M. B., Limberger, R. J., 1992. Spirochete chemotaxis, motility, and the structure of the spirochetal periplasmic flagella. Research in microbiology 143 (6), 597–603.
URL http://www.ncbi.nlm.nih.gov/pubmed/1475520

[33] Chen, Y., Erickson, H. P., Mar. 2008. In vitro assembly studies of FtsZ/tubulin-like proteins (TubZ) from Bacillus plasmids: evidence for a capping mechanism. The Journal of biological chemistry 283 (13), 8102–9.
URL http://www.pubmedcentral.nih.gov/articlerender.fcgi?artid=2276378&tool=pmcentrez&rendertype=abstract

[34] Chervitz, S. a., Falke, J. J., Mar. 1996. Molecular mechanism of transmembrane signaling by the aspartate receptor: a model. Proceedings of the National Academy of Sciences of the United States of America 93 (6), 2545–50.
URL http://www.pubmedcentral.nih.gov/articlerender.fcgi?artid=39834&tool=pmcentrez&rendertype=abstract

[35] Chiu, S.-W., Roberts, M. a. J., Leake, M. C., Armitage, J. P., Aug. 2013. Positioning of chemosensory proteins and FtsZ through the Rhodobacter sphaeroides cell cycle. Molecular microbiology, 1–16.
URL http://www.ncbi.nlm.nih.gov/pubmed/23944351

[36] Daniel, R. a., Errington, J., Jun. 2003. Control of cell morphogenesis in bacteria: two distinct ways to make a rod-shaped cell. Cell 113 (6), 767–76.
URL http://www.ncbi.nlm.nih.gov/pubmed/12809607

[37] de Boer, P. a., Crossley, R. E., Rothfield, L. I., Mar. 1989. A division inhibitor and a topological specificity factor coded for by the minicell locus determine proper placement of the division septum in E. coli. Cell 56 (4), 641–9.
URL http://www.ncbi.nlm.nih.gov/pubmed/2645057

[38] Deich, J., Judd, E. M., McAdams, H. H., Moerner, W. E., Nov. 2004. Visualization of the movement of single histidine kinase molecules in live Caulobacter cells. Proceedings of the National Academy of Sciences of the United States of America 101 (45), 15921–6.
URL http://www.pubmedcentral.nih.gov/articlerender.fcgi?artid=528753&tool=pmcentrez&rendertype=abstract

[39] del Campo, A. M., Ballado, T., de la Mora, J., Poggio, S., Camarena, L., Dreyfus, G., Nov. 2007. Chemotactic control of the two flagellar systems of Rhodobacter sphaeroides is mediated by different sets of CheY and FliM proteins. Journal of Bacteriology 189 (22), 8397–401.
URL http://www.pubmedcentral.nih.gov/articlerender.fcgi?artid=2168678&tool=pmcentrez&rendertype=abstract

[40] Deng, S., Stein, R. a., Higgins, N. P., Sep. 2005. Organization of supercoil domains and their reorganization by transcription. Molecular microbiology 57 (6), 1511–21.
URL http://www.pubmedcentral.nih.gov/articlerender.fcgi?artid=1382059&tool=pmcentrez&rendertype=abstract

[41] Derman, A. I., Lim-Fong, G., Pogliano, J., Mar. 2008. Intracellular mobility of plasmid DNA is limited by the ParA family of partitioning systems. Molecular microbiology 67 (5), 935–46.
URL http://www.ncbi.nlm.nih.gov/pubmed/18208495

[42] Dunham, T. D., Xu, W., Funnell, B. E., Schumacher, M. a., Jun. 2009. Structural basis for ADP-mediated transcriptional regulation by P1 and P7 ParA. The EMBO journal 28 (12), 1792–802.
URL http://www.pubmedcentral.nih.gov/articlerender.fcgi?artid=2699355&tool=pmcentrez&rendertype=abstract

[43] Ebersbach, G., Briegel, A., Jensen, G. J., Jacobs-Wagner, C., Sep. 2008. A self-associating protein critical for chromosome attachment, division, and polar organization in caulobacter. Cell 134 (6), 956–68.
URL http://www.pubmedcentral.nih.gov/articlerender.fcgi?artid=2614312&tool=pmcentrez&rendertype=abstract

[44] Ebersbach, G., Ringgaard, S., Mø ller Jensen, J., Wang, Q., Sherratt, D. J., Gerdes, K., Sep. 2006. Regular cellular distribution of plasmids by oscillating and filament-forming ParA ATPase of plasmid pB171. Molecular microbiology 61 (6), 1428–42.
URL http://www.ncbi.nlm.nih.gov/pubmed/16899080

[45] Elmore, S., Müller, M., Vischer, N., Odijk, T., Woldringh, C. L., Sep. 2005. Single-particle tracking of oriC-GFP fluorescent spots during chromosome segregation in Escherichia coli. Journal of structural biology 151 (3), 275–87.
URL http://www.ncbi.nlm.nih.gov/pubmed/16084110

[46] Eltsov, M., Zuber, B., Nov. 2006. Transmission electron microscopy of the bacterial nucleoid. Journal of structural biology 156 (2), 246–54.
URL http://www.ncbi.nlm.nih.gov/pubmed/16978880

[47] Erickson, H. P., Sep. 1997. FtsZ, a tubulin homologue in prokaryote cell division. Trends in

cell biology 7 (9), 362–7.
URL http://www.ncbi.nlm.nih.gov/pubmed/17708981

[48] Erickson, H. P., Anderson, D. E., Osawa, M., Dec. 2010. FtsZ in bacterial cytokinesis: cytoskeleton and force generator all in one. Microbiology and molecular biology reviews : MMBR 74 (4), 504–28.
URL http://www.pubmedcentral.nih.gov/articlerender.fcgi?artid=3008173&tool=pmcentrez&rendertype=abstract

[49] Errington, J., Daniel, R., Scheffers, D., 2003. Cytokinesis in bacteria. Microbiology and Molecular ... 67 (1).
URL http://mmbr.asm.org/content/67/1/52.short

[50] Espéli, O., Boccard, F., Nov. 2006. Organization of the Escherichia coli chromosome into macrodomains and its possible functional implications. Journal of structural biology 156 (2), 304–10.
URL http://www.ncbi.nlm.nih.gov/pubmed/16979349

[51] Eswaramoorthy, P., Erb, M., Gregory, J., Eswaramoorthy P, Erb ML, Gregory JA, Silverman J, Pogliano K, Pogliano J, R. K., 2011. Cellular architecture mediates DivIVA ultrastructure and regulates Min activity in Bacillus subtilis. MBio 2 (6).
URL http://mbio.asm.org/content/2/6/e00257-11.short

[52] Fiebig, A., Keren, K., Theriot, J. a., Jun. 2006. Fine-scale time-lapse analysis of the biphasic, dynamic behaviour of the two Vibrio cholerae chromosomes. Molecular microbiology 60 (5), 1164–78.
URL http://www.pubmedcentral.nih.gov/articlerender.fcgi?artid=2779472&tool=pmcentrez&rendertype=abstract

[53] Figge, R., Divakaruni, A., Gober, J., 2004. MreB, the cell shapedetermining bacterial actin homologue, coordinates cell wall morphogenesis in Caulobacter crescentus. Molecular microbiology 51, 1321–1332.
URL http://onlinelibrary.wiley.com/doi/10.1111/j.1365-2958.2003.03936.x/full

[54] Fisher, J. K., Bourniquel, A., Witz, G., Weiner, B., Prentiss, M., Kleckner, N., May 2013. Four-Dimensional Imaging of E. coli Nucleoid Organization and Dynamics in Living Cells. Cell 153 (4), 882–95.
URL http://www.ncbi.nlm.nih.gov/pubmed/23623305

[55] Fogel, M. a., Waldor, M. K., Jan. 2005. Distinct segregation dynamics of the two Vibrio cholerae chromosomes. Molecular microbiology 55 (1), 125–36.
URL http://www.ncbi.nlm.nih.gov/pubmed/15612922

[56] Fogel, M. a., Waldor, M. K., Dec. 2006. A dynamic, mitotic-like mechanism for bacterial chromosome segregation. Genes & development 20 (23), 3269–82.
URL http://www.pubmedcentral.nih.gov/articlerender.fcgi?artid=1686604&tool=pmcentrez&rendertype=abstract

[57] Fothergill, T., Barillà, D., Hayes, F., 2005. Protein diversity confers specificity in plasmid

segregation. Journal of Bacteriology 187 (8).
URL http://jb.asm.org/content/187/8/2651.short

[58] Garner, E. C., Campbell, C. S., Mullins, R. D., Nov. 2004. Dynamic instability in a DNA-segregating prokaryotic actin homolog. Science (New York, N.Y.) 306 (5698), 1021–5.
URL http://www.ncbi.nlm.nih.gov/pubmed/15528442

[59] Garner, E. C., Campbell, C. S., Weibel, D. B., Mullins, R. D., Mar. 2007. Reconstitution of DNA segregation driven by assembly of a prokaryotic actin homolog. Science (New York, N.Y.) 315 (5816), 1270–4.
URL http://www.pubmedcentral.nih.gov/articlerender.fcgi?artid=2851738&tool=pmcentrez&rendertype=abstract

[60] Gerdes, K., Howard, M., Szardenings, F., Jun. 2010. Pushing and pulling in prokaryotic DNA segregation. Cell 141 (6), 927–42.
URL http://www.ncbi.nlm.nih.gov/pubmed/20550930

[61] Gerdes, K., Mø ller Jensen, J., Bugge Jensen, R., Aug. 2000. Plasmid and chromosome partitioning: surprises from phylogeny. Molecular microbiology 37 (3), 455–66.
URL http://www.ncbi.nlm.nih.gov/pubmed/10931339

[62] Gitai, Z., Dye, N., Shapiro, L., Jun. 2004. An actin-like gene can determine cell polarity in bacteria. Proceedings of the National Academy of Sciences of the United States of America 101 (23), 8643–8.
URL http://www.pubmedcentral.nih.gov/articlerender.fcgi?artid=423248&tool=pmcentrez&rendertype=abstract

[63] Gluch, M. F., Typke, D., Baumeister, W., Gluch, M. F., Typke, D., Baumeister, W., 1995. Motility and thermotactic responses of Thermotoga maritima . These include : Motility and Thermotactic Responses of Thermotoga maritima. Journal of Bacteriology 177 (19).

[64] Govindarajan, S., Nevo-Dinur, K., Amster-Choder, O., Jul. 2012. Compartmentalization And Spatio-Temporal Organization Of Macromolecules In Bacteria. FEMS microbiology reviews.
URL http://www.ncbi.nlm.nih.gov/pubmed/22775310

[65] Graf, J., Dunlap, P. V., Ruby, E. G., Nov. 1994. Effect of transposon-induced motility mutations on colonization of the host light organ by Vibrio fischeri. Journal of Bacteriology 176 (22), 6986–91.
URL http://www.pubmedcentral.nih.gov/articlerender.fcgi?artid=197071&tool=pmcentrez&rendertype=abstract

[66] Greenfield, D., McEvoy, A. L., Shroff, H., Crooks, G. E., Wingreen, N. S., Betzig, E., Liphardt, J., 2009. Self-organization of the escherichia coli chemotaxis network imaged with super-resolution light microscopy. PLoS Biol. 7, e1000137 7 (6), e1000137.
URL http://www.ncbi.nlm.nih.gov/pubmed/19547746http://www.ncbi.nlm.nih.gov/pmc/articles/PMC2691949/

[67] Gregory, J., Becker, E., Pogliano, K., 2008. Bacillus subtilis MinC destabilizes FtsZ-rings at new cell poles and contributes to the timing of cell division. Genes & development 1, 3475–

3488.
URL http://genesdev.cshlp.org/content/22/24/3475.short

[68] Gruber, S., Errington, J., May 2009. Recruitment of condensin to replication origin regions by ParB/SpoOJ promotes chromosome segregation in B. subtilis. Cell 137 (4), 685–96.
URL http://www.ncbi.nlm.nih.gov/pubmed/19450516

[69] Hamblin, P. a., Maguire, B. a., Grishanin, R. N., Armitage, J. P., Dec. 1997. Evidence for two chemosensory pathways in Rhodobacter sphaeroides. Molecular microbiology 26 (5), 1083–96.
URL http://www.ncbi.nlm.nih.gov/pubmed/9426144

[70] Hamer, R., Chen, P., Armitage, J., Reinert, G., 2010. Deciphering chemotaxis pathways using cross species comparisons. BMC Systems.
URL http://www.biomedcentral.com/content/pdf/1752-0509-4-3.pdf

[71] Hamer, R., Chen, P., Armitage, J., Reinert, G., 2010. Deciphering chemotaxis pathways using cross species comparisons. BMC Systems.
URL http://www.biomedcentral.com/content/pdf/1752-0509-4-3.pdf

[72] Hatano, T., Niki, H., Dec. 2010. Partitioning of P1 plasmids by gradual distribution of the ATPase ParA. Molecular microbiology 78 (5), 1182–98.
URL http://www.ncbi.nlm.nih.gov/pubmed/21091504

[73] Hatano, T., Yamaichi, Y., Niki, H., Jun. 2007. Oscillating focus of SopA associated with filamentous structure guides partitioning of F plasmid. Molecular microbiology 64 (5), 1198–213.
URL http://www.pubmedcentral.nih.gov/articlerender.fcgi?artid=1974783&tool=pmcentrez&rendertype=abstract

[74] Hayes, F., Aug. 2000. The partition system of multidrug resistance plasmid TP228 includes a novel protein that epitomizes an evolutionarily distinct subgroup of the ParA superfamily. Molecular microbiology 37 (3), 528–41.
URL http://www.ncbi.nlm.nih.gov/pubmed/10931346

[75] Hazelbauer, G. L., Engström, P., Jan. 1981. Multiple forms of methyl-accepting chemotaxis proteins distinguished by a factor in addition to multiple methylation. Journal of bacteriology 145 (1), 35–42.
URL http://www.pubmedcentral.nih.gov/articlerender.fcgi?artid=217241&tool=pmcentrez&rendertype=abstract

[76] Hazelbauer, G. L., Falke, J. J., Parkinson, J. S., Jan. 2008. Bacterial chemoreceptors: high-performance signaling in networked arrays. Trends in biochemical sciences 33 (1), 9–19.
URL http://www.pubmedcentral.nih.gov/articlerender.fcgi?artid=2890293&tool=pmcentrez&rendertype=abstract

[77] Hazelbauer, G. L., Lai, W.-C., Apr. 2010. Bacterial chemoreceptors: providing enhanced features to two-component signaling. Current opinion in microbiology 13 (2), 124–32.
URL http://www.pubmedcentral.nih.gov/articlerender.fcgi?artid=2863001&tool=pmcentrez&rendertype=abstract

[78] Heise, B., Sonnleitner, A., Klement, E. P., Apr. 2005. DIC image reconstruction on large cell scans. Microscopy research and technique 66 (6), 312–20.
URL http://www.ncbi.nlm.nih.gov/pubmed/16003783

[79] Henriques, R., Mhlanga, M. M., 2009. PALM and STORM: what hides beyond the Rayleigh limit? Biotechnology journal 4 (6), 846–57.
URL http://www.ncbi.nlm.nih.gov/pubmed/19548237

[80] Hester, C. M., Lutkenhaus, J., Dec. 2007. Soj (ParA) DNA binding is mediated by conserved arginines and is essential for plasmid segregation. Proceedings of the National Academy of Sciences of the United States of America 104 (51), 20326–31.
URL http://www.pubmedcentral.nih.gov/articlerender.fcgi?artid=2154430&tool=pmcentrez&rendertype=abstract

[81] Holmes, V. F., Cozzarelli, N. R., Mar. 2000. Closing the ring: links between SMC proteins and chromosome partitioning, condensation, and supercoiling. Proceedings of the National Academy of Sciences of the United States of America 97 (4), 1322–4.
URL http://www.pubmedcentral.nih.gov/articlerender.fcgi?artid=34294&tool=pmcentrez&rendertype=abstract

[82] Howard, M., Rutenberg, A., de Vet, S., Dec. 2001. Dynamic Compartmentalization of Bacteria: Accurate Division in E. Coli. Physical Review Letters 87 (27), 278102.
URL http://link.aps.org/doi/10.1103/PhysRevLett.87.278102

[83] Hu, Z., Gogol, E. P., Lutkenhaus, J., May 2002. Dynamic assembly of MinD on phospholipid vesicles regulated by ATP and MinE. Proceedings of the National Academy of Sciences of the United States of America 99 (10), 6761–6.
URL http://www.pubmedcentral.nih.gov/articlerender.fcgi?artid=124476&tool=pmcentrez&rendertype=abstract

[84] Hu, Z., Lutkenhaus, J., Oct. 1999. Topological regulation of cell division in Escherichia coli involves rapid pole to pole oscillation of the division inhibitor MinC under the control of MinD and MinE. Molecular microbiology 34 (1), 82–90.
URL http://www.ncbi.nlm.nih.gov/pubmed/10540287

[85] Hu, Z., Mukherjee, a., Pichoff, S., Lutkenhaus, J., Dec. 1999. The MinC component of the division site selection system in Escherichia coli interacts with FtsZ to prevent polymerization. Proceedings of the National Academy of Sciences of the United States of America 96 (26), 14819–24.
URL http://www.pubmedcentral.nih.gov/articlerender.fcgi?artid=24731&tool=pmcentrez&rendertype=abstract

[86] Hui, M. P., Galkin, V. E., Yu, X., Stasiak, A. Z., Stasiak, A., Waldor, M. K., Egelman, E. H., Mar. 2010. ParA2, a Vibrio cholerae chromosome partitioning protein, forms left-handed helical filaments on DNA. Proceedings of the National Academy of Sciences of the United States of America 107 (10), 4590–5.
URL http://www.pubmedcentral.nih.gov/articlerender.fcgi?artid=2842031&tool=pmcentrez&rendertype=abstract

[87] Hwang, L. C., Vecchiarelli, A. G., Han, Y.-W., Mizuuchi, M., Harada, Y., Funnell, B. E.,

Mizuuchi, K., May 2013. ParA-mediated plasmid partition driven by protein pattern self-organization. The EMBO journal 32 (9), 1238–49.
URL http://www.ncbi.nlm.nih.gov/pubmed/23443047

[88] Ind, A. C., Porter, S. L., Brown, M. T., Byles, E. D., de Beyer, J. a., Godfrey, S. a., Armitage, J. P., 2009. Inducible-expression plasmid for Rhodobacter sphaeroides and Paracoccus denitrificans. Applied and environmental microbiology 75 (20), 6613–5.
URL http://www.ncbi.nlm.nih.gov/pubmed/19684165

[89] Jarrell, K. F., McBride, M. J., Jun. 2008. The surprisingly diverse ways that prokaryotes move. Nature reviews. Microbiology 6 (6), 466–76.
URL http://www.ncbi.nlm.nih.gov/pubmed/18461074

[90] Jun, S., Wright, A., Aug. 2010. Entropy as the driver of chromosome segregation. Nature reviews. Microbiology 8 (8), 600–7.
URL http://www.pubmedcentral.nih.gov/articlerender.fcgi?artid=3148256&tool=pmcentrez&rendertype=abstract

[91] Kaiser, D., Jul. 2007. Bacterial swarming: a re-examination of cell-movement patterns. Current biology : CB 17 (14), R561–70.
URL http://www.ncbi.nlm.nih.gov/pubmed/17637359

[92] Kalliomaa-Sanford, A. K., Rodriguez-Castañeda, F. a., McLeod, B. N., Latorre-Roselló, V., Smith, J. H., Reimann, J., Albers, S. V., Barillà, D., Mar. 2012. Chromosome segregation in Archaea mediated by a hybrid DNA partition machine. Proceedings of the National Academy of Sciences of the United States of America 109 (10), 3754–9.
URL http://www.pubmedcentral.nih.gov/articlerender.fcgi?artid=3309785&tool=pmcentrez&rendertype=abstract

[93] Kearns, D. B., Losick, R., Dec. 2005. Cell population heterogeneity during growth of Bacillus subtilis. Genes & development 19 (24), 3083–94.
URL http://www.pubmedcentral.nih.gov/articlerender.fcgi?artid=1315410&tool=pmcentrez&rendertype=abstract

[94] Kentner, D., Thiem, S., Hildenbeutel, M., Sourjik, V., 2006. Determinants of chemoreceptor cluster formation in Escherichia coli. Molecular microbiology 61 (2), 407–17.
URL http://www.ncbi.nlm.nih.gov/pubmed/16856941

[95] Kiekebusch, D., Michie, K. a., Essen, L.-O., Löwe, J., Thanbichler, M., May 2012. Localized dimerization and nucleoid binding drive gradient formation by the bacterial cell division inhibitor MipZ. Molecular cell 46 (3), 245–59.
URL http://www.pubmedcentral.nih.gov/articlerender.fcgi?artid=3355305&tool=pmcentrez&rendertype=abstract

[96] Kim, Y. K., McCarter, L. L., Jul. 2000. Analysis of the polar flagellar gene system of Vibrio parahaemolyticus. Journal of Bacteriology 182 (13), 3693–704.
URL http://www.pubmedcentral.nih.gov/articlerender.fcgi?artid=94540&tool=pmcentrez&rendertype=abstract

[97] Kruse, K., Mar. 2002. A dynamic model for determining the middle of Escherichia coli. Bio-

physical journal 82 (2), 618–27.
URL http://www.pubmedcentral.nih.gov/articlerender.fcgi?artid=1301873&tool=pmcentrez&rendertype=abstract

[98] Kumar, M., Mommer, M. S., Sourjik, V., 2010. Mobility of cytoplasmic, membrane, and DNA-binding proteins in Escherichia coli. Biophysical journal 98 (4), 552–9.
URL http://www.ncbi.nlm.nih.gov/pubmed/20159151

[99] Lackner, L., Raskin, D., de Boer, P., 2003. ATP-dependent interactions between Escherichia coli Min proteins and the phospholipid membrane in vitro. Journal of Bacteriology 185 (3).
URL http://jb.asm.org/content/185/3/735.short

[100] Laloux, G., Jacobs-Wagner, C., Jun. 2013. Spatiotemporal control of PopZ localization through cell cycle-coupled multimerization. The Journal of cell biology 201 (6), 827–41.
URL http://www.ncbi.nlm.nih.gov/pubmed/23751494

[101] Larsen, R. a., Cusumano, C., Fujioka, A., Lim-Fong, G., Patterson, P., Pogliano, J., Jun. 2007. Treadmilling of a prokaryotic tubulin-like protein, TubZ, required for plasmid stability in Bacillus thuringiensis. Genes & development 21 (11), 1340–52.
URL http://www.pubmedcentral.nih.gov/articlerender.fcgi?artid=1877747&tool=pmcentrez&rendertype=abstract

[102] Le Quéré, B., Ghigo, J.-M., May 2009. BcsQ is an essential component of the Escherichia coli cellulose biosynthesis apparatus that localizes at the bacterial cell pole. Molecular microbiology 72 (3), 724–40.
URL http://www.ncbi.nlm.nih.gov/pubmed/19400787

[103] Lefèvre, C. T., Bazylinski, D. a., Sep. 2013. Ecology, diversity, and evolution of magnetotactic bacteria. Microbiology and molecular biology reviews : MMBR 77 (3), 497–526.
URL http://www.ncbi.nlm.nih.gov/pubmed/24006473

[104] Leipe, D. D., Wolf, Y. I., Koonin, E. V., Aravind, L., Mar. 2002. Classification and evolution of P-loop GTPases and related ATPases. Journal of molecular biology 317 (1), 41–72.
URL http://www.ncbi.nlm.nih.gov/pubmed/11916378

[105] Leonard, T. a., Butler, P. J., Löwe, J., Jan. 2005. Bacterial chromosome segregation: structure and DNA binding of the Soj dimer–a conserved biological switch. The EMBO journal 24 (2), 270–82.
URL http://www.pubmedcentral.nih.gov/articlerender.fcgi?artid=545817&tool=pmcentrez&rendertype=abstract

[106] Li, M., Hazelbauer, G., 2004. Cellular stoichiometry of the components of the chemotaxis signaling complex. Journal of Bacteriology 186 (12).
URL http://jb.asm.org/content/186/12/3687.short

[107] Lin, D. C., Grossman, a. D., Mar. 1998. Identification and characterization of a bacterial chromosome partitioning site. Cell 92 (5), 675–85.
URL http://www.ncbi.nlm.nih.gov/pubmed/9506522

[108] Loose, M., Fischer-Friedrich, E., Ries, J., Kruse, K., Schwille, P., May 2008. Spatial regulators for bacterial cell division self-organize into surface waves in vitro. Science (New York, N.Y.)

320 (5877), 789–92.
URL http://www.ncbi.nlm.nih.gov/pubmed/18467587

[109] Lutkenhaus, J., Jun. 2012. The ParA/MinD family puts things in their place. Trends in microbiology 20 (9), 411–418.
URL http://www.ncbi.nlm.nih.gov/pubmed/22672910

[110] Macnab, R., 1992. Genetics and biogenesis of bacterial flagella. Annual review of genetics.
URL http://www.annualreviews.org/doi/pdf/10.1146/annurev.ge.26.120192.001023

[111] Marston, a. L., Thomaides, H. B., Edwards, D. H., Sharpe, M. E., Errington, J., Nov. 1998. Polar localization of the MinD protein of Bacillus subtilis and its role in selection of the mid-cell division site. Genes & Development 12 (21), 3419–3430.
URL http://www.genesdev.org/cgi/doi/10.1101/gad.12.21.3419

[112] Merritt, P. M., Danhorn, T., Fuqua, C., Nov. 2007. Motility and chemotaxis in Agrobacterium tumefaciens surface attachment and biofilm formation. Journal of Bacteriology 189 (22), 8005–14.
URL http://www.pubmedcentral.nih.gov/articlerender.fcgi?artid=2168663&tool=pmcentrez&rendertype=abstract

[113] Mignot, T., Shaevitz, J. W., Hartzell, P. L., Zusman, D. R., Feb. 2007. Evidence that focal adhesion complexes power bacterial gliding motility. Science (New York, N.Y.) 315 (5813), 853–6.
URL http://www.ncbi.nlm.nih.gov/pubmed/17289998

[114] Mø ller Jensen, J., Borch, J., Dam, M., Jensen, R. B., Roepstorff, P., Gerdes, K., Dec. 2003. Bacterial mitosis: ParM of plasmid R1 moves plasmid DNA by an actin-like insertional polymerization mechanism. Molecular cell 12 (6), 1477–87.
URL http://www.ncbi.nlm.nih.gov/pubmed/14690601

[115] Mø ller Jensen, J., Jensen, R. B., Löwe, J., Gerdes, K., Jun. 2002. Prokaryotic DNA segregation by an actin-like filament. The EMBO journal 21 (12), 3119–27.
URL http://www.ncbi.nlm.nih.gov/pubmed/20550930

[116] Mohl, D. a., Gober, J. W., Mar. 1997. Cell cycle-dependent polar localization of chromosome partitioning proteins in Caulobacter crescentus. Cell 88 (5), 675–84.
URL http://www.ncbi.nlm.nih.gov/pubmed/9054507

[117] Moorthy, S., Watnick, P. I., Sep. 2005. Identification of novel stage-specific genetic requirements through whole genome transcription profiling of Vibrio cholerae biofilm development. Molecular microbiology 57 (6), 1623–35.
URL http://www.pubmedcentral.nih.gov/articlerender.fcgi?artid=2600799&tool=pmcentrez&rendertype=abstract

[118] Mowbray, S. L., Koshland, D. E., Jul. 1987. Additive and independent responses in a single receptor: aspartate and maltose stimuli on the tar protein. Cell 50 (2), 171–80.
URL http://www.ncbi.nlm.nih.gov/pubmed/3297352

[119] Murray, H., Errington, J., Oct. 2008. Dynamic control of the DNA replication initiation protein DnaA by Soj/ParA. Cell 135 (1), 74–84.
URL http://www.ncbi.nlm.nih.gov/pubmed/18854156

[120] Murray, H., Ferreira, H., Errington, J., Sep. 2006. The bacterial chromosome segregation protein Spo0J spreads along DNA from parS nucleation sites. Molecular microbiology 61 (5), 1352–61.
URL http://www.ncbi.nlm.nih.gov/pubmed/16925562

[121] Nakane, D., Sato, K., Wada, H., McBride, M. J., Nakayama, K., Jul. 2013. Helical flow of surface protein required for bacterial gliding motility. Proceedings of the National Academy of Sciences of the United States of America 110 (27), 11145–50.
URL http://www.pubmedcentral.nih.gov/articlerender.fcgi?artid=3704026&tool=pmcentrez&rendertype=abstract

[122] Ni, L., Xu, W., Kumaraswami, M., Schumacher, M. a., Jun. 2010. Plasmid protein TubR uses a distinct mode of HTH-DNA binding and recruits the prokaryotic tubulin homolog TubZ to effect DNA partition. Proceedings of the National Academy of Sciences of the United States of America 107 (26), 11763–8.
URL http://www.pubmedcentral.nih.gov/articlerender.fcgi?artid=2900659&tool=pmcentrez&rendertype=abstract

[123] Nielsen, H. J., Ottesen, J. R., Youngren, B., Austin, S. J., Hansen, F. G., Oct. 2006. The Escherichia coli chromosome is organized with the left and right chromosome arms in separate cell halves. Molecular microbiology 62 (2), 331–8.
URL http://www.ncbi.nlm.nih.gov/pubmed/17020576

[124] Obara, B., Roberts, M., Armitage, J., Grau, V., Apr. 2013. Bacterial cell identification in differential interference contrast microscopy images. BMC bioinformatics 14 (1), 134.
URL http://www.ncbi.nlm.nih.gov/pubmed/23617824

[125] Ogura, T., Hiraga, S., Feb. 1983. Partition mechanism of F plasmid: two plasmid gene-encoded products and a cis-acting region are involved in partition. Cell 32 (2), 351–60.
URL http://www.ncbi.nlm.nih.gov/pubmed/6297791

[126] Olshausen, P. V., Defeu Soufo, H. J., Wicker, K., Heintzmann, R., Graumann, P. L., Rohrbach, A., Sep. 2013. Superresolution Imaging of Dynamic MreB Filaments in B.subtilis-A Multiple-Motor-Driven Transport? Biophysical journal 105 (5), 1171–81.
URL http://www.ncbi.nlm.nih.gov/pubmed/24010660

[127] Orlova, A., Garner, E. C., Galkin, V. E., Heuser, J., Mullins, R. D., Egelman, E. H., Oct. 2007. The structure of bacterial ParM filaments. Nature structural & molecular biology 14 (10), 921–6.
URL http://www.pubmedcentral.nih.gov/articlerender.fcgi?artid=3541950&tool=pmcentrez&rendertype=abstract

[128] Parkinson, J., 1978. Complementation analysis and deletion mapping of Escherichia coli mutants defective in chemotaxis. Journal of Bacteriology.
URL http://jb.asm.org/content/135/1/45.short

[129] Patrick, J. E., Kearns, D. B., Dec. 2008. MinJ (YvjD) is a topological determinant of cell division in Bacillus subtilis. Molecular microbiology 70 (5), 1166–79.
URL http://www.ncbi.nlm.nih.gov/pubmed/18976281

[130] Pelletier, J., Halvorsen, K., Ha, B.-Y., Paparcone, R., Sandler, S. J., Woldringh, C. L., Wong, W. P., Jun, S., Oct. 2012. Physical manipulation of the Escherichia coli chromosome reveals its soft nature. Proceedings of the National Academy of Sciences of the United States of America 109 (40), E2649–56.
URL http://www.ncbi.nlm.nih.gov/pubmed/22984156

[131] Penfold, R., Pemberton, J., 1992. An improved suicide vector for construction of chromosomal insertion mutations in bacteria. Gene 18, 18–19.
URL http://www.sciencedirect.com/science/article/pii/0378111992902630

[132] Poggio, S., Abreu-Goodger, C., Fabela, S., Osorio, A., Dreyfus, G., Vinuesa, P., Camarena, L., Apr. 2007. A complete set of flagellar genes acquired by horizontal transfer coexists with the endogenous flagellar system in Rhodobacter sphaeroides. Journal of Bacteriology 189 (8), 3208–16.
URL http://www.pubmedcentral.nih.gov/articlerender.fcgi?artid=1855832&tool=pmcentrez&rendertype=abstract

[133] Popp, D., Yamamoto, A., Iwasa, M., Narita, A., Maeda, K., Maéda, Y., Feb. 2007. Concerning the dynamic instability of actin homolog ParM. Biochemical and biophysical research communications 353 (1), 109–14.
URL http://www.ncbi.nlm.nih.gov/pubmed/17173862

[134] Porter, S., Wadhams, G., Armitage, J., 2008. Rhodobacter sphaeroides: complexity in chemotactic signalling. Trends in microbiology 16 (6), 251–60.
URL http://www.ncbi.nlm.nih.gov/pubmed/18440816

[135] Porter, S. L., Roberts, M. a. J., Manning, C. S., Armitage, J. P., Nov. 2008. A bifunctional kinase-phosphatase in bacterial chemotaxis. Proceedings of the National Academy of Sciences of the United States of America 105 (47), 18531–6.
URL http://www.pubmedcentral.nih.gov/articlerender.fcgi?artid=2587623&tool=pmcentrez&rendertype=abstract

[136] Porter, S. L., Wadhams, G. H., Martin, A. C., Byles, E. D., Lancaster, D. E., Armitage, J. P., Oct. 2006. The CheYs of Rhodobacter sphaeroides. The Journal of biological chemistry 281 (43), 32694–704.
URL http://www.ncbi.nlm.nih.gov/pubmed/16950782

[137] Porter, S. L., Warren, A. V., Martin, A. C., Armitage, J. P., Nov. 2002. The third chemotaxis locus of Rhodobacter sphaeroides is essential for chemotaxis. Molecular microbiology 46 (4), 1081–94.
URL http://www.ncbi.nlm.nih.gov/pubmed/12421313

[138] Postow, L., Hardy, C. D., Arsuaga, J., Cozzarelli, N. R., Jul. 2004. Topological domain structure of the Escherichia coli chromosome. Genes & development 18 (14), 1766–79.
URL http://www.pubmedcentral.nih.gov/articlerender.fcgi?artid=478196&tool=pmcentrez&rendertype=abstract

[139] Preza, C., Snyder, D. L., Conchello, J.-A., Apr. 1997. Image reconstruction for three-dimensional transmitted-light DIC microscopy. Proc. SPIE Symposium in Three-Dimensional Microscopy: Image Acquisition and Processing IV 2984, 220–231.
URL http://proceedings.spiedigitallibrary.org/proceeding.aspx?articleid=1028044

[140] Ptacin, J. L., Lee, S. F., Garner, E. C., Toro, E., Eckart, M., Comolli, L. R., Moerner, W. E., Shapiro, L., Jul. 2010. A spindle-like apparatus guides bacterial chromosome segregation. Nature cell biology 12 (8), 791–798.
URL http://www.ncbi.nlm.nih.gov/pubmed/20657594

[141] Ramamurthi, K. S., Dec. 2010. Protein localization by recognition of membrane curvature. Current opinion in microbiology 13 (6), 753–7.
URL http://www.pubmedcentral.nih.gov/articlerender.fcgi?artid=2994992&tool=pmcentrez&rendertype=abstract

[142] Ramamurthi, K. S., Lecuyer, S., Stone, H. a., Losick, R., Mar. 2009. Geometric cue for protein localization in a bacterium. Science (New York, N.Y.) 323 (5919), 1354–7.
URL http://www.pubmedcentral.nih.gov/articlerender.fcgi?artid=2652684&tool=pmcentrez&rendertype=abstract

[143] Ramamurthi, K. S., Losick, R., Aug. 2009. Negative membrane curvature as a cue for subcellular localization of a bacterial protein. Proceedings of the National Academy of Sciences of the United States of America 106 (32), 13541–5.
URL http://www.pubmedcentral.nih.gov/articlerender.fcgi?artid=2726380&tool=pmcentrez&rendertype=abstract

[144] Rapsomaniki, M. A., Kotsantis, P., Symeonidou, I.-E., Giakoumakis, N.-N., Taraviras, S., Lygerou, Z., Jul. 2012. easyFRAP: an interactive, easy-to-use tool for qualitative and quantitative analysis of FRAP data. Bioinformatics (Oxford, England) 28 (13), 1800–1.
URL http://www.ncbi.nlm.nih.gov/pubmed/22543368

[145] Raskin, D., de Boer, P., 1999. MinDE-dependent pole-to-pole oscillation of division inhibitor MinC in Escherichia coli. Journal of Bacteriology 181 (20).
URL http://jb.asm.org/content/181/20/6419.short

[146] Raskin, D. M., de Boer, P. a., Apr. 1999. Rapid pole-to-pole oscillation of a protein required for directing division to the middle of Escherichia coli. Proceedings of the National Academy of Sciences of the United States of America 96 (9), 4971–6.
URL http://www.pubmedcentral.nih.gov/articlerender.fcgi?artid=21801&tool=pmcentrez&rendertype=abstract

[147] Reyes-Lamothe, R., Nicolas, E., Sherratt, D. J., Jan. 2012. Chromosome replication and segregation in bacteria. Annual review of genetics 46, 121–43.
URL http://www.ncbi.nlm.nih.gov/pubmed/22934648

[148] Reyes-Lamothe, R., Wang, X., Sherratt, D., May 2008. Escherichia coli and its chromosome. Trends in microbiology 16 (5), 238–45.
URL http://www.ncbi.nlm.nih.gov/pubmed/18406139

[149] Rimsky, S., Travers, A., Apr. 2011. Pervasive regulation of nucleoid structure and function by nucleoid-associated proteins. Current opinion in microbiology 14 (2), 136–41.
URL http://www.ncbi.nlm.nih.gov/pubmed/21288763

[150] Ringgaard, S., Schirner, K., Davis, B. M., Waldor, M. K., Jul. 2011. A family of ParA-like ATPases promotes cell pole maturation by facilitating polar localization of chemotaxis proteins. Genes & Development 25 (14), 1544–1555.
URL http://www.pubmedcentral.nih.gov/articlerender.fcgi?artid=3143943&tool=pmcentrez&rendertype=abstract

[151] Ringgaard, S., van Zon, J., Howard, M., Gerdes, K., Nov. 2009. Movement and equipositioning of plasmids by ParA filament disassembly. Proceedings of the National Academy of Sciences of the United States of America 106 (46), 19369–74.
URL http://www.pubmedcentral.nih.gov/articlerender.fcgi?artid=2775997&tool=pmcentrez&rendertype=abstract

[152] Roberts, M. a. J., Wadhams, G. H., Hadfield, K. a., Tickner, S., Armitage, J. P., Apr. 2012. ParA-like protein uses nonspecific chromosomal DNA binding to partition protein complexes. Proceedings of the National Academy of Sciences, 1–6.
URL http://www.pnas.org/cgi/doi/10.1073/pnas.1114000109

[153] Rolig, A. S., Shanks, J., Carter, J. E., Ottemann, K. M., Oct. 2012. Helicobacter pylori requires TlpD-driven chemotaxis to proliferate in the antrum. Infection and immunity 80 (10), 3713–20.
URL http://www.pubmedcentral.nih.gov/articlerender.fcgi?artid=3457577&tool=pmcentrez&rendertype=abstract

[154] Romagnoli, S., Packer, H. L., Armitage, J. P., 2002. Tactic Responses to Oxygen in the Phototrophic Bacterium Rhodobacter Tactic Responses to Oxygen in the Phototrophic Bacterium Rhodobacter sphaeroides WS8N. Journal of Bacteriology 184 (20).

[155] Ross, D., Thomas, M., Williams, D., Thomas, C., 1992. Active partitioning of bacterial plasmids. Journal of general microbiology 138 (021), 1–16.
URL http://mic.sgmjournals.org/content/138/1/1.short

[156] Rudner, D. Z., Losick, R., Apr. 2002. A sporulation membrane protein tethers the prosigmaK processing enzyme to its inhibitor and dictates its subcellular localization. Genes & development 16 (8), 1007–18.
URL http://www.pubmedcentral.nih.gov/articlerender.fcgi?artid=152351&tool=pmcentrez&rendertype=abstract

[157] Rudner, D. Z., Pan, Q., Losick, R. M., Jun. 2002. Evidence that subcellular localization of a bacterial membrane protein is achieved by diffusion and capture. Proceedings of the National Academy of Sciences of the United States of America 99 (13), 8701–6.
URL http://www.pubmedcentral.nih.gov/articlerender.fcgi?artid=124362&tool=pmcentrez&rendertype=abstract

[158] Saberi, S., Emberly, E., Jan. 2010. Chromosome Driven Spatial Patterning of Proteins in Bacteria. PLoS computational biology 6 (11), e1000986.
URL http://www.ncbi.nlm.nih.gov/pubmed/21085680

[159] Sackett, M., Armitage, J., 1997. Photoresponses of the purple nonsulfur bacteria Rhodospirillum centenum and Rhodobacter sphaeroides. Journal of Bacteriology 179 (21).
URL http://jb.asm.org/content/179/21/6764.short

[160] Salje, J., Gayathri, P., Löwe, J., Oct. 2010. The ParMRC system: molecular mechanisms of plasmid segregation by actin-like filaments. Nature reviews. Microbiology 8 (10), 683–92.
URL http://www.ncbi.nlm.nih.gov/pubmed/20844556

[161] Salje, J., Löwe, J., Aug. 2008. Bacterial actin: architecture of the ParMRC plasmid DNA partitioning complex. The EMBO journal 27 (16), 2230–8.
URL http://www.pubmedcentral.nih.gov/articlerender.fcgi?artid=2519105&tool=pmcentrez&rendertype=abstract

[162] Savage, D. F., Afonso, B., Chen, A. H., Silver, P. a., Mar. 2010. Spatially ordered dynamics of the bacterial carbon fixation machinery. Science (New York, N.Y.) 327 (5970), 1258–61.
URL http://www.ncbi.nlm.nih.gov/pubmed/20203050

[163] Scholefield, G., Whiting, R., Errington, J., Murray, H., Feb. 2011. Spo0J regulates the oligomeric state of Soj to trigger its switch from an activator to an inhibitor of DNA replication initiation. Molecular microbiology 79 (4), 1089–100.
URL http://www.ncbi.nlm.nih.gov/pubmed/21235642

[164] Schulmeister, S., Ruttorf, M., Thiem, S., Kentner, D., Lebiedz, D., Sourjik, V., 2008. Protein exchange dynamics at chemoreceptor clusters in Escherichia coli. Proceedings of the National Academy of Sciences 105 (17), 6403.
URL http://www.pnas.org/content/105/17/6403.fullhttp://www.pnas.org/content/105/17/6403.short

[165] Schumacher, M. a., Glover, T. C., Brzoska, A. J., Jensen, S. O., Dunham, T. D., Skurray, R. a., Firth, N., Dec. 2007. Segrosome structure revealed by a complex of ParR with centromere DNA. Nature 450 (7173), 1268–71.
URL http://www.ncbi.nlm.nih.gov/pubmed/18097417

[166] Scott, K. a., Porter, S. L., Bagg, E. a. L., Hamer, R., Hill, J. L., Wilkinson, D. a., Armitage, J. P., Apr. 2010. Specificity of localization and phosphotransfer in the CheA proteins of Rhodobacter sphaeroides. Molecular microbiology 76 (2), 318–30.
URL http://www.ncbi.nlm.nih.gov/pubmed/20525091

[167] Shapiro, L., McAdams, H. H., Losick, R., Nov. 2009. Why and how bacteria localize proteins. Science (New York, N.Y.) 326 (5957), 1225–8.
URL http://www.ncbi.nlm.nih.gov/pubmed/19965466

[168] Shimizu, T. S., Le Novère, N., Levin, M. D., Beavil, a. J., Sutton, B. J., Bray, D., Nov. 2000. Molecular model of a lattice of signalling proteins involved in bacterial chemotaxis. Nature cell biology 2 (11), 792–6.
URL http://www.ncbi.nlm.nih.gov/pubmed/11056533

[169] Shiomi, D., Yoshimoto, M., Homma, M., Kawagishi, I., May 2006. Helical distribution of the bacterial chemoreceptor via colocalization with the Sec protein translocation machinery. Molecular microbiology 60 (4), 894–906.

URL http://www.pubmedcentral.nih.gov/articlerender.fcgi?artid=1513513&tool=pmcentrez&rendertype=abstract

[170] Simon, I., Pound, C. R., Partin, a. W., Clemens, J. Q., Christens-Barry, W. a., Apr. 1998. Automated image analysis system for detecting boundaries of live prostate cancer cells. Cytometry 31 (4), 287–94.
URL http://www.ncbi.nlm.nih.gov/pubmed/9551604

[171] Skidmore, J., Ellefson, D., 2000. Polar Clustering of the Chemoreceptor Complex in Escherichia coli Occurs in the Absence of Complete CheA Function. Journal of ....
URL http://jb.asm.org/content/182/4/967.short

[172] Sliusarenko, O., Heinritz, J., Emonet, T., Jacobs-Wagner, C., May 2011. High-throughput, subpixel precision analysis of bacterial morphogenesis and intracellular spatio-temporal dynamics. Molecular microbiology 80 (3), 612–27.
URL http://www.pubmedcentral.nih.gov/articlerender.fcgi?artid=3090749&tool=pmcentrez&rendertype=abstract

[173] Slovak, P., Wadhams, G., Armitage, J., 2005. Localization of MreB in Rhodobacter sphaeroides under conditions causing changes in cell shape and membrane structure. Journal of Bacteriology 187 (1), 54–64.
URL http://jb.asm.org/content/187/1/54.short

[174] Sockett, R. E., Armitage, J. P., May 1991. Isolation, characterization, and complementation of a paralyzed flagellar mutant of Rhodobacter sphaeroides WS8. Journal of Bacteriology 173 (9), 2786–90.
URL http://www.pubmedcentral.nih.gov/articlerender.fcgi?artid=207858&tool=pmcentrez&rendertype=abstract

[175] Sourjik, V., Armitage, J. P., Aug. 2010. Spatial organization in bacterial chemotaxis. The EMBO Journal 29 (16), 2724–2733.
URL http://www.nature.com/doifinder/10.1038/emboj.2010.178http://www.pubmedcentral.nih.gov/articlerender.fcgi?artid=2924652&tool=pmcentrez&rendertype=abstract

[176] Stragier, P., Losick, R., 1996. Molecular genetics of sporulation in Bacillus subtilis. Annual review of genetics, 297–341.
URL http://www.annualreviews.org/doi/abs/10.1146/annurev.genet.30.1.297

[177] Sullivan, N. L., Marquis, K. a., Rudner, D. Z., May 2009. Recruitment of SMC by ParB-parS organizes the origin region and promotes efficient chromosome segregation. Cell 137 (4), 697–707.
URL http://www.pubmedcentral.nih.gov/articlerender.fcgi?artid=2892783&tool=pmcentrez&rendertype=abstract

[178] Summers, D. K. D., Sherratt, D. J. D., 1984. Multimerization of high copy number plasmids causes instability: ColE 1 encodes a determinant essential for plasmid monomerization and stability. Cell 36 (April).
URL http://www.sciencedirect.com/science/article/pii/0092867484900606

[179] Swulius, M. T., Jensen, G. J., Dec. 2012. The helical MreB cytoskeleton in Escherichia coli MC1000/pLE7 is an artifact of the N-Terminal yellow fluorescent protein tag. Journal of bacteriology 194 (23), 6382–6.
URL http://www.ncbi.nlm.nih.gov/pubmed/22904287http://www.pubmedcentral.nih.gov/articlerender.fcgi?artid=3497537&tool=pmcentrez&rendertype=abstract

[180] Tang, M., Bideshi, D. K., Park, H.-W., Federici, B. a., Nov. 2006. Minireplicon from pBtoxis of Bacillus thuringiensis subsp. israelensis. Applied and environmental microbiology 72 (11), 6948–54.
URL http://www.pubmedcentral.nih.gov/articlerender.fcgi?artid=1636135&tool=pmcentrez&rendertype=abstract

[181] Taylor, B. L., Sep. 2007. Aer on the inside looking out: paradigm for a PAS-HAMP role in sensing oxygen, redox and energy. Molecular microbiology 65 (6), 1415–24.
URL http://www.pubmedcentral.nih.gov/articlerender.fcgi?artid=2586974&tool=pmcentrez&rendertype=abstract

[182] Thanbichler, M., Shapiro, L., Jul. 2006. MipZ, a spatial regulator coordinating chromosome segregation with cell division in Caulobacter. Cell 126 (1), 147–62.
URL http://www.ncbi.nlm.nih.gov/pubmed/16839883

[183] Thiem, S., Kentner, D., Sourjik, V., 2007. Positioning of chemosensory clusters in E. coli and its relation to cell division. The EMBO journal 26 (6), 1615–23.
URL http://www.ncbi.nlm.nih.gov/pubmed/17332753

[184] Thiem, S., Sourjik, V., 2008. Stochastic assembly of chemoreceptor clusters in Escherichia coli. Molecular microbiology 68 (5), 1228–36.
URL http://www.ncbi.nlm.nih.gov/pubmed/18476921

[185] Thompson, S., Wadhams, G., Armitage, J., 2006. The positioning of cytoplasmic protein clusters in bacteria. Proceedings of the National Academy of Sciences 103 (21), 8209.
URL http://www.pnas.org/cgi/content/abstract/103/21/8209http://www.pnas.org/content/103/21/8209.short

[186] Toro, E., Hong, S.-H., McAdams, H. H., Shapiro, L., Oct. 2008. Caulobacter requires a dedicated mechanism to initiate chromosome segregation. Proceedings of the National Academy of Sciences of the United States of America 105 (40), 15435–40.
URL http://www.pubmedcentral.nih.gov/articlerender.fcgi?artid=2563096&tool=pmcentrez&rendertype=abstract

[187] Toro, E., Shapiro, L., Feb. 2010. Bacterial chromosome organization and segregation. Cold Spring Harbor perspectives in biology 2 (2), a000349.
URL http://www.pubmedcentral.nih.gov/articlerender.fcgi?artid=2828278&tool=pmcentrez&rendertype=abstract

[188] Tuson, H. H., Copeland, M. F., Carey, S., Sacotte, R., Weibel, D. B., Jan. 2013. Flagellum density regulates Proteus mirabilis swarmer cell motility in viscous environments. Journal of Bacteriology 195 (2), 368–77.
URL http://www.pubmedcentral.nih.gov/articlerender.fcgi?artid=3553826&tool=pmcentrez&rendertype=abstract

[189] Uphoff, S., Reyes-Lamothe, R., Garza de Leon, F., Sherratt, D. J., Kapanidis, A. N., May 2013. Single-molecule DNA repair in live bacteria. Proceedings of the National Academy of Sciences of the United States of America 110 (20), 8063–8.
URL http://www.ncbi.nlm.nih.gov/pubmed/23630273

[190] van den Ent, F., Amos, L. a., Löwe, J., Sep. 2001. Prokaryotic origin of the actin cytoskeleton. Nature 413 (6851), 39–44.
URL http://www.ncbi.nlm.nih.gov/pubmed/11544518

[191] van den Ent, F., Mø ller Jensen, J., Amos, L. a., Gerdes, K., Löwe, J., Dec. 2002. F-actin-like filaments formed by plasmid segregation protein ParM. The EMBO journal 21 (24), 6935–43.
URL http://www.pubmedcentral.nih.gov/articlerender.fcgi?artid=139093&tool=pmcentrez&rendertype=abstract

[192] Vande Broek, a., Lambrecht, M., Vanderleyden, J., Sep. 1998. Bacterial chemotactic motility is important for the initiation of wheat root colonization by Azospirillum brasilense. Microbiology (Reading, England) 144 (Pt 9 (1 998), 2599–606.
URL http://www.ncbi.nlm.nih.gov/pubmed/9782509

[193] Vats, P., Rothfield, L., Nov. 2007. Duplication and segregation of the actin (MreB) cytoskeleton during the prokaryotic cell cycle. Proceedings of the National Academy of Sciences of the United States of America 104 (45), 17795–800.
URL http://www.pubmedcentral.nih.gov/articlerender.fcgi?artid=2077029&tool=pmcentrez&rendertype=abstract

[194] Vecchiarelli, A. G., Han, Y.-W., Tan, X., Mizuuchi, M., Ghirlando, R., Biertümpfel, C., Funnell, B. E., Mizuuchi, K., Oct. 2010. ATP control of dynamic P1 ParA-DNA interactions: a key role for the nucleoid in plasmid partition. Molecular microbiology 78 (1), 78–91.
URL http://www.pubmedcentral.nih.gov/articlerender.fcgi?artid=2950902&tool=pmcentrez&rendertype=abstract

[195] Vecchiarelli, A. G., Hwang, L. C., Mizuuchi, K., Apr. 2013. Cell-free study of F plasmid partition provides evidence for cargo transport by a diffusion-ratchet mechanism. Proceedings of the National Academy of Sciences of the United States of America 110 (15), E1390–7.
URL http://www.pubmedcentral.nih.gov/articlerender.fcgi?artid=3625265&tool=pmcentrez&rendertype=abstract

[196] Viollier, P. H., Thanbichler, M., McGrath, P. T., West, L., Meewan, M., McAdams, H. H., Shapiro, L., Jun. 2004. Rapid and sequential movement of individual chromosomal loci to specific subcellular locations during bacterial DNA replication. Proceedings of the National Academy of Sciences of the United States of America 101 (25), 9257–62.
URL http://www.pubmedcentral.nih.gov/articlerender.fcgi?artid=438963&tool=pmcentrez&rendertype=abstract

[197] Wadhams, G., Armitage, J., 2004. Making sense of it all: bacterial chemotaxis. Nature Reviews Molecular Cell Biology 5 (12), 1024–1037.
URL http://www.nature.com/nrm/journal/v5/n12/abs/nrm1524.html

[198] Wadhams, G., Warren, a. V., Martin, a. C., Armitage, J., 2003. Targeting of two signal

transduction pathways to different regions of the bacterial cell. Molecular Microbiology 50 (3), 763–770.
URL http://www.blackwell-synergy.com/links/doi/10.1046/j.1365-2958.2003.03716.x

[199] Wadhams, G. H., Martin, a. C., Armitage, J. P., Jun. 2000. Identification and localization of a methyl-accepting chemotaxis protein in Rhodobacter sphaeroides. Molecular microbiology 36 (6), 1222–33.
URL http://www.ncbi.nlm.nih.gov/pubmed/10931275

[200] Wadhams, G. H., Martin, A. C., Armitage, J. P., Warren, A. V., Nov. 2005. Requirements for chemotaxis protein localization in Rhodobacter sphaeroides. Molecular microbiology 58 (3), 895–902.
URL http://www.ncbi.nlm.nih.gov/pubmed/16238635

[201] Wadhams, G. H., Martin, a. C., Porter, S. L., Maddock, J. R., Mantotta, J. C., King, H. M., Armitage, J. P., Dec. 2002. TlpC, a novel chemotaxis protein in Rhodobacter sphaeroides, localizes to a discrete region in the cytoplasm. Molecular microbiology 46 (5), 1211–21.
URL http://www.ncbi.nlm.nih.gov/pubmed/12453209

[202] Wang, H., Wingreen, N., Mukhopadhyay, R., Nov. 2008. Self-Organized Periodicity of Protein Clusters in Growing Bacteria. Physical Review Letters 101 (21), 218101.
URL http://link.aps.org/doi/10.1103/PhysRevLett.101.218101

[203] Wang, W., Li, G.-W., Chen, C., Xie, X. S., Zhuang, X., Sep. 2011. Chromosome organization by a nucleoid-associated protein in live bacteria. Science (New York, N.Y.) 333 (6048), 1445–9.
URL http://www.pubmedcentral.nih.gov/articlerender.fcgi?artid=3329943&tool=pmcentrez&rendertype=abstract

[204] Wang, X., Liu, X., Possoz, C., Sherratt, D. J., Jul. 2006. The two Escherichia coli chromosome arms locate to separate cell halves. Genes & development 20 (13), 1727–31.
URL http://www.pubmedcentral.nih.gov/articlerender.fcgi?artid=1522069&tool=pmcentrez&rendertype=abstract

[205] Welch, M., Oosawa, K., Aizawa, S., Eisenbach, M., Oct. 1993. Phosphorylation-dependent binding of a signal molecule to the flagellar switch of bacteria. Proceedings of the National Academy of Sciences of the United States of America 90 (19), 8787–91.
URL http://www.pubmedcentral.nih.gov/articlerender.fcgi?artid=47445&tool=pmcentrez&rendertype=abstract

[206] Werner, J. N., Chen, E. Y., Guberman, J. M., Zippilli, A. R., Irgon, J. J., Gitai, Z., May 2009. Quantitative genome-scale analysis of protein localization in an asymmetric bacterium. Proceedings of the National Academy of Sciences of the United States of America 106 (19), 7858–63.
URL http://www.pubmedcentral.nih.gov/articlerender.fcgi?artid=2671984&tool=pmcentrez&rendertype=abstract

[207] Wilkinson, D. a., Chacko, S. J., Vénien-Bryan, C., Wadhams, G. H., Armitage, J. P., Aug. 2011. Regulation of flagellum number by FliA and FlgM and role in biofilm formation by

Rhodobacter sphaeroides. Journal of Bacteriology 193 (15), 4010–4.
URL http://www.pubmedcentral.nih.gov/articlerender.fcgi?artid=3147513&tool=pmcentrez&rendertype=abstract

[208] Winkler, J., Seybert, A., Pruggnaller, S., Haselmann, U., Sourjik, V., Weiss, M., Frangakis, A. S., Mogk, A., Bukau, B., 2010. Quantitative and spatio-temporal features and cellular ageing. EMBO Journal 29 (5), 910–923.

[209] Woldringh, C. L., Mulder, E., Huls, P. G., Vischer, N., 1991. Toporegulation of bacterial division according to the nucleoid occlusion model. Research in microbiology 142 (2-3), 309–20.
URL http://www.ncbi.nlm.nih.gov/pubmed/1925029

[210] Wolfe, A., Millikan, D., 2004. Vibrio fischeri σ54 controls motility, biofilm formation, luminescence, and colonization. Applied and environmental microbiology 70 (4), 2520–2524.
URL http://aem.asm.org/content/70/4/2520.short

[211] Wu, L. J., Errington, J., Aug. 2003. RacA and the Soj-Spo0J system combine to effect polar chromosome segregation in sporulating Bacillus subtilis. Molecular Microbiology 49 (6), 1463–1475.
URL http://doi.wiley.com/10.1046/j.1365-2958.2003.03643.x

[212] Wu, L. J., Errington, J., Jan. 2012. Nucleoid occlusion and bacterial cell division. Nature reviews. Microbiology 10 (1), 8–12.
URL http://www.ncbi.nlm.nih.gov/pubmed/22020262

[213] Wu, L. J., Ishikawa, S., Kawai, Y., Oshima, T., Ogasawara, N., Errington, J., Jul. 2009. Noc protein binds to specific DNA sequences to coordinate cell division with chromosome segregation. The EMBO journal 28 (13), 1940–52.
URL http://www.pubmedcentral.nih.gov/articlerender.fcgi?artid=2711181&tool=pmcentrez&rendertype=abstract

[214] Yamaichi, Y., Bruckner, R., Ringgaard, S., Möll, A., Cameron, D. E., Briegel, A., Jensen, G. J., Davis, B. M., Waldor, M. K., Oct. 2012. A multidomain hub anchors the chromosome segregation and chemotactic machinery to the bacterial pole. Genes & development 26 (20), 2348–60.
URL http://www.pubmedcentral.nih.gov/articlerender.fcgi?artid=3475806&tool=pmcentrez&rendertype=abstracthttp://www.ncbi.nlm.nih.gov/pubmed/23070816

[215] Yamaichi, Y., Fogel, M. a., Waldor, M. K., Jan. 2007. par genes and the pathology of chromosome loss in Vibrio cholerae. Proceedings of the National Academy of Sciences of the United States of America 104 (2), 630–5.
URL http://www.pubmedcentral.nih.gov/articlerender.fcgi?artid=1760642&tool=pmcentrez&rendertype=abstract

[216] Young, D., Glasbey, C. a., Gray, a. J., Martin, N. J., Nov. 1998. Towards automatic cell identification in DIC microscopy. Journal of microscopy 192 (Pt 2), 186–93.
URL http://www.ncbi.nlm.nih.gov/pubmed/9853375

[217] Zhang, P., Khursigara, C. M., Hartnell, L. M., Subramaniam, S., Mar. 2007. Direct visual-

ization of Escherichia coli chemotaxis receptor arrays using cryo-electron microscopy. Proceedings of the National Academy of Sciences of the United States of America 104 (10), 3777–81.
URL http://www.pubmedcentral.nih.gov/articlerender.fcgi?artid=1820660&tool=pmcentrez&rendertype=abstract

[218] Zimmerman, S. B., Nov. 2006. Shape and compaction of Escherichia coli nucleoids. Journal of structural biology 156 (2), 255–61.
URL http://www.ncbi.nlm.nih.gov/pubmed/16697220